

# **Microbubbles for Molecular Imaging and Drug Delivery**

Microbellen voor moleculaire beeldvorming en afgifte van geneesmiddelen

**Ilya Skachkov**  
**2016**

## Colophon

Ilya Skachkov

Microbubbles for molecular imaging and drug delivery

Thesis, Erasmus University Medical Center  
January 20, 2016.

ISBN 978-94-6233-208-9

All rights reserved. No part of this publication may be reproduced, stored in a retrieval system, or transmitted, in any form, or by any means, electronic, mechanical, photocopying, recording, or otherwise, without the prior consent from the author, or when appropriate, from the publishers of the publications.

© 2016, I. Skachkov except for the following chapters:

Chapter 2, 3: Elsevier B.V., 2012, 2014

Chapter 5: IEEE, 2014

Chapter 6: Wiley Periodicals, Inc., 2015

Chapter 8 (partly): Informa UK Limited, an Informa Group Company, 2015

Cover designed by: Natalia Shirgina and Ilya Skachkov

Printed in the Netherlands by Gildeprint.

For a printed version please contact:

Secretary Biomedical Engineering (January 2016: room Ee 2302)

Erasmus Medical Center

P.O. Box 2040

3000 CA Rotterdam

the Netherlands



# Microbubbles for Molecular Imaging and Drug Delivery

Microbellen voor moleculaire beeldvorming en afgifte van geneesmiddelen

## Proefschrift

ter verkrijging van  
de graad van doctor aan de  
Erasmus Universiteit Rotterdam  
op gezag van de  
rector magnificus

Prof.dr. H.A.P. Pols

en volgens besluit van het College voor Promoties.

De openbare verdediging zal plaatsvinden op  
woensdag 20 januari 2016 om 15:30 uur door

**Ilya Skachkov**

geboren te Gukovo, Rusland

## **Doctoral Committee**

Promotors:            Prof.dr.ir. N. de Jong  
                             Prof.dr.ir. A.F.W. van der Steen

Other members:      Prof.dr.ir. M. de Jong  
                             Prof.dr. C.K. Holland  
                             Prof.dr. A. Bouakaz

Copromotor:          Dr. K. Kooiman

The work described in this thesis was performed at the Department of Biomedical Engineering of Erasmus University Medical Center, Rotterdam, the Netherlands. This work was financially supported by NMP-LA-2008-213706 Sonodrugs.



## Financial support:



# Contents

|   |     |
|---|-----|
| Chapter 1 Introduction .....  | 9   |
| Chapter 2 <i>In Vivo</i> Characterization Of Ultrasound Contrast Agents: Microbubble Spectroscopy In A Chicken Embryo ..... | 17  |
| Chapter 3 Imaging Microvasculature With Contrast-Enhanced Ultraharmonic Ultrasound .....                                    | 31  |
| Chapter 4 Cell Membrane Permeability Dynamics After Sonoporation.....   | 45  |
| Chapter 5 Targeted Microbubble Mediated Sonoporation of Endothelial Cells <i>in vivo</i> .....                              | 59  |
| Chapter 6 Intravital Microscopy of Localized Stem Cell Delivery Using Microbubbles and Acoustic Radiation Force .....       | 69  |
| Chapter 7 SPIO Labeling of Endothelial Cells Using Ultrasound and Targeted Microbubbles at Low Mechanical Index .....       | 81  |
| Chapter 8 Adapted from: "Targeted Ultrasound Contrast Agents for Ultrasound Molecular Imaging and Therapy" .....            | 95  |
| Summary and Outlook.....  | 117 |
| Nederlandse samenvatting.....   | 121 |
| Bibliography.....   | 125 |
| Abbreviations and symbols .....   | 147 |
| Curriculum Vitae.....   | 151 |
| Acknowledgements .....  | 153 |
| Publications .....  | 157 |
| PhD Portfolio .....   | 159 |





# Chapter 1

## **Introduction**

# Chapter 1

## History of medical sound

Sound has been widely used in medicine since ancient times. The first documentation of this evidence belongs to Hippocrates describing how he would listen to the heart activity for diagnosis of disease (c. 460 – c. 370 BC). Since then physicians have used their ears as natural diagnostic equipment, listening to the sounds of various human organs for making diagnoses. This technique was named *auscultation*, based on the Latin verb *auscultare* that means, "to listen". Until the 19<sup>th</sup> century, doctors used this technique by directly putting their ears onto the patient's body which was neither hygienic nor very efficient. In 1816 the French doctor René Laennec invented the first medical acoustical device: the stethoscope. The first echo examination appeared even earlier by the Austrian doctor *Leopold von Auenbrugger* in 1761. He invented the method of percussion, where the physician analyzes the sound tones coming from the thorax or abdomen after tapping on the surface of the patient with the physician's fingers. According to some, a method similar to percussion to check the abdominal cavity was proposed even earlier by the Persian physician and philosopher Ali Abu Ibn Sina, also known as Avicenna (980-1037), [1]. The first real of ultrasound in diagnostics was in 1949 by John Wild and the first B-mode scanner appeared in 1962 developed by Joseph Holmes, William Wright, and Ralph Meyerdirk.

## Ultrasound contrast agents

In 1968 the first ultrasound contrast agent was discovered by accident when an infusion of microbubbles in agitated saline significantly increased blood contrast in ultrasound [2]. The agitated saline was saturated with small air bubbles. Since then microbubbles (1-10  $\mu\text{m}$  in size; see Figure 1) have been developed into clinical ultrasound contrast agents to aid diagnosis by ultrasound imaging [3]-[9]. Ultrasound contrast agents are widely used in echocardiography [10] for left ventricle delinearization and assessing heart perfusion for carotid artery diseases [11], for liver and kidney lesion diagnostics [12], and even for digestive tract imaging [13]. The uniqueness of the gas microbubbles is the scattering of ultrasound, which provides higher contrast imaging [7]. However, uncoated air microbubbles are not stable and their lifetime is just a few seconds after injection [2]. Therefore, microbubble stability has been improved mainly in two ways: encapsulating the gas microbubble by a shell and changing the gas core of the microbubble to a less soluble gas. Most commercial microbubble shells consist of lipids (Definity, SonoVue, Sonazoid, Lumason), and some with proteins (Albunex) or rigid polymers (PB127, BG1135). The air that we breathe has a very high solubility in blood and was therefore replaced by the inert sulfur hexafluoride or hydrophobic perfluorocarbon [9], [14]. If the shell of the microbubble is flexible, the gas core oscillates in response to the ultrasound. This oscillation can cause different linear and non-linear effects which can be beneficial to ultrasound imaging [14], [15]. In response to the ultrasound, the microbubble can jet, oscillate spherically or non-spherically, or induce micro-streaming [14]. Another valuable effect of this microbubble oscillation, a volumetric change in size, is their ability to effect the surrounding environment. It has been shown that these microbubble behaviors, when in the vicinity of a cell membrane, increase the membrane permeability, which is known as sonoporation [14], [16]. Sonoporation

## Introduction

has various applications, such as increasing cell sensitivity to drugs or contributing to local drug delivery [17]-[21]. In addition to sonoporation, there are two other known mechanisms of microbubble-mediated drug delivery: endocytosis and cell-cell contact opening [14], [22].

Depending on the drug type, different uptake routes are needed while others need to be avoided. For example, gene delivery requires direct cytosolic uptake while avoiding endocytosis as this process degrades the gene, which can be achieved with microbubbles. Direct cytosolic uptake can be achieved by vibrating microbubble-induced sonoporation, which is reversible (if pore size is  $< 100 \mu\text{m}^2$ ) or irreversible cell membrane perforation [23]

The microbubble shell can be modified by the addition of ligands that have a high affinity to cell membrane biomarkers, as illustrated in Figure 2. Disease-specific biomarkers appear on the endothelial cell surface during the growth of new vessels (for example  $\alpha_v\beta_3$  [24]), ischemia (for example P-selectin [25]), or inflammation (for example intercellular adhesion molecule-1, ICAM-1 [26]). Targeted microbubbles give rise to a new diagnostic tool, namely ultrasound molecular imaging [27], [28]. For example, BR55 (Bracco Research SA, Geneva, Switzerland) is a vascular endothelial growth factor receptor 2 (VEGFR2) targeted microbubble [29], [30]. After a successful phase 0 trial [31], BR55 is currently in a phase 1 clinical trial for prostate cancer diagnosis [32].

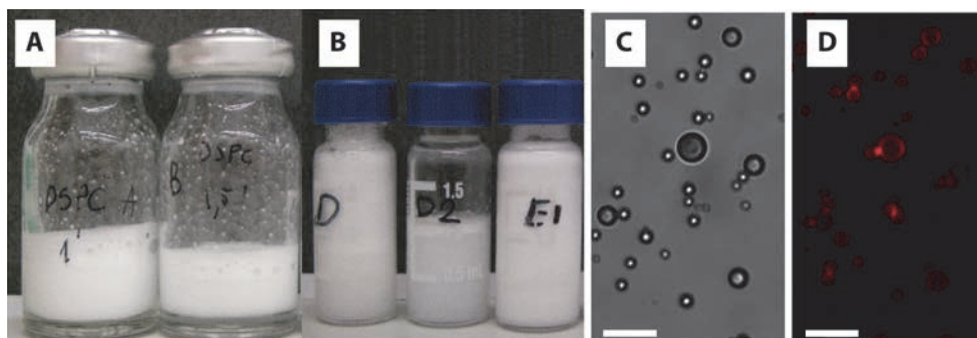


**Figure 1.** Different homemade lipid-shelled microbubbles. Microbubbles were made by sonication (A) and by agitation (B). Microscopic images ( $\times 60$ ) of lipid shell microbubbles labeled with DiI (1,1'-dioctadecyl-3,3,3',3'-tetramethylindocarbocyanine perchlorate) in bright field (C) and fluorescence (D). Scale bar:  $10 \mu\text{m}$ .

## Models for studying MB behavior

### *In vitro* models

To study microbubble behavior for ultrasound imaging and drug delivery, a simple, cheap, and relevant model is desired. All the existing models can be divided into three big groups: *in vitro*, *ex vivo* and *in vivo*. To gather knowledge on the phenomenon of microbubble oscillation, *in vitro* setups usually consist of a thin-wall capillary [33], [34] or an ultrasound transparent chamber [35]-[37]. These *in vitro* models are suitable to understand basic physical phenomena of microbubble behavior in an ultrasound field. However, these models generally cannot take into consideration the interaction of microbubbles with the human internal environment, such as the blood pool and endothelial cells that line a vessel, as depicted in Figure 2. The temperature at which these experiments are performed is usually at room temperature, not body

## Chapter 1

temperature [14]. To truly study the effect of microbubble interactions with cells and the mechanisms of drug delivery, the microbubbles have to be insonified in the presence of live cells. The two main *in vitro* models of this approach is the insonification of a cell suspension mixed with microbubbles [38] and the microbubbles near or adherent to a cell monolayer [39]. The choice of cell type is also important for the model. Escoffre et al. [40] showed that two different cell lines had different sonoporation efficacy, while insonified at the same conditions. The most widely used cell types for the *in vitro* studies are different tumor cell lines [14]. However, the clinical administration route for microbubbles is intravenous, so upon injection in the blood flow the microbubbles are only in contact with circulating blood cells and endothelial cells that line the vessels (Fig.2) as they are too large to extravasate [8], [41]. These facts are the reason why endothelial cells are more relevant to use in *in vitro* sonoporation experiments.

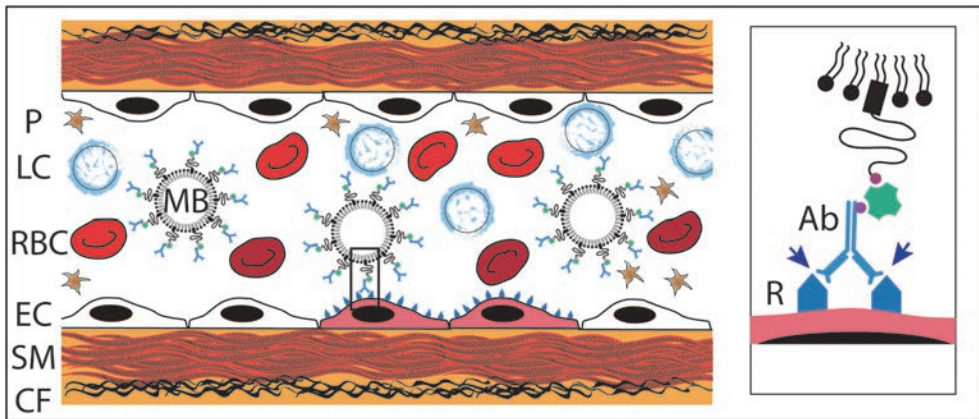


**Figure 2.** Targeted microbubbles (MB) red blood cells (RBC), leucocytes (LC) and platelets (P) inside the vessel. EC – endothelial cells, SM – smooth muscles, CF – collagen fibers. R – receptor (biomarker) on endothelial cell membrane, Ab – antibodies specific to this receptor. (Adapted from [42] i. e. Chapter 8).

### **Ex vivo models**

*Ex vivo* models aim to imitate the *in vivo* environment. These models utilize surgically dissected tissues obtained at autopsy or from freshly slaughtered animals. The most widely used *ex vivo* tissues for microbubble research are arteries [43], [44] or an entire organ, such as a liver [45], [46]. For optical imaging, the use of thin transparent tissue like mesentery [47] are often used. Although the vascular anatomy and vessels surrounding tissues remain intact in the *ex vivo* models, the blood inside the vessels is usually flushed away [47]. In addition, it is a challenge to keep a natural pressure in the vessels. As a consequence, the microbubbles can still not be studied in their *in vivo* environment within *ex vivo* models. This is why an appropriate *in vivo* model is required.

### ***In vivo* models**

One of the main requirements for an *in vivo* model is that it should be possible to study microbubble-cell interactions optically, among others, optical studies on microbubble behavior have brought the field forward. To be able to do optical studies, an optically transparent thin vascularized part of the animal should be placed under the microscope. There are several models available which fulfill these requirements, such as the mouse or rat cremaster muscle, hamster cheek pouch, dorsal skinfold model [48]-[51] and chicken embryo chorioallantoic membrane (CAM) model. The mouse or rat cremaster muscle and the hamster cheek pouch models are based on healthy animal tissues. The surgical trauma alone to expose the cremaster muscle can already upregulate the P-selectin biomarker [52]. Others induce ischemia [53] or inject substances like tumor necrosis factor  $\alpha$  (TNF $\alpha$ ) to induce inflammation and upregulate related biomarkers to make these *in vivo* models applicable to studying targeted microbubbles. The dorsal skinfold model can be combined with a subcutaneous tumor engraft, but this model requires a glass or plastic cover that is not acoustically transparent. It is therefore challenging to insonify the tissue and straight animal regulations are also applied to this model. By contrast, the latter is not the case for chicken embryos, for which the chorioallantoic membrane (CAM) has been used by several groups for studying different types of drug delivery systems [54], including microbubbles [54]-[56].

### **Chorioallantoic membrane (CAM) model**

The CAM (Fig. 3) is one of the three extraembryonic membranes that protect and nourish the embryo, the other two being the yolk sac membrane and the amnion. They are all formed during development. The CAM is a temporary embryo organ used mainly for gas exchange, but also is involved in excretion. This organ is highly vascularized, contains arteries, veins, and an intricate capillary plexus. Until day 11, capillary proliferation is rapid [54]. In addition, the CAM becomes optically transparent when the yolk is removed without losing embryo viability, as we demonstrate in Chapter 2. The CAM vessel endothelial cells uniformly express the important angiogenic marker  $\alpha_v\beta_3$ -integrin [57]. This makes the CAM model very well suited to study ultrasound molecular imaging and targeted microbubble-mediated drug delivery of angiogenesis, relevant to both tumors and atherosclerosis.

CAM vessels have shear rates of  $\sim 18\text{-}75\text{ s}^{-1}$  [58] which is similar to the shear rate in human veins [59]. A comparable heart beat rate of 60-70 beats per a minute [60] and a slightly lower hematocrit of  $\sim 24\%$  [61] make the CAM very relevant for studying microbubble behavior *in vivo*. The total embryo blood volume at day 6, a stage where the CAM already comprises many vessels as shown in Figure 3, is  $\sim 170\text{ }\mu\text{l}$  [61], and because there is almost no microbubble clearance in the lungs and liver because of an immature immune system, the microbubbles stay in circulation for hours. The combination of the small blood volume with a long lifetime allows us to use small amounts of drugs and microbubbles. Moreover, the CAM is covering the yolk and no surgery is required to get access to the vessels. To access the vessels, only the eggshell has to be opened. Also anesthesia is not required during the entire procedure. This is important because previous research has shown that high oxygen concentrations used as an anesthesia

# Chapter 1

---

carrier gas causes microbubble deflation [62]-[64]. Another advantage of the chicken embryo is that they can easily be genetically modified to express potentially any biomarker [65]. The chicken embryo model can also be used together with ultrasound because the yolk has a low scattering for ultrasound [56]. Additionally, since we used the chicken embryos at day 5-6, this model does not require laboratory animal regulation as long as the time period is before day 14 after fertilization.

## Aim of thesis

For both imaging and drug delivery the microbubble behavior in response to the ultrasound is important. This behavior can be different in different conditions [14] and is not fully understood *in vivo*. The overall aim of my thesis was to study individual microbubbles and their capacity for imaging and drug delivery in the CAM model. The exception was the studies on sonoporation dynamics and MRI-contrast agent labeling for which fundamental *in vitro* studies with human umbilical vein endothelial cells (HUVEC) were still needed.

For the majority of the chapters in my thesis, we used homemade lipid-shelled microbubbles (see Fig. 1). There are several advantages of using homemade microbubbles: 1) we can make both targeted and non-targeted microbubbles with the same lipid shell composition; 2) we can be sure to have the same size distribution; 3) they respond similarly to the ultrasound; 4) homemade microbubbles can be labeled with a fluorescent dye for easy identification under the microscope.

## Outline of thesis

To understand how MBs oscillate in response to the ultrasound in *in vivo* vessels with blood flow, heart pulsation, and circulating blood cells, ultra high-speed intravital microscopy is required. In Chapter 2 we study the microbubble oscillation while insonified at different ultrasound frequencies (microbubble spectroscopy) in the CAM model. The microbubble oscillations were recorded at 25 million frames per second with the ultrahigh-speed Brannan 128 camera [66].

The vessels in the CAM are unique because they are neovessels and thus resemble the neovessels of the atherosclerotic plaque. Atherosclerosis is a complex disease [67]. Being able to improve the diagnosis of an atherosclerotic plaque at risk for rupture in a patients is clinically important. Neovessels in a plaque are known to be a high risk for rupture [24], [68]. To resolve the composition of the vessel wall in arteries, intravascular ultrasound catheters (IVUS) are used [69]. However, conventional IVUS cannot resolve small neovessels in the plaque. It was suggested that microbubbles can help depict these vessels. In Chapter 3 we check this hypothesis first *in vitro* with a phantom with holes of different diameters. Nonetheless in conditions of real blood flow, the microbubbles could respond differently (see Chapter 2). The plaque neovessels are very similar to vessels in the chicken embryo chorioallantoic membrane (CAM) (see Fig. 3). In Chapter 3 we used the CAM model to investigate the feasibility of imaging neovessels with IVUS.

To improve drug delivery, we have to know which ultrasound setting and microbubble type to use. Moreover, different therapeutic strategies, like killing tumor cells or delivering drugs

and genes to a certain tissue, may require different levels of increased cell membrane permeability. In Chapter 4 we study the effect of ultrasound-activated targeted and non-targeted microbubbles on endothelial cell membrane permeability using different acoustical pressures and pulse lengths *in vitro*. The cell membrane permeability was correlated to cell death.

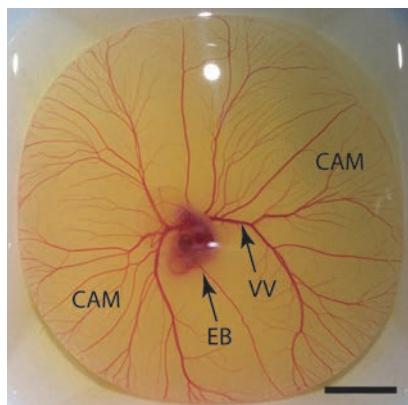


**Figure 3.** Six-day old chicken embryo extracted from the egg shell. CAM – chorioallantoic membrane, EB – embryo body, VV – vitelline vein. Scale bar: 1 cm.

In Chapter 5 we assess if ultrasound and targeted microbubbles can induce sonoporation *in vivo*. The CAM model was used again to assess how different local microbubble concentrations would increase the probability of sonoporation. This chapter shows the importance of a high local microbubble concentration, as this increases the sonoporation probability. One of the methods to increase the microbubble concentration is to use radiation force to push microbubbles to the vessel wall. If microbubbles are loaded with the drug, or a therapeutic cell, this approach could also increase the local drug concentration or therapeutic cell concentration.

In Chapter 6 we study the effect of acoustical radiation force to position stem cells incrustated with microbubbles (StemBells) to the vessel wall *in vivo* using the CAM model. This positioning could potentially increase stem cell concentration in, for example, a myocardial infarction area. In addition, it could increase stem cell extravasation from the lumen of the vessel and their migration to the ischemic area. Because this extravasation might be more efficient in small vessels where the blood flow speed is not as high as in arteries and the distance to the wall is also smaller, the CAM model is very well suited to study the effect of radiation forces for propelling StemBells to the vessel wall in blood flow conditions.

Microbubbles and ultrasound can be used for loading cells with drugs. Drugs can be small molecules (for example the chemotherapeutic Sunitinib [70], 398 Da (~1 nm in diameter based on [71]) but also large particles of 80-100 nm in size, such as liposome-encapsulated Doxorubicin [72]. Particles of different sizes require different mechanisms of microbubble-mediated uptake as shown by Meijering et al. [35]: small particles can enter cells via sonoporation while large particles can enter via endocytosis. In Chapter 7 we study *in vitro* endothelial cell labeling with a large particle, namely an MRI contrast agent, which can

## Chapter 1

---

potentially be used for *in vivo* cell labeling and tracking with MRI. We assess how different MRI contrast agent addition times in respect to the ultrasound exposure effect the loading efficiency at different acoustical pressures.

In Chapter 8 we discuss the current status of using targeted microbubbles for molecular imaging and drug delivery. This includes the important physical and chemical properties of microbubbles for this purpose. A summary of all thesis chapters and the future prospective are given in Chapter 9.



# Chapter 2

## ***In Vivo* Characterization Of Ultrasound Contrast Agents: Microbubble Spectroscopy In A Chicken Embryo**

*Ultrasound in Medicine and Biology*, 2012; 38:1608–1617

Telli Faez<sup>1</sup>, Ilya Skachkov<sup>1</sup>, Michel Versluis<sup>2</sup>, Klazina Kooiman<sup>1</sup>, Nico De Jong<sup>1,3</sup>

<sup>1</sup>Biomedical Engineering, Thoraxcenter, Erasmus Medical Center, Rotterdam, The Netherlands;

<sup>2</sup>Physics of Fluids Group and MIRA Institute of Biomedical Technology and Technical Medicine, University of Twente, Enschede, The Netherlands;

<sup>3</sup>Interuniversity Cardiology Institute of The Netherlands, Utrecht, The Netherlands

**Abstract**—The dynamics of coated microbubbles was studied in an *in vivo* model. Biotinylated lipid-coated microbubbles were prepared in-house and were injected into a chick embryo chorioallantoic membrane (CAM) model on the fifth day of incubation. The microbubbles, ranging between 1.0 and 3.5  $\mu\text{m}$  in diameter, were insonified in the frequency range of 4–7 MHz. Two amplitudes of acoustic pressure were applied: 300 kPa and 400 kPa. The fundamental and subharmonic responses were recorded optically with an ultra-fast camera (Brandaris 128) at 20 million frames per second. A subharmonic response was observed for 44% of the studied bubbles. From the data the frequency of the maximum fundamental and subharmonic response was derived for each individual bubble and resulted in the resonance curves of the microbubbles. All the bubbles showed shell (strain) hardening behavior for a higher acoustic pressure. We conclude that the subharmonic oscillations observed in this study belonged to the transmit at resonance (TR) regime.

**Key Words:** *Chicken embryo, Ultrasound contrast agent, Microbubbles, Subharmonic response, In vivo.*

## INTRODUCTION

Ultrasound contrast agents are used extensively in medical ultrasound imaging [69], [73]–[85]. An ultrasound contrast agent consists of small encapsulated microbubbles, which scatter the ultrasound very efficiently [7], [86]. The contrast agent is introduced in the blood to increase the scattering properties from the blood pool. The fundamental understanding of the interaction of these bubbles with the ultrasound and its resulting nonlinear vibration dynamics, is an ongoing field of research, since the quantitative knowledge of characterization of the bubbles is essential for a better engineered and optimal agent for its use in the clinic.

In-depth studies have been performed to quantify the acoustic response of the microbubbles acoustically, both in a bubble population [87]–[94] and for single bubbles [95], [96] as well as optically also for single bubble [36], [97]–[103]. Optical methods for acoustical characterization of contrast agent microbubbles have been a huge step forward in understanding the behavior of these bubbles in an ultrasound field. The physical properties of single bubbles reported for various contrast agents have shown that the acoustical response of a bubble is strongly size dependent [103], [104]. However, until now the physical influence of biological parameters, (e.g., blood flow, blood cells, vicinity or attachment to the vessel wall, floatation in the blood pool, etc.) on the dynamics of contrast agent microbubbles has been neglected or simplified. A genuine understanding of the acoustical behavior and resulting physical properties of the microbubbles can be achieved by investigating their acoustical response *in vivo*. For this purpose, we propose the chick embryo chorioallantoic membrane (CAM) model.

## ***In Vivo Characterization Of Ultrasound Contrast Agents: Microbubble Spectroscopy In A Chicken Embryo***

---

Chicken embryo is a well known animal model, which has been extensively used in various areas of research such as angiogenesis and anti-angiogenesis [105], [106], wound healing [107], tissue engineering [108], biomaterials and implants [109]-[111], biosensors [112] and drug delivery systems [54], [113]. The increasing interest in the chick embryo model and specifically its CAM is due to its simplicity, ease of visualization and low cost compared with mammalian models. The CAM of a developing chicken embryo is an extra-embryonic membrane and has a very dense capillary network, which makes it suitable for the intravenous injection of contrast agent microbubbles [114] and is easily accessible with standard optical microscopy. Moreover, the vascular network of a CAM is located in the chick mesoderm, a transparent matrix, which does not significantly absorb or scatter the incident visible light. This allows for high-contrast and high- resolution imaging.

It is reported that the vitelline network of a chicken embryo (extra-embryonic vessels, connecting the embryo to the yolk sac vasculature) is a good model for the human blood vessel network [58]. The CAM model is very often used in studying cardiac development and human birth defects because of similar structure and functionality between human and chicken embryonic hearts at early developmental stages [60], [115]. The chick during its morphogenesis undergoes true growth similar to the situation in the human embryo, whereas their developing organs increase dramatically in size. Therefore, the CAM model is considered to be one of the best model embryos for numerous in vivo manipulations such as, overexpressing secreted proteins and viral gene constructions [54], [115].

Another important aspect of using CAM models concerns studies on brain cancer tumors. Indeed, Hagedorn et al. [116] have proven that tumor growth with key features of human glioblastoma can occur in a highly reproducible manner on a CAM model. This opens a new option for preclinical in vivo testing of anti- cancer drugs, which to date is mainly performed in adult rodents, raising major ethical concerns. There are, however, several significant anatomic differences between chick embryo cardiovascular anatomy and the human fetal cardiovascular anatomy, such as the orientation of the heart within the chest cavity, which are explained in details by Schellpfeffer and Kolesari [117].

In vivo characterization of the microbubble dynamics is important for contrast-enhanced ultrasound imaging methods. The outcome of this type of studies defines the essential parameters for a suitable diagnostic imaging method such as the insonifying frequency and the acoustic pressure, in which microbubbles are more responsive to. So far, the results of in vitro experiments have been used as the reference. However, in vitro set-ups lack the complexity of a clinical environment and the physical effect of the major biological parameters such as blood plasma, red blood cells and proteins are simply neglected. Moreover, an in vivo study of the microbubble behavior has the advantage of testing the bioeffects, which contrast- enhanced diagnostic ultrasound can induce (e.g., capillary damage, cell sonoporation and hemolysis) [118]-[121].

To date, observations of bubble dynamics in actual vessels have been focused on the transient interaction of ultrasound-activated microbubbles and the blood vessel, by means of cavitation and microjetting phenomena [47], [121]-[123]. However, all these studies have been

## Chapter 2

---

performed ex vivo and the blood in the vessels was replaced with another fluid (e.g., saline mixed with ink), which does not represent a real clinical environment.

In the present study, the dynamics of ultrasound-activated microbubbles are studied in real-time. Home-made microbubbles are injected into a chick embryo CAM whilst, for the first time, investigating their in vivo fundamental and subharmonic responses at two different acoustic pressures. The dynamic response of a single bubble to pressure pulses driven at frequencies of 4–7 MHz is recorded optically using an ultra high-speed camera system. Microbubble spectroscopy techniques [36], [101], [103] were applied at acoustic pressures of 300 and 400 kPa to characterize the physical properties of the bubbles. The results are compared with in vitro experiments reported in the literature using the very same experimental technique.

### MATERIALS AND METHODS

#### *Microbubble preparation*

Biotinylated lipid coated microbubbles with a C<sub>4</sub>F<sub>10</sub> gas core were made by sonication as described by Klivanov et al. [124]. Biotinylation has no influence on the dynamics of microbubbles [125] and it is generally applied as a preparation step to functionalize the bubbles for targeting, which was not in the scope of this study.

The coating was composed of DSPC (59.4 mol%; P 6517; Sigma-Aldrich, Zwijndrecht, The Netherlands); PEG-40 stearate (35.7 mol%; P 3440; Sigma-Aldrich); DSPE-PEG (2000) (4.1 mol%; 880125 P; Avanti Polar Lipids, Alabaster, AL, USA) and DSPE-PEG (2000)-biotin (0.8 mol%; 880129 C; Avanti Polar Lipids). A measurement of 600 mg of DiI (Molecular Probes, Leiden, The Netherlands) fluorescent lipid dye dissolved in 20 mL of absolute ethanol was added to the lipid solution before sonication.

#### *Chicken embryo preparation*

As an animal model, the chicken embryo chorioallantoic membrane (CAM) was used and specifically prepared for ultra high-speed imaging under a microscope. Fertilized White Leghorn chicken eggs (*Gallus gallus domesticus*) were purchased from a supplier (Drost BV Loosdrecht, The Netherlands). After 5 days of incubation in a humidified incubator (Heraeus; Thermo Scientific, Erembodegem-Aalst, Belgium) at 37°C (stage HH27-271) according to Hamburger and Hamilton [126] criteria, the embryo was taken out of the eggshell. Then, 5 mL of the microbubble solution was injected in one of the vitelline veins using a home-made capillary glass needle and a commercial injection system (VisualSonics, Toronto, Canada). Next, the yolk was removed to enhance the transparency of the embryo [127]. The upper part of an OptiCell chamber (NUNC, Wiesbaden, Germany) was cut out and the space was filled with 1% agarose (Sigma Aldrich, Zwijndrecht, The Netherlands). The yolkless embryo was placed on the agarose and incubated in the humidified incubator for 5 min to allow the contrast agent to redistribute in the blood. Then, the embryo was transferred to the experimental set-up and covered with acoustically transparent polystyrene cover slip made out of OptiCell membrane. Figure 1 shows a chicken embryo before the yolk was removed.

## ***In Vivo Characterization Of Ultrasound Contrast Agents: Microbubble Spectroscopy In A Chicken Embryo***

---

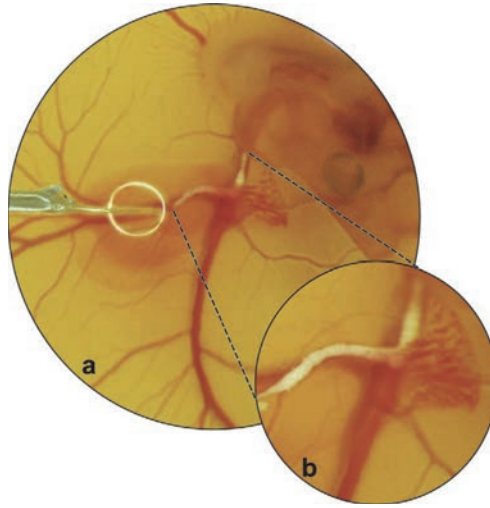


**Figure 1.** (a) Injection of microbubbles into a vitelline vein of a chicken embryo with a capillary glass needle. (b) The zoomed in area of part of the vein where the microbubbles were injected.

### ***Experimental set-up***

Figure 2 shows the schematic view of the set-up. The yolkless embryo placed on an OptiCell was fixed on a triangular water tank at the focal area of the transducer. The temperature of the water was kept at 37°C using a heating element. A wide band transducer (V311; 3–13 MHz, Panametrics, Aarselaar, Belgium, or PA076; 1–9 MHz, Precision Acoustics, Dorchester, UK) was used for transmission. The transducer was connected to a power amplifier (150A100B; Amplifier Research, Limerick, Ireland), which amplified the pulse generated by an arbitrary waveform generator (8026; Tabor Electronics Ltd., Tel Hanan, Israel). Bursts of a 25-cycle sinusoidal wave were transmitted. Microbubbles were insonified at 4–7 MHz with a frequency step of 200 kHz. Two acoustic pressures of 300 kPa and 400 kPa were applied at the focus for each experiment. These pressure values were calibrated in the same setup at the position of the embryo before placing the CAM model, using a 0.2 mm PVDF probe hydrophone (Precision Acoustics Ltd., Dorchester, UK). The region of interest was illuminated with three optical light guides (SCHOTT AG, Mainz, Germany) from below and two sides. The light guides were connected to a Xenon flash lamp (A-260; Vision Light Tech, Uden, The Netherlands). An Olympus microscope (Olympus; Zoeterwoude, The Netherlands) with a 340 water-immersed objective (NA 5 0.7) was focused on the microbubbles in the chicken embryo. The total magnification of the system was further increased to  $\times 80$  by using an additional  $\times 2$  magnification lens inside the microscope.

Before insonification the microbubbles were tracked in the vitelline vessels using a mercury lamp light source and fluorescent light (510–550 nm) excitation and a 590 nm long-pass emission filter cube (U-MWG2; Olympus Zoeterwoude, The Netherlands). With the fluorescent light we were able to differentiate the real microbubbles from other flowing

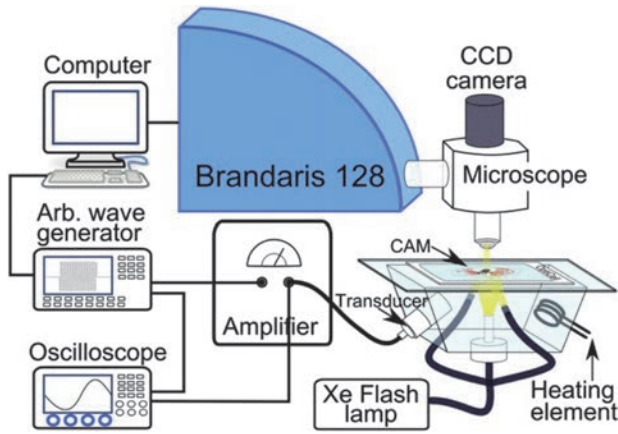


**Figure 2.** Schematic view of the set-up.

particles in the blood. Figure 3 shows the bright field and the fluorescent snapshot of a microbubble (2.3  $\mu\text{m}$  diameter) floating inside the vessel. The images were taken with a high sensitivity CCD camera (LCL-902K; Watec, Orangeburg, NY, USA) connected to the microscope. The red blood cells and vessel walls are also evident in the bright field image (Fig. 3a).

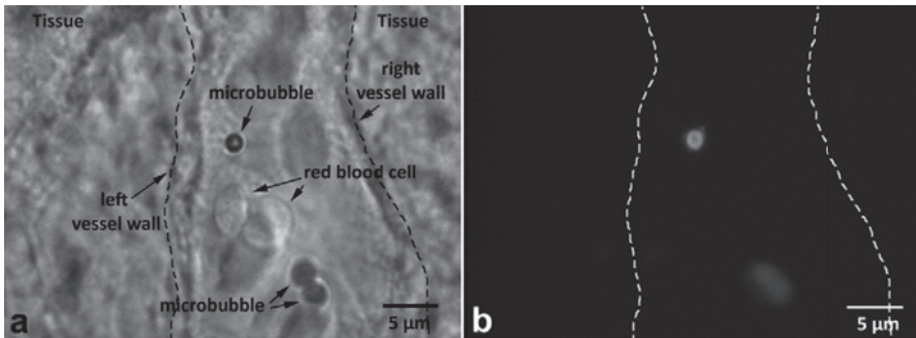


**Figure 3.** (a) Bright field and (b) fluorescent snapshots of three microbubbles, floating in a chicken embryo vein. The microbubble in focus is 2.3  $\mu\text{m}$  in diameter. The other two microbubbles are out of focus.

Different from an in vitro setting, the pulsation of the blood flow and the circulation of red blood cells add more complexity to the tracking of the bubbles. Keeping a bubble fixed and in focus for a single microbubble spectroscopy is very challenging. To overcome these difficulties, we had to look for bubbles mostly floating inside smaller capillaries with slower blood flow, relatively far from the heart or in the vicinity of a vessel wall, to avoid the vibrations and have a more stable focus. Very often the focus had to be adjusted simultaneously during the recordings.

The radial responses of the insonified bubbles were recorded with an ultra-fast recording camera, the Brandaris 128 [66] at a frame rate of 20 million frames per second. The camera

## ***In Vivo Characterization Of Ultrasound Contrast Agents: Microbubble Spectroscopy In A Chicken Embryo***

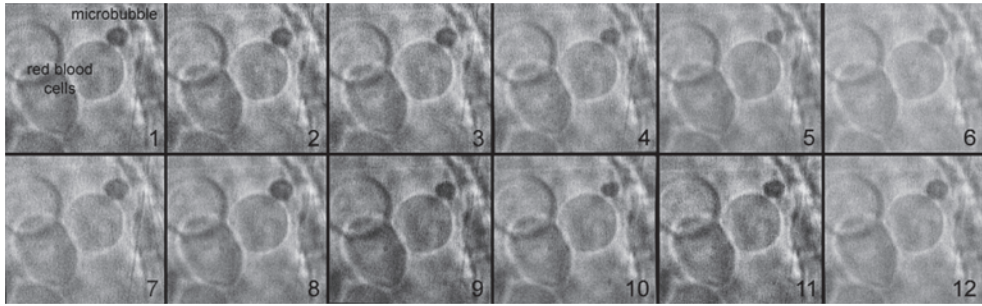


**Figure 4.** Twelve time frames out of 128 frames with 50 ns inter-frame time of a  $2.3\ \mu\text{m}$  bubble, indicating its radial oscillations, and red blood cells in a vessel. The driving frequency and acoustic pressure are 4 MHz and 300 kPa respectively.

was set to record 33 movies of 128 frames in a single run. The first recording was always done without ultrasound to estimate the resting radius of the bubbles and the noise level of the system. In the subsequent movies, the frequency was swept in 16 200-kHz steps in ascending order from 4 to 7 MHz at an acoustic pressure of 300 kPa, followed by 16 200-kHz frequency steps at 400 kPa. As an example, we display 12 time frames from the recording of a  $2.3\ \mu\text{m}$  bubble depicting the vibration at a driving frequency of 4.0 MHz and acoustic pressure of 300 kPa (Fig. 4). The bubble is located next to the right vessel wall and the red blood cells in the blood flow in the vicinity of the microbubble are also evident in the recorded frames.

From each individual movie, the diameter of the microbubble as a function of time (DT-curve) was measured using custom-designed image analysis software [101], [103]. The Discrete Fourier transform of the DT-curves was then calculated, which gives the maximum amplitude of radial excursion of the bubble at that given frequency and pressure. Plotting the maximum amplitude as a function of the frequency gives the resonance curve of the bubble. Both the fundamental and the subharmonic (at half the driving frequency) resonance curves of a bubble were measured in a single experiment. The resonance frequency and the maximum subharmonic response were extracted using the same procedure explained by Faez et al. [103]. In this method, a Lorentzian function with a functional form displaying a single absolute maximum is used to fit each resonance curve.

## **RESULTS**

A total of 80 individual bubbles were recorded and their response was analyzed. As a typical example we display five DT-curves (out of the set of 16) of a  $2.8\ \mu\text{m}$  diameter bubble in Figure 5. The transmit frequency in these selected graphs increases from 4 MHz to 5.6 MHz with a frequency interval of 400 kHz. The amplitude of the acoustic pressure is 300 kPa. The maximum amplitude in the Fourier transform of the first recording from each bubble, which was done without ultrasound, was set as the noise level (gray area in Fig. 5). The corresponding power spectra show a peak at the driving frequency and at the subharmonic frequency. In this example the fundamental amplitude decreases with increasing driving frequency, which indicates that all driving frequencies are above the resonance frequency of the bubble. At a driving frequency of 4.8 MHz the subharmonic amplitude reaches a maximum.



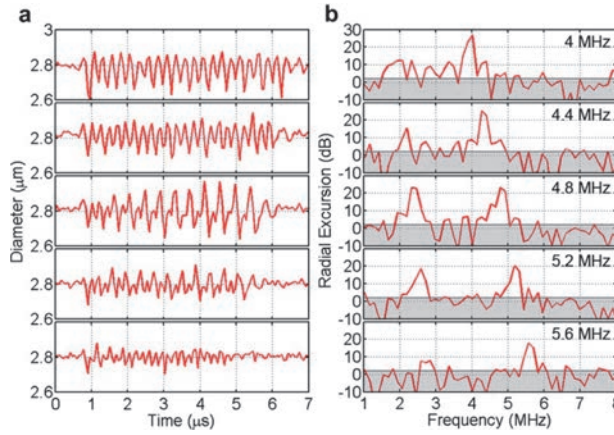


**Figure 5.** (a) Selected DT-curves and (b) corresponding power spectra of a microbubble with 2.8  $\mu\text{m}$  diameter. The selected driving frequencies range between 4–5.6 MHz with a frequency step of 400 kHz. The applied acoustic pressure is 300 kPa. The sampling time is 50 ns. The gray area in the power spectra indicates the noise floor.

For all the recordings, the amplitude of excursion at the driving frequency and subharmonic frequency were extracted from the DT-curves and plotted versus frequency. As an example, the resonance curve and subharmonic response curve of a 2.3  $\mu\text{m}$  bubble are presented in Figure 6 for two amplitudes of acoustic pressures of 300 kPa and 400 kPa. Figure 6a shows that a 2.3  $\mu\text{m}$  bubble in diameter has a resonance frequency around 4.5 MHz at a driving acoustic pressure of 300 kPa. The resonance frequency shifts slightly to 4.6 MHz by increasing the amplitude of the acoustic pressure to 400 kPa. The same bubble shows a subharmonic peak amplitude at a driving frequency of 6 MHz, which also tends to increase when driven at a frequency of 6.2 MHz when increasing the amplitude of the acoustic pressure from 300 kPa to 400 kPa (Fig. 6b).

In the studied bubble population (1.0–3.5  $\mu\text{m}$  in diameter), 44% of the microbubbles showed

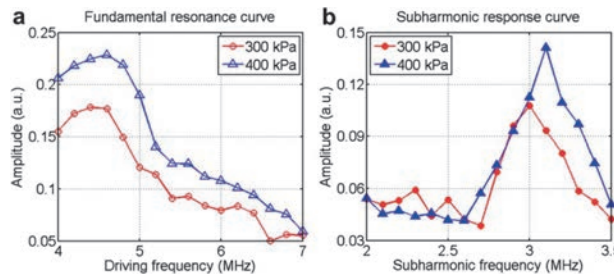


**Figure 6.** (a) The fundamental amplitude as a function of the driving frequency and (b) the subharmonic amplitude as a function of the subharmonic frequency (half the driving frequency) for a 2.3 mm bubble at acoustic pressures of 300 kPa and 400 kPa. Data on the abscissa have an uncertainty of 60.1 MHz.

subharmonic responses in the applied driving frequency range, similar to the *in vitro* results reported previously [103]. The bubbles with a subharmonic response had a size between 1.7  $\mu\text{m}$  and 3.5  $\mu\text{m}$  in diameter. In this size range, for microbubbles with a diameter smaller than



## ***In Vivo Characterization Of Ultrasound Contrast Agents: Microbubble Spectroscopy In A Chicken Embryo***

1.9  $\mu\text{m}$ , only the fundamental resonance was detectable. For bubbles larger than 2.65  $\mu\text{m}$ , only the subharmonic response peaks could be extracted as their resonance frequencies were below 4 MHz, which was the lower limit of our transmitted frequencies. However, only for bubbles between 2  $\mu\text{m}$  and 2.65  $\mu\text{m}$  in diameter, both a fundamental and a subharmonic peak in the applied driving frequency range could be clearly identified. The resonance frequency and the frequency of maximum subharmonic response of microbubbles vs. their diameters are presented in Figure 7.

To estimate a relation between the resonance frequency and the maximum subharmonic

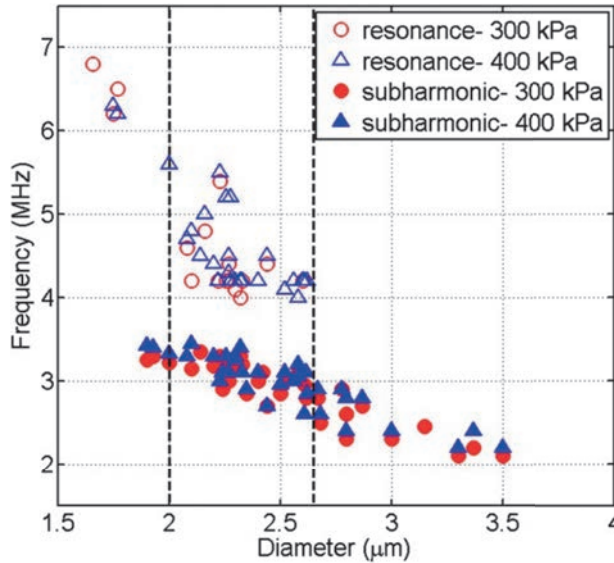


**Figure 7.** Resonance frequency and maximum subharmonic response frequency as functions of bubble size for acoustic pressure amplitudes of 300 kPa and 400 kPa. Vertical dashed lines indicate the diameter range that was used to calculate the data plotted in Figure 8.

response frequency of the microbubbles, the ratio of these two frequencies is depicted for the bubble diameters between 2  $\mu\text{m}$  and 2.65  $\mu\text{m}$  in Figure 8. It can be seen that in the mentioned diameter range the maximum subharmonic response never occurs at a frequency which is twice the resonance frequency, but slightly lower. Overall, the fundamental to subharmonic frequency ratios vary between  $1.21 \pm 0.07$  and  $1.66 \pm 0.07$  for acoustic pressure of 300 kPa. At 400 kPa, these ratios change from  $1.24 \pm 0.07$  to  $1.83 \pm 0.07$ .

## **DISCUSSION**

The fundamental and subharmonic behaviors of home made biotinylated lipid coated microbubbles were studied in vivo in the frequency range of 4–7 MHz. 44% of the total studied bubble population showed a subharmonic response in the applied driving frequency range. Similar to previous in vitro experiments [103] all the microbubbles showed asymmetrical oscillations known as compression-only behavior (Fig. 5a). The main difference between this in vivo study and the former in vitro experiments was the required higher amplitude of the

acoustic pressure. At lower acoustic pressures ( $<100$  kPa) no clear bubble oscillation could be detected for the bubbles inside the chicken embryo. We hypothesize that the main reason for this difference is due to the higher viscosity of the blood compared to water and the presence of the red blood cells [61]. The supporting argument for this assumption is the quantitative estimation of the total damping from the measured resonance curves of the microbubbles, which gives an indication of the viscous contributions of the liquid surrounding the bubble [101]. Comparing the resonance curves of a  $2.3\text{ }\mu\text{m}$  bubble in vivo (presented in Fig. 6a) and in vitro (Fig. 5, van der Meer et al. [101]), indicates that the width of the resonance curve in vivo is approximately twice that of the one in vitro. This results to a higher damping coefficient, which can be attributed to a higher viscosity of the liquid for bubble oscillations in vivo. Since the measured resonance curves in our study were not covered completely in the applied frequency range (Fig. 6a), a quantitative estimation of the values of the contributions arising from the blood viscosity was not possible. For this purpose further experiment in a wider frequency range is required.

Moreover, to study the effect of the acoustic pressure on the bubble oscillations, two amplitudes of acoustic pressure were applied (300 kPa and 400 kPa). The increase of the acoustic pressure by 100 kPa, or 33%, resulted in a slight increase of the resonance frequency and that of the subharmonic response, by 100 kHz on average, which is known as shell (strain) hardening (Fig. 6). This phenomenon was observed before for the subharmonic resonance frequency of BR14 (Bracco Research S.A., Geneva, Switzerland) microbubbles below  $3\text{ }\mu\text{m}$  in diameter [103].

The estimated resonance frequencies of the bubbles as a function of bubble size in this experiment (Fig. 7), are in a very good agreement with the reported values for the BR14 microbubbles in the literature [101], [103]. The composition of the home made bubbles used in this study is very similar to the BR14 and SonoVue (Bracco Research S.A., Geneva, Switzerland) microbubbles. Therefore, a similar range of resonance frequencies compared with the mentioned commercial microbubbles was expected. However, the values of the resonance frequencies derived in this study are slightly higher than the reported values, which can be attributed to the higher acoustic pressures applied in our case and the shell hardening phenomenon observed for increasing acoustic pressures. The differences between an in vivo and an in vitro medium in which the microbubbles are exposed can also play an important role. And finally, even though the composition of these two groups of microbubbles is very similar, the shell properties of them can be significantly different due to variations in the shell composition of the individual microbubbles, see Sijl et al. [102]. The combination of these factors can affect the physical properties of our microbubbles including resonance frequency and shell properties.

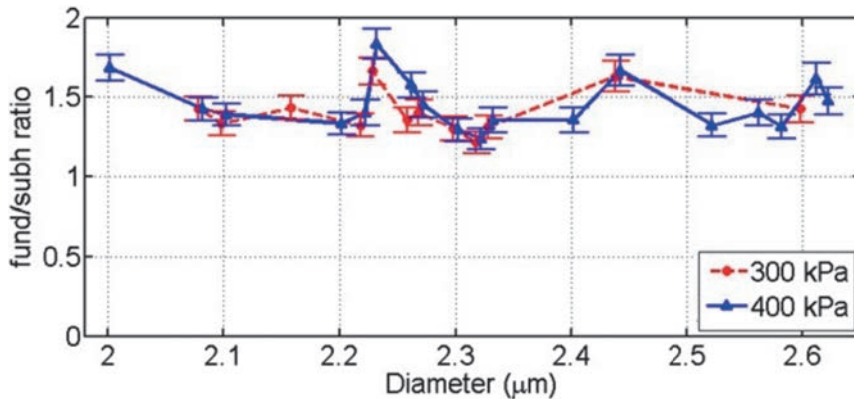


**Figure 8.** Fundamental to subharmonic response frequency ratio of microbubbles with the size range between 2–2.65  $\mu\text{m}$  for acoustic pressure amplitudes of 300 kPa and 400 kPa.

Disregarding the slight increase in the estimated resonance frequencies of biotinylated lipid coated and BR14 microbubbles, it is noted that the current values of the resonance frequencies presented in Figure 7 are in the same range as the subharmonic resonance frequencies reported recently by Faez et al. [103]. In that study, the driving frequency was set to approximately twice the resonance frequency of BR14 microbubbles. It is known that subharmonic oscillations are categorized in two regimes [128]; transmit at resonance (TR) subharmonic and transmit at twice resonance (T2R) subharmonic. The TR subharmonic oscillations are predicted to occur when a bubble is insonified at its resonance frequency. T2R subharmonic emission is predicted to occur when the transmit frequency is at twice the resonance frequency of a bubble. Therefore, the subharmonic oscillations observed in that experiment belonged to T2R subharmonic category. Consequently, the subharmonic response frequencies indicated in our study (Fig. 7) belong to the TR subharmonic regime.

The occurrence of TR and T2R subharmonic responses has been reported by Chomas et al. [128] and theoretically predicted by Katiyar and Sarkar [129]. Simulations based on Marmottant et al. [98] model are able to predict both categories of subharmonic oscillations: T2R at MI z, 0.05 and TR at MI z, 0.05 [130]. The experimental evidence on the occurrence of TR subharmonics was also reported before for BR14 bubble population [130]. However, for single bubbles in vivo this phenomenon is reported for the first time in this study.

Calculating the ratio between fundamental resonance and subharmonic response of microbubbles in the size range of 2–2.65  $\mu\text{m}$  indicates that TR subharmonic response never occurs exactly at half the resonance frequency of a microbubble. Instead, this ratio varies from 1.2 to 1.8 for different bubbles. This observation is also in accordance with the theory [129]. The comparison between the present in vivo study and a similar in vitro experiment [103] is summarized in Table 1.

## Chapter 2

Table 1. The comparison between the in vitro and in vivo microbubble spectroscopy

|                  | Microbubble spectroscopy                            | In vitro            | In vivo                  |
|------------------|---|---------------------|--------------------------|
| Input parameters | Microbubble coating                                 | Phospholipid (BR14) | Phospholipid (Home-made) |
|                  | Driving frequency (MHz)                             | 8–11                | 4–7                      |
|                  | Acoustic pressure (kPa)                             | 50–120              | 300–400                  |
| Output           | Radial oscillation                                  |                     |                          |
|                  | Subharmonic response (%)                            | Compression-only    | Compression-only         |
|                  | Subharmonic regime                                  | 40                  | 44                       |
|                  | Resonance frequency (MHz)                           | T2R                 | TR                       |
|                  | Fundamental (bubble diameter: 2–2.5 $\mu\text{m}$ ) | —                   | 5.6–4.1                  |
|                  | Subharmonic   | 5–4.5               | 3.2–2.8                  |
|                  | Shell elasticity                                    | Strain hardening    | Strain hardening         |
|                  | Shell viscosity (kg/s)                              | $\sim 10^{-9}$      | $\sim 10^9$              |
|                  | Total damping (bubble diameter: 2.3 $\mu\text{m}$ ) | $\sim 0.25$         | $\sim 0.5$               |
|                  |   |                     |                          |

Microbubble spectroscopy in vivo provides more accurate information concerning the bubble behavior and physical properties of contrast agent microbubbles. Shell properties such as elasticity and viscosity can also be extracted from this kind of experiments, similar to what has been done previously in several in vitro experiments [101]. Very often, the influence of biological aspects on the dynamics of microbubbles such as the blood flow, pulsation of the arteries, circulation of red blood cells and the vicinity of vessel walls, etc. are neglected or simplified in similar in vitro models. Compared to in vitro set-ups, the chicken embryo model is one step closer to the clinical case, which therefore makes the outcome of this kind of preclinical studies much more reliable and realistic.

More interestingly, several cases of surface modes [131] were recorded for the microbubbles confined in a vessel. As an example, five snapshots of a microbubble exhibiting surface modes of orders of 4, 5 and 6 are presented in Figure 9. Comparison between our in vitro and in vivo experiments has shown that surface modes occur more frequently in the latter case. This may be due to the additional perturbation present in the in vivo situation, possibly caused by the unsteady blood flow, the presence of the red blood cells or the rheological properties of blood

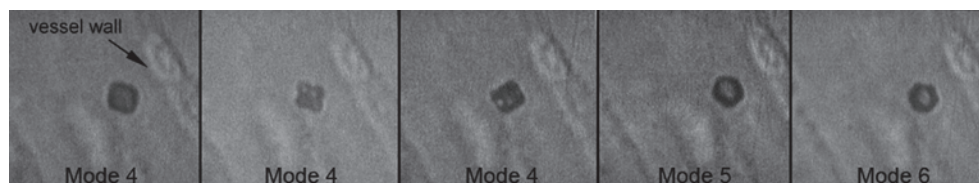


Figure 9. Surface modes of a 3  $\mu\text{m}$  bubble in orders of 4, 5 and 6.

such as viscoelasticity. However, this phenomenon certainly deserves further investigations.

Also, biological and physical phenomena involving the interaction of cells and microbubbles such as sonoporation [47], [132] can easily be investigated in similar set-ups. The following step is to characterize targeted bubbles for drug delivery purposes and experiments in this direction are currently underway.

## ***In Vivo Characterization Of Ultrasound Contrast Agents: Microbubble Spectroscopy In A Chicken Embryo***

---

### **CONCLUSION**

The fundamental and subharmonic response of home made microbubbles were measured in a chicken embryo CAM by means of microbubble spectroscopy at 4–7 MHz. Forty-four percent of the microbubbles exhibited subharmonic response that belonged to the TR subharmonic regime. All the microbubbles showed shell hardening by increasing the amplitude of acoustic pressure. Chick embryo CAM proved to be an excellent model to study microbubble dynamics in vivo.

Acknowledgments—The authors appreciate the efforts of Marcia Emmer and Miranda Foppen-Harteveld in the development of the CAM model.



# Chapter 3

## **Imaging Microvasculature With Contrast-Enhanced Ultraharmonic Ultrasound**

*Ultrasound in Medicine and Biology, 2014; 40 (6): 1318-1328*

## Chapter 3

David Maresca<sup>1</sup>, Ilya Skachkov<sup>1</sup>, Guillaume Renaud<sup>1</sup>, Krista Jansen<sup>1,2</sup>, Gijs Van Soest<sup>1</sup>, Nico De Jong<sup>1,2,3</sup>, Antonius F. W. Van Der Steen<sup>1,2,3</sup>

<sup>1</sup>Biomedical Engineering Department, Thorax Centre, Erasmus University Medical Centre, Rotterdam, The Netherlands;

<sup>2</sup>Interuniversity Cardiology Institute of the Netherlands, Utrecht, The Netherlands;

<sup>3</sup>Imaging Science and Technology Department, Delft University of Technology, Delft, The Netherlands

**Abstract—**Atherosclerotic plaque neovascularization was shown to be one of the strongest predictors of future cardiovascular events. Yet, the clinical tools for coronary wall microvasculature detection *in vivo* are lacking. Here we report an ultrasound pulse sequence capable of detecting microvasculature invisible in conventional intracoronary imaging. The method combines intravascular ultrasound with an ultrasound contrast agent, i.e., a suspension of microscopic vascular acoustic resonators that are small enough to penetrate the capillary bed after intravenous administration. The pulse sequence relies on brief chirp excitations to extract ultraharmonic echoes specific to the ultrasound contrast agent. We implemented the pulse sequence on an intravascular ultrasound probe and successfully imaged the microvasculature of a 6 days old chicken embryo respiratory organ. The feasibility of microvasculature imaging with intravascular ultrasound sets the stage for a translation of the method to studies of intra-plaque neovascularization detection in humans.

**Key Words:** *Intravascular ultrasound, Ultrasound contrast agent, Contrast-enhanced ultrasound, Ultraharmonic, Pulse inversion, Microvasculature, Vasa vasorum.*

### INTRODUCTION

The progression of human coronary atherosclerosis is associated with increased arterial wall microvasculature density [133], [134]. This network of microvasculature, the *vasa vasorum*, originates from the adventitial layer of large blood vessels to supply the deeper media and intima layers with nutrients and oxygen [135]. In atherosclerotic arteries, erratic *vasa vasorum* neovascularization can occur (Fig. 1), leading to intra-plaque hemorrhage and ultimately plaque rupture [136], [137]. It is hypothesized that atherosclerotic plaque neovascularization density could serve as surrogate marker of plaque vulnerability [136]. However, existing clinical tools are unable to detect coronary *vasa vasorum in vivo*. Intravascular ultrasound (IVUS) in combination with an ultra sound contrast agent has demonstrated potential for

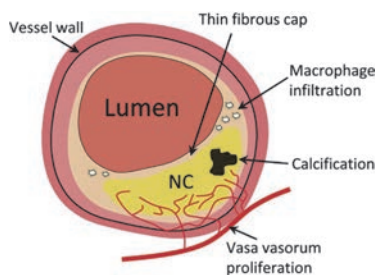


**Figure 1.** Schematic cross section of a vulnerable atherosclerotic plaque, illustrating an outside-in proliferation of the *vasa vasorum* into the atherosclerotic lesion. Other makers of atherosclerotic plaque vulnerability are represented e.g., large necrotic core, thin fibrous cap, calcification and macrophage infiltration.



*vasa vasorum* imaging [69], [79] but fails to reach clinical practice to date because of IVUS transducer limitations in frequency bandwidth and sensitivity [138]. To overcome these limitations, we developed ultraharmonic IVUS imaging, a narrow frequency bandwidth contrast detection method able to visualize subresolution microvascular networks without the blood flow velocity limitations of Doppler ultrasound [139].

Ultrasound contrast agents are suspensions of high molecular weight gas microbubbles encapsulated by thin lipid shells [140]. Bubbles are typically designed to be of a size (1–10  $\mu\text{m}$ ) that passes through capillary beds and are acoustically active at diagnostic ultrasound frequencies. The primary advantages of using ultrasound contrast agents are the improvement of the signal strength from blood, which becomes bright in echographic images (a parallel can be drawn with bright blood pulse sequences in magnetic resonance imaging), and the detection of slow micro-vascular flow in the presence of tissue motion [141]. Contrast ultrasound imaging techniques rely upon the stimulation of resonant microbubble behaviours to generate and detect harmonic ultrasound contrast agents' backscattered signals [140] that differ from tissue backscattered signals. Current harmonic contrast ultrasound imaging methods are limited to second harmonic (echo at twice the transmit frequency) or subharmonic (echo at half the transmit frequency) imaging. However, second harmonic echoes are not ultrasound contrast agent specific, while the use of subharmonic echoes lowers image resolution [78]. Furthermore, detecting second or subharmonic echoes demands a transducer frequency bandwidth of 67%, which exceeds clinical IVUS transducers specifications [138]. Several contrast echocardiography studies relied on second order ultraharmonics at 2.5 times the transmit frequency [142], [143]. But this strategy requires very wideband systems (86% frequency bandwidth) and sensitive detection of these low amplitude harmonics is further limited by the frequency-dependent ultrasound attenuation in cardiac tissue (0.5 dB/cm/MHz).

Our approach consisted in imaging contrast microbubbles using first order ultraharmonics that arise at 1.5 times the transmit frequency [140]. These signals are specific to ultrasound contrast agents and their proximity to the transmit frequency makes their capture possible with a transducer frequency bandwidth of 40% (Materials and Methods). Hence, ultraharmonic imaging allows for the emission and reception of ultrasound pulses within the sensitive frequency range of commercially available IVUS transducers. Furthermore, relying on contrast-specific ultraharmonic echoes prevents misclassifying tissue artefacts as microbubbles [144], as in the case of second harmonic imaging. For a given probe having a given bandwidth, it also provides an enhanced lateral image resolution compared to subharmonic imaging [78]. In practice, the ultrasound echoes backscattered by ultrasound contrast agents are dominated by signal at the transmit frequency. In order to isolate contrast agent ultraharmonics, we transmitted pairs of phase inverted chirp excitations, summed the backscattered echoes and filtered the residual signal in the ultraharmonic frequency range (Materials and Methods). This approach, known as pulse-inversion [145], suppresses transmit frequency signals while preserving most of harmonic signals.

### MATERIALS AND METHODS

#### Frequency bandwidth of harmonic contrast ultrasound imaging methods

The frequency bandwidth BW required for harmonic contrast ultrasound imaging is defined as the difference between the transmit ultrasound pulse frequency  $f_T$  and its harmonic echo frequency  $f_H$  over the center frequency  $f_c = (f_T + f_H)/2$ ,

$$BW = \frac{|f_T - f_H|}{f_c} = \frac{2|f_T - f_H|}{f_T + f_H} \quad (1)$$

For second harmonic ( $f_H = 2 f_T$ ) and subharmonic imaging ( $f_H = f_T/2$ ), the frequency bandwidth requirement is  $BW = 2/3$  or 67%. For ultraharmonic imaging ( $f_H = 3 f_T/2$ ), the frequency bandwidth requirement is  $BW = 2/5$  or 40%. The feasibility of a given harmonic contrast ultrasound imaging method depends on the frequency bandwidth of the ultrasound imaging probe utilized.

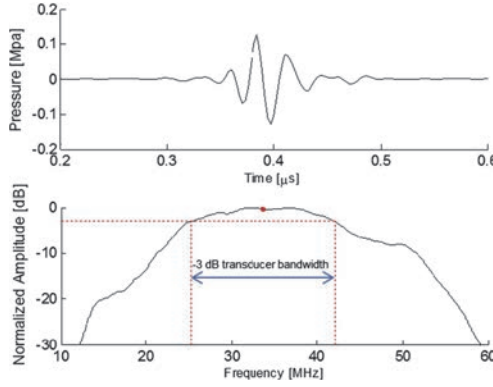


**Figure 2.** Characterization of the IVUS transducer with a needle hydrophone (Precision acoustics, Dorchester, UK). (top) Time impulse response recorded at the natural focus of the transducer (2 mm). (bottom) Frequency spectrum of the impulse response. The measured center frequency (red dot) and bandwidth (dotted lines) were in close agreement with the documented values (center frequency of 34 MHz, frequency bandwidth <60%).

#### Laboratory intravascular ultrasound imaging system

We conducted this study with a miniaturized unfocused IVUS transducer [146] (34 MHz center frequency, 56% frequency bandwidth) assembled into a side-looking IVUS probe and actuated with a rotary stage (Steinmeyer DT105, Albstadt, Germany) (Fig. 2). The transmission circuit of the IVUS imaging system comprised an arbitrary waveform generator (Tabor Electronics WW2571 A, Tel Hanan, Israel), a custom-made expander and the IVUS probe. The receive circuit consisted of a custom-made limiter, a 43 dB low noise amplifier (Miteq AU1263, Hauppauge, NY, USA) and a 12 bit digitizer (Acqiris DP310, Geneva, Switzerland) (Fig. 3). The imaging system functioned as follows: short ultrasound pulses were coded and transmitted as 16V peak-peak electric signals by the arbitrary waveform generator. The expander stopped low voltage noise while letting the pulses go to the transducer. The transducer converted electric pulses into ultrasonic pressure pulses that propagated in the medium of interest. Ultrasound echoes back-scattered in the medium and hit the transducer surface back where they were continuously converted into an electric radio frequency (RF) signal. The limiter let the low amplitude RF signal go to the low noise amplifier, while blocking the 16 V

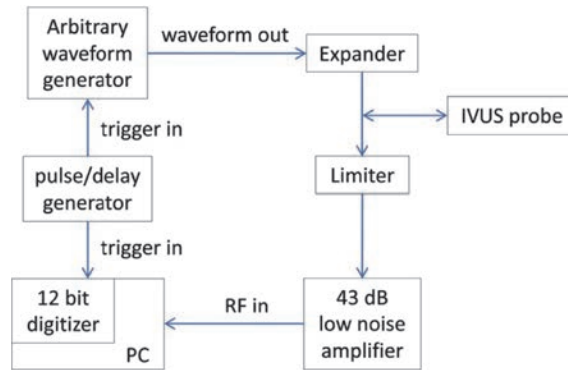


**Figure 3.** Configuration of the laboratory intravascular ultrasound electronic circuit.

pulses transmitted by the waveform generator. After amplification, the received RF signals were digitized and saved to a computer. The pulse/delay generator synchronized all instruments. We performed cross-sectional scans by rotating the IVUS probe in  $1^\circ$  steps using a motorized rotary stage. Each IVUS image consisted of 360 evenly spaced pulse-echo RF lines digitized at a sampling frequency of 350 MHz. Conventional IVUS imaging was achieved by transmitting 35 MHz 60% bandwidth Gaussian envelope sine wave pulses. These full-band pulses transmitted at the transducer center frequency provide the highest resolution attainable with our IVUS system (axial resolution =  $106\ \mu\text{m}$ , lateral resolution =  $272\ \mu\text{m}$ ). They were used to assess the microchannel's detection capabilities of conventional IVUS imaging.

### ***Ultraharmonic intravascular ultrasound pulse sequence***

The ultraharmonic pulse-inversion sequence investigated *in vitro* and *in vivo* consisted of three pairs of phase inverted [145] chirp excitations (23–29 MHz linear frequency sweep,  $0.3\ \mu\text{s}$  duration, 880 kPa peak negative pressure at focus in water, Tukey windowed with a 100% taper ratio) transmitted at each angular step. We extracted the ultraharmonic content of the digitized RF lines by summing the echoes received in response to the pairs of inverted excitations and digitally filtering the summed RF data from 33–47 MHz (Fig. 4). Frequency values were selected to operate in the most sensitive region of the IVUS transducer bandwidth (Fig. 2). Chirp excitations proved to enhance the ultraharmonic response of microbubble contrast agents by 2 dB compared to sine-bursts of identical center frequency, envelope and peak negative pressure (Fig. 5). The simulation of the pulse-inversion response of a single contrast agent [98] supported this observation (Fig. 6).

### ***Coronary vasa vasorum phantom***

The agar-based tissue mimicking material was characterized in the 10–47 MHz frequency range [147], covering our IVUS application. This ensured acoustic properties (speed of sound and attenuation) similar to those of human biological tissue. We designed a phantom geometry including a central lumen of 4 mm and two spiral arms of side channels of  $500\ \mu\text{m}$  and  $200\ \mu\text{m}$  diameters, respectively, positioned at increasing distance from the central lumen (see Fig. 8f).

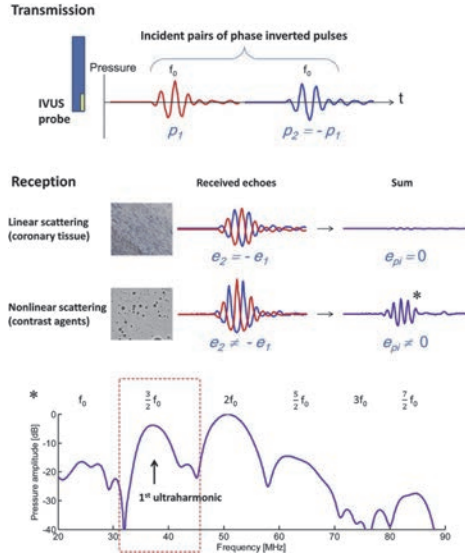


**Figure 4.** Principle of the IVUS pulse sequence. Pairs of phase-inverted pulses noted  $p_1$  and  $p_2$  are transmitted by the IVUS transducer (called a pulse-inversion sequence). Corresponding backscattered echoes  $e_1$  and  $e_2$  are received by the transducer. If the insonified medium is linear, (biological tissue) echoes stay symmetric and their sum is zero. If the medium is non-linear, (ultrasound contrast agent) echoes are distorted and their sum leaves a residue. The residual frequency spectrum of a single contrast microbubble was simulated with the Marmottant model [98] ( $1.3 \mu\text{m}$  diameter that resonates at 26 MHz, viscosity  $k_s = 4.2 \cdot 10^{-10}$ , shell elasticity  $\chi = 0.75 \text{ N/m}$ , initial surface tension  $\sigma(R_0) = 0.006 \text{ N/m}$ ). A range of harmonics are visible at multiples of the transmit IVUS frequency (26 MHz), including the first ultraharmonic response at 39 MHz, whereas the transmit frequency peak is efficiently suppressed by the pulse-inversion sequence. The waveforms utilized in the simulation are displayed in Figure 6.

### Chicken embryo model

A chicken embryo model was used for in vivo validation of the ultraharmonic ultrasound method. By day 6, chicken embryos have developed a respiratory and waste elimination organ called the allantois. This organ appears as an extra-embryonic hollow sphere delineated by a thin membrane. The allantois membrane itself is webbed with a dense network of microvessels exhibiting cross sections (diameters  $< 200 \mu\text{m}$ ) of the order of human atherosclerotic plaque *vasa vasorum* [148]. Fertilized White Leghorn chicken eggs (*Gallus gallus domesticus*) were purchased from a local supplier (Drost BV, Loosdrecht, the Netherlands). After 6 d of incubation at  $37^\circ\text{C}$  in a humidified incubator (Thermo Scientific, Erembodegem-Aalst, Belgium) corresponding to stage HH27–29 according to the Hamburger and Hamilton criteria [126], the embryos were taken out of the eggshell and placed into the experimental setup (Fig. 7). The optical reference measurements of the allantoic microvasculature imaged with IVUS were calibrated with a millimetric scale. Microvessel cross sections were measured in terms of pixel lengths using the ImageJ software (U. S. National Institutes of Health, Bethesda, MD, USA) and converted into metric units thereafter.

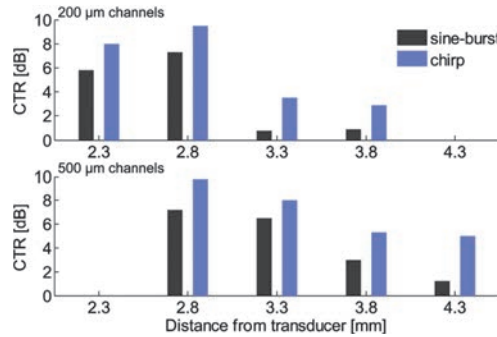


**Figure 5.** Comparison of the CTR per phantom microchannel (Fig. 8) of the ultrasound contrast agent in response to the sine-burst and chirp ultraharmonic pulse-inversion sequence. The CTR performance of the chirps was superior at every depth.

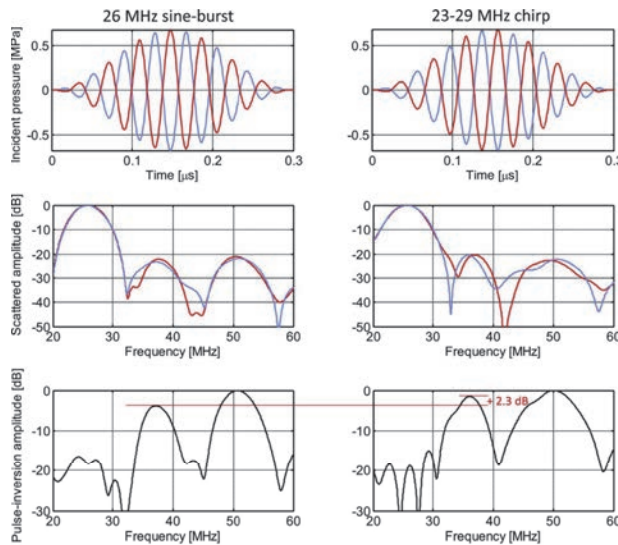


**Figure 6.** The response of a single Definity (Lantheus Medical Imaging) contrast microbubble to the sine-burst ultraharmonic pulse-inversion sequence (left column) and chirp ultraharmonic pulse-inversion sequence (right column) was simulated using the Marmottant model [98] (diameter 1.3 mm, viscosity  $k_s = 4.2.10210$ , shell elasticity  $\chi = 0.75$  N/m, initial surface tension  $\sigma(R_0) = 0.006$  N/m). The transmitted phase inverted waveforms are plotted in red and blue (top row). The frequency spectra of the waveforms scattered by a single bubble were modeled and are displayed in red and blue (middle row). The scattered pulse-inversion spectra are plotted in black (bottom row). The model predicted a 2.3 dB increase of the ultraharmonic amplitude with the use of chirps compared to sine-bursts.

## Ultrasound contrast agent handling

We used the commercial ultrasound contrast agent Definity (Lantheus Medical Imaging, N. Billerica, MA, USA). This contrast agent contains mostly microbubbles of diameters ranging from 1.1–3.3 μm, with 98% of the bubble population below 10 mm. Since a 1-μm diameter single Definity (Lantheus Medical Imaging) bubble resonates at 25 MHz [90], it is the micron- to submicron-sized bubbles that contribute mostly to the harmonic signal at IVUS frequencies.

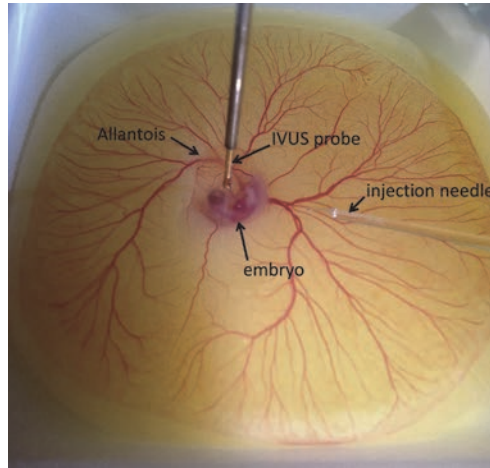


**Figure 7.** Photograph of the 6 days old chicken embryo during ultraharmonic contrast IVUS scanning. The IVUS probe was positioned next to the allantois membrane, which developed above the embryo. The bolus of ultrasound contrast agent was administered using an injection needle via the vitelline veins, upstream from the heart.

In the phantom experiment, we activated the ultrasound contrast agent according to manufacturer's recommendations (45 s controlled shaking) and diluted it in degassed water with a dilution ratio of 1:1000, which is of the order of dilutions administered in human use [149]. Subsequently, the phantom was immersed in a tank containing the prepared contrast agent solution.

In the *in vivo* experiment, we first performed a 10 min decantation of the contrast agent Definity (Lantheus Medical Imaging) after activation and subsequently extracted the bottom 0.2 mL to preferentially retain small contrast microbubbles active at our frequency range [138]. We administered a  $4 \pm 1$   $\mu$ L undiluted bolus of the ultrasound contrast agent in one of the vitelline veins of the chicken embryo using a home-made capillary glass needle and a commercial injection system (VisualSonics, Toronto, Ontario, Canada). This *in vivo* dose was shown to work in a previous chicken embryo study [117]. Due to the addition of the decantation step, however, the volumetric concentration of contrast microbubbles that we administered *in vivo* was lower [90]. In total, 14 embryos were imaged using the experimental protocol reported here.

## RESULTS

### ***Contrast agent ultraharmonic echoes locate microchannels below IVUS resolution***

We first evaluated the ultraharmonic IVUS pulse-inversion sequence by simulating [98] the scattering response of a single contrast microbubble to a pair of phase inverted chirp excitations. Transmitted IVUS chirp excitations had a 23–29 MHz frequency sweep, corresponding to a center frequency  $f_0$  equal to 26 MHz. The frequency response of the single microbubble after summing the pair phase-inverted backscattered echoes is reported (Fig. 4). The simulation result illustrates that the spectrum amplitude at the transmit frequency ( $f_0 = 26$



## Imaging Microvasculature With Contrast-Enhanced Ultraharmonic Ultrasound

MHz) and its odd multiples (third harmonic at  $3 f_0 = 78$  MHz) are significantly suppressed whereas even harmonics (second harmonic at  $2 f_0 = 52$  MHz) and ultraharmonics ( $1.5 f_0 = 39$  MHz,  $2.5 f_0 = 65$  MHz) are successfully extracted. As expected, the simulation also shows that the first ultraharmonic ( $1.5 f_0$ ) has a higher amplitude than subsequent ultraharmonics ( $2.5 f_0$ ,  $3.5 f_0$ ). Note that ultrasound attenuation in cardiac tissue, not taken into account in the simulation (Fig. 4), further increases this amplitude difference because the first ultraharmonic is less attenuated than the 2nd ultraharmonic. Experimentally, we first investigated the performance of ultraharmonic contrast IVUS in vitro by imaging a custom coronary *vasa vasorum* phantom with our laboratory IVUS imaging system (Material and Methods, Fig. 8a).

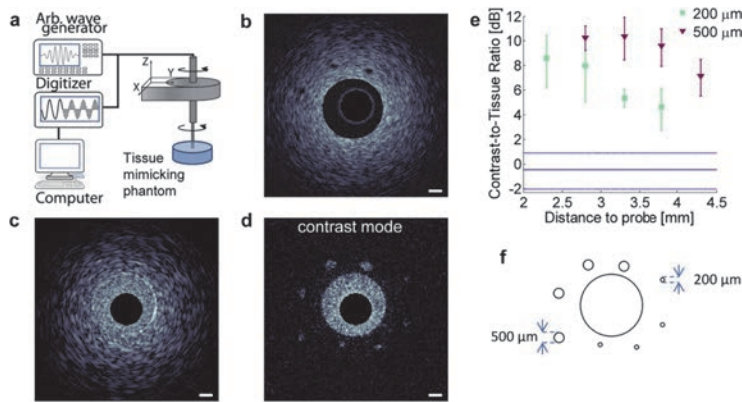


**Figure 8.** In vitro evaluation of ultraharmonic IVUS imaging. (a) Schematic setup depicting the IVUS probe actuated by the rotary stage, the arbitrary wave generator transmitting the pulse-sequence and the digitizer for data acquisition. (b) 35 MHz conventional IVUS image of the coronary *vasa vasorum* phantom; only the 500  $\mu\text{m}$  side channels were detected. Scale bars in IVUS images represent 1 mm. (c) Conventional 26 MHz IVUS image in the presence of an ultrasound contrast agent. The lumen and side channels became echogenic and could not be distinguished from the phantom material. (d) Ultraharmonic IVUS image. The lumen and all of the side channels filled with the ultrasound contrast agent were detected, including the 200  $\mu\text{m}$  sub-resolution channels. On the contrary, tissue signals were suppressed below noise level. (e) Mean CTRs of the 500  $\mu\text{m}$  and 200  $\mu\text{m}$  channels in the contrast mode image. The error bars represent one standard deviation. Note that the distances of the 500 and 200  $\mu\text{m}$  channels to the probe are shifted because the IVUS probe was not at the center of the lumen. The plain blue line represents the mean CTR in conventional IVUS imaging. The blue dotted lines represent one standard deviation. (f) Schematic cross section of the coronary *vasa vasorum* phantom channels. The lumen diameter is 4 mm.

To ensure that phantom measurements are predictive of the performance of ultraharmonic IVUS in perivascular coronary tissue, we selected a tissue mimicking material [147] that realistically renders ultrasound properties in biological tissue (speed of sound, attenuation) at our frequency range (20–50 MHz). Therefore, tissue cancellation levels observed in the phantom experiment with the pulse-inversion sequence are good predictors of the in vivo situation. We first insonified the coronary artery *vasa vasorum* phantom with conventional 35 MHz IVUS pulses in the absence of ultrasound contrast agent. As anticipated, the lumen contour and the 500  $\mu\text{m}$  side channels were detected while the 200  $\mu\text{m}$  channels, smaller than IVUS lateral resolution [150], remained undetected (Fig. 8b). Next, we immersed the coronary *vasa vasorum* phantom in a static ultrasound contrast agent suspension, using a realistic in vivo

dilution ( $10^6$  microbubbles per mL). The acoustic pressure transmitted (of the order of 600 kPa at focus in tissue) is considered non-destructive for contrast microbubbles at IVUS frequency. This time, the phantom was insonified with the IVUS pulse sequence, consisting in pairs of chirp excitations with a center frequency of 26 MHz. As a result, the lumen and side channels echogenicity rose to tissue level, making the channels invisible in the conventional IVUS image (Fig. 8c). Application of the ultraharmonic signal processing revealed all side channels, including the 200  $\mu\text{m}$  sub-resolution channels (Fig. 8d). We measured the intensity of the side channels in terms of contrast-to-tissue ratios (CTR). The CTR values were computed out of three consecutive measurements and plotted as mean values together with their respective standard deviations (Fig. 8e). In the contrast mode image (Fig. 8d), CTR values for the 500  $\mu\text{m}$  channels arm reached a maximum of 10.4 dB at a distance of 3.3 mm before decreasing to a minimum 7.1 dB at a distance of 4.3 mm, following conventional unfocused transducer beam characteristics[151]. CTR values for the 200  $\mu\text{m}$  channels arm reached a maximum of 8.6 dB

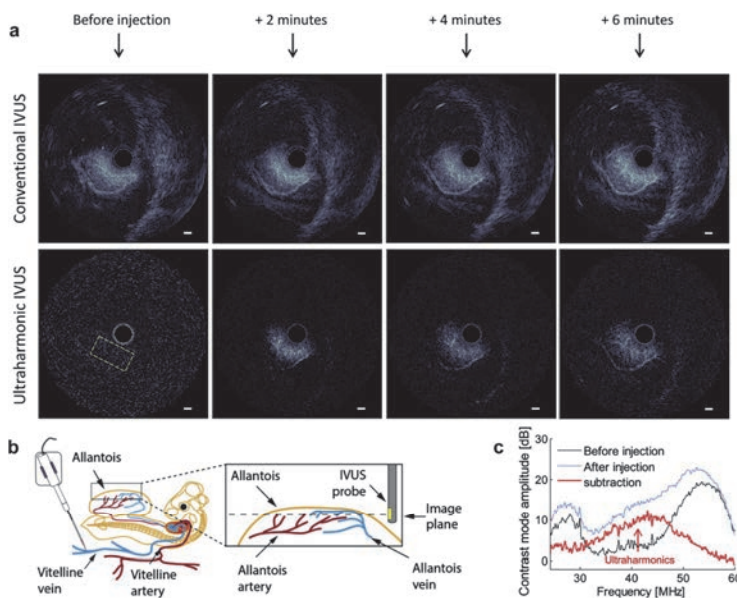


**Figure 9.** In vivo evaluation of ultraharmonic IVUS imaging. (a) Conventional 35 MHz IVUS and co-registered ultraharmonic IVUS imaging of the ultrasound contrast agent spreading in the allantois membrane of a 6 days old chicken embryo. Before injection, the allantois membrane appears echogenic in conventional IVUS, but its microvasculature is not resolved. In the corresponding ultraharmonic IVUS image, intrinsic tissue echogenicity is suppressed to noise level and the image appears black in the absence of contrast. After ultrasound contrast agent administration, ultraharmonics reveal the membrane perfusion over time. Micro-vascular structures clearly emerge after 6 min. Note that the conventional IVUS images are also enhanced, but one cannot disentangle microvessel echogenicity from the intrinsic membrane echogenicity. Scale bars in IVUS images represent 1 mm. (b) Schematic of the setup. A bolus of contrast is injected using a capillary glass needle. The IVUS probe is positioned perpendicular to the allantois membrane for insonification. (c) In vivo pulse-inversion frequency spectra before (black line) and after (blue line) contrast injection. Their subtraction (red line) reveals the ultraharmonic intensity backscattered by the ultrasound contrast agent. Frequency spectra were computed in the yellow outline depicted in Figure 3(a).



at a distance of 2.8 mm before decreasing to a minimum 4.6 dB at a distance of 3.8 mm. For reference, the CTR and standard deviation in conventional IVUS imaging (Fig. 8c) was measured by selecting a contrast-filled region located at the inner edge of the lumen and a tissue region located at the same depth. We obtained a mean CTR value of -0.4 dB (Fig. 8e). Note that in the presence of a contrast-filled lumen, which is a more attenuating medium than blood, the ultraharmonic ultrasound imaging method detected microchannels up to a distance of 4.3 mm from the transducer. This range is well adapted to the detection of intra-plaque coronary neovasculature in humans. The results also demonstrate that it is possible to perform ultraharmonic ultrasound imaging at IVUS frequency using the native size distribution of a commercial ultrasound contrast agent. In light of these results, we subsequently performed an in vivo investigation of the ultraharmonic IVUS imaging.

### ***Ultraharmonic IVUS imaging reveals an embryonic respiratory vascular plexus***

We translated the experiment in vivo to establish the capacity of ultraharmonic IVUS to image intricate microvasculature of *vasa vasorum* dimension. We selected a chicken embryo model as it enabled the optical registration of the insonified vascular geometry, contrary to former intravascular in vivo studies [69], [79]. By day 6, the chicken embryos developed a respiratory and waste elimination organ called the allantois. This organ appears as an extra-embryonic hollow sphere delineated by a thin membrane. The allantois membrane itself is webbed with a dense network of microvessels exhibiting cross sections (diameters, 200  $\mu\text{m}$ ) of the order of human atherosclerotic plaque *vasa vasorum* [148]. We positioned the IVUS probe next to the allantois membrane for insonification (Figs. 7 and 9b). We first acquired a 35 MHz conventional IVUS image as well as an ultraharmonic IVUS image of the allantois membrane before administration of the ultrasound contrast agent (Fig. 9a). The allantoic membrane appears in the bottom left quadrant of the conventional IVUS image. Because of the membrane intrinsic echogenicity, the dense allantois microvasculature is not resolved in the image. The echogenic structures on the right hand side of the conventional IVUS image correspond to the yolk. In the ultraharmonic image, the echogenicity of the allantois membrane and the yolk is suppressed to noise level by the pulseinversion sequence. Next, a 4 mL bolus of ultrasound contrast agent was administered in the vitelline vein of the chicken embryo using a capillary glass injection needle. We acquired a set of conventional and ultraharmonic IVUS images of the allantois membrane at the same location with two min intervals (Fig. 9a). The spread of the ultrasound contrast agent through the allantois microvasculature was clearly visible in the set of ultraharmonic images, indicating that hemodynamics can be tracked. Note that an enhancement of the microvessels infused with contrast is also visible in the conventional IVUS images. By subtracting the pulse-inversion frequency spectra of the allantois membrane before and after contrast administration, we observed experimentally the appearance of an ultraharmonic frequency peak induced by the ultrasound contrast agent generation in response to the pulse-inversion sequence (Fig. 9c).

Complementary to these in-plane contrast dynamic observations, we performed an in-depth scan of the allantois membrane. Conventional IVUS images at 35 MHz and ultraharmonic IVUS images were acquired at five equidistant positions in depth, covering in total a distance

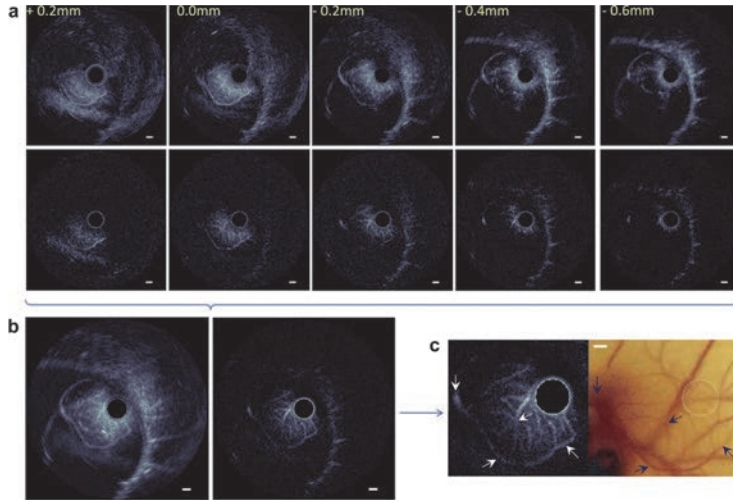


**Figure 10.** In vivo ultraharmonic IVUS scan across the allantois membrane microvasculature. (a) Conventional and ultraharmonic IVUS imaging at five different depths, equally spaced by 200 microns. Positions in mm are labeled yellow. (b) Corresponding mean intensity projections. The ultraharmonic IVUS image reveals the allantois microvasculature. (c) Zoomed in image of the membrane microvasculature imaged with ultraharmonic IVUS and comparison to an image of the same region of interest. Arrows indicate corresponding vessels in the two images. Scale bars in IVUS images represent 1 mm.

of 800  $\mu\text{m}$  (Fig. 10a). Microvessels infused with contrast appear in the ultraharmonic IVUS images, as seen at the 0 mm and 0.2 mm positions (Fig. 10a). We computed a mean intensity projection of the five planes imaged with both the conventional and ultraharmonic IVUS (Fig. 10b). In the conventional IVUS image, the presence of microvessels can be suspected thanks to the enhanced echogenicity induced by the ultrasound contrast agent. However, based on echogenicity levels alone, it is not possible to disentangle the contrast-enhanced microvessels from the intrinsic echogenicity of the allantoic membrane. On the contrary, as the ultraharmonic IVUS image displays only the microvasculature filled with contrast agents, the allantois vascular plexus appears with a superior contrast. Quantitatively, for the embryo case reported here, the contrast to tissue ratio between a microvessel and the adjacent membrane was increased by a factor of up to 2 (12.5 dB in ultraharmonic IVUS image as opposed to 6 dB in the conventional IVUS image). Note that other embryos exhibited a similar contrast enhancement but the CTR could not be reliably assessed because of the uncertain intersection of the IVUS plane with the allantois membrane. For reference, a photograph of the allantois microvasculature insonified with the IVUS probe was taken and corroborated the ultraharmonic ultrasound result with a strong agreement (Fig. 10c). Note that the photograph also displays deeper vessels that were outside of the volume insonified with IVUS. This result demonstrates the capacity of ultraharmonic IVUS to image a dense network of *vasa vasorum* sized vessels that would have been invisible in the absence of an ultrasound contrast agent (as in the conventional IVUS image before contrast injection in Fig. 10a).

### **DISCUSSION**

Intra-plaque *vasa vasorum* density was shown to be one of the strongest predictors of atherosclerotic plaques at risk that require intervention[136]. Yet, there are no clinical tools at present for coronary *vasa vasorum* detection in vivo. Our results demonstrate that the implementation of an ultrasound contrast agent detection pulse sequence enhances the physiologic contrast of IVUS by enabling the detection of intricate *vasa vasorum* sized targets. Our strategy consisted in sensing contrast agent specific echoes at 1.5 times the transmit frequency, referred to as ultraharmonics. The in vivo echolocation of ultraharmonics with an IVUS probe revealed microvasculature infused with ultrasound contrast agents (Figs. 9 and 10). The limited frequency bandwidth requirement of ultraharmonic ultrasound imaging made its implementation on a conventional IVUS transducer possible, contrary to other existing harmonic methods. We also show that one can augment the ultraharmonic response of an ultrasound contrast agent by relying on chirp excitations rather than conventional imaging pulses (Figs. 4 and 5).

To date, ultraharmonic ultrasound imaging has received little attention in the field of medical ultrasound, probably because the amplitude of ultraharmonics is usually lower than the amplitude of subharmonics. Yet, the ability to transmit and receive ultrasound pulses within the bandwidth of commercially available transducers is a major advantage for imaging as it improves sensitivity[138] (Materials and Methods). We also report in the phantom experiment that despite its high frequency range, ultraharmonic IVUS could be performed without manipulating the size distribution of a commercial ultrasound contrast agent. Finally, contrary to ultrasound Doppler techniques for blood flow imaging, contrast-enhanced IVUS is not impaired tissue motion [141]. In light of these results, the next step will consist in performing intracoronary ultraharmonic IVUS imaging in a porcine model of atherosclerosis. A limitation of the method is that, despite its enhanced microvasculature detection capabilities compared to conventional IVUS, image resolution itself is not improved. A subresolution microvessel filled with contrast will still appear as big as the imaging system's point spread function. This can be observed in Figure 10 (c). Accurate volumetric quantification of microvasculature relies on imaging resolution and remains a future target. Meanwhile, ultraharmonic IVUS fulfills its primary role of providing a metric of microvascular density in the coronary artery wall by successfully detecting small blood vessels.

The dose of ultrasound contrast agent injected in the phantom experiment was in line with current medical guidelines. In the embryo case, it was one order of magnitude higher (107 bubbles per mL). Assuming a mean embryo blood volume at 6 days of 170 mL [152], the contrast agent to blood ratio injected was 1:43. This remains inferior to contrast agent to blood ratios in mice (normative blood volume ranging from 1.5–2.5 mL), which can be 1:25 or higher [153], [154]. For larger animal models of atherosclerosis and eventually in humans, the exact dose of contrast agent is still to be determined. From the point of view of imaging, it is critical that enough ultrasound contrast agents reach the *vasa vasorum*. As the *vasa vasorum* is mostly perfused from the outside in, through the external venous network, rather than from the artery lumen [135], bolus injections of contrast will need to be performed upstream from the

## Chapter 3

---

site of interest. Studies need to be conducted to establish optimal ultrasound contrast guidelines for contrast IVUS investigations of coronary arteries. The CTR in real plaque microvessels at approved contrast agent concentration needs to be investigated. Note that we do not anticipate motion artifacts in ultraharmonic IVUS images. 20  $\mu$ s are required to transmit and receive a pair of phase-inverted excitations in order to scan a depth of 8 mm. Lateral motion of the artery wall reaches peak velocity of a few cm/s. The effect of this motion within 20  $\mu$ s is negligible.

Analogous to the development of MRI blood detection sequences, IVUS will widen its scope by adopting blood detection pulse sequences like ultraharmonic ultrasound imaging. Ultraharmonic IVUS could not only help identifying vulnerable plaques requiring intervention but could also play a role in the follow-up of cardiac patients. The resurgence of atherosclerosis at stented sites is a growing concern in interventional cardiology and became a target for novel intravascular imaging techniques [155]. Here again, the *vasa vasorum* could be a valuable early risk predictor. Beyond the scope of IVUS, ultraharmonic ultrasound imaging could be implemented on conventional medical ultrasound scanners to study inflammatory processes of clinical importance.

Acknowledgments—We thank K. Shung and Q. Zhou (University of Southern California) for providing the IVUS transducer. This research was supported by the Dutch Technology Foundation STW (2007 Simon Stevin Meester grant).

# Chapter 4

## **Cell Membrane Permeability Dynamics After Sonoporation**

*To be submitted*

Ilya Skachkov<sup>1</sup>, Tom van Rooij<sup>1</sup>, Kirby R. Lattwein<sup>1</sup>, Tom J.A. Kokhuis<sup>1</sup>, Deep Bera<sup>1</sup>, Ying Luan<sup>1</sup>, Antonius F. W. van der Steen<sup>1,2</sup>, Nico de Jong<sup>1,2</sup>, Klazina Kooiman<sup>1</sup>.

<sup>1</sup> Department of Biomedical Engineering, Thoraxcenter, Erasmus MC, P.O. Box 2040, 3000 CA Rotterdam, the Netherlands; <sup>2</sup> Interuniversity Cardiology Institute of the Netherlands (ICIN), Utrecht, the Netherlands

**Abstract — Vibrating microbubbles (MB) can increase cell membrane permeability, which is also known as sonoporation. Sonoporation can be both reversible or irreversible. When irreversible, severe cell damage is caused leading eventually to cell death. Reversible sonoporation could aid in drug delivery to cells, because the pores created in these cells are not lethal. Different therapeutic approaches may require reversible or irreversible sonoporation and there is always a balance between effectiveness and cell damage. The aim of this study was to investigate how targeted MB (tMBs) and non-targeted MB (ntMBs) effect cell membrane permeability using different ultrasound (US) settings.**

**Key Words:** *Ultrasound contrast agents, Targeted microbubbles, Sonoporation, Drug delivery.*

### INTRODUCTION

Microbubbles (MBs) are ultrasound contrast agents that consist of a gas core encapsulated by a stabilizing coating. Non-targeted microbubbles (ntMBs) are generally used as blood pool agents for contrast-enhanced ultrasound imaging [156], [157]. Targeted microbubbles (tMBs) are promising agents for molecular imaging and therapy in many areas, including cancer and inflammation [16], [28].

When microbubbles are insonified by ultrasound (US), they oscillate due to the pressure wave [14]. In close proximity to a cell membrane microbubbles can increase the permeability of the membrane and facilitate intracellular drug uptake, better known as sonoporation [14], [16]. Recent discoveries showed that sonoporation of the cell membrane can be either reversible or irreversible [23]. Irreversible sonoporation leads to significant cell damage and eventually cell death, while reversible sonoporation facilitates cellular drug uptake without causing lethal damage to the cell [18]. Different techniques can be used for monitoring cell membrane permeability such as transmembrane current or dye-uptake approaches. Deng et al. [158] used a patch clamp technique on *Xenopus laevis* oocytes and showed that oscillating microbubbles induce transient changes in transmembrane current. The change in current highly depended on the ultrasound settings that were used. Another study demonstrated that changes in cell membrane permeability could be monitored by the transmembrane current in combination with the uptake of propidium iodide (PI) [159]. This model drug is widely used to study sonoporation [159]-[164], as it can only pass the cell membrane of a live cell when it is disrupted. After entering the cell it binds to DNA and RNA where it becomes fluorescent. Fan et al. [159] showed that the fluorescence intensity is directly correlated to the amount of PI-DNA and PI-RNA complexes that are formed in the cell. Although the exact mechanism of sonoporation is still not fully understood, Fan et al. [159] proposed a model to relate the fluorescent intensity in the cell to the size of the initial pore and the resealing of this created pore, which agreed well with their experimental results. However, they only varied US pressure

in their experimental study on tMBs. In order to understand the influence of US parameters on the sonoporation dynamics, different parameters have to be investigated. In addition to the variability in US parameters, the mechanisms that result in sonoporation are expected to be different for tMBs and ntMBs due to respectively binding to the cell membrane and being in contact with the cell membrane. In addition, a bound tMB can have different microbubble dynamics as previously reported [125], [165]. Upon binding, the tMB in both studies had a lower maximum relative excursion meaning they oscillated less pronounced for the same acoustic pressure and frequency. Regarding the resonance frequency of the MBs, the two studies showed contradicting results: no change in resonance frequency upon binding of tMBs [165] versus a 30% lower resonance frequency for tMBs than for ntMBs [125]. Another study showed increased acoustic stability for streptavidin-tMBs in comparison to the ntMBs which were composed of the same lipid-coated shell but without the functionalization with streptavidin [42].

In this study we used both tMBs and ntMBs to investigate the effect of different US settings on cell membrane permeability and cell death. We used fluorescence microscopy to visualize real-time uptake of the model drug propidium iodide (PI) to study the sonoporation dynamics. The previously proposed model [159] was fitted to the experimentally obtained data to provide insights into pore sizes and resealing times, in order to differentiate reversible from irreversible sonoporation.

### Material and Methods

#### Microbubble Preparation

Lipid-coated microbubbles with a  $C_4F_{10}$  gas core (F2 Chemicals, Preston, UK) were made by sonication as described by Klibanov et al. [124].

#### Targeted microbubbles (tMBs)

The coating was composed of 1,2-distearoyl-*sn*-glycero-3-phosphocholine (DSPC; 59.4 mol%; P6517; Sigma-Aldrich, Zwijndrecht, the Netherlands), polyoxyethylene-(40)-stearate (PEG-40 stearate; 35.7 mol%; P3440; Sigma-Aldrich), 1,2-distearoyl-*sn*-glycero-3-phosphoethanolamine-N-carboxy(polyethylene glycol) (DSPE-PEG<sub>2000</sub>; MW 2000; 4.1 mol%; 880125P; Avanti Polar Lipids, Alabaster, AL, USA), and 1,2-distearoyl-*sn*-glycero-3-phosphoethanolamine-N-biotinyl(polyethylene glycol)(DSPE-PEG<sub>2000</sub>-biotin; MW2000; 0.8 mol%; 880129C; Avanti Polar Lipids). Further preparation of tMBs was performed as previously described [162], [166]. Briefly, after three washing steps by centrifugation at 400 g for 1 minute, the concentration of the MBs was measured using a Coulter Counter (N=3; Multisizer 3; Beckman Coulter, Mijdrecht, the Netherlands) and  $1 \times 10^9$  biotinylated MBs were incubated with 20  $\mu$ g streptavidin (S4762; Sigma-Aldrich) on ice for 30 minutes. Following incubation, the streptavidin-conjugated MBs were washed once to remove non-bound streptavidin. Next, 5  $\mu$ g of biotinylated anti-human CD31-antibody (BAM3567; R&D Systems, Abingdon, United Kingdom) was conjugated to DSPE-PEG(2000)-biotin in the MB shell by avidin-biotin bridging during incubation of 30 min on ice. Afterwards, tMBs were washed once to remove non-bound antibodies.



## Chapter 4

### Non-targeted microbubbles (ntMBs)

The coating of the ntMBs consisted of the same components, but DSPE-PEG(2000)-biotin was replaced with DSPE-PEG(2000) (0.8 mol%; 880129C; Avanti Polar Lipids). The solution of MBs was washed three times after sonication using centrifugation for 1 minute at 400 g.

### Microbubble size

After the last washing step of tMBs and ntMBs, just prior to the experiments, size and concentration were measured using a Coulter Counter (N=3; Multisizer 3; Beckman Coulter). The mean diameter of ntMB was  $2.54 \pm 0.02 \mu\text{m}$  and  $2.82 \pm 0.09 \mu\text{m}$  for tMB.

### Endothelial cell culture

Human umbilical vein endothelial cells (HUVECs; C2519A; Lonza, Verviers, Belgium) were cultured in EGM-2 medium (CC-3162; Lonza), in T-75 flasks (353136; BD Falcon Fisher Scientific, Breda, the Netherlands), and maintained in a humidified incubator under standard conditions (37°C, 5% CO<sub>2</sub>). Thereafter the cells were trypsinized using trypsin in EDTA (CC-5012; Lonza) and replated on one side of an OptiCell™ (Thermo Scientific, NUNC GmbH & Co, Wiesbaden, Germany). Experiments were performed two days later once HUVECs achieved 100% confluence in the OptiCell.

### Experimental set-up

For both the tMBs and ntMBs,  $\sim 10^7$  MBs were added to the OptiCell to obtain a cell to bubble ratio of 1:3. Just prior to the experiment, 25  $\mu\text{g/ml}$  propidium iodide (PI; P-4864; Sigma-Aldrich) and 5  $\mu\text{g/ml}$  Hoechst 33342 (H1399; Invitrogen, Breda, The Netherlands) were added to the extracellular medium in the OptiCell. The OptiCell was placed in a 37°C incubator with the cells on the top membrane, in order for the MBs to adhere to the cells by flotation. After 5 minutes, the OptiCell was placed into a 37°C water bath (Fig. 1A). For the experiments using tMBs, the OptiCell was placed with the cells on the bottom membrane, so any non-adhered microbubbles would float away from the cell surface, while the OptiCell for the ntMB experiments was placed with the cells on the top membrane to ensure close proximity of the ntMB to the cell membranes.

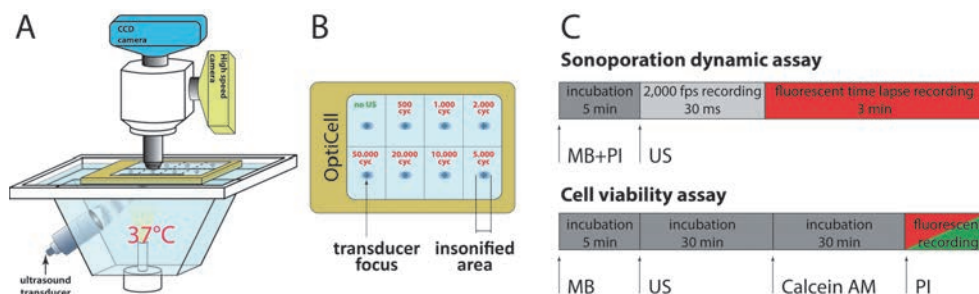


**Figure 1. Schematic illustrations and timing of the experimental set-up.** (A) Representation of the combined optical and acoustical set-up. (B) OptiCell insonification scheme. (C) Procedural time line for the sonoporation dynamic and cell viability assays.



### **Ultrasound exposure protocol**

For the acoustical set-up, a 1 MHz single element, focused transducer (focal distance 7.5 cm; V303; Panametrics-NDT, Olympus NDT, Waltham, MA, USA) was mounted in the water bath at a 45° angle below the sample (Fig. 1A). Each OptiCell was divided into eight acoustically non-overlapping areas (2 cm x 3 cm each; for schematic see Fig. 1B), which covered the beam area (-6dB beam width of 6.5 mm) at the focus of the transducer, as verified in advance with a calibrated 0.2 mm PVDF needle hydrophone (Precision Acoustics Ltd, Dorchester, UK). The acoustic focus was aligned with the optical focus.

During the experiment, the position of the OptiCell was adjusted to place the center of each subsection in the focal zone. The sample was insonified by a single Gaussian tapered sine wave burst generated by an arbitrary waveform generator (33220A, Agilent, Palo Alto, CA, USA) and amplified using a broadband amplifier (ENI A-500, Electronics & Innovation, Rochester, NY, USA). The peak negative acoustic pressure ( $P_A$ ) of the single US burst (150, 300, or 500 kPa) was kept constant for the entire Opticell, whereas the number of cycles in the single US burst (500; 1000; 2000; 5000; 10,000; 20,000; and 50,000) varied per OptiCell subsection (Fig. 1B). For each Opticell one of the subsections was used as a control where no ultrasound was applied.

### **Optical set-up and observations**

For visualization of the MBs and HUVECs, the microscopic set-up consisted of a fluorescence microscope (Olympus, Zoeterwoude, the Netherlands) equipped with a 5× objective (LMPlanFI, NA 0.13, Olympus), a high sensitivity CCD camera (AxioCam MRc, Carl Zeiss, Germany), and a suitable set of fluorescent filters for the detection of propidium iodide (U-MWG2 filter, excitation 510-550/590nm, Olympus), Hoechst 33342 (U-MWU2 filter, excitation 330-385/420nm, Olympus), and calcein-AM (U-MWIB2, 460-490/510 nm, Olympus). These filters were used for the detection of all cells (stained with Hoechst 33342), viable cells (stained with calcein), and sonoporated/dead cells (stained with PI).

The Hoechst 33342 fluorescent dye was used to stain all HUVECs, living and dead, as it rapidly diffuses into all cells, binds specifically and quantitatively to DNA, and has low toxicity to viable cells [167]. Calcein-AM (C3100MP; Invitrogen; 0.25  $\mu$ M from a 1 mM stock prepared in DMSO (Sigma-Aldrich)) passively crosses into cellular membranes, has high cell retention, and is only converted to fluorescent calcein in living cells [168]. Therefore, it was used as a live-cell stain in the cell viability assays. PI, which is cell-impermeable, was used to determine the presence and intensity of sonoporation, or disruption of cell membranes, since it only becomes fluorescent when bound to RNA and DNA inside cells [160]. After magnification of the MBs and HUVECs, the high-speed Redlake Motion Pro Camera (10K, San Diego, CA, USA), was used at 2000 fps to record MB behavior in response to US exposure.

### **Sonoporation dynamics assay**

Following the experimental set-up, recordings using the CCD camera were taken using both fluorescent and non-fluorescent settings of a target subsection. The Redlake camera was started just prior to insonification of the MBs and ran for 62 milliseconds to record the MB behavior. This meant it recorded more frames after insonification for the lower single cycle burst than

## Chapter 4

for the highest single cycle burst. After these 62 milliseconds, the CCD camera was used to record the fluorescence intensity change over time caused by cellular PI uptake after US application. This protocol was performed for 3 min after US application, with 1.5 sec exposure and at 5 sec time intervals (Fig. 1C). Detection of the entire cell nucleus was done with Hoechst 33342 and increased cell membrane permeability with PI. This procedure was performed for each subsection and in triplicate.

### Cell viability assay

For each US setting, cell viability was determined by a calcein-AM assay. Cells were treated as described in the experimental set-up, except that there was no addition of PI and Hoechst 33342. Fluorescent and non-fluorescent recordings were taken of each subsection with the CCD camera prior to insonification. After the US treatment of all 8 subsections of the OptiCell, it was incubated at 37°C, 5% CO<sub>2</sub> for thirty minutes. Thereafter calcein-AM was added to the OptiCell chamber and incubated for another 30 minutes. After the final incubation, PI and Hoechst 33342 were added to the Opticell. This procedure was followed directly with microscopic and fluorescent examination using the same setup and filter sets as described in the optical set-up using the CCD camera. For each condition, five different fields of view were acquired within the 6 mm circle around the center of the insonified area. All experiments were done in triplicate.

### Data analysis

All obtained images were analyzed using a custom built plugin for ImageJ (Rasband, W.S., ImageJ, U. S. National Institutes of Health, Bethesda, Maryland, USA). First, the position of every nucleus was extracted from the Hoechst nucleus staining images using the Find Maximum Function, this resulted in ~2500 nuclei in the field of view. To obtain the outlines of the cell membranes Voronoi Tessellation was used [169]. This function uses Voronoi diagrams, which are based on the theory that every point  $p$  has a distance to another point  $q$  that is less than or equal to its distance to any other point  $r$ . The lines of the Voronoi diagram are thus equidistant to two points in space and correspond to the most likely position of the cell boundaries. To find the closest points the automated thresholding method of Otsu [170] was used. The created Voronoi diagrams were transformed into a mask. This mask was combined with every frame of the PI fluorescence recording after the application of US, to quantify the PI intensity of every single cell.

These intensity values were loaded into R, language and environment for statistical computing (R Foundation for Statistical Computing, Vienna, Austria), for further quantification. Fan et al. [159] derived an equation (Equation 1) to model sonoporation dynamics, based on resealing of the created pore and the diffusion rate of PI into the cell.

$$F(t) = \alpha \cdot \pi D C_0 \cdot r_0 \cdot \frac{1}{\beta} (1 - e^{-\beta t}) \quad \text{Eq. 1,}$$

where  $F(t)$  is the fluorescence intensity as a function of time,  $\alpha$  is a coefficient that relates the amount of PI molecules to the fluorescence intensity of PI-RNA and PI-DNA. This coefficient is determined by the sensitivity of the fluorescence imaging system. The other parameters are the diffusion coefficient of PI,  $D$ , the extracellular PI concentration,  $C_0$ , the

initial radius of the pore,  $r_0$ , the pore resealing coefficient,  $\beta$ , and time,  $t$ . The maximum intensity is determined by the pore size coefficient ( $\alpha \cdot \pi \cdot D \cdot C_0 \cdot r_0$ ) over  $\beta$ , i.e., the factor that is multiplied with the exponential.

To obtain the pore size coefficient,  $\alpha \cdot \pi \cdot D \cdot C_0 \cdot r_0$ , and the pore resealing coefficient,  $\beta$ , a nonlinear least square curve was fitted to the experimentally obtained PI intensities over time based on Equation 1. To classify the cells into two groups namely “high PI intensity” and “low PI intensity”, Principal Component Analysis (PCA) [171], [172] was performed on the distribution of the pore size coefficient ( $\alpha \cdot \pi \cdot D \cdot C_0 \cdot r_0$ ) and pore resealing coefficient ( $\beta$ ). We chose PCA as this method captures as much of the variation in the data as possible by computing eigenvectors (for determining the direction in which the data has largest variance) and corresponding eigenvalues (to determine how much variance there is in the data in that direction). The principal components (PCs) are uncorrelated with each other as the eigenvectors are perpendicular to each other. In this data set there were only two variables (pore size coefficient ( $\alpha \cdot \pi \cdot D \cdot C_0 \cdot r_0$ ) and pore resealing coefficient ( $\beta$ )), so we had two PCs. For fine-tuning, the classification thresholding was applied on both the PCs resulting in the final classification in two groups. This threshold was determined based on the results of cell death in the viability assays.

## Results

### ***Sonoporation-induced PI uptake dynamics of individual cells***

To determine whether and to which degree sonoporation took place as a function of the different US settings, pressure and cycle combinations, we began with analyzing individual cells. Before US exposure, bright field imaging was used to discern MB locations (Fig. 2A). The black dots in figure 2A are the MBs. The background of the image is grey and has spherical structures that are raised. These are the nuclei of the endothelial cells in the monolayer. Therefore every MB is in contact with a part of the cellular membrane. Additionally, fluorescence microscopy established HUVEC membrane integrity by the absence of PI fluorescence (Fig. 2B) and individual cell nuclei locations by Hoechst 33342 staining (Fig. 2C). After insonification, the majority of MBs either were displaced from the field of view or dissolved (Fig. 2D). Intracellular PI uptake was observed by increase of fluorescence, thus indicating US-stimulated microbubble sonoporation allowing the influx of the otherwise membrane-impermeant molecule (Fig. 2E). Diverse MB displacement was observed in each US treated OptiCell subsection (Fig. 2F). Sonoporation-induced PI uptake was heterogeneous among the different cells within each subsection (Fig. 2E,G). When the fluorescence intensity was analyzed for individual cells, variances were found among the cells both in total amount of PI uptake and in the rate of uptake. Some cells attained 90% maximum fluorescence intensity quicker than others as illustrated by Figure 2G. Qualitative assessment of the maximum intensity projection images showed that the cells with a faster uptake rate and a higher amount of PI uptake, directly corresponded with more and closer to the cell nucleus displacement of the microbubble.

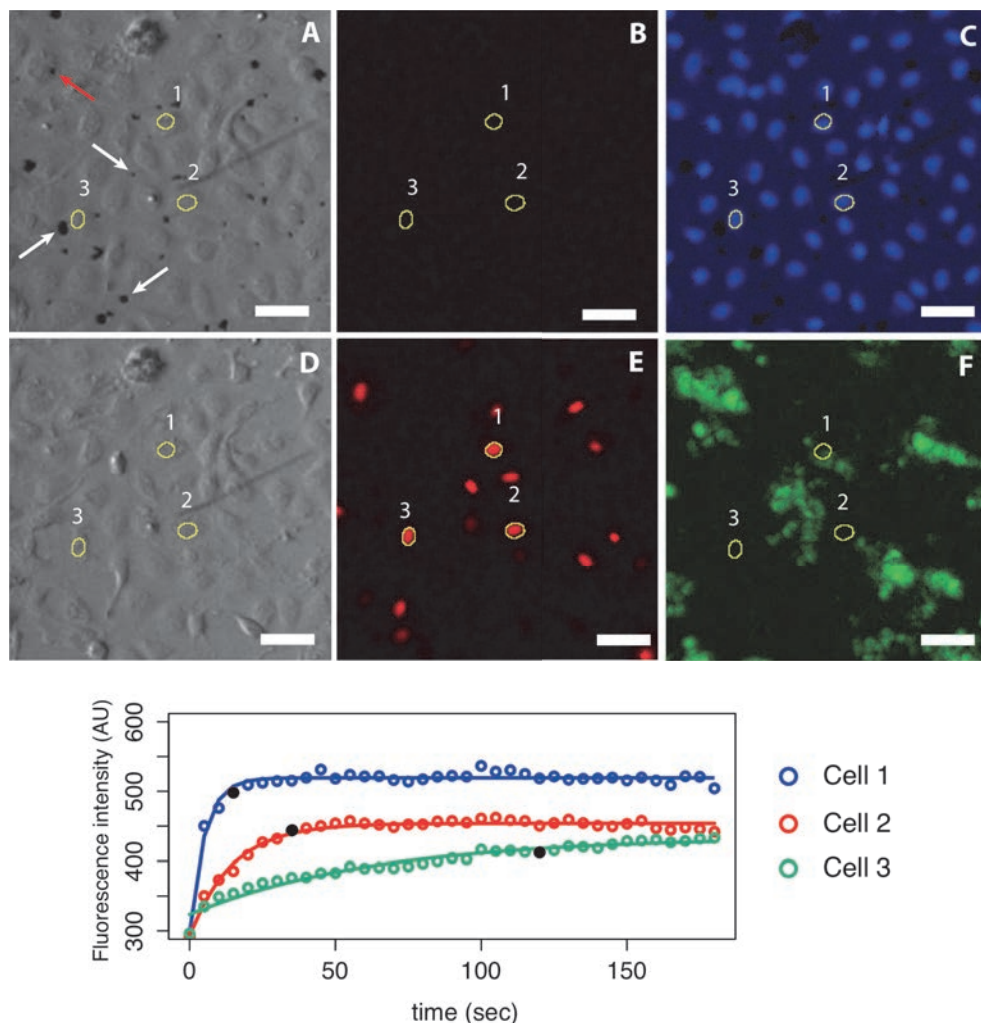


**Figure 2. Optical recordings of microbubbles and HUVECs monolayer for sonoporation analysis.** (A) Bright field image of tMBs microbubble locations before US exposure; the tMBs are the black dots in the image of which four are indicated by an arrow; the three white arrows point to a MB on the cytoplasmic part of the cell membrane whereas the red arrow denotes a MB on the nuclear part of the cell membrane. (B) Fluorescence image of PI uptake before insonification. (C) Hoechst 33342 fluorescent staining of HUVEC nuclei. (D) Bright field image after US treatment; all bubbles were dissolved (E) Fluorescence image of cells after ultrasound treatment; red stained nucleus from PI uptake. (F) Microbubble displacement using maximum intensity projection summed over all frames. (G) Relative fluorescence intensity over 3 minutes after US treatment (colored circles) and model fitted (solid lines); black circles on the lines indicate 90% of maximum PI intensity. These cells are marked with yellow circles in Fig 2A-F. US settings:  $P_A = 300$  kPa, 20,000 cycles. Scale bar 30  $\mu$ m.

### **Non-targeted and targeted microbubble sonoporation and cell death**

The influence of varying acoustical settings in relation to ntMBs and tMBs on cellular responses was evaluated by the number of sonoporated cells and sonoporated-induced cell death as illustrated in Figure 3. Sonoporation was confirmed by PI influx after insonification,

## Cell Membrane Permeability Dynamics After Sonoporation

whereas the cell viability assay cell death measured the presence of PI fluorescence signal after insonification and the calcein fluorescence signal. By looking at the total population of cells in each experimental subsection, Figure 3 confirms that as the acoustical pressure and the amount of cycles increased, both the number of sonoporated cells (A, C) and cell death (B, D) increased. This trend was seen for both ntMBs (Fig. 3A, B) and tMBs (Fig. 3C, D), although

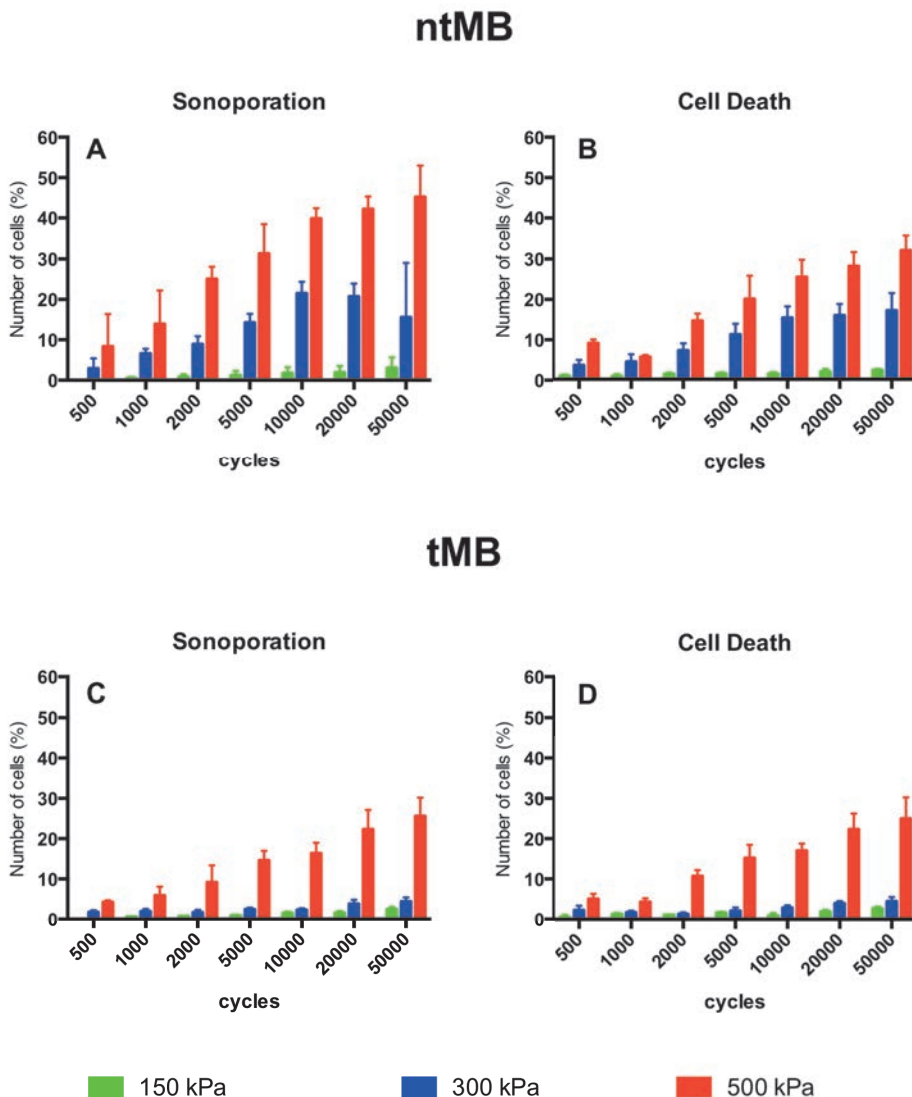


**Figure 3.** Targeted and non-targeted microbubble-mediated sonoporation and cell death after ultrasound exposure at varying  $P_A$  (150, 300, and 500 kPa) and varying number of cycles (500 – 50,000). (A) Mean number of ntMB sonoporated cells. (B) Cell death after insonification with ntMBs. (C) Mean number of tMB sonoporated cells. (D) Cell death after insonification with tMBs. Columns, means; bars,  $\pm$  SEM.

ntMBs resulted in more sonoporative responses for all cycles at 300 kPa and 500 kPa. At the lowest pressure of 150kPa, sonoporation and cell death was seen in only  $\leq 5\%$  of the total number of cells regardless of the number of US cycles that was used (Fig. 3).

There was more sonoporation than cell death for all experimental settings. For tMBs, the amount of sonoporated cells was only a couple percentage points more than the amount of cell death at almost all settings. However, ntMBs, above 1000 cycles and 150kPa, produced up to  $\sim 18\%$  higher sonoporation compared to the amount cell death for the same experimental settings.

### PI uptake as a function of pore size and resealing coefficients

The influence of the pore size and resealing coefficients on sonoporation-induced uptake was evaluated by PCA analysis. Within a population of cells experiencing sonoporation, there exists different sonoporation uptake dynamics, as indicated by Figure 4.

Using the pore size coefficient and pore-resealing coefficient derived from Eq. 1, two populations could be distinguished from the data indicated by the red and blue circles (Fig. 4A). These populations correspond to cells with either high (red circles) or low (blue circles) PI uptake (Fig. 4B). The time intensity curves (Fig. 4B) were fitted to the model (Eq. 1) and it was mathematically derived that the initial slope corresponds with the pore size coefficient. This coefficient is also the scaling factor for the exponential increase. Therefore, a steep initial slope corresponded to a larger pore size. Derived from Eq. 1, the overall slope follows  $F(t) = (\alpha \cdot \pi D C_0 \cdot r_0) \cdot e^{-\beta t}$ , with  $\beta$  determining the time to reach the asymptotic value of the maximum PI intensity. This asymptotic maximal PI intensity value is given by the inverse relationship of the pore size and pore resealing coefficients:  $F(t) = \frac{\alpha \cdot \pi D C_0 \cdot r_0}{\beta}$ . Therefore, a cell with a high pore resealing coefficient quickly reaches the asymptotic value, resulting in a quick resealing of the pore.

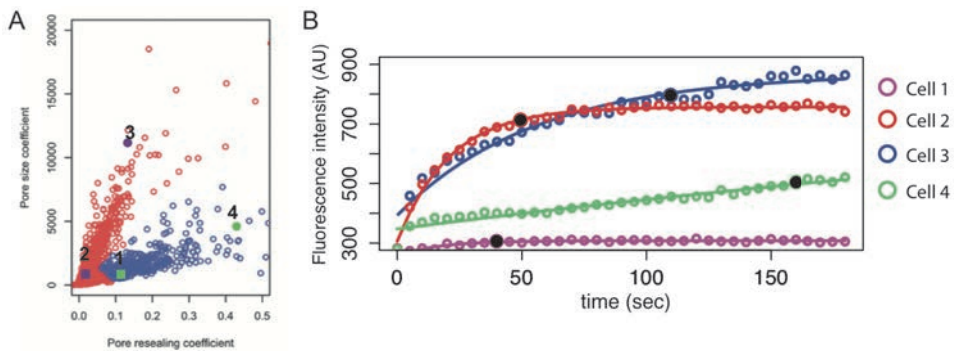


**Figure 4. Nuclear propidium iodide uptake dynamics produced by microbubble-induced sonoporation as a function of pore size and resealing time in HUVECs.** (A) PCA classification of cell populations by taking pore size coefficient as a function of the pore resealing coefficient as derived from Eq. 1; every dot represents one cell with red circles indicating high uptake and blue circles low uptake. (B) Fluorescence time-intensity curves of 4 cells with different pore resealing and pore size coefficients. The cells in this example were insonified with  $P_A = 500$  kPa, 50,000 cycles in the presence of ntMBs.



# Cell Membrane Permeability Dynamics After Sonoporation

## Non-targeted and targeted microbubble-mediated PI uptake in relation to cell death

The impact of acoustical pressure and the number of cycles in a single burst sine wave on sonoporation-induced uptake is illustrated in Figure 5. The two populations, high and low PI uptake cells, that were elucidated by PCA analysis (Figure 4A) from the sonoporation dynamic

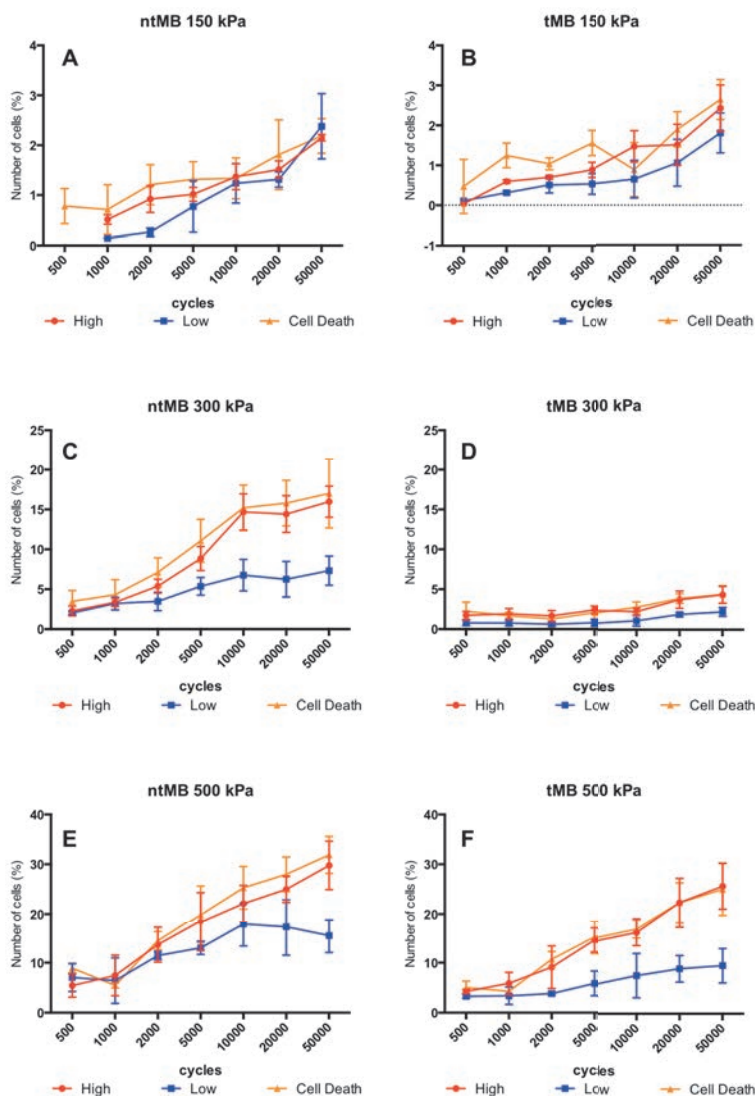


**Figure 5.** Comparison of cells with high and low PI uptake to the amount of cell death under varying experimental acoustical pressures and cycles. (A) Cellular response to ntMBs for 150 kPa. (B) Cellular response to tMBs for 150 kPa. (C) Cellular response to ntMBs for 300 kPa. (D) Cellular response to tMBs for 300 kPa. (E) Cellular response to ntMBs for 500 kPa. (F) Cellular response to tMBs for 500 kPa.

## Chapter 4

---

assays were compared against the cell death determined in the cell viability assays for each corresponding treatment. At 150 kPa, the percentage of sonoporated cells was minor (~2-3%) over all cycles, however this percentage had a slightly increasing trend as the pulse cycle increased for both ntMBs (Fig. 5A) and tMBs (Fig. 5B). The trend of increasing sonoporation, as well as cell death, over cycle increase was seen over all experiments for both cell populations, with 500kPa having the largest percentages in both ntMBs and tMBs experimental groups. However, the amount of low uptake cells was overall smaller than the amount high uptake cells for both ntMBs and tMBs at all pressures and cycle settings above 1000. The difference between these two cell populations at 300 kPa was larger for the ntMBs treatment (Fig. 5 C-D) for all cycle settings. For tMBs, the amount of sonoporation cells increased slightly for both cell populations, while ntMBs demonstrated steeper increases of high and low uptake cells. Both types of MBs, at 300 and 500 kPa, had a plateauing effect of sonoporation in low uptake cells after 10,000 cycles (Fig. 5 C-F). Above 10,000 cycles, the amount of low uptake cells plateaued or even decreased, while the amount of high uptake cells and cell death continued to increase (Fig. 5 C, D).

Sonoporation-induced cell death from tMBs and ntMBs at 300 kPa and 500 kPa was highly correlated ( $R^2 > 0.9$ ) to the amount of high PI uptake cells at all cycles (Fig. 5 C-F). However, tMBs had a closer correlation between high uptake cells and cell death than ntMBs, where cell death was consistently slightly higher than the amount of cells with high PI uptake.

### Discussion

To the best of our knowledge, this is the first study that directly compares tMBs versus ntMBs-mediated sonoporation in primary endothelial cells *in vitro*. The real-time observed uptake patterns of the cell impermeable PI were fitted using a previously reported diffusion model [159]. Cell viability highly correlated with the different patterns of PI uptake derived from this model.

For all US settings we observed two cell populations with different PI uptake profiles: one population had high uptake of PI, whereas the other population had low PI uptake. One indication for these differences in total uptake of PI can be explained by microbubble displacement (Fig. 2). Qualitative assessment of the displacement of MBs reveals higher PI uptake when MBs displace more. This phenomenon has been described by de Cock et al. [173], where they observed a bubble that is propelled into a cell with high speed and results in a high uptake of PI. Equation 1 shows us that a higher intracellular PI intensity is determined by the pore size coefficient divided by the pore resealing coefficient. Translating this to the displacement of bubbles and the higher uptake of PI, this indicates that the pore size coefficient is higher (i.e. a larger pore). In addition to this, Fig. 4A shows that a higher pore size coefficient is correlated to a lower pore resealing coefficient. The combination of a large pore and slow resealing is likely to result in irreversible sonoporation. Taken altogether, more MB displacement suggests a higher incidence of irreversible sonoporation and thus cell death.

When we compare the displacements of tMBs and ntMBs, the latter have larger displacements. Following this reasoning, ntMBs should cause a higher uptake of PI, which is



in fact illustrated by Figures 3 and 5. Additionally this suggests that MB displacement causes more cells to be sonoporated than oscillation of the MBs alone. This corresponds to ntMBs causing higher levels of PI uptake and cell death because they are free floating against the cells and therefore can displace more easily, whereas tMBs are cell-bound and their bond has to be broken before they can displace[174]. This would suggest that ntMBs are better at sonoporating cells than tMBs, however this is an *in vitro* situation without flow conditions. Under flow, ntMBs could sonoporate cells as they move along the cells, or when pressed against a thrombi occluding a blood vessel, as in the case of sonothrombolysis [175], [176]. In order for sonoporation to occur the MBs need to be within close proximity to the cell membrane [160], [177]. For therapies requiring sonoporation of specific cells under flow, ntMBs would need to be replaced with tMBs. Therefore, the use of ntMBs versus tMBs is highly dependent on the application for drug delivery.

We must also take into account the low and high uptake populations and how they correspond with cell death. At 150 kPa, the pressure is too low to cause predictable and substantial sonoporation. For treatments where cell death is desired, for example in cancer therapies, Figures 3 and 5 suggest that maximum acoustical pressures and cycles would be desired. However when cell viability is desired after high levels of sonoporation, there seems to be a limit. For these experiments, anything above 10,000 cycles only increased cell death for the high uptake population while maintaining the cell viability in the low uptake population.

Our findings that ntMBs induce a higher PI uptake than tMBs are contradicting to other *in vitro* studies that report tMBs to be more efficient for drug delivery than ntMBs. The five reported *in vitro* studies [178]-[182] all show that the lipid-shell tMBs are 1.1 [182] to 7.7[178] fold more efficient for drug delivery than ntMBs. Four out of these five studies are on drug-loaded microbubbles (paclitaxel or plasmid DNA), the other is on co-administration of PI [181]. A direct comparison between our and the five reported studies is difficult due to the differences in experimental set-up. None of these studies assessed MB-mediated drug delivery in endothelial cells. Instead, smooth muscle [179] or cancer cells were used. The study that reported the highest fold difference between tMBs and ntMBs, rinsed the cells to remove free MBs that did not attach. As a result, the ntMBs would almost all have been washed away, which could explain the large fold difference. Another study treated cancer cells in suspension [180], whereas we treated a monolayer of endothelial cells. Two studies [180], [182] even used a ntMBs with a different microbubble shell composition and smaller mean diameter in comparison to the tMBs which without doubt results in differences in microbubble behavior [14], [183]. The orientation of the MBs in respect to the cells was either not mentioned or the MBs were on top of the cells with US applied from the MB-side [178] or the tMBs and ntMBs were pushed towards the cells by the ultrasound [181]. In addition, one study reported that the 5.5 fold higher uptake could only be achieved with 70% confluent cells[179]. Consequently, more studies are needed on the difference between tMBs and ntMBs-mediated drug delivery.

To study ntMB-mediated drug delivery, buoyancy has to be used in order for the ntMB to have contact with the cells. This is the configuration that we used in the present study and the ntMBs were insonified from the MB-side at a 45 degree angle to prevent the US from reflecting

## Chapter 4

---

against the objective lens. As we wanted to be sure that our tMB were indeed targeted to the cells, we chose to reverse the Opticell after the tMB adhered to the cells via buoyancy. Any non-adherent tMB would then float up, also during the experiment, and not be in contact with the cells anymore. In our set-up this meant that the US came from the cell-side, again at a 45 degree angle. Because of these choices, the ntMBs could have been pushed to the cells by the US while the tMBs could have been pushed away from the cells. This alone may have an influence on the sonoporation efficiency and has to be investigated further.

We functionalized our tMBs with CD31 antibodies via streptavidin-biotin binding. On the other hand, we did not add streptavidin nor control-antibodies to our ntMBs as clinical ntMBs would not have this too. We did however study tMBs and ntMBs with an identical lipid shell with DSPC as the main lipid. For the same DSPC microbubbles, an identical resonance frequency and an increased elasticity has been reported after streptavidin functionalization [42]. This implicates a stiffer shell which likely lowers the maximum relative excursion of functionalized MB [14], [42], which could also explain why our tMBs were less efficient for sonoporation. Another limitation to our study is CD31 as ligand on our tMBs as this is a constitutively expressed adhesion molecule on endothelial cells [184]. It can therefore not be used *in vivo* as CD31-tMBs would adhere to the entire vasculature. *In vivo* the MBs circulate within the vasculature, while we performed our studies under static conditions. Flow is expected to have an influence on the sonoporation efficiency as ntMBs will be taken away by the flow, while tMBs will still adhere to the cell under flow and can even bind to cells under flow [185]. A higher sonoporation efficiency for tMBs is therefore expected and shown [50], [186], [187] under *in vivo* conditions.

### Conclusion

This study shows the feasibility of real-time sonoporation measurements using time-lapse fluorescent recordings in combination with a diffusion model. Different patterns of PI uptake derived from this model highly correlate with cell viability and could be used to estimate cell death in studies when direct cell viability assays are not applicable. The fact that low PI uptake cells reach the plateau with increasing amount of cycles suggests that lower ultrasound pulse durations should be used for drug delivery, where a high level of cell viability is required.

# Chapter 5

## **Targeted Microbubble Mediated Sonoporation of Endothelial Cells *in vivo***

*IEEE Transactions on Ultrasonics, Ferroelectrics and Frequency  
Control, 2014;. 61 (10): 1661-1667*

Ilya Skachkov<sup>1</sup>, Ying Luan<sup>1</sup>, Antonius F.W. van der Steen<sup>1,2,3</sup>, Nico de Jong<sup>1,3,4</sup>, Klazina Kooiman<sup>1</sup>

<sup>1</sup>Department of Biomedical Engineering, Erasmus MC, Rotterdam, the Netherlands;

<sup>2</sup>Shenzhen Institute of Advanced Technologies, Shenzhen, China;

<sup>3</sup>Interuniversity Cardiology Institute of the Netherlands, Utrecht, The Netherlands;

<sup>4</sup>Laboratory of Acoustical Wavefield Imaging, Faculty of Applied Sciences, Technical University Delft, Delft, The Netherlands;

**Abstract**—Ultrasound contrast agents as drug delivery systems are an emerging field. Recently, we reported that targeted microbubbles are able to sonoporate endothelial cells *in vitro*. In this study we investigated whether targeted microbubbles can also induce sonoporation of endothelial cells *in vivo*, thereby making it possible to combine molecular imaging and drug delivery. Live chicken embryos were chosen as *in vivo* model.  $\alpha$ , $\beta$ -targeted microbubbles attached to the vessel wall of the chicken embryo were insonified at 1 MHz at 150 kPa ( $1 \times 10,000$  cycles) and at 200 kPa ( $1 \times 1,000$  cycles) peak negative acoustic pressure. Sonoporation was studied by intravital microscopy using the model drug propidium iodide (PI). Endothelial cell PI uptake was observed in 48% at 150 kPa ( $n=140$ ) and in 33% at 200 kPa ( $n=140$ ). Efficiency of PI uptake depended on the local targeted microbubble concentration and increased up to 80% for clusters of 10-16 targeted microbubbles. Ultrasound or targeted microbubbles alone did not induce PI uptake. This intravital microscopy study reveals that sonoporation can be visualized and induced *in vivo* using targeted microbubbles.

**Keywords**— *Sonoporation, ultrasound, targeted microbubbles, intravital microscopy, chorioallantoic membrane (CAM) model.*

## INTRODUCTION

Ultrasound contrast agents (UCA) are widely used for increasing the ultrasound scattering of the blood pool. In cardiology, the contrast for example improves endocardial border delineation and allows quantification of myocardial perfusion [188]. In radiology, it, amongst others, can be used for detecting tumor perfusion [189], [190]. UCA are gas encapsulated microbubbles, which oscillate in response to ultrasound [15]. Currently, microbubbles with specific ligands attached to their coating, known as targeted microbubbles, are under investigation as contrast agents for ultrasound molecular imaging of cardiovascular disease and cancer [191], [192].

Microbubbles are also a promising concept as ultrasound-triggered local drug delivery system. In general, an oscillating microbubble can increase the permeability of adjacent cell membranes and facilitate cellular drug uptake. This is known as sonoporation and can be crucial for cellular uptake of cell-impermeable drugs. Sonoporation has mostly been studied using non-targeted microbubbles. The mechanism still remains unknown [18], [175], [193]. Sonoporation has only been reported in cells adjacent to oscillating microbubbles [160], [177], which can be a challenge *in vivo* because microbubbles circulate in the vasculature [8], [41]. Recently, we reported that targeted microbubbles, which adhered to the cell, can induce sonoporation *in vitro* [161]. At the same time, it has been reported that cells grown under flow are less susceptible to sonoporation [194]. Therefore, reliable models for studying the mechanism and efficacy of

## **Targeted Microbubble Mediated Sonoporation of Endothelial Cells *in vivo***

---

sonoporation are a prerequisite. Currently, intravital *in vivo* models exist for studying microbubble rheology and adherence of targeted microbubbles like rat or mouse cremaster muscle and dorsal skin-fold chamber, and hamster cheek pouch [49]-[51], which potentially can be used for studying sonoporation. However, these models are complicated and also fall under strict animal experiment legislation regulations. This is not the case for chicken embryos, for which the chorioallantoic membrane (CAM) has been used by several groups for studying different types of drug delivery systems, including microbubbles [54], [56]. In this study we investigated if we could use the chorioallantoic membrane (CAM) model to in real time study targeted microbubble sonoporation *in vivo*. The microbubbles were targeted to  $\alpha_v\beta_3$ -integrin, since this integrin is constitutively expressed by chicken embryo endothelial cells [57]. Using intravital microscopy, we studied the uptake of the model drug propidium iodide by ultrasound-activation of adherent targeted microbubbles.

### **Material and Methods**

#### **Targeted microbubbles**

Biotinylated lipid-coated microbubbles with a  $C_4F_{10}$  gas core were made by sonication as described by Klivanov et al [124]. The coating was composed of DSPC (59.4 mol %; P 6517; Sigma-Aldrich, Zwijndrecht, the Netherlands); PEG-40 stearate (35.7 mol %; P 3440; Sigma-Aldrich); DSPE-PEG(2000) (4.1 mol %; 880125 P; Avanti Polar Lipids, Alabaster, AL, USA) and DSPE-PEG(2000)-biotin (0.8 mol %; 880129 C; Avanti Polar Lipids). The purity of all lipids was >99%. The fluorescent lipid dye DiI (Invitrogen, Bleiswijk, the Netherlands) was added to the lipid solution before sonication. Biotinylated anti-mouse  $\alpha_v\beta_3$ -antibody (R&D Systems, Europe, Abingdon, United Kingdom) was conjugated to the biotinylated microbubbles via avidin-biotin bridging by subsequent incubation of microbubbles with streptavidin and biotin (30 min each step) on ice as described by Lindner et al [166] with the exception that less streptavidin and biotinylated antibody were added to  $1 \times 10^9$  microbubbles, namely 20  $\mu\text{g}$  and 5  $\mu\text{g}$  respectively. By Coulter Counter (Multisizer 3, Beckman Coulter, Mijdrecht, the Netherlands) measurements we determined that the MB mean diameter was 2.5  $\mu\text{m}$ .

#### **Intravital microscopy CAM model**

Fertilized White Leghorn chicken eggs (*Gallus gallus domesticus*) were purchased from Drost BV (Loosdrecht, the Netherlands). After 6 days of incubation in a humidified incubator at 37°C (stage HH27 according Hamburger-Hamilton criteria [126]), the embryo was taken out of the eggshell. Then, 7  $\mu\text{l}$  of targeted microbubbles ( $1 \times 10^8$  targeted microbubbles/ml) were mixed with 2  $\mu\text{l}$  of PI (final concentration 0.2 mg/ml Sigma Aldrich, Zwijndrecht, the Netherlands) and 1  $\mu\text{l}$  of Hoechst 33342 (final concentration 1 mg/ml Invitrogen) at room temperature just before the injection. Five  $\mu\text{l}$  of this mixture was injected in one of the vitelline veins using a capillary glass needle and the Visualsonics injection system (VisualSonics Inc., Toronto, ON, Canada). After injection, the embryo was placed back in the incubator for 15 min to allow targeted microbubbles to circulate and adhere to the vessel wall. Then, the yolk was removed [127] to increase embryo transparency. The upper part of an OptiCell chamber

## Chapter 5

(NUNC, Wiesbaden, Germany) was cut out and the space was filled with 1% agarose (Sigma Aldrich, Zwijndrecht, the Netherlands). The yolkless embryo was then placed on the agarose, pinned with entomology pins (size 000) and put in the experimental setup, with implemented heating system to keep the embryo at 37°C, see Fig. 1.

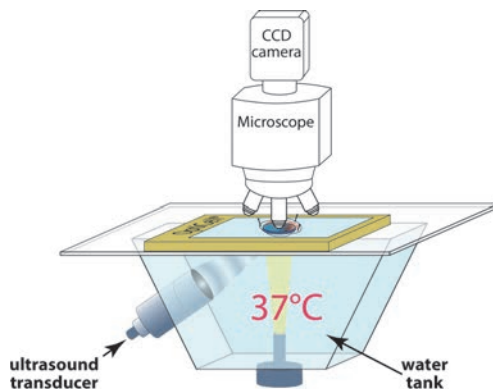


**Figure 1.** Experimental setup (not drawn to scale).

The Olympus microscope was equipped with a high sensitivity CCD camera (LCL-902K, Watec, Orangeburg, NY, USA), a 40× water-immersed objective (LUMPlanFI, NA 0.8, Olympus) and fluorescent filter sets suitable for detection of DiI and PI (U-MWG2 filter, excitation 510-550nm, emission 590nm, Olympus), and Hoechst (U-MWU2 filter, excitation 330-385nm, emission 420nm, Olympus). Targeted microbubbles were insonified with a 1 MHz single element transducer (V302; Panametrics-NDTTM, Olympus NDT, Waltham, MA, USA) using a single burst of a 10.000 cycle sine-wave at 150 kPa peak negative acoustic pressure ( $P_-$ ) or a single burst of a 1.000 cycle sine-wave burst at  $P_- = 200$  kPa. Prior to the study the transducer was calibrated with a 0.2 mm PVDF needle hydrophone (Precision Acoustics Ltd, Dorchester, UK). The -6dB diameter of the insonified area in focus was found to be 7.2 mm. To be sure that insonified areas were not overlapping every microbubble-vessel wall complex was studied in different parts of the CAM and no more than four microbubble-vessel wall complexes were studied per embryo.

Before, during and after insonification, images were recorded with a high-sensitivity CCD video camera (25 frames/second; LCL-902K, Watec). The total field of view (FOV) was 78×58  $\mu\text{m}$ . The cell membrane impermeable dye PI was used as indicator for sonoporation. The nuclear dye Hoechst 33342 was used to find the focal plane of the endothelial cell nuclei before insonification. Sonoporation was studied in CAM vessels of more than 50  $\mu\text{m}$  in diameter. The duration of the experiment with one embryo was no longer than two hours.

In all experiments, microbubbles were considered a cluster, when they were no more than 3  $\mu\text{m}$  apart, which was the average single microbubble diameter. Targeted microbubbles laying more than 10  $\mu\text{m}$  (i.e. an average nucleus size) apart from each other were considered as a separate cluster, and therefore excluded from the experiment, as we wanted to study single microbubble or single cluster-vessel wall complexes.

# Targeted Microbubble Mediated Sonoporation of Endothelial Cells *in vivo*

## Immunofluorescence

Immunofluorescent  $\alpha_v\beta_3$ -integrin staining of a vitelline vein was done on a 6-day old chicken embryo. Fluorescent Oregon Green 488 streptavidin (1 mg/ml; Invitrogen) was mixed with biotinylated  $\alpha_v\beta_3$  antibody (0.5 mg/ml; R&D Systems; see 2A) or corresponding biotinylated IgG1  $\kappa$  antibody (BD Biosciences, Breda, the Netherlands) in 1:1 volume ratio and incubated for 30 min at room temperature under agitation (30 RPM on an orbital rotator PTR-35, Grant-bio, Shepreth, UK). A glass capillary needle was placed in a vitelline vein as described before and the vessel was cut ~0.5 cm upstream and downstream to the injection site. Then, the vessel was perfused with 5  $\mu$ l of the fluorescent streptavidin antibody mixture and the needle was taken out. Perfusion with antibody only or streptavidin only was used as control. After 5 min, the vein was flushed with 5  $\mu$ l of PBS by inserting the capillary needle downstream into the lumen. Then ~1 cm<sup>2</sup> CAM tissue piece was cut and fixated with 4% formaldehyde for 5 min. After fixation, the sample was washed three times with PBS and embedded in Mowiol (Merck, Darmstadt, Germany). Confocal fluorescent microscopy was performed with an inverted microscope (LSM510META; Carl Zeiss, Germany), 10 $\times$  lens (Plan-Neofluar, NA 0.3), excitation of 488 nm, and emission of 530-600 nm.

## Results

Fig. 2 shows  $\alpha_v\beta_3$ -integrin immunofluorescent staining in chorioallantoic membrane veins of 6 day-old chicken embryos.  $\alpha_v\beta_3$ -integrin staining was observed throughout the vessel (Fig. 2 A) indicating the targeted microbubbles could bind at different locations within the vasculature. The fluorescent signal was present only in the vein (see Fig. 2 B), because only the vein was perfused with the fluorescent streptavidin -  $\alpha_v\beta_3$ -integrin antibody complex. The fluorescent streptavidin - control antibody conjugate perfusion did not show significant

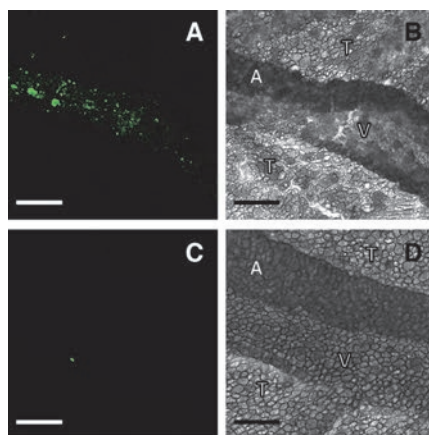


**Figure 2.**  $\alpha_v\beta_3$ -integrin expression in 6 day-old chicken embryos veins. Immunofluorescent (A, C) and corresponding bright field (B, D) image of veins (V), arteries (A) and surrounding tissue (T) of CAM vein perfused with fluorescent streptavidin  $\alpha_v\beta_3$ -integrin (A, B) and control antibody (C, D) conjugates. Scale bar 100  $\mu$ m.

fluorescence (Fig. 2C). When the vein was perfused with fluorescent streptavidin alone or with antibody alone, we did not observe any fluorescent staining.

Sonoporation was only studied in embryos that had stable and continuous blood flow. In total we studied 280 targeted microbubble-vessel wall complexes that were randomly selected ( $n = 80$  embryos) at least  $\sim 100 \mu\text{m}$  away from branches avoiding oscillatory blood flow. Only microbubble-vessel wall complexes at the top of the vessel could be studied as the red blood cells obscured other vessel wall locations.

We observed that different numbers of targeted microbubbles adhered to the vessel wall, ranging from 1 to 16. An example of six targeted microbubbles attached to the vessel wall is shown in Fig. 3. In Fig 3A the bright field image shows the six attached targeted microbubbles before insonification. Fluorescent staining with Hoechst 33342 highlighted all cell nuclei of the vessel wall surrounding the targeted microbubbles, as shown in Fig 3B. Fig. 3C shows the same six targeted microbubbles in fluorescence before ultrasound application. It also shows that the endothelial cells did not contain PI before ultrasound application. No microbubbles were observed in the FOV after ultrasound application (200 kPa, 1.000 cycles). After insonification, PI uptake was detected in the nuclei of two endothelial cells as displayed in Fig. 3D. Only the cells to which the six targeted microbubbles adhered demonstrated PI uptake, indicating these cells got sonoporated.

In total, endothelial cell PI uptake was observed in 48% at 150 kPa (10.000 cycles;  $n=140$ ) and in 33% at 200 kPa (1.000 cycles;  $n=140$ ). In all cases, we did not observe any microbubbles in the FOV after the ultrasound application. The uptake of PI as a function of the number of adherent targeted microbubbles is shown in Fig. 4. When 1 or 2 targeted microbubbles adhered, we observed no uptake for 150 kPa and 5% of PI uptake for 200 kPa. The sonoporation efficiency increased when more targeted microbubbles adhered. For both P<sub>-</sub>, PI uptake increased up to 80% when 10-16 targeted microbubbles adhered. In addition, a higher local

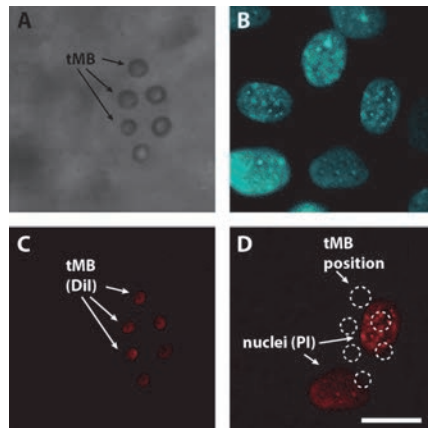


**Figure 3.** PI uptake by endothelial cells in live chicken embryo ( $35 \times 35 \mu\text{m}$  cropped images). (A) Bright field image of targeted microbubbles adhering to the vessel wall; (B) Nuclei of endothelial cells stained with Hoechst 33342; (C) Fluorescence image before ultrasound application; (D) Fluorescence image 3 min after ultrasound application. Image C and D were made with the same light filter settings. Applied ultrasound: 1 MHz, 200 kPa, 1.000 cycles. Scale bar  $10 \mu\text{m}$ .



## Targeted Microbubble Mediated Sonoporation of Endothelial Cells *in vivo*

concentration of targeted microbubbles increased the probability of sonoporation of more than one cell as also shown in Fig. 4. Sonoporation of different number of cells is indicated by the colors in the stacked columns: blue for one single sonoporated cell, red for two cells, green for three cells and purple for four sonoporated cells. When 1-5 targeted bubbles adhered, we only observed single cell sonoporation at both P<sub>-</sub>. At 150 kPa, clusters of 6-10 targeted microbubbles sonoporated one cell (15.4%), two cells (30.8%), three cells (38.5%), and four cells (15.4%). For clusters of 10-16 targeted microbubbles this was 26.7%, 40%, 33.3%, and 0% respectively. At 200 kPa, clusters of 6-10 targeted microbubbles induced sonoporation of one cell (27.3%), two cells (54.5%), and three cells (18.2%). For 10-16 adherent targeted microbubbles, this was 18.8%, 50%, and 31.2% respectively.

Extravasation of red blood cells or vessel rupture was not noticed at these low acoustic pressures. There was no significant difference in mean heart rate before ( $80 \pm 15$  beats per minute) and after the experiment ( $82 \pm 18$  beat per minute), suggesting no vasculature damage. Ultrasound or targeted microbubbles alone did not induce PI uptake.

## Discussion

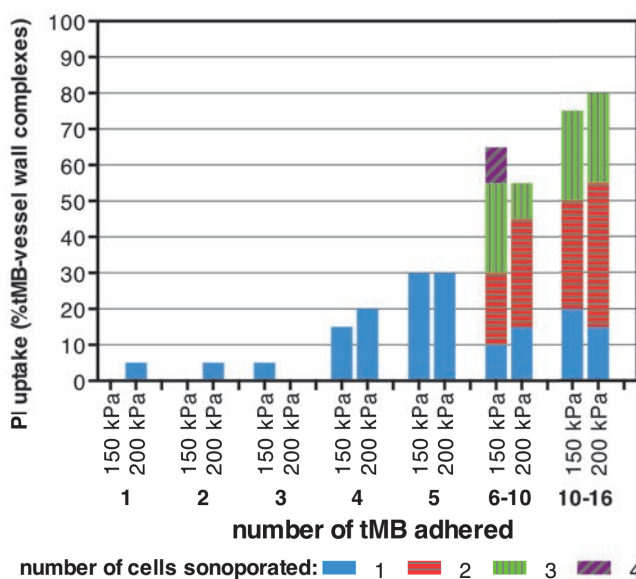


**Figure 4.** Efficiency of PI uptake as function of the number of adhered targeted microbubbles (tMB) (n=280 separate FOV). For every condition 20 single cell microbubble complexes were observed for 1, 2, 3, 4, 5, 6-10, and 10-16 adhered targeted microbubbles. Colors in stack columns indicates: blue - one cell, red - two cells, green - three cells, and purple - four cells sonoporated after sonication of one microbubble-vessel wall complex.

To the best of our knowledge, this is the first study that shows that targeted microbubbles can induce sonoporation *in vivo*. In addition, we showed the suitability of the CAM model to study sonoporation in real time using intravital microscopy.

In this study we used two DNA binding dyes: Hoechst 33342 and PI. Hoechst is a cell membrane permeable non-intercalating dye, which binds to the minor groove of DNA and stains nuclei of live cells [195]. PI binds to DNA and RNA by intercalating between the bases [196]. In addition, PI is impermeable for live cells and can only permeate live cells when the cell membrane is compromised. Because these two dyes have different DNA binding sites, it is unlikely that we underestimated sonoporation due to simultaneous use of these dyes.

In our study we applied low acoustical pressure ultrasound to targeted microbubble-vessel wall complexes. We observed similar sonoporation efficiencies at 150 kPa ( $1 \times 10,000$  cycles) and 200 kPa ( $1 \times 1,000$  cycles), suggesting both are equally well suited for inducing sonoporation *in vivo* in the CAM model. As Mannaris et al. [34] showed a gradual decrease in the scattered ultrasound by lipid-coated microbubbles at 200 kPa and 1 MHz, this may suggest our microbubbles were not responding anymore beyond 1,000 cycles and thus could explain why we found similar results.

We found that sonoporation efficiency increased when more targeted microbubbles adhered to the vessel wall. A higher local microbubble concentration also increased the chance of sonoporation more than one cell. This could be explained by more microbubbles having a larger interaction area with the cells, thus probably inducing more pores. Another reason could be that the multiple microbubbles oscillated as one cluster. A microbubble cluster may have a different resonance frequency which could have been closer to the transducer excitation frequency of 1 MHz [197]. This could have resulted into larger microbubble oscillations as microbubbles at resonance have a maximum amplitude of oscillation [15].

Recently, other groups have identified drug-loaded targeted microbubbles to be up to 5.5 times more effective than non-targeted microbubbles [50], [179], [180], [186], [187]. As we found the local targeted microbubbles concentration to be an important factor for efficiency of targeted microbubble sonoporation, getting enough microbubbles to adhere at the site of treatment is important. Studies are ongoing to improve adherence of targeted microbubbles which include dual targeting [198], [199], varying ligand linker length [200], deflating microbubbles [201], or changing microbubble shell composition [202], whilst models reveal an optimal microbubble radius of 1-2  $\mu\text{m}$  [199]. Furthermore, targeted microbubbles can be pushed towards the vessel wall to increase binding under flow conditions by acoustic radiation force [203], [204] or a magnetic field [205].

In our current study, we observed all microbubbles to be gone from the field of view after ultrasound application. This may be due to microbubble deflation, but for microbubble clusters could also have been due to microbubble detachment as it was previously reported that neighboring microbubbles attract one another. This attractive force detaches one of the microbubbles when it exceeds the binding force [174].

The dose of targeted ultrasound contrast agent used in our study was 5  $\mu\text{l}$  of  $1 \times 10^8$  microbubbles/ml. Assuming the total HH27 chicken embryo blood volume is 170  $\mu\text{l}$  [152], the final targeted microbubbles concentration in the embryo blood was  $2.8 \times 10^6$  microbubbles/ml. This concentration is similar to the recommended concentration in blood of the ultrasound contrast target-ready MicroMarker® by VisualSonics® for molecular imaging studies in mice.

## **Targeted Microbubble Mediated Sonoporation of Endothelial Cells *in vivo***

---

In our study we did not notice red blood cell extravasation, which can be a side effect or desired bio-effect of ultrasound-activated microbubble therapy. Stieger et al. [56] observed real time dextran (150 kDa; 8.5 nm) extravasation and using electron microscopy identified intracellular and intercellular gaps and extravasation of blood in the CAM model. They used higher acoustic pressures than we did, namely 500 kPa and higher. The authors attributed this to jetting of microbubbles, which is one of the proposed microbubble behaviors needed to stimulate drug uptake. As the mechanism of stimulated drug uptake by ultrasound-activated microbubbles is still unknown [175], the CAM model seems a promising model to in real time study microbubble-cell interactions to unravel the mechanism. Depending on therapeutic goals, this will allow control over the type of stimulated drug uptake so vessel damage can be avoided when desired.

We previously reported that sonoporation by targeted microbubbles *in vitro* depended upon the amplitude of oscillation as we found a threshold above which the microbubbles had to oscillate to induce sonoporation. To visualize the oscillations of the microbubbles, we used the Brandaris 128 high-speed camera in that study [161]. In another study we reported about the feasibility of using the yolkless CAM model to characterize microbubble oscillations *in vivo* with the Brandaris 128 [206]. Our future research will focus on combining *in vivo* targeted microbubble behavior and real time sonoporation using the CAM model.

The main limitation of our study is using chicken embryos as *in vivo* model as the embryonic vessels may not resemble the clinical situation. For example, they have less tight endothelial cell junctions [207], making these neovessels more permeable and hence maybe more easily affected by ultrasound-activated microbubbles. However, neovessels are also associated with tumors and atherosclerotic plaques[68], [208], [209], which may make the CAM model a relevant *in vivo* model for studying ultrasound and microbubble-mediated therapy to treat these diseases.

In conclusion, this is the first study that shows that targeted microbubbles are able to induce sonoporation *in vivo* using the low acoustic pressure of 150kPa and 200 kPa at 1 MHz. This method can be used to combine molecular ultrasound imaging with drug delivery for the detection and treatment of cardiovascular diseases and cancer.

### **Acknowledgment**

This project is supported by the Sonodrugs Project (NMP-2008-213706). The authors are grateful to Robert Beurskens, Frits Mastik and Michiel Manten from the Dept. of Biomedical Engineering, Erasmus MC for their technical assistance. The authors thank the Optical Imaging Centre of Erasmus MC for use of their confocal facilities.



# Chapter 6

## **Intravital Microscopy of Localized Stem Cell Delivery Using Microbubbles and Acoustic Radiation Force**

*Biotechnology and Bioengineering, 2015; 112(1):220-227*

T.J.A. Kokhuis<sup>1,2</sup>, I. Skachkov<sup>1</sup>, B.A. Naaijken<sup>2,3</sup>, L.J.M. Juffermans<sup>2,4</sup>, O. Kamp<sup>2,5</sup>, K. Kooiman<sup>1</sup>, A.F.W. van der Steen<sup>1,2,6,7</sup>, M. Versluis<sup>8</sup>, N. de Jong<sup>1,2,6</sup>

<sup>1</sup>Biomedical Engineering, Thorax Center, Erasmus Medical Center, Rotterdam, The Netherlands;

<sup>2</sup>Interuniversity Cardiology Institute of the Netherlands, Utrecht, The Netherlands;

<sup>3</sup>Department of Pathology, VU University Medical Center, Amsterdam, The Netherlands;

<sup>4</sup>Department of Physiology, VU University Medical Center, Amsterdam, The Netherlands;

<sup>5</sup>Department of Cardiology, VU University Medical Center, Amsterdam, The Netherlands;

<sup>6</sup>Acoustical Wavefield Imaging, Delft University of Technology, Delft, The Netherlands;

<sup>7</sup>Shenzhen Institutes of Advanced Technology, Shenzhen, China

<sup>8</sup>Physics of Fluids Group and MIRA Institute of Biomedical Technology and Technical Medicine, University of Twente, Enschede, The Netherlands

**ABSTRACT:** The use of stem cells for the repair of damaged cardiac tissue after a myocardial infarction holds great promise. However, a common finding in experimental studies is the low number of cells delivered at the area at risk. To improve the delivery, we are currently investigating a novel delivery platform in which stem cells are conjugated with targeted microbubbles, creating echogenic complexes dubbed StemBells. These StemBells vibrate in response to incoming ultrasound waves making them susceptible to acoustic radiation force. The acoustic force can then be employed to propel circulating StemBells from the centerline of the vessel to the wall, facilitating localized stem cell delivery. In this study, we investigate the feasibility of manipulating StemBells acoustically in vivo after injection using a chicken embryo model. Bare stem cells or unsaturated stem cells (<5 bubbles/cell) do not respond to ultrasound application (1 MHz, peak negative acoustical pressure  $P_- = 200$  kPa, 10% duty cycle). However, stem cells which are fully saturated with targeted microbubbles (>30 bubbles/cell) can be propelled toward and arrested at the vessel wall. The mean translational velocities measured are 61 and 177  $\mu\text{m/s}$  for  $P_- = 200$  and 450 kPa, respectively. This technique therefore offers potential for enhanced and well-controlled stem cell delivery for improved cardiac repair after a myocardial infarction.

**KEYWORDS:** *acoustic radiation force; microbubble; mesenchymal stem cell; ultrasound; stem cell delivery; StemBell*

### Introduction

Myocardial infarctions are a major burden on society and its public health systems, especially in the Western world. Continuous developments in the treatment of myocardial infarctions, have led to a growing number of patients that survive a myocardial infarction. Nevertheless, the loss of cardiac muscle cells and the formation of inflexible scar tissue makes this group of patients prone to develop congestive heart failure [210]. Restoration and repair of damaged cardiac tissue is therefore crucial for this group of patients.

Regeneration of the heart has been debated as early as the 19th century [211]. Zebrafish, for example, have the ability to fully regenerate their heart after a substantial loss of ventricular myocardial tissue [212]. Although there is evidence that the human heart is also capable of self-renewal [213], its regenerative capabilities as such are not sufficient to restore the contractile functioning of the heart after a myocardial infarction. Therefore, cardiologists started to investigate more interventional approaches like stem cell therapy, creating the field of cardiac repair. The use of mesenchymal stem cells to regenerate and repair damaged cardiac tissue

## ***Intravital Microscopy of Localized Stem Cell Delivery Using Microbubbles and Acoustic Radiation Force***

---

seems appealing. Besides their capacity for cardiomyogenesis [214], stem cells have the potential to differentiate into smooth muscle cells and endothelial cells, therefore stimulating neovascularization [215]. Furthermore, stem cells secrete a protein cocktail which has salutary effects on the microenvironment, promoting tissue protection, repair, and regeneration [216], [217].

Despite the potential of stem cell therapy for cardiac regeneration, the technique is currently hampered by the lack of persistence of a high number of stem cells at the area at risk. Typically, only a small fraction of the transplanted cells engraft within the diseased myocardium following injection, regardless of the route of administration [218],[219],[220]. However, the reduction in infarct-size and long-term improvement in cardiac functioning have been shown to correlate with the amount of cells engrafted within the infarct zone [214]. Low stem cell engraftment rates therefore limit the regenerative potential of stem cell therapy.

The cardiac microvascular endothelium (CMVE) plays an important role in the homing and migration of circulating stem cells to the myocardium [221]. In a first step, circulating stem cells need to adhere to the target proteins at the endothelial cells for which direct contact with the microvascular endothelium is necessary. Several methods have been proposed to augment stem cell homing. One approach used is priming of the target tissue, which includes vibrating microbubbles [222], shock waves [223] or cytokines [224]. Other methods focus on the active targeting of the stem cells harnessing bispecific antibodies [225], bioactive molecules [226] or mRNA-transfection of the stem cells to express homing ligands [227]. All these techniques rely on the ability of stem cells to make contact with the target endothelium. However, circulating cells will predominantly be localized around the centerline of the vessel [228], an effect known as “axial drift” [229]. This effect will therefore limit the number of stem cells that are able to adhere to the target endothelium, especially in the larger vessels of the microcirculation. A method to force the stem cells into direct and continuous contact with the vessel wall is therefore needed in order to enhance binding, retention and engraftment of stem cells in the infarcted area. Ideally, the delivery technique should be minimally invasive to avoid increased risks for morbidity and mortality.

In the field of molecular ultrasound imaging, targeted microbubble contrast agents are currently under investigation [230], [231]. Typically, these microbubbles are 1–10  $\mu\text{m}$  in size and consist of a gas core stabilized by a thin lipid, polymer or protein shell equipped with ligands against specific molecular markers. Microbubbles scatter ultrasound very effectively giving them a superior echogenicity compared with the surrounding tissue. Moreover, in contrast to tissue, the acoustic response of microbubbles can be very non-linear, which can be exploited to discriminate between echoes originating from microbubbles and tissue [145], [232]. To improve the delivery of functionalized microbubbles to target sites on the vascular endothelium, the use of low- intensity ultrasound application has been proven advantageous [203], [204], [233]. This increased delivery of microbubbles can be ascribed to the effect of acoustic radiation force [234], propelling microbubbles away from the transducer towards the vessel wall, bringing them into contact with the vascular endothelium [235].

Inspired by these findings, we have proposed a new technique to direct stem cells after injection by decorating the stem cells with functionalized microbubbles [236], [237]. We hypothesized that the conjugation with the microbubbles creates echogenic complexes, named StemBells, which are susceptible to acoustic radiation force. This force could then be employed to push the StemBells locally toward the vessel wall, arrest them in the damaged area of the heart and increase stem cell delivery.

The scope of this study is to investigate the feasibility of the ultrasonic manipulation of the position of StemBells within blood vessels in the presence of blood particles and pulsatile flow. We use intravital microscopy in a chicken embryo, which allows the direct optical observation of the effects of the acoustic radiation force *in vivo*. Translational dynamics were measured for different saturation grades (bare stem cells, unsaturated StemBells, and saturated StemBells) and acoustic pressures.

### Materials and Methods

#### Stem Cell Culture

Cells from the stromal vascular fraction of human subcutaneous adipose tissue were cultured in low glucose Dulbecco's modified Eagle's medium (DMEM; Gibco, Life Technologies Europe, Bleiswijk, the Netherlands) containing 5 U/mL heparin (Leo Pharma, Amsterdam, The Netherlands), 100 U/mL penicillin (Gibco), 100 mg/mL streptomycin (Gibco), 2 mM L-glutamine (Gibco) and 5% human platelet lysate in a humidity incubator with 5% CO<sub>2</sub> as described previously [238]. Cells from passage 2–5 were used for the experiments. Figure 1A shows the size distribution of the stem cells (passage 5). The median diameter was 18 mm.

#### Fabrication of Targeted Microbubbles

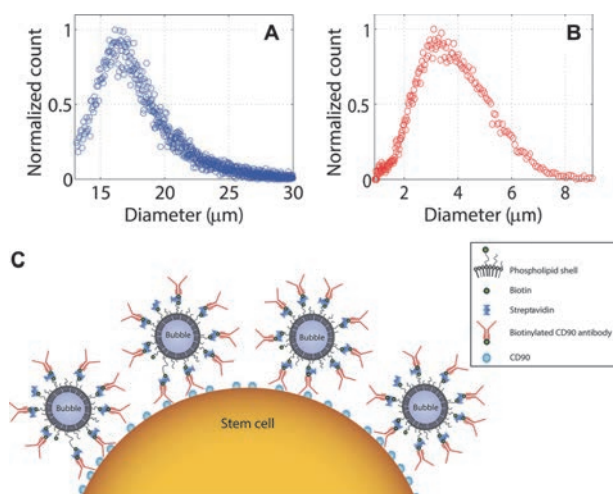


**Figure 1.** A: Size distribution of adipose derived stem cells (passage 5); the median diameter was 18 mm. B: Size distribution of CD90-targeted microbubbles; the median diameter was 3.0  $\mu\text{m}$ . Both distributions were obtained using the Coulter principle. C: Molecular architecture of a StemBell: a stem cell decorated with targeted microbubbles. Targeted microbubbles are linked to the stem cell via antibodies against the cell surface protein CD90.



Biotinylated microbubbles with a perfluorobutane (C<sub>4</sub>F<sub>10</sub>) gas core were made by sonication [124], [174]. The coating was composed of DSPC (59.4 mol%; Sigma-Aldrich, Zwijndrecht, the Netherlands), PEG-40 stearate (35.7 mol%; Sigma-Aldrich), DSPE-PEG(2000) (4.1 mol%; Avanti Polar Lipids, Alabaster, AL) and DSPE-PEG(2000)-biotin (0.8 mol%; Avanti Polar Lipids). Antibodies against the surface protein CD90, constitutionally expressed by the stem cells, were conjugated to the microbubbles using biotin-avidin bridging, as described by Lindner et al. [166]. Biotinylated microbubbles were washed three times at 400g for 1min (Heraeus Biofuge, Thermo Scientific, Etten Leur, the Netherlands). After these three washing steps, the concentration of the microbubble solution was  $\sim 1 \times 10^9$  microbubbles/mL; 0.5 mL of this microbubble solution was incubated with 20  $\mu$ g of streptavidin (S4762; Sigma-Aldrich) for 30 min on ice, after which the bubbles were washed twice and incubated with 5mg of the biotinylated monoclonal mouse anti-human CD90 antibody (BD Biosciences, Breda, the Netherlands) on ice for another 30 min. Afterwards, bubbles were washed once again and the concentration and size distribution was measured using a Multisizer 3 Coulter Counter (Beckman Coulter, Woerden, the Netherlands). The range of microbubble sizes within the solution varied between 1 and 8  $\mu$ m, with a median diameter of 3.0  $\mu$ m (see Fig. 1B).

### ***Construction of StemBells***

The stem cells were fluorescently labeled with the nucleic acid stain Hoechst 33342 (Life Technologies Europe, Bleiswijk, the Netherlands). Subsequently, cells were trypsinized, washed and mixed with the CD90-targeted microbubbles by continuous rotation at 2 rpm for 30 min at room temperature (Rotator PTR-35, Grant-bio, Shepreth, UK). The mixing ratios (stem cell: microbubble) to get unsaturated (<5 microbubbles/cell) and saturated StemBells (>30 microbubbles/cell) were 1:10 and 1:200 respectively. Figure 1C shows the molecular architecture of the StemBells used in this study.

### ***Chicken Embryo Model***

Fertilized White Leghorn chicken eggs (*Gallus gallus domesticus*) were purchased from Drost BV (Loosdrecht, the Netherlands). After 5 days of incubation in a humidified incubator at 37°C (Heraeus, Thermo Scientific, Erembodegem-Aalst, Belgium), corresponding to stage HH 27-27<sup>+</sup> according to the Hamburger–Hamilton criteria [126], the embryo and containing egg yolk was taken out of the eggshell and transferred to the experimental setup. The cup holding the chicken embryo was embedded in a water bath kept at 37°C throughout the experiment using a heating element equipped with a thermostat. For the infusion of the samples, a custom-made catheter was used. The tip of the catheter, with an inner and outer diameter near 40 and 60  $\mu$ m respectively, was pulled from a 1.2mm glass capillary (World Precision Instruments, Berlin, Germany). The tip was glued into an infusion line and connected to a 1 mL syringe. A metal wire, partly wrapped around the tubing, facilitated easy handling of the catheter. After filling the catheter with the sample (500,000 cells/mL), it was placed into one of the vitelline veins after which the position was fixed using multi-silicone grease (OKS Spezialschmierstoffe, Maisach, Germany). Injections were done manually using a micromanipulator. Typically, a few microliter of sample was infused per single injection. Due

## Chapter 6

to the use of a catheter, multiple infusions and experiments could be conducted in a single vessel.

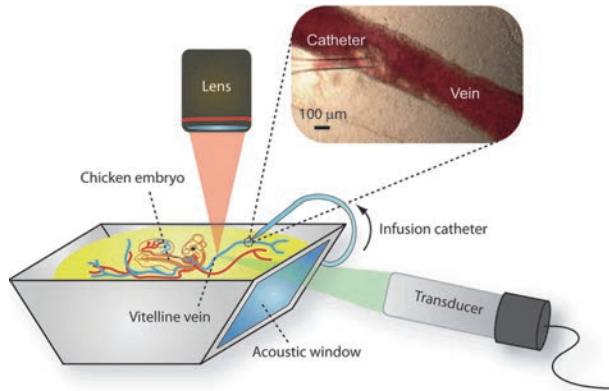


**Figure 2.** Experimental setup used for intravital microscopy. A 5-day-old chicken embryo was placed in a cup equipped with an acoustic window for the application of the acoustic radiation force. The transducer was mounted at a 20° angle with the horizontal axis and was acoustically coupled to the cup via a heated water bath. The optical focus of the objective lens was confocal with the acoustical focus of the ultrasound transducer. Samples were injected with a custom-made catheter in a vein upstream of the treated area (see inset).

### Optical and Acoustic Setup

The setup was positioned under a microscope (Olympus, Zoeterwoude, the Netherlands), equipped with a 5 objective (LMPlanFL, NA 0.13, Olympus) and an AxioCam MRc color camera (Carl Zeiss B.V., Sliedrecht, the Netherlands). The water tank was also holding a calibrated single element piston transducer (V303, Panametrics, Inc., Waltham, MA) used for the application of acoustic radiation force (1 MHz, 10% duty cycle, 10 s, peak negative acoustical pressure  $P_-$  1/4 200 kPa or 450 kPa). The optical and acoustical foci were aligned prior to each experiment. A schematic representation of the experimental setup is shown in Figure 2.

Experiments were performed in the far-field (Fraunhofer zone) at 60 mm from the surface of the transducer to assure a uniform acoustical intensity field within the optical field of view (FOV) (see Fig. 3). The maximum FOV used in this study was  $1.8 \times 1.3 \text{ mm}^2$ , in which the maximum variation in the acoustical intensity was measured to be 0.4dB, corresponding to less than 5% variation in acoustical pressure.

### Imaging Protocol

The optical field of view during the experiment was located downstream with respect to the position of the catheter. Shortly after the start of the infusion, as soon as the first fluorescently labeled cells passed by, image acquisition was initiated; ultrasound application was then automatically triggered with a time-delay of 5s. The embryo could be maneuvered independently from the ultrasound transducer and microscope objective in the xyz-direction, allowing change of the region of interest during the experiment. All experiments were performed in vessels with a diameter between 150 and 400 μm.

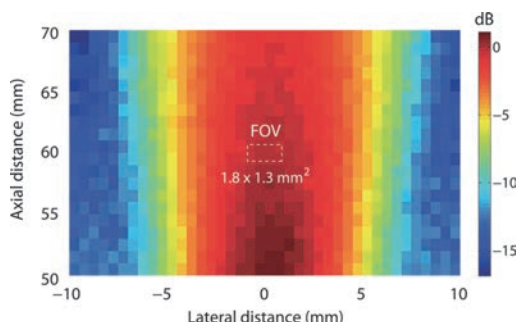


**Figure 3.** Radiation force experiments were performed in the far field at 60 mm from the transducer surface in the area indicated by the dashed box (field of view, FOV). The maximum variation in the acoustic intensity within the FOV was 0.4 dB, corresponding to less than 5% variation in acoustical pressure.

## Results

### Response Rate for Different Saturation Grades

The radial displacement of the fluorescently labeled stem cells following acoustic forcing (1 MHz,  $P_- = 200$  kPa, 10 s, 10% duty cycle) as a function of the saturation grade was studied using intravital time-lapse fluorescence microscopy. A total of 44 cells were analyzed. Figure 4A shows representative brightfield images of the three grades studied: a bare stem cell ( $n = 21$ ), an unsaturated StemBell ( $n = 11$ ) and a saturated StemBell ( $n = 12$ ) fully decorated with microbubbles. Single cells that were propelled away from the transducer toward the vessel wall after onset of the ultrasound were classified as “responders;” cells that did not respond were classified as “non-responders.” Figure 4B shows typical radial displacement–time curves obtained for responders (black curve) and non-responders (red curve). The purple bar indicates the time-window of ultrasound application. Both the bare stem cell and unsaturated StemBell population were not responsive to ultrasound application. However, 67% of the saturated StemBells responded and were propelled toward the vessel wall after onset of the ultrasound. The results are summarized in the table in Figure 4A.

After onset of the ultrasound, responding saturated StemBells exhibited a linear increase in traveled distance with time, until being immobilized at the vessel wall opposite to the location of the transducer. Figure 5 shows an example of the immobilization of three individual saturated StemBells following ultrasound application; Figure 5B shows the position of individual StemBells just before ultrasound application. The direction of the ultrasound and blood flow are shown in the schematic of Figure 5A. Application of ultrasound ( $P_- = 200$  kPa) propels the StemBells across the  $240\mu\text{m}$  sized vessel, bringing them into contact with the distal vessel wall. Figure 5C shows the position of the StemBells after the ultrasound is turned off.

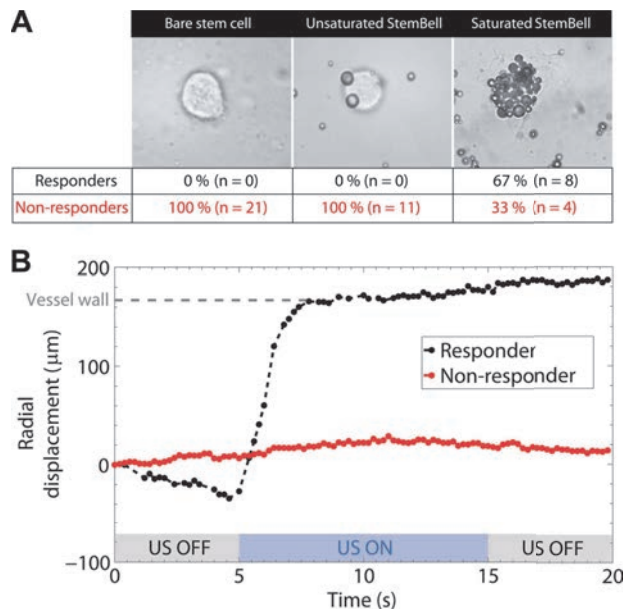


**Figure 4.** A: Brightfield images of a bare stem cell, unsaturated StemBell and saturated StemBell. The response rates are summarized in the table below. B: Typical radial displacement–time curves obtained for responders (black) and non-responders (red), both obtained using  $P_- = 200$  kPa. The blue bar indicates the time window of ultrasound (US) application.

**Radial Velocities of Saturated StemBells**

For each of the responding saturated StemBells, the radial velocity  $V_r$  was determined by differentiating the displacement curve with respect to time. Velocities were measured for  $P_- = 200$  kPa (n = 8) and  $P_- = 450$  kPa (n = 4). Because the imaging by the CCD camera is not time-resolved, this velocity reflects the time-averaged non-instantaneous velocity of the complexes. At  $P_- = 200$  kPa the StemBells were propelled with a mean velocity of  $61 \pm 41$  mm/s. Increasing the pressure to  $P_- = 450$  kPa increased the radial velocity of the StemBells by a factor of three up to  $177 \pm 105$  mm/s (see Fig. 6).

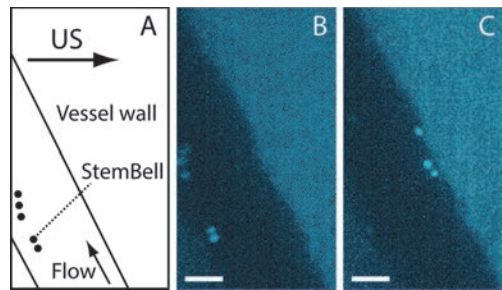


**Figure 5.** A: Schematic of the situation before ultrasound application. B: Snapshot showing the fluorescently labeled saturated StemBells before ultrasound application. C: Snapshot showing the StemBells in contact with the vessel wall right after low intensity ultrasound application (10 s,  $P_- = 1/4$  200 kPa, 10% duty cycle). The scale bar corresponds to 100  $\mu$ m. See also Video S1 online.

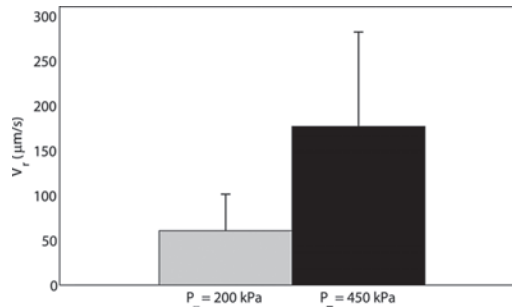


**Figure 6.** Mean radial velocity of saturated StemBells propelled by the acoustic radiation force for  $P_- = 200$  and 450 kPa.

### **Discussion**

Stem cell therapy holds the potential to transform the treatment of heart failure. Current therapies for treating heart failure only delay the progression of the disease [239]. The possibility to repair damaged myocardium using stem cells would change the course of the disease. However, so far clinical trials on stem cell therapy have shown disappointing and contradicting results, complicating the assessment of the effectiveness of the therapy in general. A major issue of stem cell therapy is the lack of an effective delivery of stem cells at the site of interest. Because functional recovery of the heart correlates with stem cell engraftment [214], a reliable and controlled method to increase the homing of stem cells to the target tissue is needed.

By using intravital microscopy we have shown that stem cells saturated with microbubbles (i.e., saturated StemBells) can be pushed in a highly localized position to the wall of small microvessels using acoustic radiation force. Evidently, in case of unsaturated StemBells, the sum of the radiation forces acting on the few microbubbles attached to the cells is insufficient to propel the entire complex. Increasing the acoustical pressure will most likely at some point also induce displacement of the unsaturated StemBell population. However, increased acoustical pressure also increases the likelihood of microbubble destruction [240], which may counteract the effect of the increased radiation force on the bubbles [233]. Moreover, a low acoustical pressure also minimizes the occurrence of any negative bioeffects. Based on our present findings, we therefore argue that saturated StemBells require the lowest pressure for acoustic forcing *in vivo*, and are therefore most favorable for ultrasound-mediated localized stem cell delivery.

Although the majority of the cells within the saturated StemBell-group responded to the acoustic radiation force, about 33% was found to be unresponsive at  $P_- = 200 \text{ kPa}$  (see table in Fig. 4A). By increasing the pressure to  $P_- = 450 \text{ kPa}$ , the percentage of non-responders in the same group decreased to 20%. The fact that not all cells within the saturated StemBell-group were propelled by the acoustic radiation force can be explained by some degree of sample heterogeneity, with a small portion of the cells having no or only a few microbubbles attached.

This effect can also be seen in the supplementary video, showing the presence of both acoustical responders and non-responders within the same sample.

### Implications for Cardiac Application

Following a myocardial infarction, reperfusion therapy of the coronary artery restores the blood flow and oxygen supply to the infarct area of the cardiac muscle. Stem cell based therapies aim to promote cardiac repair of the injured and damaged area by the delivery of stem cells to the microvessels in the infarct area. The size of these microvessels varies between 10 and 500  $\mu\text{m}$  [241]. The effect of the acoustic radiation force on the delivery of StemBells will be most beneficial in the larger vessels of the coronary circulation, in which the distance between the StemBells and the injured endothelial lining can be several hundreds of microns.

In this study we have shown that, by using 1MHz ultrasound bursts, saturated StemBells can be propelled to the wall of tiny vessels with radial velocities of 61mm/s ( $P_- = 200 \text{ kPa}$ ) and 177  $\mu\text{m/s}$  ( $P_- = 450 \text{ kPa}$ ). Similar to other particulate flows, for example, red blood cells and micro- bubbles, the majority of the StemBells can be expected to be distributed around the centerline of the cardiac microvessels [228]. Based on the radial velocities measured here, the StemBells need to be in the volume of the interrogating ultrasound beam for several seconds to facilitate optimal stem cell delivery in all the microvessels. This is feasible considering the rather low physiological blood flow velocities in the cardiac microcirculation, which are on the order of 1 mm/s [242]. It is important to emphasize that the time-averaged translational velocities measured in this study were obtained by using a ultrasound duty cycle of only 10%. In fact, the velocities can be further boosted by increasing the pulse length of each ultrasound burst, up to a factor 10 when using continuous irradiation. This would then reduce the insonification time needed for effective stem cell delivery with the same factor.

The size of a myocardial infarct typically covers ~30% of the left ventricle [243]. Therefore, to optimize stem cell delivery in the entire infarcted area, the ultrasound beam has to be scanned across the infarcted volume during the inflow of the StemBells. This can be easily overcome by the use of a 2D-matrix of transducers, facilitating simultaneous and continuous treatment of the infarcted area.

### Future Directions

The main goal of the present work was a proof of the working principle of a novel stem cell delivery technique in vivo and to study the translational dynamics of the stem cells as a function of the saturation grade (Fig. 4) and acoustic pressure (Fig. 6). The initial results look highly promising, however several aspects need further detailed studies in order to translate this technique into clinical practice.

One aspect is the long-term attachment efficiency of the StemBells which are continuously exposed to the shear forces of the blood flow. Long-term attachment is important for providing a time window for extravasation of the stem cells. Coating the stem cells with dual-targeted microbubbles, which besides the CD90 antibody, are also equipped with an antibody against a specific protein expressed on the injured endothelium, might be beneficial to further improve the delivery efficiency [237].

Another aspect is the migrational capacity of the StemBells, which is crucial for delivery and engraftment of the stem cells in the infarcted area. After being arrest at the vessel wall, StemBells have to cross the endothelial lining. Like leukocytes, bare stem cells have been shown to transmigrate over an endothelial barrier [244]. The extravasation of leukocytes is regulated via a process known as diapedesis, in which the cells squeeze through the endothelial border in a very active multi-step process [245], involving among others remodeling of the cytoskeleton. Although a similar mechanism has been proposed for the transmigration of stem cells [246], there is recent evidence that stem cells cross the endothelium via a process involving endothelial pocketing and vascular expulsion [247]. During this process, the extravasating cells themselves are rather passive and the entire process lasts up to 72h. However, the question remains whether the stem cells can already extravasate while still being surrounded by a layer of microbubbles. If not, there will be an idle period up to a few hours, dependent on the microbubble lifetime in vivo [248], [249], causing a delay in the onset of the transmigration. In that case, a microbubble destruction pulse at a high mechanical index (MI) to destroy the bubbles after the delivery of the StemBells might be beneficial to speed up the extravasation. Interestingly, microbubble destruction has been shown to improve transendothelial migration of stem cells in the myocardium [222]. Destruction of the microbubbles around the stem cell might therefore not only be a requisite, but even promote stem cell migration across the endothelium afterwards. However, in all the scenarios, the presence of the microbubbles around the cell will be temporary. The lifetime of the microbubbles is relatively short compared to the extravasation time reported for stem cells. Therefore, we do not anticipate any microbubbles present around the cell after the transendothelial passage or any interference with the engraftment at a later stage.

Finally, the effects of acoustic radiation force are known to be optimal at the resonance frequency of the microbubbles [250], [251]. Although the resonance frequency of a single lipid shelled microbubble can be expected between 1 and 4 MHz [101], the close proximity of neighboring microbubbles is known to affect the bubble dynamics and resonance frequency [252]. We therefore studied the vibrational response of Stembells as a function of the ultrasound driving frequency to further optimize our cell delivery technique. The exact details of the vibrational dynamics, both experimental and theoretical, will be the subject of a forthcoming paper.

### **Conclusions**

We have developed a new method for localized stem cell delivery using ultrasound radiation force and StemBells: stem cells decorated with targeted microbubbles. As proof of concept, StemBells were successfully delivered at the endothelium of microvessels in a chicken embryo. This ultrasound-mediated stem cell delivery technique therefore offers potential to increase the homing of stem cells to their target tissue in a minimally invasive manner.

### **Acknowledgments**

This work was financially supported by the Dutch Technology Foundation (STW). The authors would like to thank Robert Beurskens (Biomedical Engineering), Geert Springeling

## ***Chapter 6***

---

and Michiel Manten (Experimental Medical Instrumentation) of the Erasmus Medical Center for their technical assistance. The valuable remarks of Anke van der Wal are also gratefully appreciated.



# Chapter 7

**SPIO Labeling of Endothelial Cells Using  
Ultrasound and Targeted Microbubbles at Low  
Mechanical Index**

*To be submitted*

Ilya Skachkov<sup>1</sup>, Ying Luan<sup>1</sup>, Sandra van Tiel<sup>2</sup>, Ton van der Steen<sup>1,3</sup>, Nico de Jong<sup>1,3</sup>,  
Monique Bernsen<sup>2\*</sup>, Klazina Kooiman<sup>1\*</sup>

<sup>1</sup> Department of Biomedical Engineering, Thoraxcenter, Erasmus MC, Rotterdam, the Netherlands

<sup>2</sup> Department of Radiology, Erasmus MC, Rotterdam, the Netherlands

<sup>3</sup> Acoustical Wavefield Imaging, Delft University of Technology, the Netherlands

\* Contributed equally

**Abstract** – *In vivo* cell tracking of therapeutic, tumor, and endothelial cells is an emerging field and a promising technique for cardiovascular disease and cancer. The aim of this study was to find optimal ultrasound parameters for ultrasound contrast agent-mediated superparamagnetic iron oxide (SPIO)-labeling of endothelial cells at low mechanical index (MI) for future applications of MRI tracking. Optimal SPIO-labeling by CD31 targeted ultrasound contrast agents (microbubbles) at 1 megahertz ultrasound frequency was observed when the ultrasound parameters were 40 kilopascal peak negative pressure (MI 0.04), 10,000 cycles, and 20 hertz pulse repetition frequency, applied for 30 seconds just before SPIO addition. Compared to the control, this resulted in an approximate 12 times increase of SPIO uptake in endothelial cells *in vitro* with 85% cell viability. Therefore, ultrasound-activated targeted ultrasound contrast agents show great potential for effective labeling of endothelial cells with SPIO for MRI tracking.

**Key Words:** *Ultrasound contrast agents, Targeted microbubbles, Cell tracking, SPIO, MRI.*

### Introduction

*In vivo* cell tracking is a very promising technique to visualize cells of interest inside the body. It allows tracking of motile therapeutic cells like immune cells, stem cells, and endothelial progenitor cells to sites of inflammation, cancer, or ischemia [253] [254], [255]. Additionally, this technique can be used to track tumor cells [253], tumor vasculature [256], or endothelial cells in tissue engineered valves [257] and vascular grafts [258].

After labeling the cells of interest with an imaging probe, they can be tracked by an imaging modality, for example magnetic resonance imaging (MRI), positron emission tomography (PET), single-photon emission computed tomography (SPECT), or ultrasound. Each modality has its advantages and disadvantages. Ultrasound-based cell tracking is relatively safe and inexpensive, but inappropriate for whole body imaging. PET and SPECT are very sensitive techniques, and radioactive tracers can be accurately located when combined with x-ray computed tomography (CT), but cannot be used often because of ionizing radiation. MRI is the most advantageous, since it is precise, harmless, and thus better suited for longitudinal studies, but *in vivo* cell labeling is challenging [253], [259]-[261]. In addition, single cell tracking is possible by MRI [262], [263].

To increase the contrast in an MRI-image, MRI contrast agents are used. Two types of MRI contrast agents consist: 1) T1-shortening contrast agents and 2) T2- and T2\*-shortening contrast agents [264]. For cell labeling, the T2 and T2\*-shortening contrast agent superparamagnetic iron oxide nanoparticles (SPIO) of 80-180 nm in size [265] are often used [266]. They are relatively safe compounds [267]-[269], but most of the *in vitro* cell labeling techniques currently for SPIO are not applicable *in vivo*, because of their high toxicity and

## ***SPIO Labeling of Endothelial Cells Using Ultrasound and Targeted Microbubbles at Low Mechanical Index***

---

broad systemic effects [270]. Therefore, there has been growing interest in safe, site-specific cell labeling techniques. One potential method involves using ultrasound contrast agent, which are comprised of microbubbles. The microbubbles have a low diffusible gas core (e.g.  $C_4F_{10}$ ), vary in diameter from 1-10  $\mu m$ , and are encapsulated by a coating material (e.g. phospholipids). When ultrasound is applied, the microbubbles oscillate due to sequential compression and expansion caused by pressure variations in the surrounding medium. The oscillation of microbubbles has been shown to increase cell membrane permeability and capillary permeability, allowing the delivery of therapeutic materials into cells and interstitial tissue [16], [271] [14]. Up till now there is no consensus on the mechanism of the enhanced uptake. One of the theories is a phenomenon called sonoporation, when reversible or non-reversible cell membrane pores are generated upon microbubble oscillations or violent collapse [23], [160]. Recently, it was reported that the efficacy of cellular uptake of therapeutic agents can be improved by up to 7.7-fold *in vitro* [178] and up to fivefold *in vivo* [50] when using targeted microbubbles (tMB) versus non-targeted microbubbles (non-tMB). The tMB have a ligand added in their lipid coating by which they can adhere to the disease-specific cell membrane biomarkers [50], [179], [272].

Successful SPIO tumor cell labeling using ultrasound and non-tMB has been reported *in vitro* [273]. However, microbubbles are blood pool agents. Endothelial cells, which form the inner lining of vessels, are therefore the main target of intravascular administered microbubbles, not tumor cells [8], [41]. Exceptions are tumors that invade into the vasculature, as reported for hepatocellular cancer (i.e. a primary liver tumor) [261] and colorectal cancer [274]. On the other hand, microbubbles were shown to target ovarian cancer cells preclinically by an alternative administration, namely intraperitoneal injection [275]. Additionally, tMB are preferable instead of non-tMB since they can be specifically targeted to the cells of interest and upon binding are close to the endothelium, which is a prerequisite for the microbubble-mediated drug delivery effectiveness [14]. The *in vivo* study by Gao et al. demonstrated arterial wall uptake of SPIO particles using non-tMB and ultrasound [276], but only under one acoustic setting (3.5 MPa acoustic pressure, 8.5 MHz frequency, Mechanical Index (MI) of 1.2), which induced considerable arterial wall damage. To the best of our knowledge, no in-depth studies have been performed to characterize the parameters (e.g., the acoustic settings, the addition time and incubation time of SPIO) that strongly influence the efficacy and safety of SPIO-labeling of endothelial cells using tMB at low MI (<0.2).

The aim of our *in vitro* study was to find optimal parameters for non-invasive, microbubble-mediated, SPIO-labeling of endothelial cells for the future application of MRI tracking of tumor vasculature and tissue engineered vasculature structures. We used lipid-shelled microbubbles targeted against CD31 (platelet/endothelial cell adhesion molecule-1 (PECAM1)), a biomarker constitutively expressed on endothelial cell membranes [277]. Iron specific Prussian Blue staining in combination with Calcein AM based cell viability assays were applied to define the most efficient and safe conditions for SPIO-labeling of endothelial cells *in vitro*. Concerning the acoustic setting, a fixed ultrasound driving frequency of 1 MHz was used, and the pulse length and a series of low acoustical pressures (<200 kPa; MI<0.2) were varied. In our study

## Chapter 7

we used 1 MHz as the ultrasound frequency as this is the most common used frequency for microbubble-mediated drug delivery studies, and is also within the resonance frequency of microbubbles [14].

### Materials and Methods

#### *Endothelial cells*

Human umbilical vein endothelial cells (HUVECs) (Lonza, Verviers, Belgium) were cultured in EGM-2 (Lonza) medium in T75 flasks (BD, Breda, the Netherlands) in a humidified incubator at 37°C with 5% CO<sub>2</sub>. Cells were detached with 0.25% Trypsin in EDTA (Lonza) and replated on one side of the acoustically transparent OptiCell™ (NUNC, Wiesbaden, Germany) chambers. HUVECs were cultured as described before [161], for two days until 70% confluence to resemble neovasculature endothelial cells.

#### *Targeted microbubbles*

Biotinylated lipid-coated microbubbles consisting of a coating of DSPC (59.4 mol %; P 6517; Sigma-Aldrich, Zwijndrecht, the Netherlands), PEG-40 stearate (35.7 mol %; P 3440; Sigma-Aldrich), DSPE-PEG(2000) (4.1 mol %; 880125 P; Avanti Polar Lipids, Alabaster, AL, USA), and DSPE-PEG(2000)-biotin (0.8 mol %; 880129 C; Avanti Polar Lipids) with a perfluorobutane (C<sub>4</sub>F<sub>10</sub>) gas core were made by sonication as described by Klivanov et al. [124]. Biotinylated anti-human CD31-antibody (R&D Systems, Europe, Abingdon, United Kingdom) was conjugated to the microbubbles via avidin-biotin bridging as previously described [162], [166].

#### *Cell treatment*

The concentration of tMB was evaluated by Coulter Counter (Beckman Coulter, Mijdrecht, the Netherlands) measurements. Ten million tMB were added to an OptiCell™ chamber with cells plated on the bottom, which was turned upside down to let microbubbles adhere to the cells by flotation (Fig. 1B). The cell to bubble ratio was 1:3. Then the chamber was incubated at 37°C for 5 min before the experiment. SPIO nanoparticles (Endorem™, Gerber S.A., Paris, France) were added at four time-points: 5 min before, immediately before (0 min), 5 min after, and 15 min after insonification as illustrated in Figure 1A, at a final concentration of 22.4 µg Fe/ml. Each OptiCell™ chamber was divided into six acoustically non-overlapping areas (2.5 cm x 3 cm each; see Fig. 1C), which covered the beam area (6.5 mm for -6dB beam width) at the focus of the 1.0 MHz transducer (V303; Panametrics-NDTTM, Olympus NDT, Waltham, MA, USA), as verified in advance with a calibrated 0.2 mm PVDF needle hydrophone (Precision Acoustics Ltd, Dorchester, UK). The OptiCell chamber was placed into a 37 °C water bath and connected to a 2D micropositioner (Fig. 1 D). The 1 MHz focused transducer was configured at a 45° angle below the sample and the acoustic focus was aligned with the center of each subsection.

During the experiment, the position of the OptiCell chamber was manipulated so that the center of each subsection was insonified in sequence at a predefined pressure (10 to 160 kPa, Fig. 1C). A prolonged burst of 10,000 cycles with a pulse repetition rate of 20 Hz was applied. The first subsection, without the application of ultrasound application, was used as the control.

# ***SPIO Labeling of Endothelial Cells Using Ultrasound and Targeted Microbubbles at Low Mechanical Index***

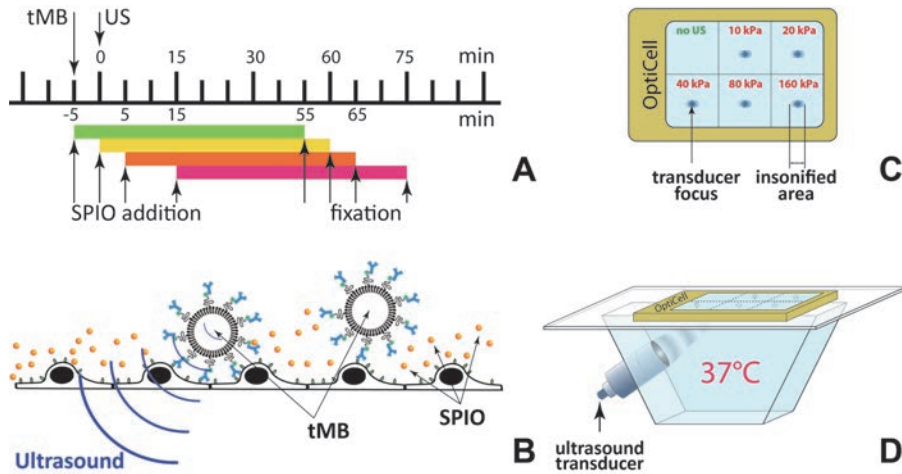


**Figure 1.** (A) Timing diagram of the experiment. The time of insonification (0 min) was used as the reference time. Targeted microbubbles (tMB) were added 5 min before the ultrasound was applied; SPIO was added 5 min before, 0 min, 5 min, and 15 min after insonification. Cells were fixated 60 min after SPIO addition. (B) Schematic representation of the tMB adhering to HUVECs. (C) Scheme of insonification subsections of the OptiCell<sup>TM</sup> chamber (to scale). (D) The experimental setup.

The effect of the different total insonification time was determined (1 sec, 10 sec, and 30 sec) at 40 kPa, 80 kPa, and 160 kPa. To investigate the effect of the incubation time with SPIO, the OptiCells were incubated at 37°C for 5 min, 1 h, and 3 h after insonification with adding SPIO 5 min prior to insonification. To check the effect of insonification of HUVECs without the presence of tMBs on SPIO uptake, the OptiCells were insonified at 40 kPa, 80 kPa, and 160 kPa for 30 sec, while SPIO was added 5 min prior to insonication (n=2). All other experiments were repeated three times. Results were derived by averaging all three datasets and the standard deviation is indicated by the error bars.

## ***SPIO labeling***

After the treatment described above (see also Fig. 1A), cells were rinsed three times with phosphate-buffer saline (PBS; Invitrogen, Groningen, the Netherlands) and fixated with 4% formaldehyde (Sigma-Aldrich, Zwijndrecht, the Netherlands) for 10 minutes. After fixation, the cells were washed three times with PBS and then incubated with Prussian Blue solution for 30 min (aqueous solution of 10% hydrochloric acid (Sigma-Aldrich) and 5% potassium ferrocyanide (Sigma-Aldrich)) to assess the SPIO-labeling [278]. Next, the cells were washed three times with PBS and the nuclei were stained with 0.1% nuclear fast red solution (Sigma-Aldrich). Thereafter the OptiCells were dried for 48 hours and microscopically examined using a microscope (Olympus, Zoeterwoude, the Netherlands) equipped with x20 Plan (NA 0.4) objective (Olympus) and a color camera (Axiocam MRc, Carl Zeiss, Germany). SPIO uptake was assessed by manually counting Prussian Blue positive cells among ~500 cells (acquired in 5 fields of view) located within a circle of 6 mm diameter around the center point of each insonified area.

### **Cell viability assay**

For each SPIO uptake measurement, cell viability was determined by Calcein AM and propidium iodide (PI) assays in parallel. Cells were treated with SPIO, tMB and ultrasound as described before (Fig. 1). Thirty minutes after SPIO addition, Calcein AM was added to the OptiCell chamber (C3100MP; Invitrogen; 0.25  $\mu$ M from a 1 mM stock prepared in DMSO (Sigma-Aldrich)) and incubated for 30 minutes. Thereafter PI (25  $\mu$ g/ml P4864, Sigma-Aldrich) and Hoechst 33342 (Invitrogen; 5  $\mu$ g/ml) were added to the Opticell chamber. Microscopic examination was performed directly after the PI and Hoechst addition with a fluorescent microscope (Olympus) equipped with the same setup as applied for SPIO labeling measurements, only that a  $\times 5$  LMPlanFI (NA 0.13) objective (Olympus) was used here. For each condition five different fields of view were acquired within the 6 mm circle around the center of the insonified area. Different filter sets (U-MWU2, 330-385/420 nm; and U-MWIB2, 460-490/510 nm, Olympus; U-MWG2, 510-550/570 nm, Olympus) were applied for detecting all cells (stained with Hoechst), viable cells (stained with Calcein AM), and dead cells (stained with propidium iodide) respectively. All images were automatically analyzed in ImageJ (Rasband, W.S., ImageJ, U. S. National Institutes of Health, Bethesda, Maryland, USA, <http://imagej.nih.gov/ij/>, 1997-2014.). The Find Maxima function in ImageJ was used to define the exact number of cells. To find an appropriate tolerance for the Find Maxima function in every image, the number of local maxima was defined for tolerance parameters of 0 to 200 in steps of two. We analyzed the differences in number of maxima between the steps. When the difference became smaller than 20, this point was considered as the correct tolerance and the corresponding number of cells as correct number of cells. This approach was validated by selective manual counting of number of cells ( $n=10$ ). The difference between manual and automatic counting was  $2.1 \pm 0.4\%$ .

## **Results**

### **Cell treatment**

During all studied ultrasound bursts, we observed displacement and disappearance of tMB. This was most pronounced for the 30 sec insonification period, as shown in Figure 2. During insonification, tMB also clustered (Fig. 2, B-D). After the 30 sec insonification period, no tMB were observed in the field of view (Fig. 2E), suggesting they had been destroyed.

### **SPIO labeling**

In the absence of ultrasound, less than 2% of cells intracellularly incorporated SPIO naturally (Fig. 3, A and B), and iron particles were detected as small aggregates distributed in the cytoplasm (Fig. 3B). By contrast, ultrasound and microbubble treated cells demonstrated much higher SPIO uptake as shown in Fig. 3, C and D. Iron particles were detected as large or small aggregates in the cytoplasm (Fig. 3D).

## ***SPIO Labeling of Endothelial Cells Using Ultrasound and Targeted Microbubbles at Low Mechanical Index***

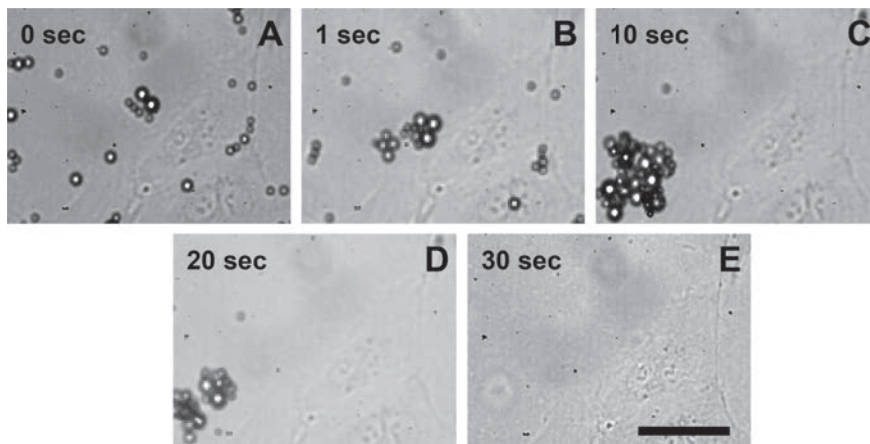


**Figure 2.** tMB displacement, destruction, and clustering during insonication (1MHz, 80 kPa, 10,000 cycles, PRF 20 Hz, 30 sec treatment). Scale bar = 10  $\mu$ m.

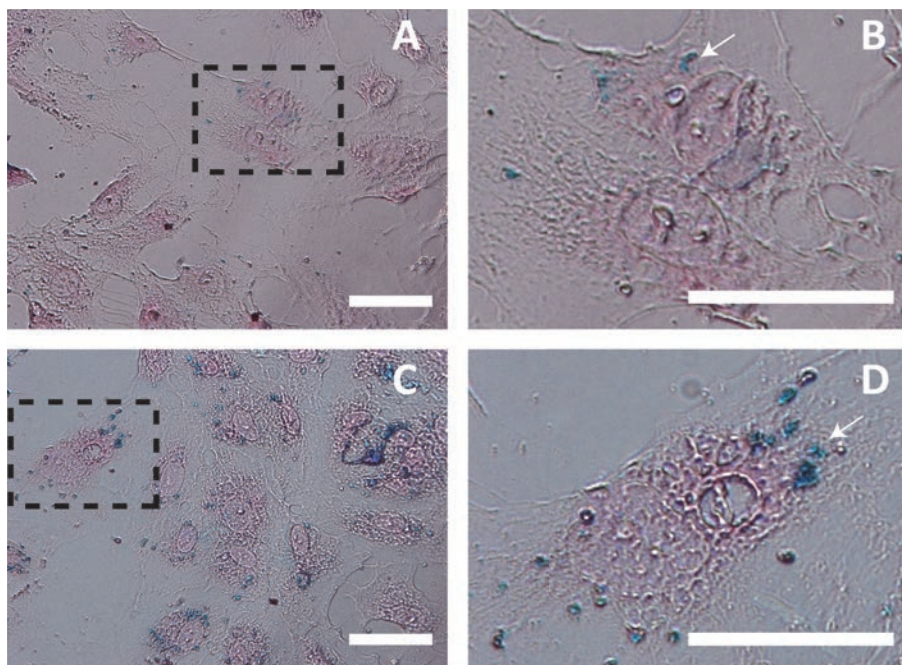


**Figure 3.** Prussian Blue staining of SPIO uptake in the control cells (A and B; i.e. no ultrasound) and in the ultrasound and tMB treated HUVEC (C and D; 80 kPa, 1 hour of incubation, SPIO was added 5 min prior to insonification). B and D are zoomed in from A and C as illustrated by the dashed rectangles. In B and D, one example of a SPIO aggregate is indicated by an arrow. Scale bar = 20  $\mu$ m.

### ***Insonification duration and acoustic pressure***

Figure 4 shows the efficacy of SPIO uptake by HUVECs and the corresponding cell viability as a function of the acoustic pressure and the total sonication duration (1, 10, or 30 seconds) at low MI (<0.16). The total ultrasound exposure time was a key factor for SPIO uptake efficacy.



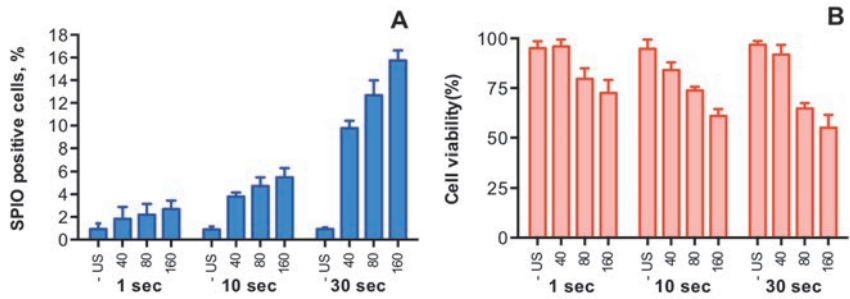


**Figure 4.** The effect of the duration of ultrasound insonification time on intracellular SPIO uptake efficiency (A) and cell viability (B).

This was demonstrated by the amount of SPIO positive cells not exceeding 4% for 1 second and 6% for 10 seconds of sonication, but with 30 seconds of insonification the amount of SPIO positive cells increased to more than 10%. Additionally, the pressure also influenced SPIO uptake significantly. With 30 seconds of insonification, the proportion of SPIO positive cells increased dramatically with the pressure (e.g., from ~10% at 40 kPa to ~16% at 160 kPa). At the same time, cell viability (Fig. 4B) decreased with both the increasing acoustical pressure and the insonification time. For example at 80 kPa, the cell viability decreased from ~70% for 10 s of insonation to ~60% for 30 sec of insonification. For an exposure time of 30 sec, the cell viability dropped by nearly two-fold from 40 kPa to 160 kPa. In general, the cell viability remained high for the pressure up to 40 kPa. Specifically, insonification for 30 sec demonstrated the best SPIO uptake and was selected for further experiments. We did not investigate a longer insonification time because after 30 seconds all tMB were destroyed (see Fig. 2E).

**SPIO incubation time**

The influence of the SPIO incubation time (5 min, 1 h or 3 h) after the treatment with ultrasound and tMB on SPIO uptake and cell viability is illustrated in Figure 5. In general, SPIO uptake increased prominently with the incubation time, for example for 180 kPa SPIO uptake increased from below ~4% to ~22%. The largest ratio between control and treated

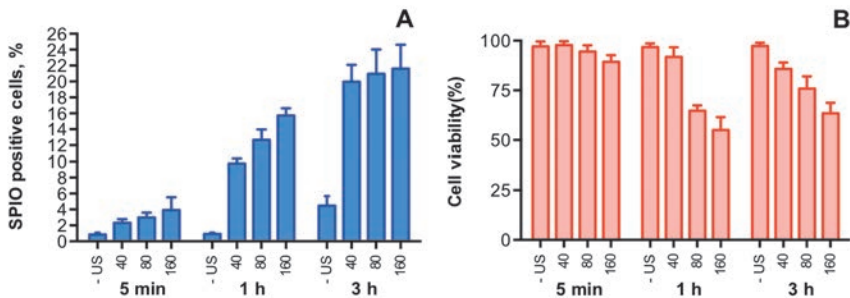


**Figure 5.** The effect of SPIO incubation time on intracellular SPIO uptake efficiency (A) and cell viability (B) after 30 sec of sonication.

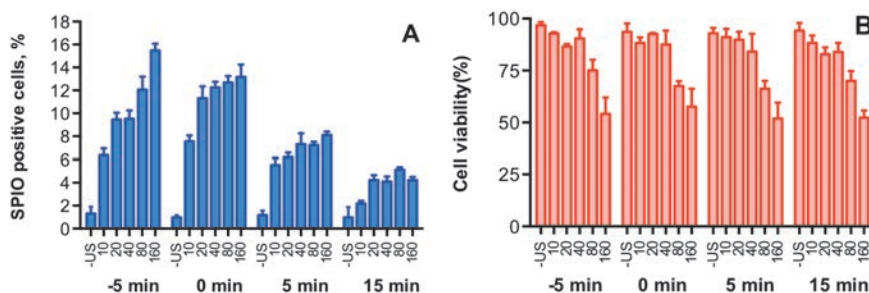


## SPIO Labeling of Endothelial Cells Using Ultrasound and Targeted Microbubbles at Low Mechanical Index

uptake was at 1 h of incubation for all pressures. Cell viability (Figure 5B) remained high (>75%) at 40 kPa for all incubation times. It decreased with the pressure (80-160 kPa) for both 1 h and 3 h of incubation time. A longer incubation time did not lower cell viability, as cell viability was slightly higher after three hours of incubation than after one hour of incubation. Based on the results from this experiment, 1 h of incubation with SPIO was selected for further investigations.

### SPIO addition time

In Fig. 6 the percentage of SPIO positive cells and cell viability are plotted for four different times between insonification and SPIO addition for different acoustic pressures. Similar to the previous measurements, no ultrasound application resulted in less than 2 % of SPIO positive cells. In addition, ultrasound application without tMBs present showed no significant difference in SPIO uptake in comparison to the control without ultrasound application for all studied pressures when the SPIO were added 5 min prior to insonification. For both additions of SPIO at 5 minutes prior (-5 min) and just before (0 min) the ultrasound application, we obtained a relatively large percentage of SPIO positive cells (~>10%) for acoustic pressures above 20 kPa. Moreover, the percentage of SPIO positive cells increased up to ~12-15 % with higher pressures for SPIO addition before the insonification. In contrast, SPIO addition at 5 and 10 minutes after ultrasound application resulted in much lower SPIO uptake (<8%). Similarly, the cell viability remained above 50% for all settings.



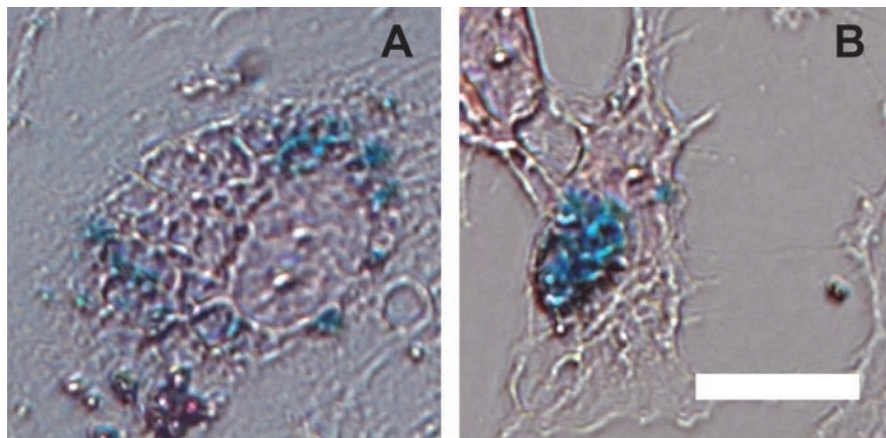
**Figure 6.** The effect of SPIO addition time on intracellular SPIO uptake efficiency (A) and cell viability (B). At fixed parameters: sonication time and SPIO incubation time.

Fig. 7 illustrates typical individual examples of SPIO distribution within the cell, indicated by Prussian Blue staining. The intensity of the stain indicates the concentration of the SPIO particles within the area qualitatively. The staining patterns can be either small (sub-micron) with a high SPIO concentration (A) or comparatively large (several microns) with a low SPIO concentration in the cytoplasm (B).

### Discussion

Tracking of endothelial cells is important for cancer and cardiovascular disease. There are several ways of SPIO cell labeling *in vitro* [269], [279]. Most of these techniques require different transfection agents, which cannot be used *in vivo* due to the associated high toxicity and systemic effects. We therefore studied a technique, based on ultrasound-activated

ultrasound contrast agents that will be *in vivo* compatible. Our results show the potential of using this technique for efficient *in vitro* SPIO endothelial cell labeling for MRI tracking.



**Figure 7.** Different intracellular SPIO distribution patterns. (A) Small SPIO aggregates distributed in the cytoplasm (-5 min SPIO addition 10 kPa); (B) A large SPIO aggregate in the nuclear area (15 min SPIO addition 160 kPa). SPIO were stained by Prussian Blue and the nuclei of cells by Nuclear Fast Red. Scale bar represents 10  $\mu\text{m}$ .

### **Microbubble oscillation dynamics**

Our study shows that ultrasound-activated tMB can greatly enhance SPIO uptake by endothelial cells *in vitro* at low MI ( $<0.2$ ). The acoustic settings (the driving pressure and insonification time) showed a significant effect on the efficacy of SPIO labeling.

Oscillating microbubbles are known to induce three drug uptake routes, namely pore formation, stimulated endocytosis, and opening of cell-cell contacts [14]. The three different drug uptake routes may require different microbubble oscillation dynamics. Although the exact link between the type of microbubble behavior and drug uptake is not known [14], it was reported that endocytosis was stimulated at longer (3,250-10,000 cycles) acoustic cycles [35], [280]. SPIO are 80-150 nm [265] nanoparticles which may require uptake by endocytosis, as this has been shown to be the main uptake mechanism for therapeutics larger than  $\sim 17$  nm in radius [35]. This is the reason why we chose to study 10,000 acoustic cycles.

We found an increasing trend of both SPIO positive cells and cell death with the acoustic pressure increase. Note that we studied acoustic pressures up to 160 peak negative pressure, a regime in which the amplitude of radial oscillations increases with pressure [125], [281]. A previous study by Vos et al. [33] has reported that highly non-spherical bubble vibrations can be induced at pressures as low as 100 kPa for bubbles at resonance. At this stage the acoustic streaming generated by vibrating microbubbles and the produced shear stresses [282]-[285] can be one of the mechanisms for enhanced permeability of the cell membrane. As was expected, the total duration of insonification also showed an effect on the SPIO uptake. It was reported that at a low mechanical index ( $\text{MI} < 0.1$ ), a bubble can repeatedly oscillate for the full duration of the prolonged pulse; while with higher MI, the bubbles are destroyed before the

## **SPIO Labeling of Endothelial Cells Using Ultrasound and Targeted Microbubbles at Low Mechanical Index**

---

ultrasound is turned off [34]. We indeed observed microbubbles still present up to 30 seconds at 80 kPa peak negative pressure (MI=0.08) (Fig. 2). The improved uptake with prolonged insonification may be related with the persistent effect produced by microstreaming generated by bubble vibrations as formulated earlier. Moreover, we noticed displacement of tMB with subsequent bubble clustering and merging driven by secondary radiation force over the prolonged burst, as illustrated by Fig. 1. Previously, tMB detachment due to the attractive secondary Bjerknes force between two tMB has been reported [174], [286]. The displacement of detached MBs and the aggregation of bubbles formed bigger bubble clusters, which have a lower resonance frequency than individual bubbles [287]. At a low driving frequency (e.g., 1 MHz as applied in this study), bubble clusters with a higher response close to resonance, which could have contributed to the enhanced SPIO uptake.

### **Microbubble selection**

It was previously shown [273] that microbubbles with SPIO incorporated in their shell in combination with ultrasound could lead to an about three fold increase of SPIO labeling *in vitro*, without compromising cell viability. Yang et al. used a polymer shell microbubble, which has been shown to behave differently than a lipid shell microbubble when exposed to ultrasound. Polymer microbubbles have a stiff shell, which can respond to ultrasound exposure under a high MI (>1) by cracking and releasing the encapsulated gas. On the contrary, lipid shelled microbubbles will oscillate at low MI and can also fuse [14]. They can therefore have a more prolonged interaction with cells than polymer microbubbles. This could explain why we found a ~12 fold increase in SPIO labeling comparing to the control group.

It was previously shown that SonoVue lipid-shelled non-tMB and ultrasound could be used to extravasate SPIO *in vivo* into the brain (28-kHz ultrasound with 100-ms burst length and 1 Hz pulse repetition frequency (PRF) at 4.8-6.0 MI for 5 min; 45-60 nm SPIO (Resovist); MRI performed 3 h after treatment) [288]) and the aortic arch (8.5 MHz ultrasound at 1.2 MI; 120-180 SPIO (Feridex); MRI performed 1 h after treatment) [276]). However these studies do not cover cell labeling, but they do demonstrate the possibility of using the co-administration approach for labeling underlying tissues and MRI imaging of the SPIO.

Aortic arch: also used Feridex + SonoVue, but only under one acoustic setting (3.5 MPa acoustic pressure, 8.5 MHz frequency, Mechanical Index (MI) of 1.2), which induced considerable arterial wall damage. First assessment also 1 hour (also 24 h, 48 h and 72 h).

### **SPIO uptake**

Although the natural uptake of SPIO (by HUVECs) was previously reported by van Tiel et al. [289], the percentage of labeled cells is not sufficient for cell tracking. In our study, HUVECs showed ~1% natural uptake after one hour of incubation, and this value increased to ~5% after three hours. The treatment with ultrasound and tMB leads to a dramatic increase of ~10-fold SPIO uptake after 1 hour incubation. We also observed that the SPIO labeling efficacy was influenced by the SPIO addition time in respect to the time of treatment with tMB and ultrasound. We observed the highest efficacy when SPIO were added with the tMB (0 min) for acoustic pressures up to 80 kPa. When SPIO were added 5 or 15 minutes after treatment, SPIO

uptake was lower, but still significantly higher (more than 5 fold) than natural uptake. This may suggest different uptake mechanisms than sonoporation, since resealing of pores created by ultrasound activated microbubbles have been reported on a relatively short time scale of up to a minute [23], [159]. One of the theories is stimulated endocytosis, when the macromolecules are actively taken up by the cells via cell membrane invagination. Our results may also suggest that both uptake by pore formation and stimulated endocytosis occurred when SPIO were added 5 minutes before or just before (0 min) treatment. This is supported by an earlier study by Meijering et al. [35]. They reported uptake by both pore formation and endocytosis using similar acoustic settings. They addressed the influence of particle size on the uptake route for dextran. For dextran larger than  $\sim 17$  nm in radius, the primary uptake route was endocytosis instead of pore formation. On the other hand, pore sizes between 1 nm [290] and  $> 100 \mu\text{m}^2$  [23] have been observed. Pores  $< 100 \mu\text{m}^2$  could still reseal, according to a recent study [23]. The SPIO colloid with low molecular weight dextran coating in Endorem<sup>TM</sup> are 120-180 nm in size [291] so they could enter cells via resealable pores. The reason why Meijering et al. [35] observed dextran particles larger than  $\sim 17$  nm mainly to be taken up by endocytosis, could be the different type of microbubble used (SonoVue versus tMB in our study) and/or the type of cells studied (bovine aortic endothelial cells versus HUVECs in our study). Moreover, induced pores  $> 100 \mu\text{m}^2$  do not tend to reseal [23] which may lead to cell death. This could explain why higher acoustic pressures (e.g.,  $\geq 80$  kPa) correspond to increased cell death.

The amount of SPIO positive cells was almost two times higher when SPIO were added five instead of fifteen min after insonification. This suggests a relatively short temporal window when the drug can be actively taken up after microbubble insonification, especially when compared to the study by Yudina et al. who reported a temporal window of 24 hours [39]. The difference could be due to the type of microbubble (SonoVue versus tMB in our study), type of cells (C6 rat glioma cells versus HUVECs in our study) and/or the therapeutic compound studied (small 1.4 kDa molecule TOTO-3 dye versus the 120-180 nm SPIO in our study).

In our study, we defined a cell as SPIO positive when we detected one or more SPIO particles within the cell. We also observed different labeling patterns, namely differences in the intensity and the intracellular distribution of the SPIO particles, although we did not quantify this degree of uptake. Some cells took up small spots (submicron) of SPIO as dense granules  $\sim 2$  nm in diameter, while others had large SPIO aggregates in the cytoplasm. This variation may also suggest uptake by pore formation and endocytosis as SPIO homogeneously distributed in the cytoplasm may suggest pore formation whilst small aggregates could indicate endocytic uptake. It was reported that the aggregate size increased with incubation time due to endosome fusion [292].

As ultrasound contrast agent-mediated SPIO-labeling of endothelial cells is likely faster clinically approved for labeling tumor vasculature, we decided to mimic the tumor vasculature's defective endothelial monolayer with poorly connected and sprouting endothelial cells [293] by culturing the HUVECs till 70% confluence. Our findings of effective tMB-mediated SPIO-labeling may therefore not be applicable to a monolayer of HUVECs, i.e. 100% confluence, applicable to vascular grafts. Different ultrasound pressures may be needed for

## **SPIO Labeling of Endothelial Cells Using Ultrasound and Targeted Microbubbles at Low Mechanical Index**

---

effective tMB-mediated SPIO-labeling HUVECs in a monolayer as cells in a monolayer are more likely in the senescent cell cycle phase ( $G_0$ ) and have a more organized cytoskeleton. With respect to sensitivity to ultrasound treatment, cells in the mitosis(M)-phase [294], [295] and synthesis(S)-phase [294] are most sensitive whereas cells in the senescent cell cycle phase are least sensitive. By contrast, another study showed the opposite: cells in the M and S-phases are more resistant to ultrasound treatment [296]. However, these ultrasound sensitivity studies were performed without the presence of MB and on cancer/epithelial cells. These studies may therefore not translate to our study and it needs further investigation whether the amount of cell confluence influences the response to tMB-treatment.

### **Clinical implications**

It was shown before that single cell tracking is possible by MRI using iron oxide as the label [289]. The micron-sized paramagnetic iron oxide (MPIO) particles used in that study are ten times bigger ( $1.6\ \mu\text{m}$ ) than SPIO. As it was revealed before [289] that the iron content of cells labeled with SPIO is less ( $\sim 10$  folds) than with MPIO, more cells may have to be labeled by SPIO to be detectable by MRI *in vivo*.

From the *in vivo* perspective, using tMB instead of non-tMB is preferable for endothelial cell labeling and drug delivery since tMB can be specifically targeted to diseased endothelial cells [192]. In addition, when ultrasound is applied to bound tMB, the vibrations of the ultrasound-activated tMB will have a direct effect on the cell membrane. This may be the reason why tMB have been shown to be  $\sim 5$  times more effective in stimulating cellular uptake of therapeutics *in vitro* as well as *in vivo* [50], [179]. On the other hand, we found ntMB to be more efficient than tMB in sonoporation endothelial cells *in vitro* when the small model drug propidium iodide was co-administered, as described in Chapter 4. CD31 used as target in this study was chosen as model ligand because it is constitutively expressed on endothelial cell membranes. It can therefore be used to label endothelial cells with SPIO in tissue-engineered valves or vascular grafts *in vitro*. However, CD31 cannot be used *in vivo* as it is expressed throughout the entire vasculature tree [184]. For targeting tMB to tumor vasculature,  $\alpha_v\beta_3$  or vascular endothelial growth factor receptor 2 (VEGFR2) can be used [192].

SPIO uptake by ultrasound-activated tMB *in vivo* is expected as we recently reported that tMB bound to  $\alpha_v\beta_3$  can stimulate endothelial cell drug uptake *in vivo* [162]. VEGFR2 is another biomarker of interest for tMB. BR55, a tMB against VEGFR2, has recently successfully been used in a phase 0 clinical trial for prostate cancer [31]. Our future studies will focus on *in vivo* SPIO labeling as well as *in vivo* MRI tracking of the labeled endothelial cells. For our *in vitro* study we incubated the HUVECs for 1 h with the SPIO. As the elimination half-life of Endorem<sup>TM</sup> (Feridex<sup>®</sup> in the USA) is  $2.4 \pm 0.2$  h in humans and the SPIO are administered as a drip infusion over  $\sim 30$  minutes [291], [297], it may be expected that the SPIO will circulate long enough *in vivo* to also achieve the 1 h incubation period.

### **Conclusion**

Our study shows that ultrasound-activated tMB are a promising technique to non-invasively enhance SPIO uptake by endothelial cells. From the current *in vitro* study, we derived optimal

## **Chapter 7**

---

ultrasound parameters for SPIO delivery to HUVECs, that is, 40 kPa at 1 MHz (MI 0.04), 10000 cycles, 20 Hz pulse repetition frequency, applied for 30 seconds just before SPIO addition. This setting increases SPIO uptake to 12 times compared to the control with 85% cell viability. The SPIO uptake was dependent on multiple factors, including the ultrasound settings, the time of SPIO addition, and the incubation time of SPIO with cells after the ultrasound treatment. Our data also suggests that SPIO uptake took place by pore formation and stimulated endocytosis, though neither of these mechanisms was observed directly.

### **Acknowledgement**

The authors are grateful to Prof. Dr. A.L. Klibanov from the University of Virginia, Cardiovascular Division, Charlottesville, Virginia, USA for discussions about the microbubble preparation. The authors thank Robert Beurskens, Kirby Lattwein, Michiel Manten, and Tom van Rooij from the Department of Biomedical Engineering, Erasmus MC, and Gaby Doeswijk from the Department of Radiology, Erasmus MC, for technical assistance.

# Chapter 8

**Adapted from: “Targeted Ultrasound Contrast  
Agents for Ultrasound Molecular Imaging and  
Therapy”**

*International Journal of Hyperthermia, 2015; 31 (2); 90-106*



## Chapter 8

Tom van Rooij<sup>1\*</sup>, Varya Daeichin<sup>1\*</sup>, Ilya Skachkov<sup>1</sup>, Nico de Jong<sup>1, 2, 3</sup>, Klazina Kooiman<sup>1</sup>

<sup>1</sup>Department of Biomedical Engineering, Thoraxcenter, Erasmus MC, Rotterdam, the Netherlands,

<sup>2</sup>Interuniversity Cardiology <sup>2</sup>Institute of the Netherlands (ICIN), Utrecht, the Netherlands

<sup>3</sup>Laboratory of Acoustical Wavefield Imaging, Faculty of Applied Sciences, Technical University Delft, the Netherlands

\* contributed equally

### Abstract

Ultrasound contrast agents (UCAs) are used routinely in the clinic to enhance contrast in ultrasonography. More recently, UCAs have been functionalised by conjugating ligands to their surface to target specific biomarkers of a disease or a disease process. These targeted UCAs (tUCAs) are used for a wide range of pre-clinical applications including diagnosis, monitoring of drug treatment, and therapy. In this review, recent achievements with tUCAs in the field of molecular imaging, evaluation of therapy, drug delivery, and therapeutic applications are discussed. We present the different coating materials and aspects that have to be considered when manufacturing tUCAs. Next to tUCA design and the choice of ligands for specific biomarkers, additional techniques are discussed that are applied to improve binding of the tUCAs to their target and to quantify the strength of this bond. As imaging techniques rely on the specific behaviour of tUCAs in an ultrasound field, it is crucial to understand the characteristics of both free and adhered tUCAs. To image and quantify the adhered tUCAs, the state-of-the-art techniques used for ultrasound molecular imaging and quantification are presented. This review concludes with the potential of tUCAs for drug delivery and therapeutic applications.

**Keywords -** *Drug delivery, microbubble, molecular imaging, targeted ultrasound contrast agents, therapy*

### Introduction

Local drug and gene delivery with ultrasound contrast microbubbles has been around for more than 20 years and is subject to extensive studies. Next to delivering drugs, it is highly desirable to assess the diseased areas before treatment and monitor therapy outcome. It will be most favorable to combine the two modalities 1) targeted ultrasound contrast imaging (diagnostic) and 2) ultrasound controlled drug delivery (therapy) in one. The concept of ultrasound contrast agent for molecular (targeted) imaging consists of using contrast particles with a specific ligand to the target receptors that are expressed in the area of disease. Targeted contrast is administered intravenously, circulates in the bloodstream, and accumulates in the area of interest via a ligand-receptor interaction. Free circulating agent clears from the bloodstream, and targeted agent signal is then used to demarcate the site and condition of the target diseased tissue. Receptors of interest, upregulated on the inner surface of endothelial layer of the vasculature, include proteins from integrin and selectin families. For instance, P-selectin and ICAM-1 are known to be upregulated on the surface of activated endothelium in the tissue that is undergoing inflammatory processes; selectin and integrin upregulation is applied by the body to direct leukocyte accumulation and transmigration into these areas. For successful strategies of drug delivery and molecular imaging the design of the bubbles is essential.



### Coating materials

The commercially available UCAs have different coating materials to reduce the surface tension and gas diffusion out of the UCAs, thereby increasing their lifetime. These are: albumin (Albunex, Cardiosphere, Optison), galactose (Echovist, Levovist), lipids (Definity, Imagent, Levovist, Lumason, MicroMarker, Sonazoid, SonoVue, Targestar), or polymers (Acusphere, Sonovist) [298] [299]. The main advantage of lipid-coated bubbles is that different mixtures can be easily formulated and modified [299]. Very recently, super-resolution fluorescence microscopy revealed that the main lipid in the coating (1,2-distearoyl-*sn*-glycero-3-phosphocholine, DSPC or 1,2-dipalmitoyl-*sn*-glycero-3-phosphocholine, DPPC) influences the ligand distribution on the shell [300] and it was also shown that the difference in ligand distribution also changes the acoustical properties [301]. This offers opportunities for designing UCAs with very specific and known properties. Most lipid-coated UCAs have a brush of polyethylene glycol (PEG) incorporated in their shell to prevent close contact between neighboring bubbles to inhibit their fusion and to shield them from the immune system [299]. But although this is generally accepted as a method to increase UCA lifetime, the necessity of incorporating PEG for tUCAs has been questioned [302]. This study indicated that small peptides either conjugated to the lipid directly or via a PEG-spacer (~10 monomers), might hinder access of the ligand to the target receptors when short PEG brushes (molecular weight of 350 kDa; i.e. 8 monomers) are part of the coating. Even when the MBs were prepared without a PEG brush in their coating, the introduction of a PEG spacer between the ligand and the lipid seemed to reduce binding. Their hypothesis is that the flexibility of the spacer possibly enabled the peptide to loop back onto the bubble surface. According to Marsh et al. [303] this is indeed what happens: due to their choice of incorporating relatively short PEG chains in the coating, the PEG chains will be in the mushroom regime and therefore assume a random configuration. If they would have used similar concentrations of PEG with longer chains, such as PEG(2000) containing 45 monomers, these chains would be in the brush state: a more stretched and less random configuration [303]. The random configuration of the PEG chain in the study of Myrset [302] could thus shield the ligand, whilst a brush configuration may have been advantageous.

Polymer tUCAs have a stiffer and thicker coating than lipid-coated bubbles, and the main acoustic difference is their echogenicity: usually a polymer bubble is destructed and the free gas bubble is detected, whereas a lipid-coated bubble can be used for non-destructive imaging [14]. Combinations of different shell materials have also been reported; Ottoboni et al. [304] used microcapsules with a cross-linked albumin outer layer and a poly-(DL-lactide) inner layer. The advantage of the two different layers is the possibility to tweak the acoustic performance via the inner polymer layer in terms of their stiffness and thickness, and to change the biological activity via the protein outer layer.

*In vivo*, the adsorption of serum proteins on the shell (opsonization) is a major challenge in the design of UCA, as it might inhibit binding of the tUCA to its target. Lipid-coated MBs based on phosphatidylcholine (PC)—especially pure DSPC—have lower serum protein adsorption, higher stability in serum, and lower uptake by the reticuloendothelial system (RES) than negatively charged phospholipids, such as phosphatidylserine (PS) [302]. Another problem

caused by opsonization is its triggering capacity for phagocytosis. As targeting ligands typically present nucleophilic groups (e.g., hydroxyl or amino) this could trigger complement C3/C3b activation to promote phagocytosis and decrease the tUCA circulation time. This can be partly overcome by using longer PEG chains that are in the brush state [303] to shield the ligands from complement activation (“overbrushing”) and thus reduce immunogenicity [305]. Unnikrishnan and Klibanov [299] on the other hand, state that complement activation aids MB adherence in the microvasculature. Although PEGylation of UCAs might decrease the circulation time, it does reduce immunogenicity and thus seems to be desirable.

### **Attaching ligands**

The ligand that makes the tUCA functional is typically a peptide, protein, polymer, antibody, nanobody or aptamer [298] [306] [307] [308] (Figure 1A). A reactive moiety suitable for conjugation with the ligand of interest needs to be attached to the tUCA shell, of which biotin (noncovalent), or covalent coupling via a carboxylate group, thiol, or maleimide are most common [299], [309] (Figure 1A3). Covalent coupling does not require foreign proteins such as streptavidin, so the chances of immune response in a clinical setting are low [310]. A carboxyl group incorporated in the tUCA shell can be activated with carbodiimide, forming an active ester that reacts with the protein amino group, forming an amide bond. However, proteins possess multiple lysine residues, so coupling via amide bonds is random and may therefore interfere with ligand-receptor interaction. As an alternative, a maleimide on the shell is coupled to a thiol group on the ligand (or vice versa), forming a thioether. The advantage of maleimide-thiol coupling is oriented coupling: a ligand protein possessing a single thiol then has a single point attachment to the bubble shell. This retains the affinity of the ligand to its target [299]. A new class of ligands are camelid-derived single-domain antibody-fragments (~15 kDa) called nanobodies, that do not induce an immune response in humans [307].

### **Biomarkers and targeting strategies**

tUCAs can be decorated with ligands against various diseases. As typical UCAs are confined to the vascular tree [8], the most commonly targeted biological processes are angiogenesis, inflammation, and thrombosis. With the introduction of smaller tUCAs that can extravasate, apoptosis can also be targeted [311].

#### **Angiogenesis**

Generally, tumors can be targeted by means of biomarkers for angiogenesis:  $\alpha_v\beta_3$  integrin, vascular endothelial growth factor (VEGF), vascular endothelial growth factor receptor 2 (VEGFR2), endoglin (CD105) [30], [298], [306], [312], or a combination hereof [313]. Cyclic RGD is a clinically translatable ligand that was confirmed to adhere to endothelial cells expressing  $\alpha_v\beta_3$ . In addition, the bubbles conjugated to cRGD had sufficient residence time to attach to the integrin and were specific for  $\alpha_v\beta_3$ -expressing cells [314]. Another strategy to target  $\alpha_v\beta_3$  used the clinically approved contrast agent Sonazoid. The PS incorporated in the UCA coating was conjugated to lactaderin. This is analogous to the process of phagocytosis: apoptotic cells externalize PS allowing lactaderin to bind to PS to promote binding to the integrins on the surface of phagocytic cells [315]. Since adherence of the MBs functionalized

## Targeted Ultrasound Contrast Agents For Ultrasound Molecular Imaging and Therapy

---

with lactadherin to human umbilical vein endothelial cells (HUVEC) under flow was higher than for bare MBs, this complex has potential to be translated to the clinic for targeting angiogenesis.

For VEGFR2 targeting the lipid-coated BR55 bubble (Bracco Diagnostics) is most promising for translation to the clinic for which a heterodimer peptide is directly conjugated to the PEGylated lipid [30]. Recently, a phase 0 clinical trial with this agent for prostate cancer was successfully conducted [31].

### Inflammation

Inflammation plays a role in several diseases, such as atherosclerosis, and transient ischemia [53], [316]-[318]. Specific inflammation markers that have been used for tUCAs are intracellular adhesion molecule 1 (ICAM-1), vascular cell adhesion molecule 1 (VCAM-1), E-selectin, and P-selectin [201], [304], [306], [319]. MBs targeted to VCAM-1 can be used to discriminate the severity of inflammatory burden in mice with various degrees of atherosclerosis [316]. This suggests that assessment of early inflammation in plaques is feasible. However, the same study showed that MB attachment to endothelial cells exposed to high wall shear stresses was very low (*in vitro*). This did improve with short interruptions of the high shear rate, as is the case with a pulsatile blood flow. Since the adhesion molecules ICAM-1 and VCAM-1 mediate the firmer adhesion of the leukocytes to the endothelium, and E-selectin and P-selectin promote the initial attachment and rolling of leukocytes [306], targeting both selectin and adhesion molecules can potentially improve initial binding and increase the binding strength.

### Thrombosis

Targeting of thrombi is mainly focused on the glycoprotein IIb-IIIa (GPIIb-IIIa or CD41/CD61) expressed by activated platelets in the thrombus [298], [306], [320], [321]. This glycoprotein mediates platelet-aggregation and is the most abundant receptor on the platelet surface [321]. Using Targestar-SA conjugated with anti-GPIIb/IIIa single-chain antibodies, these bubbles bound specifically to activated platelets *in vitro*. This may allow for real-time *in vivo* molecular imaging of acute arterial thrombosis and monitoring of pharmacological thrombolysis. Next to antibodies, it has been shown that cRGD can also be used to target GPIIb-IIIa. Although this ligand is generally known as a marker for angiogenesis, cRGD was shown to be specific for GPIIb-IIIa (also known as integrin  $\alpha_{IIb}\beta_3$ ) as well [322]. cRGD was conjugated to the MBs via thiol-maleimide coupling and binding to GPIIb-IIIa was evaluated *in vitro* in the presence of plasma and under wall shear stresses up to 8 dynes/cm<sup>2</sup> [320]—a value representative for the human aorta averaged over the heart cycle [323]. Several studies have demonstrated that cRGD exhibits an ~30× higher binding efficiency than linear RGD, and indeed significantly more cRGD bubbles adhered up to the highest shear rate *in vitro* and in the larger arteries of mice [320].

Nakatsuka et al. [308] recently introduced a new concept using MBs that are only acoustically active at thrombin levels associated with clot formation. The targeting moiety of these bubbles was a thrombin aptamer crosslinking strand (TACS). Crosslinking limits the

nonlinear signal generation of the MB due to the immobilization of the lipids in the shell. Upon decrosslinking the polymer-DNA strands completely displace from the TACS, allowing the MB to oscillate freely, enhancing their nonlinear response. The MBs consisted of DSPC, DPPA (1,2-dipalmitoyl-sn-glycero-3-phosphate), and 1,2-distearoyl-sn-glycero-3-phosphoethanolamine-poly(acrylic acid)-TACS (DSPE-PAA-TACS). When the bubbles are in contact with thrombin in the thrombus, this protein binds to the aptamer, which results in decrosslinking. The *in vitro* onset of decrosslinking was about 20 nM thrombin. Since *in vivo* clot formation starts with a concentration of ~25 nM thrombin this offers opportunities to detect small clots at an early stage [308]. This has been shown *in vivo* using similar MBs, but with different amounts of DSPE-PEG(5000) added to the mixture [324]. Small amounts of PEG were found to improve stability, while higher concentrations did not contribute significantly to stability. Indeed, it was also shown that these aptamer MBs enhanced US signal in the vicinity of clots.

### **Novel targeting strategies**

The last few years molecular imaging using MBs has emerged and multiple novel targets have been proposed and investigated. Prostate cancer is difficult to diagnose noninvasively, and common practice is routine clinical testing in the laboratory to determine the level of prostate-specific antigen in the blood. However, this test lacks sensitivity and specificity [325]. The prostate-specific membrane antigen (PSMA) has higher expression levels in prostate cancer epithelial tissue than in normal prostate tissue and benign prostatic hyperplasia [326], and is therefore very promising for UMI and staging of prostate cancer as shown *in vitro* [327]. Next to prostate cancer, other types of cancers have been successfully targeted *in vivo* using tUCA: 1) tumor vessels of angiosarcoma that were targeted via secreted frizzled related protein 2 (SFRP2) using DSPC:PEG(2000)-PE bubbles [328]; 2) ovarian cancer tumor vasculature that expresses CD276 with Target-Ready MicroMarker conjugated to anti-CD276 [329]; and 3) the neovasculature of pancreatic ductal adenocarcinoma targeted to thymocyte differentiation antigen 1 (Thy1 or CD90) using anti-Thy1 MBs [330]. The latter two are specific endothelial markers for human cancer types, which are a challenge to investigate in a preclinical setting. The group of Willmann [329], [330] therefore developed a mouse model that expresses human vascular biomarkers by transfecting mouse endothelial cells with the human biomarker of interest and implanting these together with the tumor cells of interest.

In a preclinical setting Targestar-B was targeted to epidermal growth factor receptor (EGFR) and CD147 expressed in head and neck squamous cell carcinoma, where using the dual targeting was reported as most promising [331]. Although E-selectin is not a novel target, its upregulation due to inflammation can also be used to monitor tumor progression and metastasis. E-selectin can therefore be used as a new targeting strategy for early screening for tumors with metastatic potential [312]. Next to novel targeting strategies for tumors, ischemia-reperfusion after myocardial infarction was targeted to matrix metalloproteinase-2 (MMP-2) using polymer-shelled microcapsules. Apoptosis is another recently studied target, typically

## **Targeted Ultrasound Contrast Agents For Ultrasound Molecular Imaging and Therapy**

---

targeted to PS. Annexin V is known to specifically bind to PS [332] and was used for apoptosis imaging in breast cancer cells using nanobubbles [311].

### **Techniques to enhance binding**

Binding of tUCAs to target biomarkers under *in vivo* conditions is a key factor for successful application of molecular imaging for diagnosis and therapy (Figure A). Methods to enhance binding of tMBs generally depend on adjustments in the coating of the tMBs and/or applying acoustic radiation force to push the tMBs to the target cells. Deflating the tMBs to increase the shell surface area [201], conjugating two [198] or three [333] different ligands to the coating, or optimizing the length of the ligand linker [200] are among those studies optimizing the tMBs for an enhanced binding effect. Also, the probability of successful binding may be increased by homogenizing the ligand distribution on the MB shell [300], but needs further investigation. In addition, larger tMBs have a higher binding force because of their larger binding area. Nevertheless, the shear forces induced by the blood flow experienced by larger tMBs are higher than those experienced by smaller tMBs: this increases the risk of detachment of larger tMBs from their targets. In a numerical study, the optimal tMB size for enhanced binding (assuming they keep their spherical shape) is suggested to be in the range of 2–4  $\mu\text{m}$  in diameter [199]. In a very recent study, super-resolution microscopy was used to compare tMBs based on DSPC or DPPC in terms of ligand distribution, binding area, and their shape upon binding (Figure 1B) [300]. This study shows that DSPC tMBs keep their spherical shapes after binding (Figure 1B1) and have significantly smaller binding areas than DPPC tMBs, which had a dome-shape after binding (Figure 1B2). Magnetic MBs have also been developed to enhance the targeting in UMI and therapy [334]–[336]. Magnetic targeting uses an externally applied magnetic field, typically applied using a permanent magnet, to control the location of magnetically responsive MBs. Various magnetic MB preparations and applications have been published by Stride et al. in 2009 and 2012 [335], [337]. For instance, the gas core of the MB can be surrounded by a ferrofluid and stabilized by an outer coating of L- $\alpha$ -PC. Such a magnetic MB could increase the dwell time of tMBs in a target volume, whilst specificity could be provided by biochemical targeting [337].

In addition to the tMB shell modifications, acoustic radiation force [338] can be used to push the MBs against the vessel wall to further improve the targeting rate of the MBs [233], [339]–[341]. This technique was also successfully used to improve the delivery of stem cells to the vessel wall which can be used for the repair of damaged tissue (Figure 1C) by developing echogenic complexes by conjugating tMBs to stem cells (StemBells) [342].

### **Measuring binding force**

To evaluate the efficacy and strength of tUCAs, a measurement system capable of assessing the strength of various binding configurations is necessary. Several *in vitro* methods have been proposed. Kim et al. [343] used a micromanipulation technique to adhere a single tMB to an individual glass bead using two separate pipets (Figure 1D). The pressure applied by the bead pipet was incrementally increased until the MB detached from the bead. Using this method, the binding force was measured as a function of composition and structure of the lipid shell and

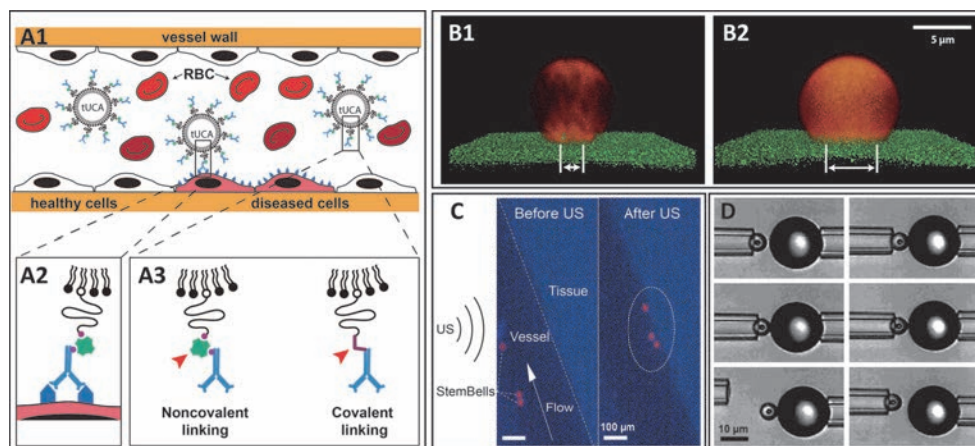


**Figure 1.** Targeting and binding of tUCAs. (A) tUCAs targeted to their specific biomarker via an antibody (the antibody is used as an example and can be replaced by other ligands, as mentioned in the text). A1 shows both free and adhered tUCAs in a blood vessel (RBC 1/4 red blood cell). A2 shows a detailed representation of a ligand that is coupled to the lipid shell via biotin-streptavidin bridging, where the ligand adheres to the biomarker. The red arrows in A3 point to an example of a non-covalent linker (i.e. biotin-streptavidin bridging) and a covalent linker. (B) A lipid-coated MB with a shell based on DSPC (B1) or DPPC (B2), where the DSPC-based MB has a smaller binding area (indicated by white arrow) and a more spherical shape than the DPPC-based MB (reprinted (adapted) from Kooiman et al. [13], with permission from John Wiley and Sons). (C) StemBells before the application of US (left panel) are pushed towards the vessel wall due to acoustic radiation force (right panel) (reprinted (adapted) from Kokhuis et al. [62] with permission from John Wiley and Sons). (D) A MB attached to a glass bead via two micropipettes. The force needed to separate them is used to measure the binding force (reprinted (adapted) with permission from Kim et al. [63]. B2014 American Chemical Society).

the receptor-ligand pair in a controlled *in vitro* environment. For instance, the detachment force for the biotin-PEG-avidin system was measured to be in the order of 100 nN assuming the contact area of the MBs and the coated surface to be around  $10 \mu\text{m}^2$ . In another study, atomic force microscopy (AFM) was used for assessing the adhesive interactions of tMBs with their target cells *in vitro* [344]. They used in-house developed lipid-shelled tMBs conjugated to the CD31 antibody using biotin-avidin bridging for adhesion to Sk-Hep1 hepatic endothelial cells and measured single distributions of the binding forces with a median of 93 pN. Controlled shear flow has also shown potential for monitoring the binding force of MBs targeted to P-selectin *in vitro* [345]. In this experiment attachment and detachment of tMBs to P-selectin immobilized on a culture dish was investigated in a parallel-plate flow chamber by increasing shear stress at intervals of 30 seconds. The accumulation rate first increased with shear stress, reached a maximum at  $\sim 0.6 \text{ dyn/cm}^2$  and then decreased. Half-maximal detachment was reached at  $34 \text{ dyn/cm}^2$ . These results suggest that accumulation and retention of tMBs are possible under physiologic flow conditions [323]. Another approach for measuring binding force is the effect of secondary Bjerknes forces on tMBs, which was studied using a high-speed camera [174], [252]. The secondary Bjerknes force is an averaged net force that neighboring MBs experience due to their oscillations in an ultrasound field. The direction of the force depends on the phase difference between the MB oscillations and the oscillating pressure gradient [234]. Kokhuis et al. [174] observed that bound tMBs deform in the direction of their



## ***Targeted Ultrasound Contrast Agents For Ultrasound Molecular Imaging and Therapy***

---

neighboring MB when they were subjected to secondary Bjerknes forces. If low-intensity ultrasound is applied, the deformation induces an elastic restoring force, causing the MBs to recoil back to their equilibrium position. For higher acoustic pressures, the secondary Bjerknes force can break the bond between the tMB and the surface. Using this technique, the binding force between a single biotinylated MB and an avidin-coated surface was measured to be between 0.9 and 2 nN. In addition, the optical observation of the event suggests that lipid anchors are pulled out of the MBs shell, rather than destruction of the strong bond between biotin and avidin [174].

### **Characterization of tUCA**

Non-targeted MBs for contrast-enhanced imaging, such as SonoVue and Definity, have been thoroughly characterized in terms of their acoustic behavior in an US field [88], [93], [346], [347]. These studies mainly focused on bulk measurements, as regular contrast-enhanced US imaging is also performed in vessels containing high concentrations of microbubbles. However, for imaging of tMBs where only very few adhered MBs may be in the imaging field, the response of only a single MB or a cluster of MBs has to be detected [124]. The response of a single MB in an US field is therefore of high interest to aid enhancement of the backscattered signal to improve imaging. A first step is to determine the MB properties after attaching a targeting ligand to it. The next step is the characterization of tMBs adhered to their molecular targets, and comparing this to the response of non-adhered tMBs to find parameters to distinguish them from each other.

### **Functionalized lipid-coated MBs**

Only a few studies used functionalized MBs to determine the effect of functionalization on the MB properties; in particular, their elasticity using either atomic force microscopy (AFM) or high-speed optical imaging. Using AFM, an elasticity was found that was almost 30× higher for streptavidin-functionalized bubbles than for bare lipid-coated bubbles ( $710 \pm 41$  vs  $25 \pm 1.4$  mN/m; DPPC:PE-biotin, 90:10 mol%) [348]. Recently, the same group performed AFM studies on bubbles with a  $C_3F_8$  core and a lipid-coating of DPPC:DSPE-PEG(2000)-biotin or DPPC:DOPE-biotin (1,2-dioleoyl-sn-glycero-3-phosphoethanolamine-biotin) in a 90:10 ratio [349]. Both types were functionalized with streptavidin and bubbles with diameters between 3 and 4  $\mu\text{m}$  were deformed up to 20% of their original size, whereas non-functionalized bubbles were deformed up to 50%. Here, streptavidin functionalization increased the elasticity to  $26.9 \pm 1.4$  mN/m for the PEGylated bubbles, but PEGylation itself was also found to increase the elasticity ( $17.7 \pm 0.7$  vs  $10.7 \pm 0.5$  mN/m). However, the increase in elasticity between PEGylated and non-PEGylated MBs might actually be a consequence of the different lipids that were used for both bubble types: DSPE or DOPE as it has recently been shown that the main lipid of non-targeted biotinylated MBs changes the distribution of the lipids in the shell and its shell properties [300], [301]. The authors do not explain the large difference in stiffness values between both studies [348], [349]. Indeed, there does not seem to be a straightforward explanation. The preparation method is identical, but although the biotinylated lipids are different this cannot explain such a large difference. The major difference between both studies

is the PEGylation [349], but this was found to increase the stiffness, and contradicts with their results.

To study the influence of functionalization on several MB properties, we functionalized identical biotinylated MBs—with either DSPC or DPPC as the main coating lipid [300]—with streptavidin via avidin-biotin bridging [166]. These unbound bubbles were investigated at frequencies between 1 and 4 MHz at a pressure of 50 kPa and their vibrational response was recorded by optical ultrahigh-speed imaging [101], [301]. For DSPC and DPPC-based bubbles the acoustic stability increased after functionalization, although their shrinkage remained significant (Table I). The resonance frequencies of functionalized and non-functionalized DSPC MBs were similar, whereas those of DPPC MBs were higher for the functionalized ones. The number of MBs responsive at the subharmonic (SH) frequency was slightly lower for functionalized DSPC bubbles than for non-functionalized DSPC bubbles. For DPPC there was no change after functionalization. At the second harmonic frequency the functionalized and non-functionalized DSPC bubbles behaved similar, whereas after functionalization hardly any DPPC bubbles responded. The viscoelastic shell properties of both functionalized and non-functionalized MBs were estimated [101], [301] using the Marmottant model [98]. The shell elasticity for DSPC slightly increased after functionalization, whereas for DPPC the elasticity increased almost fourfold. The shell damping and viscosity, on the other hand, did not change after functionalization.

Table 1. Characteristics of streptavidin-functionalized and non-functionalized DSPC and DPPC bubbles

| Type | Streptavidin functionalized | Number of bubbles | Stability (%) <sup>*</sup> | Bubbles responding at the subharmonic frequency (%) | Bubbles responding at the second harmonic frequency (%) | Elasticity (N/m) | Viscosity ( $\times 10^{-8}$ kg/s) <sup>*</sup> |
|------|-----------------------------|-------------------|----------------------------|---|---|------------------|---|
| DSPC | No <sup>#</sup>             | 15                | 95.9 (3.5)                 | 27  | 67  | 0.17 $\pm$ 0.06  | 1.2 (0.9)                                       |
|      | Yes                         | 12                | 99.1 (2.8)                 | 17  | 75  | 0.23 $\pm$ 0.06  | 1.0 (0.5)                                       |
| DPPC | No <sup>#</sup>             | 14                | 90.3 (8.2)                 | 67  | 17  | 0.06 $\pm$ 0.08  | 1.0 (0.3)                                       |
|      | Yes                         | 6                 | 94.4 (4.3)                 | 71  | 79  | 0.21 $\pm$ 0.08  | 1.8 (0.6)                                       |

<sup>\*</sup> Median (IQR)

<sup>#</sup> Data adapted from van Rooij et al. [301].

A critical side note regarding the elasticity estimated for the functionalized DPPC MBs is the narrow size distribution that did not cover the same range as the DSPC bubbles (DPPC: 4.8-6.2  $\mu$ m; DSPC: 3.1-7.3  $\mu$ m). However, our results clearly show an increase of the resonance frequency and thus of the elasticity, which corresponds with the results obtained using AFM [348], [349]. The increase in elasticity after functionalization is believed to be due to the presence of crystallization of streptavidin around the lipid shell forming a stiffer external layer [349] as also observed on streptavidin-functionalized giant unilamellar phospholipid vesicles [350], [351]. This is also consistent with the increased stability: a stiffer and thicker shell better



prevents gas escape [352]. The above mentioned studies all found differences between streptavidin-functionalized MBs and non-functionalized MBs. In contrast, Overvelde et al. [125] concluded that the frequency of maximum response and the maximum amplitude of oscillation of functionalized bubbles (BG-6438, Bracco Imaging S.p.A., Milan, Italy) and non-functionalized bubbles (BG-6437, Bracco) did not seem to change.

Although streptavidin-biotin binding is a useful tool to gain insights into the effects of coupling of relatively large and heavy ligands to MBs *in vitro*, it can never be used clinically due to strong immune responses [310]. Therefore, alternatives for *in vivo* targeting have to be considered, such as peptides, polymers, or antibodies, as discussed in the Targeting and binding section. Peptides consist of a few amino acids (~100-200 Da) [353] and the RGD-peptide used typically for targeting has a molecular mass of ~380 Da. Since functionalizing bubbles with a small, low molecular mass ligand such as biotin (~250 Da) has hardly any effect on the MB response, it is expected that functionalization of MBs with a peptide has also minimal effect. Polymers are regularly used in MB designs to increase circulation times and to function as a stealth mechanism, mostly in the form of a PEG-lipid [272]. Abou-Saleh et al. [349] only mentioned a slight increase in elasticity upon PEGylation, but it is not known whether addition of a polymer changes other properties. Streptavidin-functionalization, on the other hand, has a significant effect on MB response. Since antibodies (~150 kDa) are more than 2× heavier than streptavidin (~60 kDa) an even larger effect, especially on the elasticity and resonance frequency, is expected. In addition, coupling an antibody covalently to a lipid could also induce cross-linking of the lipids as there are usually several reactive groups on an antibody.

### **Discriminating free from adhered MBs**

The next step after functionalization of MBs is studying their behavior when they have bound to their molecular target. Moreover, the differences in acoustical signals between free and adhered bubbles are the key feature to facilitate discrimination.

Some of the non-functionalized biotinylated bubble types described in the previous section [124], [300], [301] were used to target an avidin-coated cellulose capillary using acoustic radiation force to promote binding [354]. Optical imaging was used to confirm bubble adhesion and high-speed optical imaging was used to visualize the oscillations [355]. The adherent MBs oscillated symmetrically in the plane parallel to the wall (similar to a free-floating MB) and asymmetrically in the plane normal to the wall. The side of the MB near the boundary expanded and contracted to a lesser extent than the side away from the boundary. The normalized radial expansion was larger for adherent bubbles in both imaging planes. When the transmission pressure was increased from 240 to 450 kPa, the center of the microbubble began to collapse toward the fixed boundary, producing a jet. At even higher pressures (650 kPa) fragmentation was observed in the plane parallel to the boundary, where the remaining fragments expanded and contracted, and were displaced along the wall away from the ultrasound source [354]. This can be advantageous for drug delivery applications when the drug is incorporated in or attached to the shell of the MB. The response at the fundamental frequency was larger for adherent bubbles than for free bubbles [355], the responses at the SH frequency were similar, and the

second harmonic component also increased [354]. At increasing pressures the signals at the third and fourth harmonic frequency were also higher for adhered MBs. One of the underlying causes of the higher fundamental (and maybe also harmonic) signals of adherent bubbles could be due to the small diameter of the bubbles ( $\ll$  acoustical wavelength) and the nearly uniform spatial distribution of free bubbles, resulting in incoherent echo summation and a small backscattered intensity from each sample volume. Alternatively, a layer of tUCA adherent to the inside of a vessel wall reflects US coherently, resulting in a large reflection of the fundamental component. Secondly, the adherent bubbles formed aggregates, which increase the coupling between adjacent bubbles and thus their effective scattering cross section [355].

In addition to adhered and free floating microbubbles, Overvelde et al. [125] studied bubbles close to an OptiCell wall, using ultrahigh-speed imaging. For non-functionalized bubbles close to the wall the amplitudes at the frequency of maximum response were lower than for free-floating non-functionalized MBs. However, the OptiCell wall was not blocked for unspecific binding, hence these bubbles probably also adhered to the wall and cannot be considered as non-adherent. The observation that still holds is the 50% lower frequency of maximum response for adherent functionalized MBs than for functionalized and non-functionalized MBs in the unbounded fluid (150  $\mu\text{m}$  away from the wall). The lower frequency of maximum response for bubbles bound to the OptiCell wall might be due to an increase in damping due to the coupling of the bubble and the wall.

Besides optical interrogation of bubbles, acoustical measurements have been used to characterize tMBs. Prior to the acoustical measurements, the biotinylated bubbles were sized by optical microscopy and subsequently injected in a capillary with or without streptavidin-coating [356]. Scattering of non-biotinylated bubbles and biotinylated bubbles at the fundamental frequency (2 MHz) was similar, whether or not the capillary was coated. The second harmonic resonance radius of an adherent MB was higher than that of a non-adherent targeted bubble, i.e. the second harmonic resonance frequency was higher. The reason that a difference between biotinylated and non-biotinylated bubbles was not found might be just a size or mass effect of the functionalization ligand. Not only is biotin (~250 Da) much smaller than streptavidin (~60 kDa), but one streptavidin molecule can bind up to four biotin molecules [272] that could form a protein layer around the shell, as suggested by others [349], [351]. The effect of biotinylation on the resonance frequency might therefore be only minimal.

The most recent study that compared free with bound MBs focused on the SH response frequencies at 11 and 25 MHz [357]. The rationale behind applying higher frequencies is imaging in a preclinical setting, but also in a clinical setting for the assessment of atherosclerosis in the carotid or for superficial tumors these high frequencies are needed. This study used the commercially available Target-ready MicroMarker (lipid-coated and streptavidin functionalized) which had stronger SH activity for larger bubbles when insonified at 11 MHz, i.e. the SH resonance frequency decreased upon binding. At 25 MHz the difference was smaller between free and bound MBs, but the amplitude of the adhered bubbles was 20% higher. In general, the pressure thresholds for SHs were lower at 11 MHz than at 25 MHz.

## **Targeted Ultrasound Contrast Agents For Ultrasound Molecular Imaging and Therapy**

---

Bound bubbles disrupted at lower pressure thresholds than unbound, especially at 11 MHz. At this frequency mainly compression-only behavior was observed for both bound and unbound MBs, whereas at 25 MHz the oscillations were expansion-dominated. Although differences in SH resonance were present, no shift in the fundamental resonance frequency was observed. This study also aimed to find a strategy to enhance the SH signal for imaging. Optimal pulse-inversion techniques require the same phase (0 radian phase shift) of the responses induced by both transmit pulses. Consequently, due to complete constructive interference (much like an opposite phase of  $\pi$  radian is desirable between fundamental echoes to ensure complete destructive interference) this would yield the maximal SH amplitude. At 11 MHz the SH emissions were consistently half a wavelength ( $\pi/2$  radian) out of phase and at 25 MHz it varied more, but a similar trend was observed. This suggests that with the incorporation of a phase-shifting strategy; SH signal amplitudes from pulse-inversion techniques can be increased to 60% to enhance imaging.

Interestingly, the before mentioned studies show an opposite effect on the resonance frequency upon binding of the MBs. For streptavidin-functionalized MBs in an OptiCell insonified at pressures between 2 and 4 MHz, the resonance frequency decreased [125], while for biotinylated MBs in a streptavidin-coated capillary insonified at 2 and 3.5 MHz the resonance frequency increased [356]. At higher frequencies streptavidin-coated bubbles at 11 MHz showed an increase in resonance frequency, while it showed a decrease at 25 MHz [357]. A potential explanation for the observed opposing trends may be frequency-dependent boundary effects, for example caused by frequency-dependent boundary stiffness [357]. Nevertheless, these contradictions show that much is still unknown concerning the effects of binding on the bubble response. As this is the key factor for acoustical differentiation between bound and unbound MBs, single MB studies are needed for reliable determination of the bubble properties. Especially *in vivo* studies could aid the understanding of MB behavior in a clinically-translatable environment.

### **Other types of targeted tUCA**

Next to the lipid-coated MBs described above, the characteristics of other types of tUCAs such as polymer and nanobubbles have been studied. Schmidt et al. [358] used poly(l-lactic acid) (PLA) capsules that bound to a neutravidin-adsorbed polystyrene surface (similar to an OptiCell wall). In this study the microcapsules adhered to the surface under flow conditions with wall shear stresses between 0.2 dyn/cm<sup>2</sup> and 1.5 dyn/cm<sup>2</sup>. The capsules first slowed down before binding and were easier to detach at higher shear stresses and higher acoustic pressures. At the highest pressure of 291 kPa an appreciable fraction of the capsules also ruptured and released their gas content.

Recently, polyvinylalcohol (PVA) capsules gained specific interest due to their chemical versatility that enables functionalization with different ligands, for instance hyaluronic acid for the targeting of tumor cells and tissues [359]. The properties of the air-filled PVA capsules were compared to other polymer-coated capsules and commercially available bubbles with lipid and protein coatings [360]. At very high pressures up to 2.344 MPa (mechanical index (MI) = 1.58) the shell's shear modulus was estimated to be 3.7 MPa. Assuming a shell thickness

of 0.5  $\mu\text{m}$  [360] this corresponds to an elasticity parameter of 5.6 N/m: an order of magnitude higher than for lipid-coated bubbles [88], [101], [347]. The *in vitro* capsule concentration necessary to obtain the same signal was similar to Albunex, 5 to 10-fold lower than for SonoVue and Definity and even 35-fold lower than for Optison. Using the same concentrations for SonoVue and PVA bubbles the second and higher harmonic signals for PVA were up to 10 dB higher.

Sub-micron sized nanobubbles ( $\sim 200$  nm) may potentially extravasate by passing the capillary barrier to reach cells at the tumor cell target site [320]. This property makes them promising for targeted molecular imaging and drug delivery in tumors. Due to the higher permeability of tumor vasculature—enhanced permeability and retention (EPR) effect—nanobubbles are more likely to accumulate in tumors, known as passive targeting. The stability of the lipid-Pluronic nanobubbles was higher than that of Definity (*in vitro*). In mice, the lipid-Pluronic nanobubbles were imaged using contrast harmonic imaging at 8 MHz and their contrast in the tumor was higher than for Definity. This was ascribed to the possible extravasation of the nanobubbles, which retains them in the tumor and thus increased the signal.

### Ultrasound molecular imaging

UMI that uses tUCAs is a multidisciplinary technology applicable for both diagnosis, monitoring of lesion formation, and therapy evaluation.

#### Contrast-specific imaging techniques

MBs generate higher harmonics, SH and ultraharmonic of the excitation frequency [69], [128], [361]–[364]. Upon excitation by multi-frequency bursts, MBs can also act as nonlinear mixers of the excitation frequencies and produce cross-products [365]–[367]. Conventional nonlinear imaging techniques, at lower frequencies ( $< 15$  MHz), focus mainly on detection of higher harmonics [73], [145], [368]–[370]. The need for high resolution UMI in small animal applications has pushed the frequencies used in preclinical imaging to above 15 MHz [371]. At these frequencies similar nonlinear techniques have been implemented [83], [372]–[375]. However, performance of these imaging methods is degraded because the excitation frequency is much higher than the resonance frequency of the MBs, attenuation is higher, and far-wall artifacts [144], [376]–[379]. Therefore, improved imaging methods have been extensively studied, such as improved harmonic imaging methods [151], [380], [381], chirp coded excitation alone [382], [383] or combined with pulse inversion [384], [385]. Among the nonlinear components of the MB response the SH signal has drawn much attention lately, due to its MB specificity and artifact-free characteristics. Moreover, SH response of the MB has shown its potential for selectively imaging bound tMBs [357], [386]. The SH signal is strongly dependent on the applied acoustic pressures, the ambient pressure variations [362] [80], [103], [387]–[389], and the envelope of the excitation signal [390]–[394]. The SH signal is also less attenuated than the ultraharmonic and higher harmonics, and therefore a more suitable choice for high frequency applications. Next to the different strategies to improve the sensitivity of MB detection, adjusting the MBs is another approach to gain sensitivity. It has been shown that UMI of sorted 3  $\mu\text{m}$  MBs results in an approximately 20 times higher video intensity than for

unsorted populations [395]. This size lies within the optimal tMB size distribution for enhanced binding, as shown numerically [199]. This can significantly maximize the sensitivity to small numbers of MBs for UMI.

Selective imaging of true bound tMBs from free flowing unbound ones is another challenge that is extensively studied [396]-[400]. The most common approach for imaging and quantification of tMBs is to wait for a few minutes (2 [401] to 20 minutes [402]) so most of the circulating MBs have been taken up by the lungs and liver (i.e. RES system), or have been dissolved. This time also allows the tMBs to accumulate at the site of their targets. Then low power nondestructive pulses are applied to image the tMBs, followed by a high power disruptive pulse (flash) to eliminate the MBs within the imaging plane which is again followed by low power pulses to image the residual circulating MBs (Figure 2A). The intensity difference before and after the flash corresponds to the amount of bound tMBs and is a measure for the biomarker concentration [403]-[406], as shown in Figure 2A. In such methods the quantification of bound tMBs strongly depends on the injected dose, imaging system gain, and local perfusion [396]. In addition, the influence of inhaled gasses in the anesthetic protocols influences the MBs longevity [62]-[64], [407]. These studies confirmed longer circulation times of in-house lipid-shell decafluorobutane-filled UCAs and commercially available UCAs such as Definity® and Albunex® when animals breathe medical air instead of pure oxygen as the carrier gas for the isoflurane anesthetic. This is perhaps due to a reduced ventilation/perfusion mismatch and classical diffusion between the blood gasses and the gas inside the MBs (e. g. perfluorobutane), in which nitrogen plays a role by increasing the volume of the MBs and diluting other gas species in the MBs gas core [62].

The presence of tissue motion can compromise quantification, as well as high concentrations of freely recirculating MBs after the waiting period. Several methods for selectively imaging the bound tMBs in real time have been proposed: utilizing an image-push-image sequence [396]; transmission at a low frequency and reception at a high frequency [397]; using the SH response of the MBs and interframe filtering [398]; and using singular value spectra properties [399]. However, none of the proposed methods have yet been applied *in vivo*. Only Pysz et al. developed a quantification method based on dwell time MB signal measurements, which was tested *in vivo* in well vascularized tumors in mice [408]. However, in this *in vivo* model where attachment of tMBs is significant, the classical way of quantification also performs well. Thus, the performance of the method developed by Pysz et al. in applications with very few tMBs in the presence of circulating MBs remains unclear. Daeichin et al. have developed an off-line quantification method for the detection of biomarker concentrations *in vivo* in cases with a high number of bound MBs, as well as only very few bound MBs [409]. This method benefits from motion compensation and individual contrast spot detection, and is capable of distinguishing bound MBs from unbound MBs based on their displacement. Such a quantification method can be applied in studies performed with different imaging settings because it is less sensitive to imaging parameters.

## In vivo molecular imaging

As discussed previously, the diagnostic focus of UMI is mainly on inflammation, thrombosis and angiogenesis. Assessment of angiogenesis is perhaps the application where UMI is used the most [53], [230], [313], [316]–[318], [410]–[414]. For evaluating tumor growth noninvasively, successful *in vivo* quantification of the expression levels of the angiogenetic biomarkers  $\alpha_v\beta_3$  integrin, endoglin, and VEGFR2, which vary during tumor growth in subcutaneous cancer xenografts, have been reported [413]. Recently, an UMI study using MBs targeted to  $\alpha_v\beta_3$  in an ovarian cancer model in hens [415], suggested that the detection of ovarian tumor-associated angiogenic microvessels improved when using UMI. For assessing the efficacy of cell-based therapies, UMI has been used to image a genetically engineered cell-surface marker on endothelial progenitor cells to track the fate of these progenitor cells after their delivery into vascular engraftment *in vivo* within Matrigel plugs [416]. Next to the basic research that is performed using UMI, numerous studies are putting a step forward by

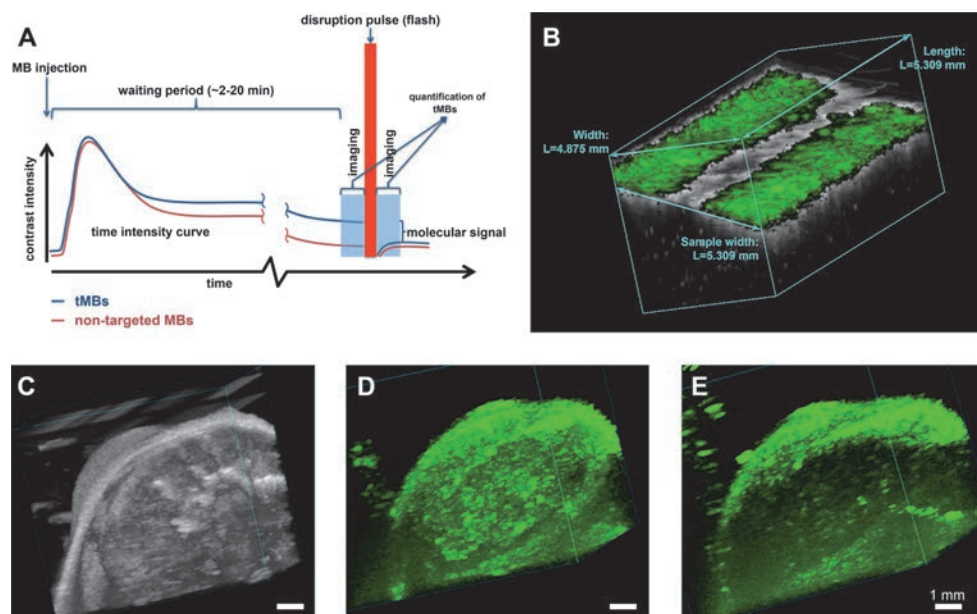


**Figure 2.** Ultrasound molecular imaging. (A) Timeline of the imaging protocol and schematic representation of a typical time intensity curve in the region of interest (e.g. tumor). (B) B-mode (grey) overlaid with non-linear contrast mode (green) US imaging in 3D to detect the  $\alpha_v\beta_3$  expression via  $\alpha_v\beta_3$ -tMBs (MicroMarker) adhered to the SVEC cells (SV40-transformed murine endothelial cell line), which were cultured in an OptiCell. The band in the middle of the figure in which there is no green signal present shows the destruction of the tMBs with the flash burst. (C–E) 3D micro-UMI using VEGFR-2 Target-Ready MicroMarker on a subcutaneous human hepatocellular carcinoma tumor which was developed by injection of HuH7 cells in male nude NMRI mice. All animal work was approved by the regulatory authority of Erasmus MC and performed in compliance with the Dutch government regulation guidelines. (C) 3D B-mode US render of the tumor. (D) 3D render of contrast images 10 min after bound tMBs within the entire volume of the tumor. (E) 3D render of contrast images 10 min after injecting the control MBs. Lack of signals within the tumor indicates no attachment of control MBs to the VEGFR-2 receptors. For (B–E), imaging was performed with a Vevo 2100 US imaging system and MS250 probe at 18 MHz. The probe was moved with increments of 32 mm using a step motor (VisualSonics).



## ***Targeted Ultrasound Contrast Agents For Ultrasound Molecular Imaging and Therapy***

---

investigating the possibilities of clinically translatable targeted MBs. In humans, the first phase 0 clinical trial for prostate cancer UMI was presented recently using BR55, a VEGFR2-tUCA [31]. Although it was only a safety study it was reported that 12 out of 14 lesions (proven by histology) could be detected with UMI. Bachawal et al. [417] used BR55 in transgenic mice with breast cancer and ductal carcinoma. UMI allowed for highly accurate detection of both breast cancer and ductal carcinoma in situ and this can be a promising clinical approach for early breast cancer detection. In addition, BR55 has shown its potential for early detection of liver dysplasia in transgenic mice [418].

UMI has also been used to noninvasively assess the effects of anti-inflammatory treatment on endothelial inflammation in early atherosclerosis in genetically modified mice [419], [420]. UMI has also proven its ability to detect biomarkers of early response to chemotherapy in several cancer types by MBs targeted to single biomarker expressions (VEGFR2,  $\alpha_v\beta_3$ , endoglin, Annexin V, or VEGF-VEGFR complex) [311], [412], [421], [422] [423] and MBs targeted to two or more of these biomarker expressions [401]. Impressively, studies have shown that UMI using  $\alpha_v\beta_3$ -tMBs is a consistent method that can classify a tumor as a responder or a non-responder as early as two days after treatment [424], [425]. To establish the link to clinical oncology Flisikowska et al. [426] have suggested the use of larger animal cancer models with more similarities to humans, such as genetically modified pigs. They proposed programs to generate gene-targeted pigs with mutations in tumor suppressor genes and proto-oncogenes that replicate key lesions responsible for a variety of human cancers. Whilst tumor models in large animals are challenging, cardiovascular disease can more easily be modeled. A study on miniswines suffering from atherosclerosis showed that an improved endothelial permeability through ultrasound-activated nitric oxide loaded echogenic immunoliposomes, can facilitate the delivery of anti-ICAM-1 conjugated echogenic immunoliposomes to inflammatory components in the arterial wall. This approach therefore has the potential to improve UMI of atheroma [427]. Next to pigs, the expression of P-selectin and VCAM-1 expression in the carotid of nonhuman primates has also been recently assessed with UMI. This study showed that endothelial cell adhesion molecule expression in large arteries could be an early event that coincides with diet-induced obesity and insulin resistance in nonhuman primates [428]. In another recent study on nonhuman primates with myocardial ischemia, UMI showed to be both safe and effective for imaging recent myocardial ischemia. Lipid-coated MBs were functionalized with dimeric recombinant human P-selectin glycoprotein ligand-1, a recombinant ligand appropriate for humans were used [52]. The study suggests that UMI can be useful for detecting recent ischemia in patients with chest pain, even in the absence of necrosis [52].

### ***Three dimensional UMI***

It is challenging to image the same plane repeatedly in 2D UMI serial studies and small misalignments can already introduce a substantial error. tMBs are attached to their targets and are therefore stationary in UMI applications where tissue motion is absent. This thus opens up opportunities for three dimensional (3D) UMI using 2D probes, by mechanically moving the ultrasound probe over the target of interest. This is illustrated in Figure 2 where 3D UMI is

performed with VEGFR2 Target-ready MicroMarker (VisualSonics Inc.) on subcutaneous human hepatocellular carcinoma tumor in a mouse.

Feasibility of 3D UMI has also been proven by other groups. Streeter et al. [402] performed 3D UMI of tumors expressing  $\alpha_v\beta_3$  integrin by mechanically stepping the transducer across the tumor in 800  $\mu\text{m}$  increments. In another study, it was shown that multiple injections of tMBs did not block sufficient binding sites to bias molecular imaging data in serial studies [429], which is an important finding. Using the clinically promising BR55 agent, 3D UMI was shown to be very well suited in depicting the angiogenic activity in very small breast lesions, suggesting its potential for detecting and characterizing these lesions in a very early stages [430]. Combining the effort to selectively image bound tMBs and 3D UMI, Hu et al. [431] used a broadband single pulse imaging sequence (transmitting at low frequencies and receiving at high frequencies) that is faster than the multi-pulse methods. Then, this method was combined with interframe filtering to selectively image targeted MBs without waiting for clearance of unbound MBs, thereby reducing acquisition time from 10 to 2 minutes. Their results suggest a feasible method for 3D UMI that is faster than current multi-pulse strategies.

### tUCA as theranostics

#### **Enhanced drug delivery**

In combination with ultrasound, UCAs are known to enhance drug delivery. Despite the fact that the mechanism behind this enhancement is not well known, vibrating MBs can stimulate drug uptake through cell membrane pore formation, a process also known as sonoporation, opening of intercellular junctions, or endocytosis [14], [16]. Whilst UCA-mediated drug delivery has been studied since 1997[432], tUCA-mediated drug delivery is relatively new. In 2011, Kooiman et al. were the first to show that CD31-tUCAs could sonoporate primary endothelial cells *in vitro* [161]. Cell membrane permeability was already induced at acoustic pressures as low as 80-200 kPa (1 MHz, 6x10 cycles burst), indicated by uptake of the co-administered model drug propidium iodide (PI). Since then, several other studies reported tUCAs for drug delivery by either co-administering the drug with the tUCAs or loading the drug in/on the tUCAs. Another co-administration *in vitro* study using PI showed that sonoporation of cancer cells by  $\alpha_v\beta_6$ -tUCAs was higher with chirp pulses from 3-7 MHz than with chirp pulses between 1.3 and 3.1 MHz or single frequency insonification at 2.2 or 5 MHz (110 kPa, 10  $\mu\text{s}$  burst, pulse repetition frequency (PRF) 1 kHz, 2 min treatment) [181]. This can be explained by the fact that chirp pulses cover a broader range of resonance frequencies, as MBs with various sizes have different resonance frequencies; chirp pulses are therefore more efficient than single frequency pulses. In the chicken embryo model (*in vivo*), a single sine-wave burst (1 MHz, 1000 cycles at 150 or 200 kPa) was sufficient for vascular PI uptake using  $\alpha_v\beta_3$ -tUCA [162].

tUCAs can also be loaded with genetic drugs (plasmid DNA, siRNA, mRNA) or drugs for local gene/drug delivery. Philips et al. [179] used VCAM-1-tUCAs loaded with plasmid DNA to transfect smooth muscle cells with the model gene green fluorescent protein (GFP) *in vitro* at 1 MHz (200-300 kPa, PRF 100 Hz, ~5 sec per cell) and at 1.5 MHz (200 kPa, PRF 8 kHz,



~5 sec per cell). In another study ovarian cancer cells were transfected with wild-type p53 tumor suppressor gene using Luteinizing Hormone-Releasing Hormone analog (LHRHa)-tUCA to induce apoptosis (1 MHz, 0.5 W/cm<sup>2</sup>, 30 s treatment) [180]. Two studies [50], [186] showed that tUCAs loaded with luciferase plasmid can transfect vasculature *in vivo*. Xie et al. [50] used P-selectin tUCAs in a hindlimb ischemia skeletal muscle model (1.6 MHz, 0.6-1.8 MPa, Power Doppler, pulsing interval 5 s, PRF 2.5 kHz for 10 min), whereas Tlaxca et al. [186] used mucosal addressin cell adhesion molecule-1 or VCAM-1-tUCA in a model for Crohn's disease (1 MHz, 5 W/cm<sup>2</sup>, 25% duty cycle for 5 min).

Two types of drugs loaded in tUCAs have been reported for cancer treatment. Paclitaxel loaded into tUCAs induced tumor cell apoptosis *in vitro* in ovarian cancer cells (LHRHa-tUCAs, 0.3 MHz, 0.5 W/cm<sup>2</sup>, 30 sec treatment) [182] and breast cancer cells (LyP-1-tUCA, 1 MHz, 4 W/cm<sup>2</sup>, 50% duty cycle, 2 min. treatment) [178] as well as *in vivo* (LHRHa-tUCAs, 0.3 MHz, 1 W/cm<sup>2</sup>, 50% duty cycle, 3 min treatment) [275]. *In vivo*, the tUCAs were administered intraperitoneally allowing the tUCAs to adhere to the ovarian cancer cells. The other anti-cancer drug loaded into VEGFR2-tUCAs was BCNU (1,3-bis(2-chloroethyl)-1-nitrosourea) for the treatment of glioma brain tumors *in vitro* (1 MHz, 0.5 MPa, 10,000 cycles, PRF 5 Hz for 1 min treatment at 2 sites) and *in vivo* (1 MHz, 0.7 MPa, 10 ms burst, 5% duty cycle, PRF 5 Hz, 1 min treatment at 2 sites), where *in vivo* the tUCAs were also used to open the blood brain barrier [187].

### **tUCA versus non-tUCA for enhanced drug delivery**

Strikingly, when tUCAs for drug delivery are directly compared with their non-targeted UCA counterparts, tUCAs are more efficient both *in vitro* [178]-[182] (up to 7.7-fold higher [178]) and *in vivo* [50], [186], [187], [275] (up to 5-fold higher [50]), irrelevant whether the drug was co-administered with the tUCAs or whether the drug was loaded on/in the tUCAs. Although the reasons for this higher efficiency have not yet been investigated, several could be possible. Possibly the main reason could be that tUCAs vibrate against the cells directly as they are bound to the cells, which may result in a more efficient transfer of acoustic energy, especially because sonoporation was only reported in cells adjacent to vibrating microbubbles for non-tUCAs [160], [177]. The acoustic behavior of the tUCAs itself could also explain this difference, as *in vitro* studies have shown that tUCAs are acoustically more stable, vibrate with a larger amplitude at the fundamental frequency, fragment in the plane parallel to the boundary and have a different resonance frequency (see characterization of tUCA section). Microbubble clustering could also be a phenomenon contributing to the higher efficiency of tUCAs, as a cluster of bubbles is known to behave as one large bubble, which is also associated with a shift in their resonance frequency [197]. This is substantiated by the chicken embryo study in which clusters of 10 to 16 tMBs had a 16-fold higher sonoporation efficacy than single tMBs [300].

A disadvantage of using tUCAs for drug delivery was reported by Hu et al. [433] who showed that insonified  $\alpha_v\beta_3$ -tUCAs temporarily decreased blood flow within the insonified area after application of a 5 MHz, 2 or 4 MPa color-Doppler destruction pulse (6-cycle pulse length, PRF 124 Hz, 900 ms duration). Although such high frequency and pressure pulses are not typically used for drug delivery, temporarily reducing the blood flow could be advantageous to

keep the delivered drug in the treated area. The reduced blood flow could also reduce tumor size by itself as has been reported for non-tUCA [434].

With tUCAs now also being used for drug delivery, the terms ultrasound-mediated targeted drug delivery or ultrasound and microbubble targeted drug delivery (UMTD) have become confusing. UMTD is used for drug delivery using non-targeted UCA where “targeted” refers to the local application of the ultrasound itself. We therefore suggest banning the UMTD term and use ultrasound and microbubble mediated drug delivery (UMMD) for non-targeted UCAs and ultrasound and targeted microbubble mediated drug delivery (UtMMD) for tUCAs instead.

### Outlook and conclusions

Recent studies on larger human-like animals such as pigs and nonhuman primates, as well as the first phase 0 clinical trial for prostate cancer with the VEGFR2 tUCA BR55 show the capability of clinical UMI in the near future. Recent insights in shell coating properties of tUCAs, new strategies for targeting, and the development of nanoscale tUCAs will open up a new range of opportunities and will broaden the spectrum of diseases that can be targeted.

Intrinsic properties of the tUCAs, such as deformability due to low elasticity could be used as an advantage to improve binding. This underlines the necessity of single tMB investigation to further understand their properties. Upon binding, opposite effects on the resonance frequency are reported, which also reflects a change in harmonic frequencies. The increase in their SH amplitude upon binding could potentially be utilized for selective imaging of adhered tMBs, which could speed up the UMI and increase its specificity. Obviously, 3D imaging is desired for UMI applications, either by mechanically moving a two dimensional probe or using a volumetric 3D probe.

By using tUCAs as local drug delivery systems, intracellular drug uptake can be enhanced several fold in comparison to non-tUCAs. tUCAs able to carry and deliver a high payload are needed, as is the elucidation of the mechanism by which tUCA stimulate drug uptake. A novel therapeutic use of tUCAs for cancer treatment could be the functionalization with kinase inhibitors. These molecules have a high affinity for cancer cell receptors and are already approved or in clinical trials as anticancer drugs, such as gefitinib (EGFR), sunitinib (FLT-1), and Bevacizumab (VEGF) [435]. Bound kinase inhibitor-tUCAs could therefore facilitate both UMI and act as inhibitor activators for apoptosis. With BR55 now undergoing regulatory approval for clinical use, this will hopefully pave the way for other tUCA with other targets as well. However, for every new tUCA or drug-loaded tUCA regulatory approval will be needed before clinical use.

tUCAs can also be used as theranostic agent without the addition of a drug or gene, but in combination with high intensity focused ultrasound (HIFU) techniques instead. These techniques utilize high-energy focused ultrasound to locally increase the temperature at the focal point for ablation of tumors. UCAs, as synergists, have become a research topic to improve the efficiency of HIFU treatment [436], [437]. In this field, a folate-tUCA (phase transition nanoemulsion) has shown great potential to enhance HIFU ablation of ovarian cancer *in vivo* [438].

## ***Targeted Ultrasound Contrast Agents For Ultrasound Molecular Imaging and Therapy***

---

In conclusion, adding to the wide applications of UMI for diagnosis, the therapeutic benefits of this technology also play a major role in its popularity. Detection of diseased cells using tUCAs combined with local drug delivery, sonoporation, and HIFU are good examples of the applications and the potential of UMI for therapy.



## Summary and Outlook

In my thesis, microbubbles (MBs) for ultrasound (US) imaging, ultrasound molecular imaging, and drug delivery were studied. Microbubbles are gas-encapsulated lipid or polymer shell coated micro-particles, widely used as ultrasound contrast agents (UCA). MBs oscillate in response to the ultrasound and can interact with surrounding cells and tissues. This interaction can be enhanced by ligands, which have an affinity to biomarkers on the cell surface. These qualities of MBs make them very promising for molecular imaging of diseased tissues by means of local and specific treatment of certain areas i.e. drug delivery.

In the first chapter we introduce MBs as UCA and describe their response to ultrasound. We also describe how microbubbles could be modified to target them to a specific antigen in the body. The visualization of the bound targeted microbubbles by ultrasound is referred to as ultrasound molecular imaging. Microbubbles functionalised in such a way are known as targeted microbubbles (tMBs), while bare microbubbles are called non-targeted microbubbles (ntMB) or simply MBs. We also introduce the ability of oscillating MBs to increase cell membrane permeability, enabling drugs to penetrate into the cell. This process is also known as sonoporation. We give an overview of the *in vitro*, *ex vivo*, and *in vivo* models used to study the MBs' oscillations in response to US. The chicken embryo chorioallantoic membrane model (CAM) is introduced and its advantages as the *in vivo* model are described for both optical and acoustical studies of UCAs for imaging and drug delivery.

In Chapter 2 we present for the first time optical *in vivo* study of microbubble oscillation in chicken embryos under blood flow conditions. This study used the ultra-high-speed Brandaris 128 camera at 20 millions frames per second to record the MBs oscillation. In these experiments we studied the effect of blood flow, blood viscosity, red blood cells, and vessel wall vicinity to MBs oscillation, which are usually neglected in microbubble behaviour studies. We have demonstrated that all the bubbles showed shell hardening behaviour with increasing acoustic pressure and 44 % of the MBs exhibited subharmonic response when insonified at resonance.

In Chapter 3 we show the feasibility of using MBs for imaging the microvasculature. For atherosclerotic plaque vulnerability, the development of microvasculature in the plaque is one of the key risk factors. This microvascularisation cannot be measured during regular intravascular ultrasound examinations because small vessels cannot be resolved using conventional methods. Using the chicken embryo model we have proven that microvessels can be detected with MBs using ultraharmonic imaging with chirp excitation. This technique allows imaging the microvascularisation in plaques to assess their vulnerability.

Chapter 4 is a broad study of the effect of US excitation of targeted and non-targeted MBs on cell membrane permeability increase (sonoporation). In this study we investigated the dynamics of cell membrane permeability, by means of a diffusion model (Fan et al. [98]). This model allowed us to obtain the pore size and pore resealing coefficient for every single cell, which we correlated with sonoporation efficiency and cell death. We studied these effects for tMBs and ntMBs at different acoustical pressures (150, 300, 500 kPa) and different pulse

## Summary and Outlook

---

durations (500-50,000 cycles). Based on pore size and pore resealing coefficients we could differentiate two groups of cells with different sonoporation patterns. The cells in one group highly correlated with cell death, suggesting irreversible sonoporation. The cells in the second group slower PI uptake were suggested to correlate with reversible sonoporation. Both reversible and irreversible sonoporation are always present in the cell population. Different therapeutic strategies may require adjustment of the reversible/irreversible sonoporation ratio by varying the ultrasound parameters (acoustic pressure and pulse length) and choosing either tMBs or ntMBs. Changing this ratio can increase cell death or load cells with the drug without killing them.

In Chapter 5 we show the feasibility of *in vivo* sonoporation of endothelial cells with tMBs in a chicken embryo in the presence of blood flow. In this study we revealed the importance of high local tMB concentration to increase the probability of sonoporation. The probability of sonoporation varied from 5% for 1-3 tMBs up to 80% for 10-16 tMBs that had adhered to the endothelial cell membrane.

Chapter 6 shows how tMBs can be used in stem cell therapy. For stem cells injected into the blood pool it is crucial that they end up in a certain organ of interest. The probability of this outcome is rather low. Using the chicken embryo model and stem cells encased by tMBs we proved that stem cells could be propelled to the vessel wall with US for further extravasation. This technique therefore has a potential for controlled stem cell therapy.

*In vivo* cell tracking using MRI requires an effective MRI contrast agent cell labeling technique. The current variety of labeling techniques are too toxic to be applied *in vivo*. Chapter 7 is the *in vitro* proof of concept for safe tMB-mediated labeling of endothelial cells with SPIO (MRI contrast agent) for further MRI tracking, which could be potentially used *in vivo*. In this study we revealed the optimal acoustical pressure, sonication time, and SPIO incubation time for safe endothelial cell labeling.

Chapter eight is an overview of the current state and outlook of the future of tMBs for molecular imaging and therapy. It includes the overview of different targeting ligands, biomarkers, techniques aiming to increase tMB binding, and for discriminating acoustically between adherent and free floating tMBs.

### Future perspectives

As the power of the CAM-model for studies on ultrasound contrast enhanced imaging and MB-mediated drug delivery was clearly shown in this thesis, it should be used more often in future MB-studies. The reason why this is not the primary choice yet is likely due to the technical difficulty of injecting MBs into the veins. This protocol requires special skills, especially when a catheter has to be used (as described in Chapter 6). The next step for the *in vitro* sonoporation dynamics experiments in Chapter 4 and the SPIO *in vitro* experiments in Chapter 7 is undoubtedly the CAM-model. In addition, the tMB sonoporation study in the CAM model in Chapter 5 should be extended with the recording of the microbubble behavior using an ultra high-speed camera. Until now MB vibration was only studied in the CAM model for imaging purposes not yet for drug delivery. It is the combination of the microbubble behavior

## Summary and Outlook

---

and the cellular and tissue response to this microbubble behavior that allows us to understand and control the microbubble-drug-cell interaction. In Chapter 4 and 5 we only studied one mechanism of ultrasound-mediated drug delivery, namely cell membrane pore formation, also known as sonoporation. There are also two other mechanisms with great potential to facilitate drug delivery: stimulated endocytosis and opening of cell-cell contacts. The CAM model can without doubt contribute in studying these processes. The stimulation of endocytosis in CAM endothelial cells can be studied in real time by different size model drug molecules like fluorescent dextran as used in the *in vitro* study of Meijering et al. [35]. The effect of different MBs oscillation regimes on cell-cell contact opening could also be studied by fluorescent dextran extravasation [56]. Another advantage of the CAM model is histological evaluation at the end of the experiment (see also Chapter 5). Cell-cell contact opening could for example be assessed by electron microscopy when the *in vivo* study is performed with lanthanum [439], a contrast agent for electron microscopy.

MBs can be loaded with drugs. These can be attached to the shell surface, incorporated into the shell or loaded inside the bubble [14]. One of the problems of drug-loaded microbubbles is the drug payload, which is restricted by the gas core. Nanodroplets do not have this restriction because their core is a liquid perfluorocarbon or oil and therefore the entire core volume can be loaded with an oil-soluble drug. Nanodroplets have gained enormous popularity in the ultrasound contrast agent field. They are small (~100 nm in diameter), can be easily produced, and even made monodisperse [440]. Most of the current studies in this field are based on *in vitro* optical observations in media like phosphate-buffered saline [441]. These *in vitro* approach do not take into account red blood cells, the vessel lumen or surrounding tissue. The CAM model also has great potential for studying nanodroplets. Because of the optical transparency of CAM ultrasound and laser vaporization of nanodroplets into microbubbles can be studied. In addition the microbubble oscillation inside the vessel or in the extravascular tissue can be visualised. The advantage of the CAM model is the ability to perform the studies in real time, which will certainly aid in discovering the full potential of the nanodroplets. The key application will be drug delivery into tumors.

For IVUS imaging the CAM model was used as a proof of principal in Chapter 3. The next step is transferring this technique to atherosclerotic arteries in a large animal like the pig [442]. The challenging part of using IVUS for plaque neovascularization would be artifacts in the vessel wall caused by the presence of large amount of microbubbles in the artery lumen [443]. In combination with artery deformation caused by pulsation and movement [444], and the narrow ultrasound beam width it will be challenging to detect MBs passing through the tiny intraplaque capillaries. One of the possible solutions for this problem could be tMBs. Microbubbles labeled with a neovascularization marker such as  $\alpha_v\beta_3$ -integrin will accumulate in the plaque neovessels and can be imaged once all the free-floating non-adhered tMBs in the lumen are gone (~10 minutes). Adhered tMBs will also allow for a 3D scan. Labeling of MBs with  $\alpha_v\beta_3$ -integrin will also be also useful for imaging of neovessels in tumor, giving  $\alpha_v\beta_3$ -tMBs a dual purpose.

## ***Summary and Outlook***

---

Personalized medicine is the a new and promising approach to healthcare. The current progress in genomics and proteomics together with uprising Big Data approaches are going to change the patient treatment strategies in the coming decades. This progress opens new frontiers for ultrasound molecular imaging and tMB-mediated drug delivery as well. The ultrasound scanners are getting smarter, cheaper, and more portable. Self-assembling microbubbles in the form of a kit will let us construct tMBs with a patient-specific ligand [445] within a few minutes. The ligands of the future will be aptamers, RNA molecules with a very high affinity for a target. They can be produced with a tag for linkage to the shell of the MB within a few hours, while you need months to make antibodies. Based on a patient biopsy and with the use of an approved aptamer library, physicians would make tMBs specific for a particular patient. In cancer diagnostics, these tMBs will allow us to visualize the primary tumor and to track metastases with whole-body ultrasound scanners. In combination with MB-mediated drug delivery approaches, tMBs can significantly increase treatment efficiency and decrease the risk of relapse.



## Nederlandse samenvatting

Dit proefschrift beschrijft de resultaten van het onderzoek naar microbellen (MBs) als contrastmiddel voor beeldvorming met ultrageluid (echografie), moleculaire beeldvorming met ultrageluid en lokale medicijnafgifte. Microbellen zijn kleine gasbelletjes omgeven door een dunne schil bestaande uit lipiden (vetachtige stoffen) of een polymeer en worden veelvuldig gebruikt als contrastmiddel voor echografie. Microbellen vertonen oscillaties als gevolg van de excitatie door ultrageluid en kunnen interactie ondergaan met omliggende cellen en weefsel. Deze interactie kan versterkt worden door gebruik te maken van specifieke liganden die een grote affiniteit hebben voor specifieke 'biomarkers' op het celoppervlak. Bovengenoemde eigenschappen maken MBs veelbelovend voor moleculaire beeldvorming en lokale medicijnafgifte voor de specifieke behandeling van ziek weefsel.

In Hoofdstuk 1 geven we een introductie van MBs als contrastmiddel voor echografie en beschrijven we het gedrag van MBs in een ultrageluid veld. Verder beschrijven we hoe MBs gemodificeerd kunnen worden om ervoor te zorgen dat ze binden aan specifieke antigenen in het lichaam. Het visualiseren van gebonden MBs met behulp van ultrageluid wordt ook wel moleculaire echografie genoemd. Gefunctionaliseerde MBs worden ook wel aangeduid met de term getargete microbellen (tMBs); niet gefunctionaliseerde MBs worden ook wel ongetargete (ntMBs) of gewoonweg MBs genoemd. Ook beschrijven we in Hoofdstuk 1 de eigenschap van MBs om de permeabiliteit van celmembranen te verhogen, wat ervoor zorgt dat medicijn de cel in kan penetreren. Dit proces wordt ook wel sonoporië genoemd. We geven vervolgens een overzicht van de *in vitro*, *ex vivo* en *in vivo* modellen die worden gebruikt om de oscillaties van MBs in respons op ultrageluid excitatie te bestuderen. Het kippenembryo model (chorioallantoic membrane model, CAM) wordt beschreven en de voordelen als *in vivo* model voor zowel optische als akoestische studies van MBs voor beeldvorming en lokale medicijnafgifte worden uiteengezet.

In Hoofdstuk 2 beschrijven we de resultaten van de eerste *in vivo* studie van MB oscillaties in de aanwezigheid van bloedstroming. Naast het hierboven beschreven kippenembryo model, hebben we voor deze studie gebruik gemaakt van de Brandaris128 hogesnelheidscamera (opererend bij 20 miljoen frames per seconde) om het oscillatiegedrag van de MBs vast te leggen. In deze experimenten hebben we het effect bestudeerd van de bloedstroming, bloedviscositeit, rode bloed cellen en de nabijheid van een vaatwand. Het effect van laatstgenoemde wordt namelijk vaak verwaarloosd in studies met betrekking tot het oscillatiegedrag van MBs. We laten zien dat alle MBs bij toenemende akoestische druk zogenaamd 'shell hardening' gedrag vertonen en dat 44% van de MBs een subharmonische response geeft wanneer de MBs op hun resonantiefrequentie worden aangestruild.

In Hoofdstuk 3 laten we zien dat MBs gebruikt kunnen worden voor het afbeelden van microvasculatuur. De aanwezigheid van microvasculatuur binnen een atherosclerotische plaque is een belangrijke risicofactor voor plaque instabiliteit. Microvasculatuur kan echter niet worden gevisualiseerd met reguliere intravasculair ultrageluid (IVUS) technieken aangezien het oplossend vermogen niet toereikend is. Echter, door gebruik te maken van MBs,

in combinatie met de zogenaamde ultraharmonische IVUS methode met tijp excitatie, laten we zien dat het afbeelden van microvasculatuur wel mogelijk is. Deze techniek stelt ons daarom in staat de aanwezigheid van microvasculatuur in plaques te visualiseren om zo de mate van stabiliteit te bepalen.

Hoofdstuk 4 beschrijft de resultaten van onze studie naar de verhoging van de celmembraan permeabiliteit ten gevolge van ultrageluid excitatie van getargete en ongetargete MBs. De dynamica van het celmembraan permeabiliteit is benaderd met een diffusiemodel (Fan et al. [98]), waaruit voor iedere cel unieke waarden voor de porie grootte en de herstelcoëfficiënt van de porie konden worden afgeleid. Deze parameters werden vervolgens gecorreleerd met de sonoporatie efficiëntie en celdood. De effecten werden onderzocht voor zowel tMBs als ntMBs bij diverse akoestische drukken (150, 300, 500 kPa) en pulsduratie (500 – 50.000 cycli). Op basis van de porie grootte en herstelcoëfficiënt van de porie konden twee groepen cellen met verschillende sonoporatie patronen worden geïdentificeerd. Cellen uit de ene groep vertoonden een sterke correlatie met celdood, wat duidt op irreversibele sonoporatie. Cellen uit de andere groep correleerden met reversibele sonoporatie. Binnen elke populatie cellen zijn zowel reversibele als irreversibele sonoporatie patronen aanwezig. Diverse therapieën vereisen wellicht een verschillend reversibele/irreversibele sonoporatie ratio, ietwat gereguleerd kan worden met de ultrageluid parameters (druk en pulseduratie) en type MBs (d.w.z. tMBs of ntMBs). Verandering van de ratio is bepalend voor de uitkomst van de therapie: vooral celdood of voornamelijk opname van medicijn zonder celdood.

In Hoofdstuk 5 presenteren we de resultaten van een haalbaarheidsstudie naar de *in vivo* sonoporatie van endotheelcellen met behulp van tMBs in de aanwezigheid van bloedstroming. Deze studie, uitgevoerd in een kippenembryo, laat zien dat een lokaal hoge concentratie van tMBs de kans op sonoporatie vergroot. Deze kans op sonoporatie varieerde van 5% voor 1-3 tMBs tot 80% in het geval 10-16 tMBs waren gebonden aan het celmembraan van de endotheelcel.

In Hoofdstuk 6 beschrijven we de toepassing van tMBs voor stamceltherapie. Voor stamceltherapie is het cruciaal dat geïnjecteerde stamcellen terechtkomen in het te behandelen orgaan. Het percentage stamcellen dat uiteindelijk wordt afgegeven op de juiste plek is doorgaans echter vrij laag. Door de buitenkant van de stamcellen te voorzien van een laagje microbellen laten we zien dat ultrageluid kan worden gebruikt om stamcellen lokaal af te leveren. Deze techniek heeft daarom potentie voor gecontroleerde stamceltherapie.

Het volgen van cellen *in vivo* ('cell tracking') met behulp van MRI vereist een effectieve manier om cellen te labelen met MRI contrastmiddel. Beschikbare technieken zijn echter te toxisch voor *in vivo* toepassing. Hoofdstuk 7 beschrijft het principe achter een nieuwe labelingstechniek van endotheelcellen met SPIO (MRI contrastmiddel) door gebruikt te maken van tMBs. Deze techniek kan mogelijk ook in een later stadium ook *in vivo* toegepast worden. In deze studie zijn de meest optimale parameters (akoestische druk, tijdsduur van ultrageluid en SPIO incubatietijd) voor het labelen van endotheelcellen bepaald.

Hoofdstuk 8 geeft tot slot een overzicht van de huidige status en de toekomst van tMBs met betrekking tot zowel moleculaire beeldvorming als therapie. Onderwerpen als de diverse

## ***Nederlandse samenvatting***

---

(targeting) liganden, biomarkers, technieken voor verhoogde tMBs binding en de akoestische discriminatie tussen gebonden en ongebonden tMBs passeren de revue.



# Bibliography

- [1] W. D. Hall, J. W. Hurst, and H. K. Walker, *The Origins of the History and Physical Examination*, 3rd ed. Boston: Butterworths, 1990.
- [2] R. Gramiak and P. M. Shah, "Echocardiography of the aortic root.," *Invest Radiol*, vol. 3, no. 5, pp. 356–366, Sep. 1968.
- [3] B. B. Goldberg, J. B. Liu, and F. Forsberg, "Ultrasound contrast agents: a review.," *Ultrasound Med Biol*, vol. 20, no. 4, pp. 319–333, 1994.
- [4] D. Cosgrove, "Ultrasound contrast agents: an overview.," *Eur J Radiol*, vol. 60, no. 3, pp. 324–330, Dec. 2006.
- [5] M. Postema and O. H. Gilja, "Contrast-enhanced and targeted ultrasound.," *World J. Gastroenterol.*, vol. 17, no. 1, pp. 28–41, Jan. 2011.
- [6] S. Kaul, "Myocardial contrast echocardiography: a 25-year retrospective.," *Circulation*, vol. 118, no. 3, pp. 291–308, Jul. 2008.
- [7] A. L. Klibanov, "Ultrasound Contrast Agents: Development of the Field and Current Status," in *Contrast Agents II*, vol. 222, no. 3, Berlin, Heidelberg: Springer Berlin Heidelberg, 2002, pp. 73–106.
- [8] C. Greis, "Ultrasound contrast agents as markers of vascularity and microcirculation.," *Clin. Hemorheol. Microcirc.*, vol. 43, no. 1, pp. 1–9, 2009.
- [9] T. Faez, M. Emmer, K. Kooiman, M. Versluis, A. van der Steen, and N. de Jong, "20 years of ultrasound contrast agent modeling.," *IEEE Trans Ultrason Ferroelectr Freq Control*, vol. 60, no. 1, pp. 7–20, Jan. 2013.
- [10] R. M. Lang and V. Mor Avi, "Clinical utility of contrast-enhanced echocardiography," *Clinical Cardiology*, vol. 29, no. 1, pp. 15–25, Sep. 2006.
- [11] J. Shalhoub, D. R. J. Owen, T. Gauthier, C. Monaco, E. L. S. Leen, and A. H. Davies, "The use of Contrast Enhanced Ultrasound in Carotid Arterial Disease," *European Journal of Vascular & Endovascular Surgery*, vol. 39, no. 4, pp. 381–387, Apr. 2010.
- [12] Y. E. Chung and K. W. Kim, "Contrast-enhanced ultrasonography: advance and current status in abdominal imaging," *Ultrasonography*, vol. 34, no. 1, pp. 3–18, Sep. 2014.
- [13] C. Neciu, R. Badea, L. Chiorean, and A. F. Badea, "Oral and IV Contrast Enhanced Ultrasonography of the digestive tract—a useful completion of the B-mode examination: a literature review and an exhaustive ....," *Medical ...*, 2015.
- [14] K. Kooiman, H. J. Vos, M. Versluis, and N. de Jong, "Acoustic behavior of microbubbles and implications for drug delivery.," *Adv. Drug Deliv. Rev.*, vol. 72, pp. 28–48, Jun. 2014.
- [15] E. Stride, "Physical principles of microbubbles for ultrasound imaging and therapy.," *Cerebrovasc. Dis.*, vol. 27, no. 2, pp. 1–13, 2009.
- [16] I. Lentacker, I. De Cock, R. Deckers, S. C. De Smedt, and C. T. W. Moonen, "Understanding ultrasound induced sonoporation: definitions and underlying mechanisms.," *Adv. Drug Deliv. Rev.*, vol. 72, pp. 49–64, Jun. 2014.
- [17] J. Wu and W. L. Nyborg, "Ultrasound, cavitation bubbles and their interaction with cells.," *Adv. Drug Deliv. Rev.*, vol. 60, no. 10, pp. 1103–1116, Jun. 2008.
- [18] S. Hernot and A. L. Klibanov, "Microbubbles in ultrasound-triggered drug and gene delivery.," *Adv. Drug Deliv. Rev.*, vol. 60, no. 10, pp. 1153–1166, Jun. 2008.
- [19] A. L. Klibanov, "Microbubble contrast agents: targeted ultrasound imaging and ultrasound-assisted drug-delivery applications.," *Invest Radiol*, vol. 41, no. 3, pp. 354–362, Mar. 2006.
- [20] K. W. Ferrara, "Driving delivery vehicles with ultrasound.," *Adv. Drug Deliv. Rev.*, vol. 60, no. 10, pp. 1097–1102, Jun. 2008.
- [21] P. A. Dijkmans, L. J. M. Juffermans, R. Musters, A. van Wamel, F. J. ten Cate, W. van Gilst, C. A. Visser, N. de Jong, and O. Kamp, "Microbubbles and ultrasound: from diagnosis to therapy.," *Eur J Echocardiogr*, vol. 5, no. 4, pp. 245–256, Aug. 2004.
- [22] A. Zeghimi, J. M. Escoffre, and A. Bouakaz, "Role of endocytosis in sonoporation-mediated membrane permeabilization and uptake of small molecules: a electron microscopy study.," *Phys Biol*, vol. 12, no. 6, p. 066007, 2015.
- [23] Y. Hu, J. M. F. Wan, and A. C. H. Yu, "Membrane perforation and recovery dynamics in microbubble-mediated sonoporation.," *Ultrasound Med Biol*, vol. 39, no. 12, pp. 2393–2405, Dec. 2013.
- [24] M. Scatena and C. Giachelli, "The alpha(v)beta3 integrin, NF-kappaB, osteoprotegerin endothelial cell survival pathway. Potential role in angiogenesis.," *Trends Cardiovasc. Med.*, vol. 12, no. 2, pp. 83–88, Feb. 2002.

# Bibliography

- [25] A. D. Blann, S. K. Nadar, and G. Y. H. Lip, "The adhesion molecule P-selectin and cardiovascular disease.," *Eur. Heart J.*, vol. 24, no. 24, pp. 2166–2179, Dec. 2003.
- [26] C. Lawson and S. Wolf, "ICAM-1 signaling in endothelial cells.," *Pharmacol Rep*, vol. 61, no. 1, pp. 22–32, Jan. 2009.
- [27] F. Tranquart, M. Arditi, T. Bettinger, P. Frinking, J. M. Hyvelin, A. Nunn, S. Pochon, and I. Tardy, "Ultrasound contrast agents for ultrasound molecular imaging.," *Z Gastroenterol*, vol. 52, no. 11, pp. 1268–1276, Nov. 2014.
- [28] L. Abou-Elkacem, S. V. Bachawal, and J. K. Willmann, "Ultrasound molecular imaging: Moving toward clinical translation.," *Eur J Radiol*, vol. 84, no. 9, pp. 1685–1693, Sep. 2015.
- [29] R. Pillai, E. R. Marinelli, H. Fan, P. Nanjappan, B. Song, M. A. von Wronski, S. Cherkaoui, I. Tardy, S. Pochon, M. Schneider, A. D. Nunn, and R. E. Swenson, "A phospholipid-PEG2000 conjugate of a vascular endothelial growth factor receptor 2 (VEGFR2)-targeting heterodimer peptide for contrast-enhanced ultrasound imaging of angiogenesis.," *Bioconjug. Chem.*, vol. 21, no. 3, pp. 556–562, Mar. 2010.
- [30] S. Pochon, I. Tardy, P. Bussat, T. Bettinger, J. Brochot, M. von Wronski, L. Passantino, and M. Schneider, "BR55: a lipopeptide-based VEGFR2-targeted ultrasound contrast agent for molecular imaging of angiogenesis.," *Invest Radiol*, vol. 45, no. 2, pp. 89–95, Feb. 2010.
- [31] H. Wijkstra, M. Smeenge, and J. de la Rosette, "Targeted microbubble prostate cancer imaging with BR55. 17th European Symposium on Ultrasound Contrast Imaging 2012, Rotterdam, The Netherlands," presented at the 17th European Symposium on Ultrasound Contrast Imaging 2010, 2012.
- [32] "A Pilot Trial Using BR55 Ultrasound Contrast Agent in the Assessment of Prostate Cancer (NCT02142608).," *ClinicalTrials.gov*.
- [33] H. J. Vos, B. Dollet, M. Versluis, and N. de Jong, "Nonspherical shape oscillations of coated microbubbles in contact with a wall.," *Ultrasound Med Biol*, vol. 37, no. 6, pp. 935–948, Jun. 2011.
- [34] C. Mannaris and M. A. Averkiou, "Investigation of microbubble response to long pulses used in ultrasound-enhanced drug delivery.," *Ultrasound Med Biol*, vol. 38, no. 4, pp. 681–691, Apr. 2012.
- [35] B. D. M. Meijering, L. J. M. Juffermans, A. van Wamel, R. H. Henning, I. S. Zuhorn, M. Emmer, A. M. G. Versteilen, W. J. Paulus, W. H. van Gilst, K. Kooiman, N. de Jong, R. J. P. Musters, L. E. Deelman, and O. Kamp, "Ultrasound and microbubble-targeted delivery of macromolecules is regulated by induction of endocytosis and pore formation.," *Circ. Res.*, vol. 104, no. 5, pp. 679–687, Mar. 2009.
- [36] M. Overvelde, V. Garbin, J. Sijl, B. Dollet, N. de Jong, D. Lohse, and M. Versluis, "Nonlinear shell behavior of phospholipid-coated microbubbles.," *Ultrasound Med Biol*, vol. 36, no. 12, pp. 2080–2092, Dec. 2010.
- [37] Y. Luan, T. Faez, E. Gelderblom, I. Skachkov, B. Geers, I. Lentacker, T. van der Steen, M. Versluis, and N. de Jong, "Acoustical properties of individual liposome-loaded microbubbles.," *Ultrasound Med Biol*, vol. 38, no. 12, pp. 2174–2185, Dec. 2012.
- [38] F. Prat, J. Y. Chapelon, B. Chauffert, T. Ponchon, and D. Cathignol, "Cytotoxic effects of acoustic cavitation on HT-29 cells and a rat peritoneal carcinomatosis in vitro.," *Cancer Res.*, vol. 51, no. 11, pp. 3024–3029, Jun. 1991.
- [39] A. Yudina, M. Lepetit-Coiffé, and C. T. W. Moonen, "Evaluation of the Temporal Window for Drug Delivery Following Ultrasound-Mediated Membrane Permeability Enhancement," *Mol Imaging Biol*, vol. 13, no. 2, pp. 239–249, 2011.
- [40] J. M. Escoffre, J. Piron, A. Novell, and A. Bouakaz, "Doxorubicin delivery into tumor cells with ultrasound and microbubbles.," *Mol. Pharm.*, vol. 8, no. 3, pp. 799–806, Jun. 2011.
- [41] J. M. Correas, O. Hélénou, L. Pourcelot, and J. F. Moreau, "Ultrasound contrast agents. Examples of blood pool agents.," *Acta Radiol Suppl*, vol. 412, pp. 101–112, 1997.
- [42] T. van Rooij, V. Daeichin, I. Skachkov, N. de Jong, and K. Kooiman, "Targeted ultrasound contrast agents for ultrasound molecular imaging and therapy.," *Int J Hyperthermia*, vol. 31, no. 2, pp. 90–106, Mar. 2015.
- [43] J. P. Kilroy, A. L. Klibanov, B. R. Wamhoff, D. K. Bowles, and J. A. Hossack, "Localized in vivo model drug delivery with intravascular ultrasound and microbubbles.," *Ultrasound Med Biol*, vol. 40, no. 10, pp. 2458–2467, Oct. 2014.
- [44] J. T. Sutton, J. L. Raymond, M. C. Verleye, G. J. Pyne-Geithman, and C. K. Holland, "Pulsed ultrasound enhances the delivery of nitric oxide from bubble liposomes to ex vivo porcine carotid tissue.," *Int J Nanomedicine*, vol. 9, no. 1, pp. 4671–4683, 2014.
- [45] M.-L. Izamis, A. Efstathiades, C. Keravnou, E. L. Leen, and M. A. Averkiou, "Dynamic Contrast-Enhanced Ultrasound of Slaughterhouse Porcine Livers in Machine Perfusion," *Ultrasound Med Biol*,

# Bibliography

- vol. 40, no. 9, pp. 2217–2230, Sep. 2014.
- [46] J. Owen, P. Rademeyer, D. Chung, Q. Cheng, D. Holroyd, C. Coussios, P. Friend, Q. A. Pankhurst, and E. Stride, “Magnetic targeting of microbubbles against physiologically relevant flow conditions,” *Interface Focus*, vol. 5, no. 5, pp. 20150001–12, Aug. 2015.
- [47] H. Chen, W. Kreider, A. A. Brayman, M. R. Bailey, and T. J. Matula, “Blood vessel deformations on microsecond time scales by ultrasonic cavitation,” *Phys. Rev. Lett.*, vol. 106, no. 3, p. 034301, Jan. 2011.
- [48] M. D. Menger, M. W. Laschke, and B. Vollmar, “Viewing the microcirculation through the window: some twenty years experience with the hamster dorsal skinfold chamber,” *Eur Surg Res*, vol. 34, no. 1, pp. 83–91, Jan. 2002.
- [49] M. Schneider, A. Broillet, I. Tardy, S. Pochon, P. Bussat, T. Bettinger, A. Helbert, M. Costa, and F. Tranquart, “Use of intravital microscopy to study the microvascular behavior of microbubble-based ultrasound contrast agents,” *Microcirculation*, vol. 19, no. 3, pp. 245–259, Apr. 2012.
- [50] A. Xie, T. Belcik, Y. Qi, T. K. Morgan, S. A. Champaneri, S. Taylor, B. P. Davidson, Y. Zhao, A. L. Klibanov, M. A. Kuliszewski, H. Leong-Poi, A. Ammi, and J. R. Lindner, “Ultrasound-mediated vascular gene transfection by cavitation of endothelial-targeted cationic microbubbles,” *JACC Cardiovasc Imaging*, vol. 5, no. 12, pp. 1253–1262, Dec. 2012.
- [51] F. S. Villanueva, E. Lu, S. Bowry, S. Kilic, E. Tom, J. Wang, J. Gretton, J. J. Pacella, and W. R. Wagner, “Myocardial ischemic memory imaging with molecular echocardiography,” *Circulation*, vol. 115, no. 3, pp. 345–352, Jan. 2007.
- [52] B. P. Davidson, S. M. Chadderdon, J. T. Belcik, S. Gupta, and J. R. Lindner, “Ischemic memory imaging in nonhuman primates with echocardiographic molecular imaging of selectin expression,” *J Am Soc Echocardiogr*, vol. 27, no. 7, pp. 786–793.e2, Jul. 2014.
- [53] B. A. Kaufmann, C. Lewis, A. Xie, A. Mirza-Mohd, and J. R. Lindner, “Detection of recent myocardial ischaemia by molecular imaging of P-selectin with targeted contrast echocardiography,” *Eur. Heart J.*, vol. 28, no. 16, pp. 2011–2017, Aug. 2007.
- [54] A. Vargas, M. Zeisser-Labou  be, N. Lange, R. Gurny, and F. Delie, “The chick embryo and its chorioallantoic membrane (CAM) for the in vivo evaluation of drug delivery systems,” *Adv. Drug Deliv. Rev.*, vol. 59, no. 11, pp. 1162–1176, Sep. 2007.
- [55] S. Ohta, K. Suzuki, K. Tachibana, and G. Yamada, “Microbubble-enhanced sonoporation: efficient gene transduction technique for chick embryos,” *Genesis*, vol. 37, no. 2, pp. 91–101, Oct. 2003.
- [56] S. M. Stieger, C. F. Caskey, R. H. Adamson, S. Qin, F.-R. E. Curry, E. R. Wisner, and K. W. Ferrara, “Enhancement of vascular permeability with low-frequency contrast-enhanced ultrasound in the chorioallantoic membrane model,” *Radiology*, vol. 243, no. 1, pp. 112–121, Apr. 2007.
- [57] S. M. Jilani, T. J. Murphy, S. N. M. Thai, A. Eichmann, J. A. Alva, and M. L. Iruela-Arispe, “Selective binding of lectins to embryonic chicken vasculature,” *J. Histochem. Cytochem.*, vol. 51, no. 5, pp. 597–604, May 2003.
- [58] C. Poelma, P. Vennemann, R. Lindken, and J. Westerweel, “In vivo blood flow and wall shear stress measurements in the vitelline network,” *Exp Fluids*, vol. 45, no. 4, pp. 703–713, 2008.
- [59] A. M. Malek, S. L. Alper, and S. Izumo, “Hemodynamic shear stress and its role in atherosclerosis,” *JAMA*, vol. 282, no. 21, pp. 2035–2042, Dec. 1999.
- [60] A. Liu, A. Nickerson, A. Troyer, X. Yin, R. Cary, K. Thornburg, R. Wang, and S. Rugonyi, “Quantifying blood flow and wall shear stresses in the outflow tract of chick embryonic hearts,” *Comput Struct*, vol. 89, no. 11, pp. 855–867, Jun. 2011.
- [61] S. Al-Roubaie, E. D. Jahnsen, M. Mohammed, C. Henderson-Toth, and E. A. V. Jones, “Rheology of embryonic avian blood,” *Am. J. Physiol. Heart Circ. Physiol.*, vol. 301, no. 6, pp. H2473–81, Dec. 2011.
- [62] L. Mullin, R. Gessner, J. Kwan, M. Kaya, M. A. Borden, and P. A. Dayton, “Effect of anesthesia carrier gas on in vivo circulation times of ultrasound microbubble contrast agents in rats,” *Contrast Media Mol Imaging*, vol. 6, no. 3, pp. 126–131, May 2011.
- [63] M. Itani and R. F. Mattrey, “The effect of inhaled gases on ultrasound contrast agent longevity in vivo,” *Mol Imaging Biol*, vol. 14, no. 1, pp. 40–46, Feb. 2012.
- [64] J. H. Wible, J. K. Wojdyla, G. L. Bales, W. N. McMullen, E. A. Geiser, and D. D. Buss, “Inhaled gases affect the ultrasound contrast produced by Alunex in anesthetized dogs,” *J Am Soc Echocardiogr*, vol. 9, no. 4, pp. 442–451, Jul. 1996.
- [65] S. G. Tyack, K. A. Jenkins, T. E. O’Neil, T. G. Wise, K. R. Morris, M. P. Bruce, S. McLeod, A. J. Wade, J. McKay, R. J. Moore, K. A. Schat, J. W. Lowenthal, and T. J. Doran, “A new method for producing transgenic birds via direct in vivo transfection of primordial germ cells,” *Transgenic Res.*, vol. 22, no. 6, pp. 1257–1264, Dec. 2013.

## Bibliography

- [66] C. T. Chin, C. Lancée, J. Borsboom, F. Mastik, M. E. Frijlink, N. de Jong, M. Versluis, and D. Lohse, "Brandaris 128: A digital 25 million frames per second camera with 128 highly sensitive frames," *Review of Scientific Instruments*, vol. 74, no. 12, pp. 5026–5034, Dec. 2003.
- [67] N. Kher and J. D. Marsh, "Pathobiology of atherosclerosis--a brief review.," *Semin. Thromb. Hemost.*, vol. 30, no. 6, pp. 665–672, Dec. 2004.
- [68] J.-B. Michel, R. Virmani, E. Arbustini, and G. Pasterkamp, "Intraplaque haemorrhages as the trigger of plaque vulnerability.," *Eur. Heart J.*, vol. 32, no. 16, pp. 1977–85– 1985a– 1985b– 1985c, Aug. 2011.
- [69] D. E. Goertz, M. E. Frijlink, D. Tempel, V. Bhagwandas, A. Gisolf, R. Krams, N. de Jong, and A. F. W. van der Steen, "Subharmonic contrast intravascular ultrasound for vasa vasorum imaging.," *Ultrasound Med Biol*, vol. 33, no. 12, pp. 1859–1872, Dec. 2007.
- [70] A.-M. O'Farrell, T. J. Abrams, H. A. Yuen, T. J. Ngai, S. G. Louie, K. W. H. Yee, L. M. Wong, W. Hong, L. B. Lee, A. Town, B. D. Smolich, W. C. Manning, L. J. Murray, M. C. Heinrich, and J. M. Cherrington, "SU11248 is a novel FLT3 tyrosine kinase inhibitor with potent activity in vitro and in vivo.," *Blood*, vol. 101, no. 9, pp. 3597–3605, May 2003.
- [71] J. K. Armstrong, R. B. Wenby, H. J. Meiselman, and T. C. Fisher, "The hydrodynamic radii of macromolecules and their effect on red blood cell aggregation.," *Biophys. J.*, vol. 87, no. 6, pp. 4259–4270, Dec. 2004.
- [72] E. A. Forssen and Z. A. Tökés, "Use of anionic liposomes for the reduction of chronic doxorubicin-induced cardiotoxicity.," *Proc. Natl. Acad. Sci. U.S.A.*, vol. 78, no. 3, pp. 1873–1877, Mar. 1981.
- [73] P. H. Chang, K. K. Shun, and S. J. Wu, "Second harmonic imaging and harmonic Doppler measurements with Albunex.," ..., 1995.
- [74] P. N. Burns, "Harmonic imaging with ultrasound contrast agents.," *Clin Radiol*, vol. 51, pp. 50–55, Feb. 1996.
- [75] W. T. Shi, F. Forsberg, A. L. Hall, R. Y. Chiao, J. B. Liu, S. Miller, K. E. Thomenius, M. A. Wheatley, and B. B. Goldberg, "Subharmonic imaging with microbubble contrast agents: initial results.," *Ultrason Imaging*, vol. 21, no. 2, pp. 79–94, Apr. 1999.
- [76] P. A. Dayton and K. W. Ferrara, "Targeted imaging using ultrasound.," *J Magn Reson Imaging*, vol. 16, no. 4, pp. 362–377, Oct. 2002.
- [77] G. Bhagavatheeshwaran, W. T. Shi, F. Forsberg, and P. M. Shankar, "Subharmonic signal generation from contrast agents in simulated neovessels.," *Ultrasound Med Biol*, vol. 30, no. 2, pp. 199–203, Feb. 2004.
- [78] D. E. Goertz, E. Chérin, A. Needles, R. Karshafian, A. S. Brown, P. N. Burns, and F. S. Foster, "High frequency nonlinear B-scan imaging of microbubble contrast agents.," *IEEE Trans Ultrason Ferroelectr Freq Control*, vol. 52, no. 1, pp. 65–79, Jan. 2005.
- [79] D. E. Goertz, M. E. Frijlink, D. Tempel, L. C. A. van Damme, R. Krams, J. A. Schaar, F. J. ten Cate, P. W. Serruys, N. de Jong, and A. F. W. van der Steen, "Contrast harmonic intravascular ultrasound: a feasibility study for vasa vasorum imaging.," *Invest Radiol*, vol. 41, no. 8, pp. 631–638, Aug. 2006.
- [80] F. Forsberg, C. W. Piccoli, D. A. Merton, J. J. Palazzo, and A. L. Hall, "Breast lesions: imaging with contrast-enhanced subharmonic US--initial experience.," *Radiology*, vol. 244, no. 3, pp. 718–726, Sep. 2007.
- [81] E. Chérin, J. Brown, S.-E. Måsøy, H. Shariff, R. Karshafian, R. Williams, P. N. Burns, and F. S. Foster, "Radial modulation imaging of microbubble contrast agents at high frequency.," *Ultrasound Med Biol*, vol. 34, no. 6, pp. 949–962, Jun. 2008.
- [82] S. E. Masoy, O. Standal, P. Nasholm, T. F. Johansen, B. Angelsen, and R. Hansen, "SURF imaging: in vivo demonstration of an ultrasound contrast agent detection technique.," *IEEE Trans Ultrason Ferroelectr Freq Control*, vol. 55, no. 5, pp. 1112–1121, May 2008.
- [83] A. Needles, M. Ardit, N. G. Rognin, J. Mehi, T. Coulthard, C. Bilan-Tracey, E. Gaud, P. Frinking, D. Hirson, and F. S. Foster, "Nonlinear contrast imaging with an array-based micro-ultrasound system.," *Ultrasound Med Biol*, vol. 36, no. 12, pp. 2097–2106, Dec. 2010.
- [84] J. R. Eisenbrey, J. K. Dave, V. G. Halldorsdottir, D. A. Merton, P. Machado, J. B. Liu, C. Miller, J. M. Gonzalez, S. Park, S. Dianis, C. L. Chalek, K. E. Thomenius, D. B. Brown, V. Navarro, and F. Forsberg, "Simultaneous grayscale and subharmonic ultrasound imaging on a modified commercial scanner.," *Ultrasonics*, vol. 51, no. 8, pp. 890–897, Dec. 2011.
- [85] C.-C. Shen, C.-H. Cheng, and C.-K. Yeh, "Phase-dependent dual-frequency contrast imaging at sub-harmonic frequency.," *IEEE Trans Ultrason Ferroelectr Freq Control*, vol. 58, no. 2, pp. 379–388, Feb. 2011.
- [86] N. de Jong, "Acoustic properties of ultrasound contrast agents," Erasmus University Rotterdam, 1993.
- [87] N. de Jong, L. Hoff, T. Skotland, and N. Bom, "Absorption and scatter of encapsulated gas filled



# Bibliography

- microspheres: theoretical considerations and some measurements.," *Ultrasonics*, vol. 30, no. 2, pp. 95–103, Mar. 1992.
- [88] J. M. Gorce, M. Arditi, and M. Schneider, "Influence of bubble size distribution on the echogenicity of ultrasound contrast agents: a study of SonoVue.," *Invest Radiol*, vol. 35, no. 11, pp. 661–671, Nov. 2000.
- [89] K. Sarkar, W. T. Shi, D. Chatterjee, and F. Forsberg, "Characterization of ultrasound contrast microbubbles using in vitro experiments and viscous and viscoelastic interface models for encapsulation.," *The Journal of the Acoustical Society of America*, vol. 118, no. 1, pp. 539–550, Jul. 2005.
- [90] D. E. Goertz, N. de Jong, and A. F. W. van der Steen, "Attenuation and size distribution measurements of Definity and manipulated Definity populations.," *Ultrasound Med Biol*, vol. 33, no. 9, pp. 1376–1388, Sep. 2007.
- [91] M. Emmer, H. J. Vos, D. E. Goertz, A. van Wamel, M. Versluis, and N. de Jong, "Pressure-dependent attenuation and scattering of phospholipid-coated microbubbles at low acoustic pressures.," *Ultrasound Med Biol*, vol. 35, no. 1, pp. 102–111, Jan. 2009.
- [92] F. Conversano, R. Franchini, and S. Casciaro, "Characterization of microbubble contrast agents for echographic imaging through time-scheduled size distribution measurements," *Sensors & ...*, 2010.
- [93] T. Faez, D. Goertz, and N. de Jong, "Characterization of Definity™ ultrasound contrast agent at frequency range of 5–15 MHz.," *Ultrasound Med Biol*, vol. 37, no. 2, pp. 338–342, Feb. 2011.
- [94] L. Hoff, "Acoustic characterization of contrast agents for medical ultrasound imaging. Ph.D. Thesis," Norwegian University of Science and Technology, Trondheim, Norway, 2000.
- [95] J. Sijl, E. Gaud, P. J. A. Frinking, M. Arditi, N. de Jong, D. Lohse, and M. Versluis, "Acoustic characterization of single ultrasound contrast agent microbubbles.," *The Journal of the Acoustical Society of America*, vol. 124, no. 6, pp. 4091–4097, Dec. 2008.
- [96] J. Sijl, H. J. Vos, T. Rozendal, N. de Jong, D. Lohse, and M. Versluis, "Combined optical and acoustical detection of single microbubble dynamics.," *The Journal of the Acoustical Society of America*, vol. 130, no. 5, pp. 3271–3281, Nov. 2011.
- [97] K. E. Morgan, J. S. Allen, P. A. Dayton, J. E. Chomas, A. L. Klibanov, and K. W. Ferrara, "Experimental and theoretical evaluation of microbubble behavior: effect of transmitted phase and bubble size.," *IEEE Trans Ultrason Ferroelectr Freq Control*, vol. 47, no. 6, pp. 1494–1509, 2000.
- [98] P. Marmottant, S. van der Meer, M. Emmer, M. Versluis, N. de Jong, S. Hilgenfeldt, and D. Lohse, "A model for large amplitude oscillations of coated bubbles accounting for buckling and rupture," *The Journal of the Acoustical Society of America*, vol. 118, no. 6, pp. 3499–3505, Dec. 2005.
- [99] N. de Jong, M. Emmer, C. T. Chin, A. Bouakaz, F. Mastik, D. Lohse, and M. Versluis, "'Compression-only' behavior of phospholipid-coated contrast bubbles.," *Ultrasound Med Biol*, vol. 33, no. 4, pp. 653–656, Apr. 2007.
- [100] M. Emmer, A. van Wamel, D. E. Goertz, and N. de Jong, "The onset of microbubble vibration.," *Ultrasound Med Biol*, vol. 33, no. 6, pp. 941–949, Jun. 2007.
- [101] S. M. van der Meer, B. Dollet, M. M. Voormolen, C. T. Chin, A. Bouakaz, N. de Jong, M. Versluis, and D. Lohse, "Microbubble spectroscopy of ultrasound contrast agents.," *The Journal of the Acoustical Society of America*, vol. 121, no. 1, pp. 648–656, Jan. 2007.
- [102] J. Sijl, B. Dollet, M. Overvelde, V. Garbin, T. Rozendal, N. de Jong, D. Lohse, and M. Versluis, "Subharmonic behavior of phospholipid-coated ultrasound contrast agent microbubbles.," *The Journal of the Acoustical Society of America*, vol. 128, no. 5, pp. 3239–3252, Nov. 2010.
- [103] T. Faez, M. Emmer, M. Docter, J. Sijl, M. Versluis, and N. de Jong, "Characterizing the subharmonic response of phospholipid-coated microbubbles for carotid imaging.," *Ultrasound Med Biol*, vol. 37, no. 6, pp. 958–970, Jun. 2011.
- [104] M. Emmer, H. J. Vos, M. Versluis, and N. de Jong, "Radial modulation of single microbubbles.," *IEEE Trans Ultrason Ferroelectr Freq Control*, vol. 56, no. 11, pp. 2370–2379, Nov. 2009.
- [105] D. Ribatti, A. Vacca, L. Roncali, and F. Dammacco, "The chick embryo chorioallantoic membrane as a model for in vivo research on anti-angiogenesis.," *Curr Pharm Biotechnol*, vol. 1, no. 1, pp. 73–82, Jul. 2000.
- [106] M. Richardson and G. Singh, "Observations on the use of the avian chorioallantoic membrane (CAM) model in investigations into angiogenesis.," *Curr Drug Targets Cardiovasc Haematol Disord*, vol. 3, no. 2, pp. 155–185, Jun. 2003.
- [107] D. Ribatti, A. Vacca, G. Ranieri, S. Sorino, and L. Roncali, "The chick embryo chorioallantoic membrane as an in vivo wound healing model.," *Pathol. Res. Pract.*, vol. 192, no. 10, pp. 1068–1076, Oct. 1996.
- [108] J. Borges, F. T. Tegtmeier, N. T. Padron, M. C. Mueller, E. M. Lang, and G. B. Stark, "Chorioallantoic

- p>membrane angiogenesis model for tissue engineering: a new twist on a classic model.,”
- Tissue Eng.*
- , vol. 9, no. 3, pp. 441–450, Jun. 2003.
- [109] G. Zwadlo-Klarwasser, K. Görlitz, B. Hafemann, D. Klee, and B. Klosterhalfen, “The chorioallantoic membrane of the chick embryo as a simple model for the study of the angiogenic and inflammatory response to biomaterials.,” *J Mater Sci Mater Med*, vol. 12, no. 3, pp. 195–199, Mar. 2001.
- [110] T. I. Valdes, D. Kreutzer, and F. Moussy, “The chick chorioallantoic membrane as a novel in vivo model for the testing of biomaterials.,” *J. Biomed. Mater. Res.*, vol. 62, no. 2, pp. 273–282, Nov. 2002.
- [111] U. Klueh, D. I. Dorsky, F. Moussy, and D. L. Kreutzer, “Ex ova chick chorioallantoic membrane as a novel model for evaluation of tissue responses to biomaterials and implants.,” *J Biomed Mater Res A*, vol. 67, no. 3, pp. 838–843, Dec. 2003.
- [112] T. I. Valdes, U. Klueh, D. Kreutzer, and F. Moussy, “Ex ova chick chorioallantoic membrane as a novel in vivo model for testing biosensors.,” *J Biomed Mater Res A*, vol. 67, no. 1, pp. 215–223, Oct. 2003.
- [113] M. S. Tartis, J. McCallan, A. F. H. Lum, R. LaBell, S. M. Stieger, T. O. Matsunaga, and K. W. Ferrara, “Therapeutic effects of paclitaxel-containing ultrasound contrast agents.,” *Ultrasound Med Biol*, vol. 32, no. 11, pp. 1771–1780, Nov. 2006.
- [114] N. Lange, J. P. Ballini, and G. Wagnieres, “A new drug-screening procedure for photosensitizing agents used in photodynamic therapy for CNV,” ... and *Visual Science*, 2001.
- [115] P. B. Antin, J. F. Fallon, and G. C. Schoenwolf, “The chick embryo rules (still).,” *Dev. Dyn.*, vol. 229, no. 3, pp. 413–413, Mar. 2004.
- [116] M. Hagedorn, S. Javerzat, D. Gilges, A. Meyre, B. de Lafarge, A. Eichmann, and A. Bikfalvi, “Accessing key steps of human tumor progression in vivo by using an avian embryo model.,” *Proc. Natl. Acad. Sci. U.S.A.*, vol. 102, no. 5, pp. 1643–1648, Feb. 2005.
- [117] M. A. Schellpfeffer and G. L. Kolesari, “Microbubble contrast imaging of the cardiovascular system of the chick embryo.,” *Ultrasound Med Biol*, vol. 38, no. 3, pp. 504–510, Mar. 2012.
- [118] D. M. Skyba, R. J. Price, A. Z. Linka, T. C. Skalak, and S. Kaul, “Direct in vivo visualization of intravascular destruction of microbubbles by ultrasound and its local effects on tissue.,” *Circulation*, vol. 98, no. 4, pp. 290–293, Jul. 1998.
- [119] M. W. Miller, E. C. Everbach, C. Cox, R. R. Knapp, A. A. Brayman, and T. A. Sherman, “A comparison of the hemolytic potential of Optison and Albunex in whole human blood in vitro: acoustic pressure, ultrasound frequency, donor and passive cavitation detection considerations.,” *Ultrasound Med Biol*, vol. 27, no. 5, pp. 709–721, May 2001.
- [120] P. Li, W. F. Armstrong, and D. L. Miller, “Impact of myocardial contrast echocardiography on vascular permeability: comparison of three different contrast agents.,” *Ultrasound Med Biol*, vol. 30, no. 1, pp. 83–91, Jan. 2004.
- [121] S. Samuel, M. A. Cooper, J. L. Bull, J. B. Fowlkes, and D. L. Miller, “An ex vivo study of the correlation between acoustic emission and microvascular damage.,” *Ultrasound Med Biol*, vol. 35, no. 9, pp. 1574–1586, Sep. 2009.
- [122] C. F. Caskey, S. M. Stieger, S. Qin, P. A. Dayton, and K. W. Ferrara, “Direct observations of ultrasound microbubble contrast agent interaction with the microvessel wall.,” *The Journal of the Acoustical Society of America*, vol. 122, no. 2, pp. 1191–1200, Aug. 2007.
- [123] H. Chen, A. A. Brayman, W. Kreider, M. R. Bailey, and T. J. Matula, “Observations of translation and jetting of ultrasound-activated microbubbles in mesenteric microvessels.,” *Ultrasound Med Biol*, vol. 37, no. 12, pp. 2139–2148, Dec. 2011.
- [124] A. L. Klibanov, P. T. Rasche, M. S. Hughes, J. K. Wojdyla, K. P. Galen, J. H. Wible, and G. H. Brandenburger, “Detection of individual microbubbles of ultrasound contrast agents: imaging of free-floating and targeted bubbles.,” *Invest Radiol*, vol. 39, no. 3, pp. 187–195, Mar. 2004.
- [125] M. Overvelde, V. Garbin, B. Dollet, N. de Jong, D. Lohse, and M. Versluis, “Dynamics of coated microbubbles adherent to a wall.,” *Ultrasound Med Biol*, vol. 37, no. 9, pp. 1500–1508, Sep. 2011.
- [126] V. Hamburger and H. L. Hamilton, *A series of normal stages in the development of the chick embryo. 1951.*, vol. 195, no. 4. Wiley Subscription Services, Inc., A Wiley Company, 1992, pp. 231–272.
- [127] B. A. Williams and C. P. Ordahl, “Manipulation of the avian segmental plate in vivo.,” *Methods Cell Biol.*, vol. 51, pp. 81–92, 1996.
- [128] J. Chomas, P. Dayton, D. May, and K. Ferrara, “Nondestructive subharmonic imaging.,” *IEEE Trans Ultrason Ferroelectr Freq Control*, vol. 49, no. 7, pp. 883–892, Jul. 2002.
- [129] A. Katiyar and K. Sarkar, “Excitation threshold for subharmonic generation from contrast microbubbles.,” *The Journal of the Acoustical Society of America*, vol. 130, no. 5, pp. 3137–3147, Nov. 2011.
- [130] T. Faez, G. Renaud, M. Defontaine, S. Calle, and N. de Jong, “Dynamic manipulation of the

- p subharmonic scattering of phospholipid-coated microbubbles.,”
- Phys Med Biol*
- , vol. 56, no. 19, pp. 6459–6473, Oct. 2011.
- [131] B. Dollet, S. M. van der Meer, V. Garbin, N. de Jong, D. Lohse, and M. Versluis, “Nonspherical oscillations of ultrasound contrast agent microbubbles,” *Ultrasound Med Biol*, vol. 34, no. 9, pp. 1465–1473, Sep. 2008.
- [132] A. van Wamel and K. Kooiman, “Ultrasound contrast agents pushing drug delivery: high speed optical observations,” *Journal of the Acoustical ...*, 2008.
- [133] A. C. Barger, R. Beeuwkes, L. L. Lainey, and K. J. Silverman, “Hypothesis: vasa vasorum and neovascularization of human coronary arteries. A possible role in the pathophysiology of atherosclerosis,” *N. Engl. J. Med.*, vol. 310, no. 3, pp. 175–177, Jan. 1984.
- [134] M. Gössl, D. Versari, H. A. Hildebrandt, T. Bajanowski, G. Sangiorgi, R. Erbel, E. L. Ritman, L. O. Lerman, and A. Lerman, “Segmental heterogeneity of vasa vasorum neovascularization in human coronary atherosclerosis,” *JACC Cardiovasc Imaging*, vol. 3, no. 1, pp. 32–40, Jan. 2010.
- [135] M. J. Mulligan-Kehoe, “The vasa vasorum in diseased and nondiseased arteries,” *Am. J. Physiol. Heart Circ. Physiol.*, vol. 298, no. 2, pp. H295–305, Feb. 2010.
- [136] W. E. Hellings, W. Peeters, F. L. Moll, S. R. D. Piers, J. van Setten, P. J. Van der Spek, J.-P. P. M. de Vries, K. A. Seldenrijk, P. C. De Bruin, A. Vink, E. Velema, D. P. V. de Kleijn, and G. Pasterkamp, “Composition of carotid atherosclerotic plaque is associated with cardiovascular outcome: a prognostic study,” *Circulation*, vol. 121, no. 17, pp. 1941–1950, May 2010.
- [137] R. Virmani, F. D. Kolodgie, A. P. Burke, A. V. Finn, H. K. Gold, T. N. Tulenko, S. P. Wrenn, and J. Narula, “Atherosclerotic plaque progression and vulnerability to rupture: angiogenesis as a source of intraplaque hemorrhage,” *Arterioscler. Thromb. Vasc. Biol.*, vol. 25, no. 10, pp. 2054–2061, Oct. 2005.
- [138] D. Maresca, G. Renaud, G. van Soest, X. Li, Q. Zhou, K. K. Shung, N. de Jong, and A. F. W. van der Steen, “Contrast-enhanced intravascular ultrasound pulse sequences for bandwidth-limited transducers,” *Ultrasound Med Biol*, vol. 39, no. 4, pp. 706–713, Apr. 2013.
- [139] E. Macé, G. Montaldo, I. Cohen, M. Baulac, M. Fink, and M. Tanter, “Functional ultrasound imaging of the brain,” *Nat. Methods*, vol. 8, no. 8, pp. 662–664, Aug. 2011.
- [140] P. J. Frinking, A. Bouakaz, J. Kirkhorn, F. J. ten Cate, and N. de Jong, “Ultrasound contrast imaging: current and new potential methods,” *Ultrasound Med Biol*, vol. 26, no. 6, pp. 965–975, Jul. 2000.
- [141] P. N. Burns, “Instrumentation for contrast echocardiography,” *Echocardiography*, vol. 19, no. 3, pp. 241–258, Apr. 2002.
- [142] B. Kuersten, T. H. Murthy, P. Li, Z. Liu, E. Locricchio, C. Baisch, P. Rafter, and M. Vannan, “Ultraharmonic myocardial contrast imaging: in vivo experimental and clinical data from a novel technique,” *J Am Soc Echocardiogr*, vol. 14, no. 9, pp. 910–916, Sep. 2001.
- [143] T. Shiogai, N. Takayasu, T. Mizuno, M. Nakagawa, and H. Furuhashi, “Comparison of transcranial brain tissue perfusion images between ultraharmonic, second harmonic, and power harmonic imaging,” *Stroke*, vol. 35, no. 3, pp. 687–693, Mar. 2004.
- [144] G. L. ten Kate, G. G. J. Renaud, Z. Akkus, S. C. H. van den Oord, F. J. ten Cate, V. Shamdasani, R. R. Entekhin, E. J. G. Sijbrands, N. de Jong, J. G. Bosch, A. F. L. Schinkel, and A. F. W. van der Steen, “Far-wall pseudoenhancement during contrast-enhanced ultrasound of the carotid arteries: clinical description and in vitro reproduction,” *Ultrasound Med Biol*, vol. 38, no. 4, pp. 593–600, Apr. 2012.
- [145] D. H. Simpson, C. T. Chin, and P. N. Burns, “Pulse inversion Doppler: a new method for detecting nonlinear echoes from microbubble contrast agents,” *Ultrasonics, Ferroelectrics, and Frequency Control, IEEE Transactions on*, vol. 46, no. 2, pp. 372–382, 1999.
- [146] Q. Zhou, X. Xu, E. J. Gottlieb, L. Sun, J. M. Cannata, H. Ameri, M. S. Humayun, P. Han, and K. K. Shung, “PMN-PT single crystal, high-frequency ultrasonic needle transducers for pulsed-wave Doppler application,” *Ultrasonics, Ferroelectrics, and Frequency Control, IEEE Transactions on*, vol. 54, no. 3, pp. 668–675, Mar. 2007.
- [147] C. Sun, S. D. Pye, J. E. Browne, A. Janeczko, B. Ellis, M. B. Butler, V. Sboros, A. J. W. Thomson, M. P. Brewin, C. H. Earnshaw, and C. M. Moran, “The speed of sound and attenuation of an IEC agar-based tissue-mimicking material for high frequency ultrasound applications,” *Ultrasound Med Biol*, vol. 38, no. 7, pp. 1262–1270, Jul. 2012.
- [148] J. C. Sluimer and M. J. Daemen, “Novel concepts in atherogenesis: angiogenesis and hypoxia in atherosclerosis,” *J. Pathol.*, vol. 218, no. 1, pp. 7–29, May 2009.
- [149] D. Staub, M. B. Patel, A. Tibrewala, D. Ludden, M. Johnson, P. Espinosa, B. Coll, K. A. Jaeger, and S. B. Feinstein, “Vasa vasorum and plaque neovascularization on contrast-enhanced carotid ultrasound imaging correlates with cardiovascular disease and past cardiovascular events,” *Stroke*, vol. 41, no. 1, pp. 41–47, Jan. 2010.

## Bibliography

- [150] D. Maresca, K. Jansen, G. Renaud, G. van Soest, X. Li, Q. Zhou, N. de Jong, K. K. Shung, and A. F. W. van der Steen, "Intravascular ultrasound chirp imaging," *Appl Phys Lett*, vol. 100, no. 4, p. 043703, Jan. 2012.
- [151] M. E. Frijlink, D. E. Goertz, A. Bouakaz, and A. F. W. van der Steen, "A simulation study on tissue harmonic imaging with a single-element intravascular ultrasound catheter.," *The Journal of the Acoustical Society of America*, vol. 120, no. 3, pp. 1723–1731, Sep. 2006.
- [152] C. Kind, "The development of the circulating blood volume of the chick embryo.," *Anat. Embryol.*, vol. 147, no. 2, pp. 127–132, Aug. 1975.
- [153] K. J. Niermann, A. C. Fleischer, J. Huamani, T. E. Yankeelov, D. W. Kim, W. D. Wilson, and D. E. Hallahan, "Measuring tumor perfusion in control and treated murine tumors: correlation of microbubble contrast-enhanced sonography to dynamic contrast-enhanced magnetic resonance imaging and fluorodeoxyglucose positron emission tomography.," *J Ultrasound Med*, vol. 26, no. 6, pp. 749–756, Jun. 2007.
- [154] C. M. Sehgal, T. W. Cary, P. H. Arger, and A. K. W. Wood, "Delta-projection imaging on contrast-enhanced ultrasound to quantify tumor microvasculature and perfusion.," *Acad Radiol*, vol. 16, no. 1, pp. 71–78, Jan. 2009.
- [155] C. Vinegoni, I. Botnaru, E. Aikawa, M. A. Calfon, Y. Iwamoto, E. J. Folco, V. Ntziachristos, R. Weissleder, P. Libby, and F. A. Jaffer, "Indocyanine green enables near-infrared fluorescence imaging of lipid-rich, inflamed atherosclerotic plaques.," *Sci Transl Med*, vol. 3, no. 84, pp. 84ra45–84ra45, May 2011.
- [156] D. Cosgrove and C. Harvey, "Clinical uses of microbubbles in diagnosis and treatment.," *Med Biol Eng Comput*, vol. 47, no. 8, pp. 813–826, Aug. 2009.
- [157] S. B. Feinstein, B. Coll, D. Staub, D. Adam, A. F. L. Schinkel, F. J. ten Cate, and K. Thomenius, "Contrast enhanced ultrasound imaging.," *J Nucl Cardiol*, vol. 17, no. 1, pp. 106–115, Jan. 2010.
- [158] C. X. Deng, F. Sieling, H. Pan, and J. Cui, "Ultrasound-induced cell membrane porosity.," *Ultrasound Med Biol*, vol. 30, no. 4, pp. 519–526, Apr. 2004.
- [159] Z. Fan, H. Liu, M. Mayer, and C. X. Deng, "Spatiotemporally controlled single cell sonoporation.," *Proc. Natl. Acad. Sci. U.S.A.*, vol. 109, no. 41, pp. 16486–16491, Oct. 2012.
- [160] A. van Wamel, K. Kooiman, M. Hartevelde, M. Emmer, F. J. ten Cate, M. Versluis, and N. de Jong, "Vibrating microbubbles poking individual cells: drug transfer into cells via sonoporation.," *J Control Release*, vol. 112, no. 2, pp. 149–155, May 2006.
- [161] K. Kooiman, M. Foppen-Hartevelde, A. F. W. van der Steen, and N. de Jong, "Sonoporation of endothelial cells by vibrating targeted microbubbles.," *J Control Release*, vol. 154, no. 1, pp. 35–41, Aug. 2011.
- [162] I. Skachkov, Y. Luan, A. F. W. van der Steen, N. de Jong, and K. Kooiman, "Targeted microbubble mediated sonoporation of endothelial cells in vivo.," *IEEE Trans Ultrason Ferroelectr Freq Control*, vol. 61, no. 10, pp. 1661–1667, Oct. 2014.
- [163] J. Park, Z. Fan, R. E. Kumon, M. E. H. El-Sayed, and C. X. Deng, "Modulation of intracellular Ca<sup>2+</sup> concentration in brain microvascular endothelial cells in vitro by acoustic cavitation.," *Ultrasound Med Biol*, vol. 36, no. 7, pp. 1176–1187, Jul. 2010.
- [164] F. E. Shamout, A. N. Pouliopoulos, P. Lee, S. Bonaccorsi, L. Towhidi, R. Krams, and J. J. Choi, "Enhancement of non-invasive trans-membrane drug delivery using ultrasound and microbubbles during physiologically relevant flow.," *Ultrasound Med Biol*, vol. 41, no. 9, pp. 2435–2448, Sep. 2015.
- [165] T. van Rooij, A. F. W. van der Steen, N. de Jong, and K. Kooiman, "Influence of binding on the vibrational responses of targeted lipid-coated microbubbles," *2014 IEEE International Ultrasonics Symposium (IUS)*, pp. 413–416, 2014.
- [166] J. R. Lindner, J. Song, J. Christiansen, A. L. Klivanov, F. Xu, and K. Ley, "Ultrasound assessment of inflammation and renal tissue injury with microbubbles targeted to P-selectin.," *Circulation*, vol. 104, no. 17, pp. 2107–2112, Oct. 2001.
- [167] K. A. Smith, S. A. Hill, A. C. Begg, and J. Denekamp, "Validation of the fluorescent dye Hoechst 33342 as a vascular space marker in tumours.," *Br. J. Cancer*, vol. 57, no. 3, pp. 247–253, Mar. 1988.
- [168] D. Bratosin, L. Mitrofan, C. Paliu, J. Estaquier, and J. Montreuil, "Novel fluorescence assay using calcein-AM for the determination of human erythrocyte viability and aging.," *Cytometry A*, vol. 66, no. 1, pp. 78–84, Jul. 2005.
- [169] T. R. Jones, A. Carpenter, and P. Golland, "Voronoi-Based Segmentation of Cells on Image Manifolds," in *Computer Vision for Biomedical Image Applications*, vol. 3765, no. 54, Berlin, Heidelberg: Springer Berlin Heidelberg, 2005, pp. 535–543.
- [170] N. Otsu, "A threshold selection method from gray-level histograms," *Automatica*, 1975.

## Bibliography

- [171] S. Wold, K. Esbensen, and P. Geladi, "Principal component analysis," *Chemometrics and Intelligent Laboratory Systems*, vol. 2, no. 1, pp. 37–52, Aug. 1987.
- [172] R. L. Tatusov, D. A. Natale, I. V. Garkavtsev, T. A. Tatusova, U. T. Shankavaram, B. S. Rao, B. Kiryutin, M. Y. Galperin, N. D. Fedorova, and E. V. Koonin, "The COG database: new developments in phylogenetic classification of proteins from complete genomes.," *Nucleic Acids Res.*, vol. 29, no. 1, pp. 22–28, Jan. 2001.
- [173] I. De Cock, E. Zagato, K. Braeckmans, Y. Luan, N. de Jong, S. C. De Smedt, and I. Lentacker, "Ultrasound and microbubble mediated drug delivery: acoustic pressure as determinant for uptake via membrane pores or endocytosis.," *J Control Release*, vol. 197, pp. 20–28, Jan. 2015.
- [174] T. J. A. Kokhuis, V. Garbin, K. Kooiman, B. A. Naaijken, L. J. M. Juffermans, O. Kamp, A. F. W. van der Steen, M. Versluis, and N. de Jong, "Secondary Bjerknes forces deform targeted microbubbles.," *Ultrasound Med Biol*, vol. 39, no. 3, pp. 490–506, Mar. 2013.
- [175] J. T. Sutton, K. J. Haworth, G. Pyne-Geithman, and C. K. Holland, "Ultrasound-mediated drug delivery for cardiovascular disease.," *Expert Opin Drug Deliv*, vol. 10, no. 5, pp. 573–592, May 2013.
- [176] M. de Saint Victor, C. Drake, C. C. Coussios, and E. Stride, "Properties, characteristics and applications of microbubbles for sonothrombolysis.," *Expert Opin Drug Deliv*, vol. 11, no. 2, pp. 187–209, Feb. 2014.
- [177] Z. Fan, R. E. Kumon, J. Park, and C. X. Deng, "Intracellular delivery and calcium transients generated in sonoporation facilitated by microbubbles.," *J Control Release*, vol. 142, no. 1, pp. 31–39, Feb. 2010.
- [178] F. Yan, X. Li, Q. Jin, C. Jiang, Z. Zhang, T. Ling, B. Qiu, and H. Zheng, "Therapeutic ultrasonic microbubbles carrying paclitaxel and LyP-1 peptide: preparation, characterization and application to ultrasound-assisted chemotherapy in breast cancer cells.," *Ultrasound Med Biol*, vol. 37, no. 5, pp. 768–779, May 2011.
- [179] L. C. Phillips, A. L. Klivanov, B. R. Wamhoff, and J. A. Hossack, "Intravascular ultrasound detection and delivery of molecularly targeted microbubbles for gene delivery.," *IEEE Trans Ultrason Ferroelectr Freq Control*, vol. 59, no. 7, pp. 1596–1601, Jul. 2012.
- [180] S. Chang, J. Guo, J. Sun, S. Zhu, Y. Yan, Y. Zhu, M. Li, Z. Wang, and R. X. Xu, "Targeted microbubbles for ultrasound mediated gene transfection and apoptosis induction in ovarian cancer cells.," *Ultrason Sonochem*, vol. 20, no. 1, pp. 171–179, Jan. 2013.
- [181] J. McLaughlan, N. Ingram, P. R. Smith, S. Harput, P. L. Coletta, S. Evans, and S. Freear, "Increasing the sonoporation efficiency of targeted polydisperse microbubble populations using chirp excitation.," *IEEE Trans Ultrason Ferroelectr Freq Control*, vol. 60, no. 12, pp. 2511–2520, Dec. 2013.
- [182] H. Liu, S. Chang, J. Sun, S. Zhu, C. Pu, Y. Zhu, Z. Wang, and R. X. Xu, "Ultrasound-mediated destruction of LHRHa-targeted and paclitaxel-loaded lipid microbubbles induces proliferation inhibition and apoptosis in ovarian cancer cells.," *Mol. Pharm.*, vol. 11, no. 1, pp. 40–48, Jan. 2014.
- [183] T. van Rooij, Y. Luan, G. Renaud, A. F. W. van der Steen, M. Versluis, N. de Jong, and K. Kooiman, "Non-linear response and viscoelastic properties of lipid-coated microbubbles: DSPC versus DPPC.," *Ultrasound Med Biol*, vol. 41, no. 5, pp. 1432–1445, May 2015.
- [184] H. M. DeLisser, P. J. Newman, and S. M. Albelda, "Molecular and functional aspects of PECAM-1/CD31.," *Immunol. Today*, vol. 15, no. 10, pp. 490–495, Oct. 1994.
- [185] L. M. Kornmann, K. D. Reesink, R. S. Reneman, and A. P. G. Hoeks, "Critical appraisal of targeted ultrasound contrast agents for molecular imaging in large arteries.," *Ultrasound Med Biol*, vol. 36, no. 2, pp. 181–191, Feb. 2010.
- [186] J. L. Tlaxca, J. J. Rychak, P. B. Ernst, P. R. Konkalmatt, T. I. Shevchenko, T. T. Pizarro, T. T. Pizzaro, J. Rivera-Nieves, A. L. Klivanov, and M. B. Lawrence, "Ultrasound-based molecular imaging and specific gene delivery to mesenteric vasculature by endothelial adhesion molecule targeted microbubbles in a mouse model of Crohn's disease.," *J Control Release*, vol. 165, no. 3, pp. 216–225, Feb. 2013.
- [187] C.-H. Fan, C.-Y. Ting, H.-L. Liu, C.-Y. Huang, H.-Y. Hsieh, T.-C. Yen, K.-C. Wei, and C.-K. Yeh, "Antiangiogenic-targeting drug-loaded microbubbles with focused ultrasound for glioma treatment.," *Biomaterials*, vol. 34, no. 8, pp. 2142–2155, Mar. 2013.
- [188] K. Wei, "Contrast echocardiography: applications and limitations.," *Cardiol Rev*, vol. 20, no. 1, pp. 25–32, Jan. 2012.
- [189] H. H. T. Madsen and F. Rasmussen, "Contrast-enhanced ultrasound in oncology.," *Cancer Imaging*, vol. 11, no. 1, pp. S167–73, 2011.
- [190] A. Alzarra, G. Gravante, W. Y. Chung, D. Al-Leswas, B. Morgan, A. Dennison, and D. Lloyd, "Contrast-enhanced ultrasound in the preoperative, intraoperative and postoperative assessment of liver lesions.," *Hepatol. Res.*, vol. 43, no. 8, pp. 809–819, Aug. 2013.



# Bibliography

- [191] J. R. Lindner, "Molecular imaging of myocardial and vascular disorders with ultrasound.," *JACC Cardiovasc Imaging*, vol. 3, no. 2, pp. 204–211, Feb. 2010.
- [192] F. Kiessling, J. Bzyl, S. Fokong, M. Siepmann, G. Schmitz, and M. Palmowski, "Targeted ultrasound imaging of cancer: an emerging technology on its way to clinics.," *Curr. Pharm. Des.*, vol. 18, no. 15, pp. 2184–2199, 2012.
- [193] M. R. Böhmer, A. L. Klibanov, K. Tiemann, C. S. Hall, H. Gruell, and O. C. Steinbach, "Ultrasound triggered image-guided drug delivery.," *Eur J Radiol*, vol. 70, no. 2, pp. 242–253, May 2009.
- [194] J. Park, Z. Fan, and C. X. Deng, "Effects of shear stress cultivation on cell membrane disruption and intracellular calcium concentration in sonoporation of endothelial cells.," *J Biomech*, vol. 44, no. 1, pp. 164–169, Jan. 2011.
- [195] M. Sriram, G. A. van der Marel, H. L. Roelen, J. H. van Boom, and A. H. Wang, "Conformation of B-DNA containing O6-ethyl-G-C base pairs stabilized by minor groove binding drugs: molecular structure of d(CGC[e6G]AATTCGCG complexed with Hoechst 33258 or Hoechst 33342.," *EMBO J.*, vol. 11, no. 1, pp. 225–232, Jan. 1992.
- [196] W. D. Wilson, C. R. Krishnamoorthy, Y. H. Wang, and J. C. Smith, "Mechanism of intercalation: ion effects on the equilibrium and kinetic constants for the interaction of propidium and ethidium with DNA.," *Biopolymers*, vol. 24, no. 10, pp. 1941–1961, Oct. 1985.
- [197] S. Kotopoulis and M. Postema, "Microfoam formation in a capillary.," *Ultrasonics*, vol. 50, no. 2, pp. 260–268, Feb. 2010.
- [198] E. A. Ferrante, J. E. Pickard, J. Rychak, A. L. Klibanov, and K. Ley, "Dual targeting improves microbubble contrast agent adhesion to VCAM-1 and P-selectin under flow.," *J Control Release*, vol. 140, no. 2, pp. 100–107, Dec. 2009.
- [199] T. M. Maul, D. D. Dudgeon, M. T. Beste, D. A. Hammer, J. S. Lazo, F. S. Villanueva, and W. R. Wagner, "Optimization of ultrasound contrast agents with computational models to improve selection of ligands and binding strength.," *Biotechnol. Bioeng.*, vol. 107, no. 5, pp. 854–864, Dec. 2010.
- [200] A. S. Ham, A. L. Klibanov, and M. B. Lawrence, "Action at a distance: lengthening adhesion bonds with poly(ethylene glycol) spacers enhances mechanically stressed affinity for improved vascular targeting of microparticles.," *Langmuir*, vol. 25, no. 17, pp. 10038–10044, Sep. 2009.
- [201] J. J. Rychak, J. R. Lindner, K. Ley, and A. L. Klibanov, "Deformable gas-filled microbubbles targeted to P-selectin.," *J Control Release*, vol. 114, no. 3, pp. 288–299, Sep. 2006.
- [202] K. Kooiman, T. J. A. Kokhuis, I. Skachkov, J. G. Bosch, A. F. W. van der Steen, W. A. van Cappellen, and N. de Jong, "Surface contact of bound targeted microbubbles," *2012 IEEE International Ultrasonics Symposium*, pp. 2161–2163, 2012.
- [203] J. J. Rychak, A. L. Klibanov, K. F. Ley, and J. A. Hossack, "Enhanced targeting of ultrasound contrast agents using acoustic radiation force.," *Ultrasound Med Biol*, vol. 33, no. 7, pp. 1132–1139, Jul. 2007.
- [204] R. C. Gessner, J. E. Streeter, R. Kothadia, S. Feingold, and P. A. Dayton, "An in vivo validation of the application of acoustic radiation force to enhance the diagnostic utility of molecular imaging using 3-d ultrasound.," *Ultrasound Med Biol*, vol. 38, no. 4, pp. 651–660, Apr. 2012.
- [205] J. W. Owen, P. Rademeyer, and E. Stride, "Magnetic targeting of microbubbles at physiologically relevant flow rates," *The Journal of the Acoustical Society of America*, vol. 134, no. 5, pp. 3992–3992, Nov. 2013.
- [206] T. Faez, I. Skachkov, M. Versluis, K. Kooiman, and N. de Jong, "In vivo characterization of ultrasound contrast agents: microbubble spectroscopy in a chicken embryo.," *Ultrasound Med Biol*, vol. 38, no. 9, pp. 1608–1617, Sep. 2012.
- [207] D. Ribatti, B. Nico, A. Vacca, L. Roncali, P. H. Burri, and V. Djonov, "Chorioallantoic membrane capillary bed: a useful target for studying angiogenesis and anti-angiogenesis in vivo.," *Anat. Rec.*, vol. 264, no. 4, pp. 317–324, Dec. 2001.
- [208] M. G. Lampugnani, "Endothelial cell-to-cell junctions: adhesion and signaling in physiology and pathology.," *Cold Spring Harb Perspect Med*, vol. 2, no. 10, Oct. 2012.
- [209] A. Bottons and A. Bardelli, "Oncogenes and angiogenesis: a way to personalize anti-angiogenic therapy?," *Cell. Mol. Life Sci.*, vol. 70, no. 21, pp. 4131–4140, Nov. 2013.
- [210] B. A. Naaijken, A. van Dijk, O. Kamp, P. A. J. Krijnen, H. W. M. Niessen, and L. J. M. Juffermans, "Therapeutic application of adipose derived stem cells in acute myocardial infarction: lessons from animal models.," *Stem Cell Rev*, vol. 10, no. 3, pp. 389–398, Jun. 2014.
- [211] A. B. Carvalho and A. C. de Carvalho, "Heart regeneration: Past, present and future.," *World J Cardiol*, vol. 2, no. 5, pp. 107–111, May 2010.
- [212] K. D. Poss, L. G. Wilson, and M. T. Keating, "Heart regeneration in zebrafish.," *Science*, vol. 298, no. 5601, pp. 2188–2190, Dec. 2002.
- [213] O. Bergmann, R. D. Bhardwaj, S. Bernard, S. Zdunek, F. Barnabé-Heider, S. Walsh, J. Zupicich, K.

## Bibliography

- Alkass, B. A. Buchholz, H. Druid, S. Jovinge, and J. Frisén, "Evidence for cardiomyocyte renewal in humans.," *Science*, vol. 324, no. 5923, pp. 98–102, Apr. 2009.
- [214] H. C. Quevedo, K. E. Hatzistergos, B. N. Oskouei, G. S. Feigenbaum, J. E. Rodriguez, D. Valdes, P. M. Pattany, J. P. Zambrano, Q. Hu, I. McNiece, A. W. Heldman, and J. M. Hare, "Allogeneic mesenchymal stem cells restore cardiac function in chronic ischemic cardiomyopathy via trilineage differentiating capacity.," *Proc. Natl. Acad. Sci. U.S.A.*, vol. 106, no. 33, pp. 14022–14027, Aug. 2009.
- [215] G. V. Silva, S. Litovsky, J. A. R. Assad, A. L. S. Sousa, B. J. Martin, D. Vela, S. C. Coulter, J. Lin, J. Ober, W. K. Vaughn, R. V. C. Branco, E. M. Oliveira, R. He, Y.-J. Geng, J. T. Willerson, and E. C. Perin, "Mesenchymal stem cells differentiate into an endothelial phenotype, enhance vascular density, and improve heart function in a canine chronic ischemia model.," *Circulation*, vol. 111, no. 2, pp. 150–156, Jan. 2005.
- [216] M. Gnechchi, Z. Zhang, A. Ni, and V. J. Dzau, "Paracrine mechanisms in adult stem cell signaling and therapy.," *Circ. Res.*, vol. 103, no. 11, pp. 1204–1219, Nov. 2008.
- [217] Y. L. Tang, Q. Zhao, Y. C. Zhang, L. Cheng, M. Liu, J. Shi, Y. Z. Yang, C. Pan, J. Ge, and M. I. Phillips, "Autologous mesenchymal stem cell transplantation induce VEGF and neovascularization in ischemic myocardium.," *Regul. Pept.*, vol. 117, no. 1, pp. 3–10, Jan. 2004.
- [218] I. M. Barbash, P. Chouraqui, J. Baron, M. S. Feinberg, S. Etzion, A. Tessone, L. Miller, E. Guetta, D. Zipori, L. H. Kedes, R. A. Kloner, and J. Leor, "Systemic delivery of bone marrow-derived mesenchymal stem cells to the infarcted myocardium: feasibility, cell migration, and body distribution.," *Circulation*, vol. 108, no. 7, pp. 863–868, Aug. 2003.
- [219] J. Bartunek, W. Sherman, M. Vanderheyden, F. Fernandez-Aviles, W. Wijns, and A. Terzic, "Delivery of biologics in cardiovascular regenerative medicine.," *Clin. Pharmacol. Ther.*, vol. 85, no. 5, pp. 548–552, May 2009.
- [220] M. Hofmann, K. C. Wollert, G. P. Meyer, A. Menke, L. Arseniev, B. Hertenstein, A. Ganser, W. H. Knapp, and H. Drexler, "Monitoring of bone marrow cell homing into the infarcted human myocardium.," *Circulation*, vol. 111, no. 17, pp. 2198–2202, May 2005.
- [221] V. F. M. Segers, I. Van Riet, L. J. Andries, K. Lemmens, M. J. Demolder, A. J. M. L. De Becker, M. M. Kockx, and G. W. De Keulenaer, "Mesenchymal stem cell adhesion to cardiac microvascular endothelium: activators and mechanisms.," *Am. J. Physiol. Heart Circ. Physiol.*, vol. 290, no. 4, pp. H1370–7, Apr. 2006.
- [222] A. Ghanem, C. Steingen, F. Brenig, F. Funcke, Z.-Y. Bai, C. Hall, C. T. Chin, G. Nickenig, W. Bloch, and K. Tiemann, "Focused ultrasound-induced stimulation of microbubbles augments site-targeted engraftment of mesenchymal stem cells after acute myocardial infarction.," *J. Mol. Cell. Cardiol.*, vol. 47, no. 3, pp. 411–418, Sep. 2009.
- [223] F. H. Seeger, A. M. Zeiher, and S. Dimmeler, "Cell-enhancement strategies for the treatment of ischemic heart disease.," *Nat Clin Pract Cardiovasc Med*, vol. 4, pp. S110–3, Feb. 2007.
- [224] J.-I. Yamaguchi, K. F. Kusano, O. Masuo, A. Kawamoto, M. Silver, S. Murasawa, M. Bosch-Marce, H. Masuda, D. W. Losordo, J. M. Isner, and T. Asahara, "Stromal cell-derived factor-1 effects on ex vivo expanded endothelial progenitor cell recruitment for ischemic neovascularization.," *Circulation*, vol. 107, no. 9, pp. 1322–1328, Mar. 2003.
- [225] R. J. Lee, Q. Fang, P. A. Davol, Y. Gu, R. E. Sievers, R. C. Grabert, J. M. Gall, E. Tsang, M. S. Yee, H. Fok, N. F. Huang, J. F. Padbury, J. W. Larrick, and L. G. Lum, "Antibody targeting of stem cells to infarcted myocardium.," *Stem Cells*, vol. 25, no. 3, pp. 712–717, Mar. 2007.
- [226] J. H. Jeong, J. J. Schmidt, R. E. Kohman, A. T. Zill, R. J. DeVolder, C. E. Smith, M.-H. Lai, A. Shkumatov, T. W. Jensen, L. G. Schook, S. C. Zimmerman, and H. Kong, "Leukocyte-mimicking stem cell delivery via in situ coating of cells with a bioactive hyperbranched polyglycerol.," *J. Am. Chem. Soc.*, vol. 135, no. 24, pp. 8770–8773, Jun. 2013.
- [227] O. Levy, W. Zhao, L. J. Mortensen, S. Leblanc, K. Tsang, M. Fu, J. A. Phillips, V. Sagar, P. Anandakumaran, J. Ngai, C. H. Cui, P. Eimon, M. Angel, C. P. Lin, M. F. Yanik, and J. M. Karp, "mRNA-engineered mesenchymal stem cells for targeted delivery of interleukin-10 to sites of inflammation.," *Blood*, vol. 122, no. 14, pp. e23–32, Oct. 2013.
- [228] M. W. Keller, S. S. Segal, S. Kaul, and B. Duling, "The behavior of sonicated albumin microbubbles within the microcirculation: a basis for their use during myocardial contrast echocardiography.," *Circ. Res.*, vol. 65, no. 2, pp. 458–467, Aug. 1989.
- [229] L. E. BAYLISS, "The axial drift of the red cells when blood flows in a narrow tube.," *J. Physiol. (Lond.)*, vol. 149, no. 3, pp. 593–613, Dec. 1959.
- [230] N. Deshpande, A. Needles, and J. K. Willmann, "Molecular ultrasound imaging: current status and future directions.," *Clin Radiol*, vol. 65, no. 7, pp. 567–581, Jul. 2010.

# Bibliography

- [231] J. R. Lindner, "Microbubbles in medical imaging: current applications and future directions.," *Nat Rev Drug Discov*, vol. 3, no. 6, pp. 527–532, Jun. 2004.
- [232] N. de Jong, M. Emmer, A. van Wamel, and M. Versluis, "Ultrasonic characterization of ultrasound contrast agents.," *Med Biol Eng Comput*, vol. 47, no. 8, pp. 861–873, Aug. 2009.
- [233] P. J. A. Frinking, I. Tardy, M. Théaulaz, M. Arditi, J. Powers, S. Pochon, and F. Tranquart, "Effects of acoustic radiation force on the binding efficiency of BR55, a VEGFR2-specific ultrasound contrast agent.," *Ultrasound Med Biol*, vol. 38, no. 8, pp. 1460–1469, Aug. 2012.
- [234] T. Leighton, *The Acoustic Bubble*. Academic Press, 2012.
- [235] P. Dayton, A. L. Klibanov, G. Brandenburger, and K. Ferrara, "Acoustic radiation force in vivo: a mechanism to assist targeting of microbubbles.," *Ultrasound Med Biol*, vol. 25, no. 8, pp. 1195–1201, Oct. 1999.
- [236] L. J. M. Juffermans, "Ultrasound and microbubble-targeted delivery of drugs and genes: Cellular bioeffects and mechanisms. PhD Thesis.," Amsterdam: Vrije Universiteit, 2009.
- [237] L. J. M. Juffermans, A. van Dijk, B. A. Naaijken, T. J. A. Kokhuis, M. Hartevelde, R. Musters, V. Hinsbergh, M. Helder, O. Kamp, N. de Jong, and H. Niessen, "Directing adipose derived stem cells to the area at risk in the heart after myocardial infarction using targeted microbubbles. 15th European Symposium on Ultrasound Contrast Imaging 2010, Rotterdam, The Netherlands," presented at the 15th European Symposium on Ultrasound Contrast Imaging 2010, Rotterdam, Rotterdam, 2010.
- [238] B. A. Naaijken, H. W. M. Niessen, H.-J. Prins, P. A. J. Krijnen, T. J. A. Kokhuis, N. de Jong, V. W. M. van Hinsbergh, O. Kamp, M. N. Helder, R. Musters, A. van Dijk, and L. J. M. Juffermans, "Human platelet lysate as a fetal bovine serum substitute improves human adipose-derived stromal cell culture for future cardiac repair applications.," *Cell Tissue Res.*, vol. 348, no. 1, pp. 119–130, Apr. 2012.
- [239] V. F. M. Segers and R. T. Lee, "Stem-cell therapy for cardiac disease.," *Nature*, vol. 451, no. 7181, pp. 937–942, Feb. 2008.
- [240] J. E. Chomas, P. A. Dayton, D. May, and J. Allen, "Optical observation of contrast agent destruction," *Applied Physics ...*, 2000.
- [241] J. F. Beltrame, F. Crea, and P. Camici, "Advances in coronary microvascular dysfunction.," *Heart Lung Circ*, vol. 18, no. 1, pp. 19–27, Feb. 2009.
- [242] S. Kaul and H. Ito, "Microvasculature in acute myocardial ischemia: part I: evolving concepts in pathophysiology, diagnosis, and treatment.," *Circulation*, vol. 109, no. 2, pp. 146–149, Jan. 2004.
- [243] T. D. Miller, T. F. Christian, M. R. Hopfenspirger, D. O. Hodge, B. J. Gersh, and R. J. Gibbons, "Infarct size after acute myocardial infarction measured by quantitative tomographic 99mTc sestamibi imaging predicts subsequent mortality.," *Circulation*, vol. 92, no. 3, pp. 334–341, Aug. 1995.
- [244] A. Schmidt, D. Ladage, C. Steingen, K. Brixius, T. Schinköthe, F.-J. Klinz, R. H. G. Schwinger, U. Mehlhorn, and W. Bloch, "Mesenchymal stem cells transmigrate over the endothelial barrier.," *Eur. J. Cell Biol.*, vol. 85, no. 11, pp. 1179–1188, Nov. 2006.
- [245] W. A. Muller, "Mechanisms of leukocyte transendothelial migration.," *Annu Rev Pathol*, vol. 6, no. 1, pp. 323–344, 2011.
- [246] E. Chavakis and S. Dimmeler, "Homing of progenitor cells to ischemic tissues.," *Antioxid. Redox Signal.*, vol. 15, no. 4, pp. 967–980, Aug. 2011.
- [247] K. Cheng, D. Shen, Y. Xie, E. Cingolani, K. Malliaras, and E. Marbán, "Brief report: Mechanism of extravasation of infused stem cells.," *Stem Cells*, vol. 30, no. 12, pp. 2835–2842, Dec. 2012.
- [248] R. Basilico, M. J. K. Blomley, D. O. Cosgrove, J.-B. Liull, A. Broillet, A. Bauer, and L. Bonomo, "The first phase I study of a novel ultrasound contrast agent (BR14): assessment of safety and efficacy in liver and kidneys.," *Acad Radiol*, vol. 9, pp. S380–1, Aug. 2002.
- [249] B. Wang, W.-J. Zang, M. Wang, H. Ai, Y.-W. Wang, Y.-P. Li, G.-S. He, L. Wang, and X.-J. Yu, "Prolonging the ultrasound signal enhancement from thrombi using targeted microbubbles based on sulfur-hexafluoride-filled gas.," *Acad Radiol*, vol. 13, no. 4, pp. 428–433, Apr. 2006.
- [250] T. Segers and M. Versluis, "Acoustic bubble sorting for ultrasound contrast agent enrichment.," *Lab Chip*, vol. 14, no. 10, pp. 1705–1714, May 2014.
- [251] S. Zhao, M. Borden, S. H. Bloch, D. Kruse, K. W. Ferrara, and P. A. Dayton, "Radiation-force assisted targeting facilitates ultrasonic molecular imaging.," *Mol Imaging*, vol. 3, no. 3, pp. 135–148, Jul. 2004.
- [252] V. Garbin, D. Cojoc, E. Ferrari, E. Di Fabrizio, M. L. J. Overvelde, S. M. van der Meer, N. de Jong, D. Lohse, and M. Versluis, "Changes in microbubble dynamics near a boundary revealed by combined optical micromanipulation and high-speed imaging," *Appl Phys Lett*, vol. 90, no. 11, p. 114103, Mar. 2007.
- [253] H. Hong, Y. Yang, Y. Zhang, and W. Cai, "Non-invasive cell tracking in cancer and cancer therapy.," *Curr Top Med Chem*, vol. 10, no. 12, pp. 1237–1248, 2010.
- [254] F. Gazeau and C. Wilhelm, "Magnetic labeling, imaging and manipulation of endothelial progenitor



- p>cells using iron oxide nanoparticles.,”
- Future Med Chem*
- , vol. 2, no. 3, pp. 397–408, Mar. 2010.
- [255] M. Edmundson, N. T. Thanh, and B. Song, “Nanoparticles based stem cell tracking in regenerative medicine.,” *Theranostics*, vol. 3, no. 8, pp. 573–582, 2013.
- [256] B. Gimi, N. Mori, E. Ackerstaff, E. E. Frost, J. W. M. Bulte, and Z. M. Bhujwala, “Noninvasive MRI of endothelial cell response to human breast cancer cells.,” *Neoplasia*, vol. 8, no. 3, pp. 207–213, Mar. 2006.
- [257] S. Ramaswamy, P. A. Schornack, A. G. Smelko, S. M. Boronyak, J. Ivanova, J. E. Mayer, and M. S. Sacks, “Superparamagnetic iron oxide (SPIO) labeling efficiency and subsequent MRI tracking of native cell populations pertinent to pulmonary heart valve tissue engineering studies.,” *NMR Biomed*, vol. 25, no. 3, pp. 410–417, Mar. 2012.
- [258] D. Fayol, C. Le Visage, J. Ino, F. Gazeau, D. Letourneur, and C. Wilhelm, “Design of biomimetic vascular grafts with magnetic endothelial patterning.,” *Cell Transplant*, vol. 22, no. 11, pp. 2105–2118, 2013.
- [259] Y. Fu, N. Azene, Y. Xu, and D. L. Kraitchman, “Tracking stem cells for cardiovascular applications in vivo: focus on imaging techniques.,” *Imaging Med*, vol. 3, no. 4, pp. 473–486, Aug. 2011.
- [260] H. Youn and K.-J. Hong, “In vivo non invasive molecular imaging for immune cell tracking in small animals.,” *Immune Netw*, vol. 12, no. 6, pp. 223–229, Dec. 2012.
- [261] S. Eguchi, M. Takatsuki, M. Hidaka, A. Soyama, T. Tomonaga, I. Muraoka, and T. Kanematsu, “Predictor for histological microvascular invasion of hepatocellular carcinoma: a lesson from 229 consecutive cases of curative liver resection.,” *World J Surg*, vol. 34, no. 5, pp. 1034–1038, May 2010.
- [262] E. M. Shapiro, K. Sharer, S. Skrtic, and A. P. Koretsky, “In vivo detection of single cells by MRI.,” *Magn Reson Med*, vol. 55, no. 2, pp. 242–249, Feb. 2006.
- [263] N. Lee, H. Kim, S. H. Choi, M. Park, D. Kim, H.-C. Kim, Y. Choi, S. Lin, B. H. Kim, H. S. Jung, H. Kim, K. S. Park, W. K. Moon, and T. Hyeon, “Magnetosome-like ferrimagnetic iron oxide nanocubes for highly sensitive MRI of single cells and transplanted pancreatic islets.,” *Proc. Natl. Acad. Sci. U.S.A.*, vol. 108, no. 7, pp. 2662–2667, Feb. 2011.
- [264] G. J. Strijkers, W. J. M. Mulder, G. A. F. van Tilborg, and K. Nicolay, “MRI contrast agents: current status and future perspectives.,” *Anticancer Agents Med Chem*, vol. 7, no. 3, pp. 291–305, May 2007.
- [265] L. F. Gamarra, G. E. S. Brito, W. M. Pontuschka, E. Amaro, A. H. C. Parma, and G. F. Goya, “Biocompatible superparamagnetic iron oxide nanoparticles used for contrast agents: a structural and magnetic study,” *Journal of Magnetism and Magnetic Materials*, vol. 289, pp. 439–441, Mar. 2005.
- [266] A. Neuwelt, N. Sidhu, C.-A. A. Hu, G. Mlady, S. C. Eberhardt, and L. O. Sillerud, “Iron-based superparamagnetic nanoparticle contrast agents for MRI of infection and inflammation.,” *AJR Am J Roentgenol*, vol. 204, no. 3, pp. W302–13, Mar. 2015.
- [267] L. H. Reddy, “Drug delivery to tumours: recent strategies.,” *J. Pharm. Pharmacol.*, vol. 57, no. 10, pp. 1231–1242, Oct. 2005.
- [268] L. H. Reddy, J. L. Arias, J. Nicolas, and P. Couvreur, “Magnetic nanoparticles: design and characterization, toxicity and biocompatibility, pharmaceutical and biomedical applications.,” *Chem. Rev.*, vol. 112, no. 11, pp. 5818–5878, Nov. 2012.
- [269] J. A. Frank, S. A. Anderson, H. Kalsih, E. K. Jordan, B. K. Lewis, G. T. Yocum, and A. S. Arbab, “Methods for magnetically labeling stem and other cells for detection by in vivo magnetic resonance imaging.,” *Cytotherapy*, vol. 6, no. 6, pp. 621–625, 2004.
- [270] M. Rodriguez-Porcel, M. W. Kronenberg, T. D. Henry, J. H. Traverse, C. J. Pepine, S. G. Ellis, J. T. Willerson, L. A. Moyé, and R. D. Simari, “Cell tracking and the development of cell-based therapies: a view from the Cardiovascular Cell Therapy Research Network.,” *JACC Cardiovasc Imaging*, vol. 5, no. 5, pp. 559–565, May 2012.
- [271] K. Ferrara, R. Pollard, and M. Borden, “Ultrasound microbubble contrast agents: fundamentals and application to gene and drug delivery.,” *Annu Rev Biomed Eng*, vol. 9, no. 1, pp. 415–447, 2007.
- [272] A. L. Klibanov, “Preparation of targeted microbubbles: ultrasound contrast agents for molecular imaging.,” *Med Biol Eng Comput*, vol. 47, no. 8, pp. 875–882, Aug. 2009.
- [273] F. Yang, M. Zhang, W. He, P. Chen, X. Cai, L. Yang, N. Gu, and J. Wu, “Controlled release of Fe<sub>3</sub>O<sub>4</sub> nanoparticles in encapsulated microbubbles to tumor cells via sonoporation and associated cellular bioeffects.,” *Small*, vol. 7, no. 7, pp. 902–910, Apr. 2011.
- [274] A. Sternberg, M. Amar, R. Alfici, and G. Groisman, “Conclusions from a study of venous invasion in stage IV colorectal adenocarcinoma.,” *J. Clin. Pathol.*, vol. 55, no. 1, pp. 17–21, Jan. 2002.
- [275] C. Pu, S. Chang, J. Sun, S. Zhu, H. Liu, Y. Zhu, Z. Wang, and R. X. Xu, “Ultrasound-mediated destruction of LHRHa-targeted and paclitaxel-loaded lipid microbubbles for the treatment of intraperitoneal ovarian cancer xenografts.,” *Mol. Pharm.*, vol. 11, no. 1, pp. 49–58, Jan. 2014.
- [276] W.-Q. Gao, X. Li, P.-C. Liu, Z.-Y. Bai, Y.-F. Zhong, H.-B. Han, J.-F. Li, W. Liu, Z.-Z. Zheng, Y.-J.

- Sui, X.-L. Ma, X.-J. Lü, H. Xu, and X.-Z. Zeng, "[Investigation in vivo of effect of ultrasound-mediated microbubble destruction on entrance of feridex into the aortal wall].," *Zhonghua Yi Xue Za Zhi*, vol. 89, no. 39, pp. 2797–2801, Oct. 2009.
- [277] P. J. Newman and D. K. Newman, "Signal transduction pathways mediated by PECAM-1: new roles for an old molecule in platelet and vascular cell biology.," *Arterioscler. Thromb. Vasc. Biol.*, vol. 23, no. 6, pp. 953–964, Jun. 2003.
- [278] G. Clark, *Staining Procedures used by the Biological Stain Commision*. 1973.
- [279] M. R. Bernsen, A. D. Moelker, P. A. Wielopolski, S. T. van Tiel, and G. P. Krestin, "Labelling of mammalian cells for visualisation by MRI.," *Eur Radiol*, vol. 20, no. 2, pp. 255–274, Feb. 2010.
- [280] L.-F. Jin, F. Li, H.-P. Wang, F. Wei, P. Qin, and L.-F. Du, "Ultrasound targeted microbubble destruction stimulates cellular endocytosis in facilitation of adeno-associated virus delivery.," *Int J Mol Sci*, vol. 14, no. 5, pp. 9737–9750, 2013.
- [281] H. J. Vos, B. Dollet, J. G. Bosch, M. Versluis, and N. de Jong, "Nonspherical vibrations of microbubbles in contact with a wall: a pilot study at low mechanical index.," *Ultrasound Med Biol*, vol. 34, no. 4, pp. 685–688, Apr. 2008.
- [282] P. Prentice, A. Cuschieri, K. Dholakia, M. Prausnitz, and P. Campbell, "Membrane disruption by optically controlled microbubble cavitation," *Nature Physics*, vol. 1, no. 2, pp. 107–110, Nov. 2005.
- [283] S. Mukherjee, H. Raghuraman, and A. Chattopadhyay, "Membrane localization and dynamics of Nile Red: effect of cholesterol.," *Biochim. Biophys. Acta*, vol. 1768, no. 1, pp. 59–66, Jan. 2007.
- [284] C.-D. Ohl, M. Arora, R. Ikink, N. de Jong, M. Versluis, M. Delius, and D. Lohse, "Sonoporation from jetting cavitation bubbles.," *Biophys. J.*, vol. 91, no. 11, pp. 4285–4295, Dec. 2006.
- [285] A. Ooi, P. Tho, and R. Manasseh, "Cavitation microstreaming patterns in single and multiple bubble systems," *The Journal of the Acoustical Society of America*, vol. 122, no. 5, pp. 3051–3051, Nov. 2007.
- [286] V. Garbin, B. Dollet, M. Overvelde, D. Cojoc, E. Di Fabrizio, L. van Wijngaarden, A. Prosperetti, N. de Jong, D. Lohse, and M. Versluis, "History force on coated microbubbles propelled by ultrasound," *Physics of Fluids (1994-present)*, vol. 21, no. 9, p. 092003, Sep. 2009.
- [287] P. A. Dayton, K. E. Morgan, A. L. Klivanov, G. H. Brandenburger, and K. W. Ferrara, "Optical and acoustical observations of the effects of ultrasound on contrast agents.," *Ultrasonics, Ferroelectrics, and Frequency Control, IEEE Transactions on*, vol. 46, no. 1, pp. 220–232, 1999.
- [288] H.-L. Liu, P.-Y. Chen, H.-W. Yang, J.-S. Wu, I.-C. Tseng, Y.-J. Ma, C.-Y. Huang, H.-C. Tsai, S.-M. Chen, Y.-J. Lu, C.-Y. Huang, M.-Y. Hua, Y.-H. Ma, T.-C. Yen, and K.-C. Wei, "In vivo MR quantification of superparamagnetic iron oxide nanoparticle leakage during low-frequency-ultrasound-induced blood-brain barrier opening in swine.," *J Magn Reson Imaging*, vol. 34, no. 6, pp. 1313–1324, Dec. 2011.
- [289] S. T. van Tiel, P. A. Wielopolski, G. C. Houston, G. P. Krestin, and M. R. Bernsen, "Variations in labeling protocol influence incorporation, distribution and retention of iron oxide nanoparticles into human umbilical vein endothelial cells.," *Contrast Media Mol Imaging*, vol. 5, no. 5, pp. 247–257, Sep. 2010.
- [290] F. Yang, N. Gu, D. Chen, X. Xi, D. Zhang, Y. Li, and J. Wu, "Experimental study on cell self-sealing during sonoporation.," *J Control Release*, vol. 131, no. 3, pp. 205–210, Nov. 2008.
- [291] Y.-X. J. Wang, "Superparamagnetic iron oxide based MRI contrast agents: Current status of clinical application.," *Quant Imaging Med Surg*, vol. 1, no. 1, pp. 35–40, Dec. 2011.
- [292] J. F. Dice and H. L. Chiang, "Lysosomal degradation of microinjected proteins.," *Revis. Biol. Celular*, vol. 20, pp. 13–33, 1989.
- [293] H. Hashizume, P. Baluk, S. Morikawa, J. W. McLean, G. Thurston, S. Roberge, R. K. Jain, and D. M. McDonald, "Openings between defective endothelial cells explain tumor vessel leakiness.," *Am. J. Pathol.*, vol. 156, no. 4, pp. 1363–1380, Apr. 2000.
- [294] I. Hrazdira, J. Skorpíková, and M. Dolníková, "Ultrasonically induced alterations of cultured tumour cells.," *Eur J Ultrasound*, vol. 8, no. 1, pp. 43–49, Sep. 1998.
- [295] P. R. Clarke and C. R. Hill, "Biological action of ultrasound in relation to the cell cycle.," *Exp. Cell Res.*, vol. 58, no. 2, pp. 443–444, Dec. 1969.
- [296] Y. K. Fu, M. W. Miller, C. S. Lange, T. D. Griffiths, and G. E. Kaufman, "Ultrasound lethality to synchronous and asynchronous Chinese hamster V-79 cells.," *Ultrasound Med Biol*, vol. 6, no. 1, pp. 39–46, 1980.
- [297] "Feridex - FDA," *fda.gov*. [Online]. Available: [http://www.fda.gov/ohrms/dockets/ac/05/briefing/2005-4095B1\\_02\\_14-FDA-Tab-7-9.pdf](http://www.fda.gov/ohrms/dockets/ac/05/briefing/2005-4095B1_02_14-FDA-Tab-7-9.pdf). [Accessed: 11-Dec-2015].
- [298] A. Alzarraa, G. Gravante, W. Y. Chung, D. Al-Leswas, M. Bruno, A. R. Dennison, and D. M. Lloyd,

- “Targeted microbubbles in the experimental and clinical setting.,” *Am. J. Surg.*, vol. 204, no. 3, pp. 355–366, Sep. 2012.
- [299] S. Unnikrishnan and A. L. Klibanov, “Microbubbles as ultrasound contrast agents for molecular imaging: preparation and application.,” *AJR Am J Roentgenol*, vol. 199, no. 2, pp. 292–299, Aug. 2012.
- [300] K. Kooiman, T. J. A. Kokhuis, T. van Rooij, I. Skachkov, A. Nigg, J. G. Bosch, A. F. W. van der Steen, W. A. van Cappellen, and N. de Jong, “DSPC or DPPC as main shell component influences ligand distribution and binding area of lipid-coated targeted microbubbles,” *European Journal of Lipid Science and Technology*, vol. 116, no. 9, pp. 1217–1227, Sep. 2014.
- [301] T. van Rooij, Y. Luan, G. Renaud, A. F. W. van der Steen, N. de Jong, and K. Kooiman, “Acoustical response of DSPC versus DPPC lipid-coated microbubbles. 2013 IEEE International Ultrasonics Symposium (IUS).,” presented at the 2013 IEEE International Ultrasonics Symposium (IUS), 2013, pp. 310–313.
- [302] A. H. Myrset, H. B. Fjeringstad, R. Bendiksen, B. E. Arbo, R. M. Bjerke, J. H. Johansen, M. A. Kulseth, and R. Skurtveit, “Design and characterization of targeted ultrasound microbubbles for diagnostic use.,” *Ultrasound Med Biol*, vol. 37, no. 1, pp. 136–150, Jan. 2011.
- [303] D. Marsh, R. Bartucci, and L. Sportelli, “Lipid membranes with grafted polymers: physicochemical aspects.,” *Biochim. Biophys. Acta*, vol. 1615, no. 1, pp. 33–59, Sep. 2003.
- [304] S. Ottoboni, R. E. Short, M. B. Kerby, E. G. Tickner, E. Steadman, and T. B. Ottoboni, “Characterization of the in vitro adherence behavior of ultrasound responsive double-shelled microspheres targeted to cellular adhesion molecules.,” *Contrast Media Mol Imaging*, vol. 1, no. 6, pp. 279–290, Nov. 2006.
- [305] C. C. Chen and M. A. Borden, “The role of poly(ethylene glycol) brush architecture in complement activation on targeted microbubble surfaces.,” *Biomaterials*, vol. 32, no. 27, pp. 6579–6587, Sep. 2011.
- [306] F. Kiessling, S. Fokong, J. Bzyl, W. Lederle, M. Palmowski, and T. Lammers, “Recent advances in molecular, multimodal and theranostic ultrasound imaging.,” *Adv. Drug Deliv. Rev.*, vol. 72, pp. 15–27, Jun. 2014.
- [307] S. Hernot, S. Unnikrishnan, Z. Du, T. Shevchenko, B. Cosyns, A. Broisat, J. Toczek, V. Caveliers, S. Muyldermans, T. Lahoutte, A. L. Klibanov, and N. Devoogdt, “Nanobody-coupled microbubbles as novel molecular tracer.,” *J Control Release*, vol. 158, no. 2, pp. 346–353, Mar. 2012.
- [308] M. A. Nakatsuka, R. F. Mattrey, S. C. Esener, J. N. Cha, and A. P. Goodwin, “Aptamer-crosslinked microbubbles: smart contrast agents for thrombin-activated ultrasound imaging.,” *Adv. Mater. Weinheim*, vol. 24, no. 45, pp. 6010–6016, Nov. 2012.
- [309] M. A. Wheatley, J. D. Lathia, and K. L. Oum, “Polymeric ultrasound contrast agents targeted to integrins: importance of process methods and surface density of ligands.,” *Biomacromolecules*, vol. 8, no. 2, pp. 516–522, Feb. 2007.
- [310] G. Paganelli, C. Belloni, P. Magnani, F. Zito, A. Pasini, I. Sassi, M. Meroni, M. Mariani, M. Vignali, and A. G. Siccardi, “Two-step tumour targeting in ovarian cancer patients using biotinylated monoclonal antibodies and radioactive streptavidin.,” *Eur J Nucl Med*, vol. 19, no. 5, pp. 322–329, 1992.
- [311] X. Wei, Y. Li, S. Zhang, X. Gao, Y. Luo, and M. Gao, “Ultrasound targeted apoptosis imaging in monitoring early tumor response of trastuzumab in a murine tumor xenograft model of her-2-positive breast cancer(1.).,” *Transl Oncol*, vol. 7, no. 2, pp. 284–291, Apr. 2014.
- [312] S. Fokong, A. Fragoso, A. Rix, A. Curaj, Z. Wu, W. Lederle, O. Iranzo, J. Gätjens, F. Kiessling, and M. Palmowski, “Ultrasound molecular imaging of E-selectin in tumor vessels using poly n-butyl cyanoacrylate microbubbles covalently coupled to a short targeting peptide.,” *Invest Radiol*, vol. 48, no. 12, pp. 843–850, Dec. 2013.
- [313] J. K. Willmann, A. M. Lutz, R. Paulmurugan, M. R. Patel, P. Chu, J. Rosenberg, and S. S. Gambhir, “Dual-targeted contrast agent for US assessment of tumor angiogenesis in vivo.,” *Radiology*, vol. 248, no. 3, pp. 936–944, Sep. 2008.
- [314] H. Y. Jun, S. H. Park, H. S. Kim, and K.-H. Yoon, “Long residence time of ultrasound microbubbles targeted to integrin in murine tumor model.,” *Acad Radiol*, vol. 17, no. 1, pp. 54–60, Jan. 2010.
- [315] K. Otani and K. Yamahara, “Feasibility of lactadherin-bearing clinically available microbubbles as ultrasound contrast agent for angiogenesis.,” *Mol Imaging Biol*, vol. 15, no. 5, pp. 534–541, Oct. 2013.
- [316] B. A. Kaufmann, J. M. Sanders, C. Davis, A. Xie, P. Aldred, I. J. Sarembock, and J. R. Lindner, “Molecular imaging of inflammation in atherosclerosis with targeted ultrasound detection of vascular cell adhesion molecule-1.,” *Circulation*, vol. 116, no. 3, pp. 276–284, Jul. 2007.
- [317] H. Kim, M. R. Moody, S. T. Laing, P. H. Kee, S.-L. Huang, M. E. Klegerman, and D. D. McPherson,

- [318] "In vivo volumetric intravascular ultrasound visualization of early/inflammatory arterial atheroma using targeted echogenic immunoliposomes.," *Invest Radiol*, vol. 45, no. 10, pp. 685–691, Oct. 2010.
- [319] B. A. Kaufmann, C. L. Carr, J. T. Belcik, A. Xie, Q. Yue, S. Chadderdon, E. S. Caplan, J. Khangura, S. Bullens, S. Bunting, and J. R. Lindner, "Molecular imaging of the initial inflammatory response in atherosclerosis: implications for early detection of disease.," *Arterioscler. Thromb. Vasc. Biol.*, vol. 30, no. 1, pp. 54–59, Jan. 2010.
- [320] Q. Wen, S. Wan, Z. Liu, S. Xu, H. Wang, and B. Yang, "Ultrasound contrast agents and ultrasound molecular imaging.," *J Nanosci Nanotechnol*, vol. 14, no. 1, pp. 190–209, Jan. 2014.
- [321] H. Wu, N. G. Rognin, T. M. Krupka, L. Solorio, H. Yoshiara, G. Guenette, C. Sanders, N. Kamiyama, and A. A. Exner, "Acoustic characterization and pharmacokinetic analyses of new nanobubble ultrasound contrast agents.," *Ultrasound Med Biol*, vol. 39, no. 11, pp. 2137–2146, Nov. 2013.
- [322] X. Wang, C. E. Hagemeyer, J. D. Hohmann, E. Leitner, P. C. Armstrong, F. Jia, M. Olschewski, A. Needles, K. Peter, and I. Ahrens, "Novel single-chain antibody-targeted microbubbles for molecular ultrasound imaging of thrombosis: validation of a unique noninvasive method for rapid and sensitive detection of thrombi and monitoring of success or failure of thrombolysis in mice.," *Circulation*, vol. 125, no. 25, pp. 3117–3126, Jun. 2012.
- [323] P. A. Schumann, J. P. Christiansen, R. M. Quigley, T. P. McCreery, R. H. Sweitzer, E. C. Unger, J. R. Lindner, and T. O. Matsunaga, "Targeted-microbubble binding selectively to GPIIb IIIa receptors of platelet thrombi.," *Invest Radiol*, vol. 37, no. 11, pp. 587–593, Nov. 2002.
- [324] C. Cheng, F. Helderman, D. Tempel, D. Segers, B. Hierck, R. Poelmann, A. van Tol, D. J. Duncker, D. Robbers-Visser, N. T. C. Ursem, R. van Haperen, J. J. Wentzel, F. Gijzen, A. F. W. van der Steen, R. de Crom, and R. Krams, "Large variations in absolute wall shear stress levels within one species and between species.," *Atherosclerosis*, vol. 195, no. 2, pp. 225–235, Dec. 2007.
- [325] M. A. Nakatsuka, C. V. Barback, K. R. Fitch, A. R. Farwell, S. C. Esener, R. F. Mattrey, J. N. Cha, and A. P. Goodwin, "In vivo ultrasound visualization of non-occlusive blood clots with thrombin-sensitive contrast agents.," *Biomaterials*, vol. 34, no. 37, pp. 9559–9565, Dec. 2013.
- [326] I. M. Thompson, D. K. Pauler, P. J. Goodman, C. M. Tangen, M. S. Lucia, H. L. Parnes, L. M. Minasian, L. G. Ford, S. M. Lippman, E. D. Crawford, J. J. Crowley, and C. A. Coltman, "Prevalence of prostate cancer among men with a prostate-specific antigen level < or =4.0 ng per milliliter.," *N. Engl. J. Med.*, vol. 350, no. 22, pp. 2239–2246, May 2004.
- [327] S. Perner, M. D. Hofer, R. Kim, R. B. Shah, H. Li, P. Möller, R. E. Hautmann, J. E. Gschwend, R. Kuefer, and M. A. Rubin, "Prostate-specific membrane antigen expression as a predictor of prostate cancer progression.," *Hum. Pathol.*, vol. 38, no. 5, pp. 696–701, May 2007.
- [328] V. Sanna, G. Pintus, P. Bandiera, R. Anedda, S. Punzoni, B. Sanna, V. Migaletto, S. Uzzau, and M. Sechi, "Development of polymeric microbubbles targeted to prostate-specific membrane antigen as prototype of novel ultrasound contrast agents.," *Mol. Pharm.*, vol. 8, no. 3, pp. 748–757, Jun. 2011.
- [329] J. K. Tsuruta, N. Klauber-DeMore, J. Streeter, J. Samples, C. Patterson, R. J. Mumper, D. Ketelsen, and P. Dayton, "Ultrasound molecular imaging of secreted frizzled related protein-2 expression in murine angiosarcoma.," *PLoS ONE*, vol. 9, no. 1, p. e86642, 2014.
- [330] A. M. Lutz, S. V. Bachawal, C. W. Drescher, M. A. Pysz, J. K. Willmann, and S. S. Gambhir, "Ultrasound molecular imaging in a human CD276 expression-modulated murine ovarian cancer model.," *Clin. Cancer Res.*, vol. 20, no. 5, pp. 1313–1322, Mar. 2014.
- [331] K. Foygel, H. Wang, S. Machtaler, A. M. Lutz, R. Chen, M. Pysz, A. W. Lowe, L. Tian, T. Carrigan, T. A. Brentnall, and J. K. Willmann, "Detection of pancreatic ductal adenocarcinoma in mice by ultrasound imaging of thymocyte differentiation antigen 1.," *Gastroenterology*, vol. 145, no. 4, pp. 885–894.e3, Oct. 2013.
- [332] J. A. Knowles, C. H. Heath, R. Saini, H. Umphrey, J. Warram, K. Hoyt, and E. L. Rosenthal, "Molecular targeting of ultrasonographic contrast agent for detection of head and neck squamous cell carcinoma.," *Arch. Otolaryngol. Head Neck Surg.*, vol. 138, no. 7, pp. 662–668, Jul. 2012.
- [333] G. Koopman, C. P. Reutelingsperger, G. A. Kuijten, R. M. Keehnen, S. T. Pals, and M. H. van Oers, "Annexin V for flow cytometric detection of phosphatidylserine expression on B cells undergoing apoptosis.," *Blood*, vol. 84, no. 5, pp. 1415–1420, Sep. 1994.
- [334] J. M. Warram, A. G. Sorace, R. Saini, H. R. Umphrey, K. R. Zinn, and K. Hoyt, "A triple-targeted ultrasound contrast agent provides improved localization to tumor vasculature.," *J Ultrasound Med*, vol. 30, no. 7, pp. 921–931, Jul. 2011.
- [335] K. Soetanto and H. Watarai, "Development of Magnetic Microbubbles for Drug Delivery System (DDS).," *Jpn. J. Appl. Phys.*, vol. 39, no. 5, pp. 3230–3232, May 2000.
- [336] E. Stride, C. Porter, A. G. Prieto, and Q. Pankhurst, "Enhancement of microbubble mediated gene delivery by simultaneous exposure to ultrasonic and magnetic fields.," *Ultrasound Med Biol*, vol. 35,

# Bibliography

- no. 5, pp. 861–868, May 2009.
- [336] K. Soetanto and H. Watarai, “Ferromagnetic ultrasound microbubbles contrast agent,” *IEMBS-03*, vol. 2, pp. 1226–1229 Vol.2, 2003.
- [337] J. Owen, Q. Pankhurst, and E. Stride, “Magnetic targeting and ultrasound mediated drug delivery: benefits, limitations and combination.,” *Int J Hyperthermia*, vol. 28, no. 4, pp. 362–373, 2012.
- [338] G. R. Torr, “The acoustic radiation force,” *American Journal of Physics*, vol. 52, no. 5, pp. 402–408, May 1984.
- [339] M. A. Borden, M. R. Sarantos, S. M. Stieger, S. I. Simon, K. W. Ferrara, and P. A. Dayton, “Ultrasound radiation force modulates ligand availability on targeted contrast agents.,” *Mol Imaging*, vol. 5, no. 3, pp. 139–147, Jul. 2006.
- [340] M. A. Borden, J. E. Streeter, S. R. Sirsi, and P. A. Dayton, “In vivo demonstration of cancer molecular imaging with ultrasound radiation force and buried-ligand microbubbles.,” *Mol Imaging*, vol. 12, no. 6, pp. 357–363, Sep. 2013.
- [341] S. Wang, J. A. Hossack, A. L. Klibanov, and F. W. Mauldin, “Binding dynamics of targeted microbubbles in response to modulated acoustic radiation force.,” *Phys Med Biol*, vol. 59, no. 2, pp. 465–484, Jan. 2014.
- [342] T. J. A. Kokhuis, I. Skachkov, B. A. Naaijken, L. J. M. Juffermans, O. Kamp, K. Kooiman, A. F. W. van der Steen, M. Versluis, and N. de Jong, “Intravital microscopy of localized stem cell delivery using microbubbles and acoustic radiation force.,” *Biotechnol. Bioeng.*, vol. 112, no. 1, pp. 220–227, Jan. 2015.
- [343] D. H. Kim, A. L. Klibanov, and D. Needham, “The influence of tiered layers of surface-grafted poly (ethylene glycol) on receptor-ligand-mediated adhesion between phospholipid monolayer-stabilized ...,” *Langmuir*, 2000.
- [344] V. Sboros, E. Glynos, J. A. Ross, C. M. Moran, S. D. Pye, M. Butler, W. N. McDicken, S. B. Brown, and V. Koutsos, “Probing microbubble targeting with atomic force microscopy.,” *Colloids Surf B Biointerfaces*, vol. 80, no. 1, pp. 12–17, Oct. 2010.
- [345] A. M. Takalkar, A. L. Klibanov, J. J. Rychak, J. R. Lindner, and K. Ley, “Binding and detachment dynamics of microbubbles targeted to P-selectin under controlled shear flow.,” *J Control Release*, vol. 96, no. 3, pp. 473–482, May 2004.
- [346] K. Chetty, E. Stride, C. A. Sennoga, J. V. Hajnal, and R. J. Eckersley, “High-speed optical observations and simulation results of SonoVue microbubbles at low-pressure insonation.,” *IEEE Trans Ultrason Ferroelectr Freq Control*, vol. 55, no. 6, pp. 1333–1342, 2008.
- [347] B. L. Helfield and D. E. Goertz, “Nonlinear resonance behavior and linear shell estimates for Definity™ and MicroMarker™ assessed with acoustic microbubble spectroscopy.,” *The Journal of the Acoustical Society of America*, vol. 133, no. 2, pp. 1158–1168, Feb. 2013.
- [348] J. E. McKendry, C. A. Grant, B. R. G. Johnson, P. L. Coletta, J. A. Evans, and S. D. Evans, “Force spectroscopy of streptavidin conjugated lipid coated microbubbles,” *Bubble Science, Engineering & Technology*, vol. 2, no. 2, pp. 48–54, Jul. 2013.
- [349] R. H. Abou-Saleh, S. A. Peyman, K. Critchley, S. D. Evans, and N. H. Thomson, “Nanomechanics of lipid encapsulated microbubbles with functional coatings.,” *Langmuir*, vol. 29, no. 12, pp. 4096–4103, Mar. 2013.
- [350] S. Dieluweit, A. Csizsár, W. Rubner, J. Fleischhauer, S. Houben, and R. Merkel, “Mechanical properties of bare and protein-coated giant unilamellar phospholipid vesicles. A comparative study of micropipet aspiration and atomic force microscopy.,” *Langmuir*, vol. 26, no. 13, pp. 11041–11049, Jul. 2010.
- [351] S. A. Darst, M. Ahlers, P. H. Meller, E. W. Kubalek, R. Blankenburg, H. O. Ribi, H. Ringsdorf, and R. D. Kornberg, “Two-dimensional crystals of streptavidin on biotinylated lipid layers and their interactions with biotinylated macromolecules.,” *Biophys. J.*, vol. 59, no. 2, pp. 387–396, Feb. 1991.
- [352] M. A. Borden, D. E. Kruse, C. F. Caskey, S. Zhao, P. A. Dayton, and K. W. Ferrara, “Influence of lipid shell physicochemical properties on ultrasound-induced microbubble destruction.,” *Ultrasonics, Ferroelectrics, and Frequency Control, IEEE Transactions on*, vol. 52, no. 11, pp. 1992–2002, Nov. 2005.
- [353] Thermo Fisher Scientific, “Proteins and Amino Acids,” [www.thermofisher.com](http://www.thermofisher.com). [Online]. Available: <http://www.thermofisher.com/ru/ru/home/references/ambion-tech-support/rna-tools-and-calculators/proteins-and-amino-acids.html>. [Accessed: 20-Sep-2015].
- [354] S. Zhao, K. W. Ferrara, and P. A. Dayton, “Asymmetric oscillation of adherent targeted ultrasound contrast agents.,” *Appl Phys Lett*, vol. 87, no. 13, pp. 1341031–1341033, Sep. 2005.
- [355] S. Zhao, D. E. Kruse, K. W. Ferrara, and P. A. Dayton, “Acoustic response from adherent targeted contrast agents.,” *The Journal of the Acoustical Society of America*, vol. 120, no. 6, pp. EL63–9, Dec.



## Bibliography

- 2006.
- [356] J. Casey, C. Sennoga, H. Mulvana, J. V. Hajnal, M.-X. Tang, and R. J. Eckersley, "Single bubble acoustic characterization and stability measurement of adherent microbubbles.," *Ultrasound Med Biol*, vol. 39, no. 5, pp. 903–914, May 2013.
- [357] B. L. Helfield, E. Chérin, F. S. Foster, and D. E. Goertz, "The effect of binding on the subharmonic emissions from individual lipid-encapsulated microbubbles at transmit frequencies of 11 and 25 MHz.," *Ultrasound Med Biol*, vol. 39, no. 2, pp. 345–359, Feb. 2013.
- [358] B. J. Schmidt, I. Sousa, A. A. van Beek, and M. R. Böhmer, "Adhesion and ultrasound-induced delivery from monodisperse microbubbles in a parallel plate flow cell.," *J Control Release*, vol. 131, no. 1, pp. 19–26, Oct. 2008.
- [359] B. Cerroni, E. Chiessi, S. Margheritelli, L. Oddo, and G. Paradossi, "Polymer shelled microparticles for a targeted doxorubicin delivery in cancer therapy.," *Biomacromolecules*, vol. 12, no. 3, pp. 593–601, Mar. 2011.
- [360] D. Grishenkov, L. Kari, L.-K. Brodin, T. B. Brismar, and G. Paradossi, "In vitro contrast-enhanced ultrasound measurements of capillary microcirculation: comparison between polymer- and phospholipid-shelled microbubbles.," *Ultrasonics*, vol. 51, no. 1, pp. 40–48, Jan. 2011.
- [361] N. de Jong, A. Bouakaz, and P. Frinking, "Basic acoustic properties of microbubbles.," *Echocardiography*, vol. 19, no. 3, pp. 229–240, Apr. 2002.
- [362] A. Eller and H. G. Flynn, "Generation of Subharmonics of Order One-Half by Bubbles in a Sound Field.," *The Journal of the Acoustical Society of America*, vol. 46, no. 3, pp. 722–727, Sep. 1969.
- [363] A. Needles, D. E. Goertz, R. Karshafian, E. Cherin, A. S. Brown, P. N. Burns, and F. S. Foster, "High-frequency subharmonic pulsed-wave Doppler and color flow imaging of microbubble contrast agents.," *Ultrasound Med Biol*, vol. 34, no. 7, pp. 1139–1151, Jul. 2008.
- [364] C.-Y. Wu, J. Tsao, and Y.-H. Chou, "An ultrasonic microbubble semi-intermodulated imaging technique.," *Ultrasound Med Biol*, vol. 31, no. 9, pp. 1199–1210, Sep. 2005.
- [365] C. X. Deng, F. L. Lizzi, A. Kalisz, A. Rosado, R. H. Silverman, and D. J. Coleman, "Study of ultrasonic contrast agents using a dual-frequency band technique.," *Ultrasound Med Biol*, vol. 26, no. 5, pp. 819–831, Jun. 2000.
- [366] W. T. Shi and F. Forsberg, "Ultrasonic characterization of the nonlinear properties of contrast microbubbles.," *Ultrasound Med Biol*, vol. 26, no. 1, pp. 93–104, Jan. 2000.
- [367] S. Chen, R. Kinnick, J. F. Greenleaf, and M. Fatemi, "Difference frequency and its harmonic emitted by microbubbles under dual frequency excitation.," *Ultrasonics*, vol. 44, pp. e123–6, Dec. 2006.
- [368] P. N. Burns, J. E. Powers, D. H. Simpson, A. Brezina, A. Kolin, C. T. Chin, V. Uhlendorf, and T. Fritzsche, *Harmonic power mode Doppler using microbubble contrast agents: an improved method for small vessel flow imaging*, vol. 3. IEEE, 1994, pp. 1547–1550 vol.3.
- [369] N. de Jong, P. J. Frinking, A. Bouakaz, and F. J. ten Cate, "Detection procedures of ultrasound contrast agents.," *Ultrasonics*, vol. 38, no. 1, pp. 87–92, Mar. 2000.
- [370] C. X. Deng and F. L. Lizzi, "A review of physical phenomena associated with ultrasonic contrast agents and illustrative clinical applications.," *Ultrasound Med Biol*, vol. 28, no. 3, pp. 277–286, Mar. 2002.
- [371] F. S. Foster, J. Hossack, and S. L. Adamson, "Micro-ultrasound for preclinical imaging.," *Interface Focus*, vol. 1, no. 4, pp. 576–601, Aug. 2011.
- [372] A. Lyshchik, A. C. Fleischer, J. Huamani, D. E. Hallahan, M. Brissova, and J. C. Gore, "Molecular imaging of vascular endothelial growth factor receptor 2 expression using targeted contrast-enhanced high-frequency ultrasonography.," *J Ultrasound Med*, vol. 26, no. 11, pp. 1575–1586, Nov. 2007.
- [373] J. J. Rychak, J. Graba, A. M. Y. Cheung, B. S. Mystry, J. R. Lindner, R. S. Kerbel, and F. S. Foster, "Microultrasound molecular imaging of vascular endothelial growth factor receptor 2 in a mouse model of tumor angiogenesis.," *Mol Imaging*, vol. 6, no. 5, pp. 289–296, Sep. 2007.
- [374] J. K. Willmann, R. Paulmurugan, K. Chen, O. Gheysens, M. Rodriguez-Porcel, A. M. Lutz, I. Y. Chen, X. Chen, and S. S. Gambhir, "US imaging of tumor angiogenesis with microbubbles targeted to vascular endothelial growth factor receptor type 2 in mice.," *Radiology*, vol. 246, no. 2, pp. 508–518, Feb. 2008.
- [375] C. M. Moran, R. J. Watson, K. A. A. Fox, and W. N. McDicken, "In vitro acoustic characterisation of four intravenous ultrasonic contrast agents at 30 MHz.," *Ultrasound Med Biol*, vol. 28, no. 6, pp. 785–791, Jun. 2002.
- [376] M.-X. Tang, N. Kamiyama, and R. J. Eckersley, "Effects of nonlinear propagation in ultrasound contrast agent imaging.," *Ultrasound Med Biol*, vol. 36, no. 3, pp. 459–466, Mar. 2010.
- [377] G. Renaud, J. G. Bosch, N. de Jong, A. F. W. van der Steen, V. Shamdassani, and R. Entekin, "Counter-propagation interaction for contrast-enhanced ultrasound imaging.," *2012 IEEE*

## Bibliography

- International Ultrasonics Symposium*, pp. 1–4, 2012.
- [378] H. Yu, H.-J. Jang, T. K. Kim, K. Khalili, R. Williams, G. Lueck, J. Hudson, and P. N. Burns, “Pseudoenhancement within the local ablation zone of hepatic tumors due to a nonlinear artifact on contrast-enhanced ultrasound,” *AJR Am J Roentgenol*, vol. 194, no. 3, pp. 653–659, Mar. 2010.
  - [379] A. Thapar, J. Shalhoub, M. Averkiou, C. Mannaris, A. H. Davies, and E. L. S. Leen, “Dose-dependent artifact in the far wall of the carotid artery at dynamic contrast-enhanced US,” *Radiology*, vol. 262, no. 2, pp. 672–679, Feb. 2012.
  - [380] R. Hansen, B. Angelsen, P. Burns, A. Bouakaz, J. Borsboom, and M. Versluis, “Radial modulation imaging. 10th European Symp Ultrasound Contrast Imaging,” presented at the 10th European Symposium Ultrasound Contrast Imaging, Rotterdam, The Netherlands, 2005.
  - [381] J. Jiménez-Fernández, “Nonlinear response to ultrasound of encapsulated microbubbles,” *Ultrasonics*, vol. 52, no. 6, pp. 784–793, Aug. 2012.
  - [382] J. Park, X. Li, Q. Zhou, and K. K. Shung, “Combined chirp coded tissue harmonic and fundamental ultrasound imaging for intravascular ultrasound: 20–60 MHz phantom and ex vivo results,” *Ultrasonics*, vol. 53, no. 2, pp. 369–376, Feb. 2013.
  - [383] C.-C. Shen and C.-H. Lin, “Chirp-encoded excitation for dual-frequency ultrasound tissue harmonic imaging,” *IEEE Trans Ultrason Ferroelectr Freq Control*, vol. 59, no. 11, pp. 2420–2430, Nov. 2012.
  - [384] J. Park, Y. Huang, R. Chen, J. Lee, T. M. Cummins, Q. Zhou, C.-L. Lien, and K. K. Shung, “Pulse inversion chirp coded tissue harmonic imaging (PI-CTHI) of Zebrafish heart using high frame rate ultrasound biomicroscopy,” *Ann Biomed Eng*, vol. 41, no. 1, pp. 41–52, Jan. 2013.
  - [385] A. Novell, C. A. Sennoga, J. M. Escoffre, J. Chaline, and A. Bouakaz, “Evaluation of chirp reversal power modulation sequence for contrast agent imaging,” *Phys Med Biol*, vol. 59, no. 17, pp. 5101–5117, Sep. 2014.
  - [386] M. R. Sprague, E. Chérin, D. E. Goertz, and F. S. Foster, “Nonlinear emission from individual bound microbubbles at high frequencies,” *Ultrasound Med Biol*, vol. 36, no. 2, pp. 313–324, Feb. 2010.
  - [387] J. N. Tjøtta and S. Tjøtta, “An analytical model for the nearfield of a baffled piston transducer,” *The Journal of the Acoustical Society of America*, vol. 68, no. 1, pp. 334–339, Jul. 1980.
  - [388] P. M. Shankar, P. Dala Krishna, and V. L. Newhouse, “Advantages of subharmonic over second harmonic backscatter for contrast-to-tissue echo enhancement,” *Ultrasound Med Biol*, vol. 24, no. 3, pp. 395–399, Mar. 1998.
  - [389] D. Zhang, Y. Gong, X. Gong, Z. Liu, K. Tan, and H. Zheng, “Enhancement of subharmonic emission from encapsulated microbubbles by using a chirp excitation technique,” *Phys Med Biol*, vol. 52, no. 18, pp. 5531–5544, Sep. 2007.
  - [390] V. Daeichin, T. Faez, G. Renaud, J. G. Bosch, A. F. W. van der Steen, and N. de Jong, “Effect of self-demodulation on the subharmonic response of contrast agent microbubbles,” *Phys Med Biol*, vol. 57, no. 12, pp. 3675–3691, Jun. 2012.
  - [391] H. Zheng, O. Mukdadi, H. Kim, J. R. Hertzberg, and R. Shandas, “Advantages in using multifrequency excitation of contrast microbubbles for enhancing echo particle image velocimetry techniques: initial numerical studies using rectangular and triangular waves,” *Ultrasound Med Biol*, vol. 31, no. 1, pp. 99–108, Jan. 2005.
  - [392] E. Biagi, L. Breschi, E. Vannacci, and L. Masotti, “Subharmonic emissions from microbubbles: effect of the driving pulse shape,” *Ultrasonics, Ferroelectrics, and Frequency Control, IEEE Transactions on*, vol. 53, no. 11, pp. 2174–2182, Nov. 2006.
  - [393] L. Masotti, E. Biagi, L. Breschi, and E. Vannacci, “Study and Characterization of Subharmonic Emissions by Using Shaped Ultrasonic Driving Pulse,” in *Acoustical Imaging*, vol. 28, no. 33, Dordrecht: Springer Netherlands, 2007, pp. 307–315.
  - [394] D. Zhang, X. Xi, Z. Zhang, X. Gong, G. Chen, and J. Wu, “A dual-frequency excitation technique for enhancing the sub-harmonic emission from encapsulated microbubbles,” *Phys Med Biol*, vol. 54, no. 13, pp. 4257–4272, Jul. 2009.
  - [395] J. E. Streeter, R. Gessner, I. Miles, and P. A. Dayton, “Improving sensitivity in ultrasound molecular imaging by tailoring contrast agent size distribution: in vivo studies,” *Mol Imaging*, vol. 9, no. 2, pp. 87–95, Apr. 2010.
  - [396] S. Zhao, D. E. Kruse, K. W. Ferrara, and P. A. Dayton, “Selective imaging of adherent targeted ultrasound contrast agents,” *Phys Med Biol*, vol. 52, no. 8, pp. 2055–2072, Apr. 2007.
  - [397] X. Hu, H. Zheng, D. E. Kruse, P. Sutcliffe, D. N. Stephens, and K. W. Ferrara, “A sensitive TLRH targeted imaging technique for ultrasonic molecular imaging,” *IEEE Trans Ultrason Ferroelectr Freq Control*, vol. 57, no. 2, pp. 305–316, 2010.
  - [398] A. Needles, O. Couture, and F. S. Foster, “A method for differentiating targeted microbubbles in real time using subharmonic micro-ultrasound and interframe filtering,” *Ultrasound Med Biol*, vol. 35,



## Bibliography

- no. 9, pp. 1564–1573, Sep. 2009.
- [399] F. W. Mauldin, A. H. Dhanaliwala, A. V. Patil, and J. A. Hossack, “Real-time targeted molecular imaging using singular value spectra properties to isolate the adherent microbubble signal.,” *Phys Med Biol*, vol. 57, no. 16, pp. 5275–5293, Aug. 2012.
- [400] M. A. Pysz, S. S. Gambhir, and J. K. Willmann, “Molecular imaging: current status and emerging strategies.,” *Clin Radiol*, vol. 65, no. 7, pp. 500–516, Jul. 2010.
- [401] A. G. Sorace, R. Saini, M. Mahoney, and K. Hoyt, “Molecular ultrasound imaging using a targeted contrast agent for assessing early tumor response to antiangiogenic therapy.,” *J Ultrasound Med*, vol. 31, no. 10, pp. 1543–1550, Oct. 2012.
- [402] J. E. Streeter, R. C. Gessner, J. Tsuruta, S. Feingold, and P. A. Dayton, “Assessment of molecular imaging of angiogenesis with three-dimensional ultrasonography.,” *Mol Imaging*, vol. 10, no. 6, pp. 460–468, Dec. 2011.
- [403] S. M. Stieger, P. A. Dayton, M. A. Borden, C. F. Caskey, S. M. Griffey, E. R. Wisner, and K. W. Ferrara, “Imaging of angiogenesis using Cadence contrast pulse sequencing and targeted contrast agents.,” *Contrast Media Mol Imaging*, vol. 3, no. 1, pp. 9–18, Jan. 2008.
- [404] M. Piedra, A. Allroggen, and J. R. Lindner, “Molecular imaging with targeted contrast ultrasound.,” *Cerebrovasc. Dis.*, vol. 27, no. 2, pp. 66–74, 2009.
- [405] P. A. Dayton and J. J. Rychak, “Molecular ultrasound imaging using microbubble contrast agents.,” *Front. Biosci.*, vol. 12, pp. 5124–5142, 2007.
- [406] C. R. Anderson, X. Hu, H. Zhang, J. Tlaxca, A.-E. Declèves, R. Houghtaling, K. Sharma, M. Lawrence, K. W. Ferrara, and J. J. Rychak, “Ultrasound molecular imaging of tumor angiogenesis with an integrin targeted microbubble contrast agent.,” *Invest Radiol*, vol. 46, no. 4, pp. 215–224, Apr. 2011.
- [407] N. McDannold, Y. Zhang, and N. Vykhodtseva, “Blood-brain barrier disruption and vascular damage induced by ultrasound bursts combined with microbubbles can be influenced by choice of anesthesia protocol.,” *Ultrasound Med Biol*, vol. 37, no. 8, pp. 1259–1270, Aug. 2011.
- [408] M. A. Pysz, I. Guracar, L. Tian, and J. K. Willmann, “Fast microbubble dwell-time based ultrasonic molecular imaging approach for quantification and monitoring of angiogenesis in cancer.,” *Quant Imaging Med Surg*, vol. 2, no. 2, pp. 68–80, Jun. 2012.
- [409] V. Daeichin, Z. Akkus, A. Hoogi, J. G. Bosch, A. Needles, K. Kooiman, I. Skachkov, J. Sluimer, B. Janssen, M. J. A. P. Daemen, A. F. W. van der Steen, and N. de Jong, “Quantification of targeted microbubbles in contrast enhanced ultrasound,” *2013 IEEE International Ultrasonics Symposium (IUS)*, pp. 1825–1828, 2013.
- [410] H. Liu, X. Wang, K.-B. Tan, P. Liu, Z.-X. Zhuo, Z. Liu, X. Hua, Q.-Q. Zhuo, H.-M. Xia, and Y.-H. Gao, “Molecular imaging of vulnerable plaques in rabbits using contrast-enhanced ultrasound targeting to vascular endothelial growth factor receptor-2.,” *J Clin Ultrasound*, vol. 39, no. 2, pp. 83–90, Feb. 2011.
- [411] A. Hamilton, S.-L. Huang, D. Warnick, A. Stein, M. Rabbat, T. Madhav, B. Kane, A. Nagaraj, M. Klegerman, R. MacDonald, and D. McPherson, “Left ventricular thrombus enhancement after intravenous injection of echogenic immunoliposomes: studies in a new experimental model.,” *Circulation*, vol. 105, no. 23, pp. 2772–2778, Jun. 2002.
- [412] G. Korpanty, J. G. Carbon, P. A. Grayburn, J. B. Fleming, and R. A. Brekken, “Monitoring response to anticancer therapy by targeting microbubbles to tumor vasculature.,” *Clin. Cancer Res.*, vol. 13, no. 1, pp. 323–330, Jan. 2007.
- [413] N. Deshpande, Y. Ren, K. Foygel, J. Rosenberg, and J. K. Willmann, “Tumor angiogenic marker expression levels during tumor growth: longitudinal assessment with molecularly targeted microbubbles and US imaging.,” *Radiology*, vol. 258, no. 3, pp. 804–811, Mar. 2011.
- [414] D. B. Ellegala, H. Leong-Poi, J. E. Carpenter, A. L. Klibanov, S. Kaul, M. E. Shaffrey, J. Sklenar, and J. R. Lindner, “Imaging tumor angiogenesis with contrast ultrasound and microbubbles targeted to  $\alpha(v)\beta3$ .,” *Circulation*, vol. 108, no. 3, pp. 336–341, Jul. 2003.
- [415] A. Barua, A. Yellapa, J. M. Bahr, S. A. Machado, P. Bitterman, S. Basu, S. Sharma, and J. S. Abramowicz, “Enhancement of ovarian tumor detection with  $\alpha v \beta 3$  integrin-targeted ultrasound molecular imaging agent in laying hens: a preclinical model of spontaneous ovarian cancer.,” *Int. J. Gynecol. Cancer*, vol. 24, no. 1, pp. 19–28, Jan. 2014.
- [416] M. A. Kuliszewski, H. Fujii, C. Liao, A. H. Smith, A. Xie, J. R. Lindner, and H. Leong-Poi, “Molecular imaging of endothelial progenitor cell engraftment using contrast-enhanced ultrasound and targeted microbubbles.,” *Cardiovasc. Res.*, vol. 83, no. 4, pp. 653–662, Sep. 2009.
- [417] S. V. Bachawal, K. C. Jensen, A. M. Lutz, S. S. Gambhir, F. Tranquart, L. Tian, and J. K. Willmann, “Earlier detection of breast cancer with ultrasound molecular imaging in a transgenic mouse model.,”

- Cancer Res.*, vol. 73, no. 6, pp. 1689–1698, Mar. 2013.
- [418] C. Grouls, M. Hating, A. Rix, S. Pochon, W. Lederle, I. Tardy, C. K. Kuhl, C. Trautwein, F. Kiessling, and M. Palmowski, “Liver dysplasia: US molecular imaging with targeted contrast agent enables early assessment,” *Radiology*, vol. 267, no. 2, pp. 487–495, May 2013.
- [419] E. Khanicheh, M. Mitterhuber, L. Xu, S. P. Haeuselmann, G. M. Kuster, and B. A. Kaufmann, “Noninvasive ultrasound molecular imaging of the effect of statins on endothelial inflammatory phenotype in early atherosclerosis,” *PLoS ONE*, vol. 8, no. 3, p. e58761, 2013.
- [420] E. Khanicheh, Y. Qi, A. Xie, M. Mitterhuber, L. Xu, M. Mochizuki, Y. Daali, V. Jaquet, K.-H. Krause, Z. M. Ruggeri, G. M. Kuster, J. R. Lindner, and B. A. Kaufmann, “Molecular imaging reveals rapid reduction of endothelial activation in early atherosclerosis with apocynin independent of antioxidative properties,” *Arterioscler. Thromb. Vasc. Biol.*, vol. 33, no. 9, pp. 2187–2192, Sep. 2013.
- [421] M. A. Pysz, K. Foygel, J. Rosenberg, S. S. Gambhir, M. Schneider, and J. K. Willmann, “Antiangiogenic cancer therapy: monitoring with molecular US and a clinically translatable contrast agent (BR55),” *Radiology*, vol. 256, no. 2, pp. 519–527, Aug. 2010.
- [422] M. Baron Toaldo, V. Salvatore, S. Marinelli, C. Palamà, M. Milazzo, L. Croci, L. Venerandi, M. Cipone, L. Bolondi, and F. Piscaglia, “Use of VEGFR-2 targeted ultrasound contrast agent for the early evaluation of response to sorafenib in a mouse model of hepatocellular carcinoma,” *Mol Imaging Biol*, vol. 17, no. 1, pp. 29–37, Feb. 2015.
- [423] M. Palmowski, J. Huppert, G. Ladewig, P. Hauff, M. Reinhardt, M. M. Mueller, E. C. Woenne, J. W. Jenne, M. Maurer, G. W. Kauffmann, W. Semmler, and F. Kiessling, “Molecular profiling of angiogenesis with targeted ultrasound imaging: early assessment of antiangiogenic therapy effects,” *Mol. Cancer Ther.*, vol. 7, no. 1, pp. 101–109, Jan. 2008.
- [424] S. R. Sirsi, M. L. Flexman, F. Vlachos, J. Huang, S. L. Hernandez, H. K. Kim, T. B. Johung, J. W. Gander, A. R. Reichstein, B. S. Lampl, A. Wang, A. H. Hielscher, J. J. Kandel, D. J. Yamashiro, and M. A. Borden, “Contrast ultrasound imaging for identification of early responder tumor models to anti-angiogenic therapy,” *Ultrasound Med Biol*, vol. 38, no. 6, pp. 1019–1029, Jun. 2012.
- [425] J. E. Streeter, S. G. Herrera-Loeza, N. F. Neel, J. J. Yeh, and P. A. Dayton, “A comparative evaluation of ultrasound molecular imaging, perfusion imaging, and volume measurements in evaluating response to therapy in patient-derived xenografts,” *Technol. Cancer Res. Treat.*, vol. 12, no. 4, pp. 311–321, Aug. 2013.
- [426] T. Flisikowska, A. Kind, and A. Schnieke, “The new pig on the block: modelling cancer in pigs,” *Transgenic Res.*, vol. 22, no. 4, pp. 673–680, Aug. 2013.
- [427] H. Kim, G. L. Britton, T. Peng, C. K. Holland, D. D. McPherson, and S.-L. Huang, “Nitric oxide-loaded echogenic liposomes for treatment of vasospasm following subarachnoid hemorrhage,” *Int J Nanomedicine*, vol. 9, no. 1, pp. 155–165, 2014.
- [428] S. M. Chadderdon, J. T. Belcik, L. Bader, M. A. Kirigiti, D. M. Peters, P. Kievit, K. L. Grove, and J. R. Lindner, “Proinflammatory endothelial activation detected by molecular imaging in obese nonhuman primates coincides with onset of insulin resistance and progressively increases with duration of insulin resistance,” *Circulation*, vol. 129, no. 4, pp. 471–478, Jan. 2014.
- [429] J. E. Streeter and P. A. Dayton, “An in vivo evaluation of the effect of repeated administration and clearance of targeted contrast agents on molecular imaging signal enhancement,” *Theranostics*, vol. 3, no. 2, pp. 93–98, 2013.
- [430] J. Bzyl, M. Palmowski, A. Rix, S. Arns, J.-M. Hyvelin, S. Pochon, J. Ehling, S. Schradling, F. Kiessling, and W. Lederle, “The high angiogenic activity in very early breast cancer enables reliable imaging with VEGFR2-targeted microbubbles (BR55),” *Eur Radiol*, vol. 23, no. 2, pp. 468–475, Feb. 2013.
- [431] X. Hu, C. F. Caskey, L. M. Mahakian, D. E. Kruse, J. R. Beegle, A.-E. Declèves, J. J. Rychak, P. L. Sutcliffe, K. Sharma, and K. W. Ferrara, “In vivo validation and 3D visualization of broadband ultrasound molecular imaging,” *Am J Nucl Med Mol Imaging*, vol. 3, no. 4, pp. 336–349, 2013.
- [432] S. Bao, B. D. Thrall, and D. L. Miller, “Transfection of a reporter plasmid into cultured cells by sonoporation in vitro,” *Ultrasound Med Biol*, vol. 23, no. 6, pp. 953–959, 1997.
- [433] X. Hu, A. Kheirloomoom, L. M. Mahakian, J. R. Beegle, D. E. Kruse, K. S. Lam, and K. W. Ferrara, “Insonation of targeted microbubbles produces regions of reduced blood flow within tumor vasculature,” *Invest Radiol*, vol. 47, no. 7, pp. 398–405, Jul. 2012.
- [434] A. K. W. Wood, S. M. Schultz, W. M.-F. Lee, R. M. Bunte, and C. M. Sehgal, “Antivascular ultrasound therapy extends survival of mice with implanted melanomas,” *Ultrasound Med Biol*, vol. 36, no. 5, pp. 853–857, May 2010.
- [435] M. Rask-Andersen, J. Zhang, D. Fabbro, and H. B. Schiöth, “Advances in kinase targeting: current clinical use and clinical trials,” *Trends Pharmacol. Sci.*, vol. 35, no. 11, pp. 604–620, Nov. 2014.

## Bibliography

---

- [436] J. H. Hwang and L. A. Crum, "Current status of clinical high-intensity focused ultrasound.," *Conf Proc IEEE Eng Med Biol Soc*, vol. 2009, pp. 130–133, 2009.
- [437] L. Xiaoping and Z. Leizhen, "Advances of high intensity focused ultrasound (HIFU) for pancreatic cancer.," *Int J Hyperthermia*, vol. 29, no. 7, pp. 678–682, Nov. 2013.
- [438] Y. Zhou, Z. Wang, Y. Chen, H. Shen, Z. Luo, A. Li, Q. Wang, H. Ran, P. Li, W. Song, Z. Yang, H. Chen, Z. Wang, G. Lu, and Y. Zheng, "Microbubbles from gas-generating perfluorohexane nanoemulsions for targeted temperature-sensitive ultrasonography and synergistic HIFU ablation of tumors.," *Adv. Mater. Weinheim*, vol. 25, no. 30, pp. 4123–4130, Aug. 2013.
- [439] N. Sheikov, N. McDannold, S. Sharma, and K. Hynynen, "Effect of focused ultrasound applied with an ultrasound contrast agent on the tight junctional integrity of the brain microvascular endothelium.," *Ultrasound Med Biol*, vol. 34, no. 7, pp. 1093–1104, Jul. 2008.
- [440] W. J. Duncanson, L. R. Arriaga, W. L. Ung, J. A. Kopechek, T. M. Porter, and D. A. Weitz, "Microfluidic fabrication of perfluorohexane-shelled double emulsions for controlled loading and acoustic-triggered release of hydrophilic agents.," *Langmuir*, vol. 30, no. 46, pp. 13765–13770, Nov. 2014.
- [441] C.-Y. Lin and W. G. Pitt, "Acoustic droplet vaporization in biology and medicine.," *Biomed Res Int*, vol. 2013, no. 10, pp. 404361–13, 2013.
- [442] T. Thim, "Human-like atherosclerosis in minipigs: a new model for detection and treatment of vulnerable plaques.," *Dan Med Bull*, vol. 57, no. 7, p. B4161, Jul. 2010.
- [443] G. Renaud, J. G. Bosch, A. F. W. van der Steen, and N. de Jong, "Increasing specificity of contrast-enhanced ultrasound imaging using the interaction of quasi counter-propagating wavefronts: a proof of concept.," *IEEE Trans Ultrason Ferroelectr Freq Control*, vol. 62, no. 10, pp. 1768–1778, Oct. 2015.
- [444] E. L. Ritman and A. Lerman, "The dynamic vasa vasorum.," *Cardiovasc. Res.*, vol. 75, no. 4, pp. 649–658, Sep. 2007.
- [445] C. R. Anderson, J. J. Rychak, M. Backer, J. Backer, K. Ley, and A. L. Klibanov, "scVEGF microbubble ultrasound contrast agents: a novel probe for ultrasound molecular imaging of tumor angiogenesis.," *Invest Radiol*, vol. 45, no. 10, pp. 579–585, Oct. 2010.

## Abbreviations and symbols

|                                |  |
|--------------------------------|--|
| 2D                             | 2-Dimensional  |
| 3D                             | 3-Dimensional  |
| $\alpha$                       | coefficient that relates the amount of PI molecules to the fluorescence intensity of PI-RNA and PI-DNA |
| $\beta$                        | pore resealing coefficient   |
| $\sigma$                       | surface tension  |
| $\chi$                         | elasticity   |
| Ab                             | antibody   |
| AFM                            | atomic force microscopy  |
| bpm                            | Beats per minute   |
| BW                             | Bandwidth  |
| C <sub>4</sub> F <sub>10</sub> | Perfluorobutane  |
| C <sub>0</sub>                 | extracellular PI concentration   |
| CAM                            | chorioallantoic membrane   |
| CMVE                           | cardiac micovascular endothelium   |
| CT                             | computed tomography  |
| CTR                            | contrast to tissue ratio   |
| D                              | diffusion coefficient  |
| Da                             | Dalton   |
| dB                             | decibel  |
| dB                             | Decibel  |
| DMEM                           | Dulbecco's modified Eagle's medium   |
| DMSO                           | Dimethylsulfoxide  |
| DNA                            | Deoxyribonucleic acid  |
| DPPC                           | 1,2-dipalmitoyl- <i>sn</i> -glycero-3-phosphocholine / 16:0 phosphocholine                             |

## Abbreviations and symbols

---

|                |   |
|----------------|---|
| DPPE           | 1,2-dipalmitoyl-sn-glycero-3-phosphoethanolamine / 16:0 phosphoethanolamine             |
| DSPC           | 1,2-distearoyl- <i>sn</i> -glycero-3-phosphocholine / 18:0 phosphocholine               |
| DSPE           | 1,2-distearoyl-sn-glycero-3-phosphoethanolamine / 18:0 phosphoethanolamine              |
| DT             | diameter-time   |
| EC             | endothelial cell  |
| EDTA           | Ethylenediaminetetraacetic acid   |
| EGFR           | epidermal growth factor receptor  |
| EM             | electron microscopy   |
| f              | frequency (Herz)  |
| f <sub>c</sub> | center frequency (Herz)   |
| f <sub>H</sub> | harmonic frequency (Herz)   |
| f <sub>T</sub> | transmit frequency (Herz)   |
| F(t)           | fluorescence intensity as a function of time  |
| FOV            | field of view   |
| GP             | glycoprotein  |
| HIFU           | high intensity focused ultrasound   |
| HUVEC          | Human umbilical vein endothelial cell   |
| Hz             | Herz  |
| ICAM-1         | Intercellular adhesion molecule 1 / CD54  |
| IVUS           | intravascular ultrasound  |
| k <sub>s</sub> | viscosity   |
| M              | Molarity  |
| MB             | microbubble/microbubbles  |
| MI             | Mechanical index; $MI = \frac{P_-}{\sqrt{f}}$ , with P <sub>-</sub> in MPa and f in MHz |

## ***Abbreviations and symbols***

---

|                |  |
|----------------|--|
| MIP            | Maximum intensity projection                         |
| MMP            | matrix metalloproteinase-2                           |
| MRI            | magnetic resonance imaging                           |
| mRNA           | messenger ribonucleic acid                           |
| MW             | Molecular weight                                     |
| ntMB           | non-targeted microbubble / microbubbles              |
| P <sub>A</sub> | Peak negative acoustic pressure                      |
| Pa             | Pascal   |
| PAA            | poly(acrylic acid)                                   |
| PBS            | Phosphate-buffered saline                            |
| PC             | Principal Component                                  |
| PCA            | Principal Component Analysis                         |
| PECAM-1        | Platelet/endothelial cell adhesion molecule-1 / CD31 |
| PEG-40         | polyoxyethylene-(40)                                 |
| PEG(2000)      | Polyethylene glycol with molecular weight of 2000    |
| PET            | positron emission tomography                         |
| PI             | Propidium iodide                                     |
| PSMA           | prostate-specific membrane antigen                   |
| PS             | phosphatidylserine                                   |
| PVA            | Poly-vinylalcohol                                    |
| PVDF           | polyvinylidene difluoride                            |
| R              | radius (m)   |
| $r_0$          | intial radius of the pore                            |
| $R_0$          | resting radius (m)                                   |
| RF             | radio frequency                                      |
| RNA            | Ribonucleic acid                                     |
| rpm            | Rotations per minute                                 |

## ***Abbreviations and symbols***

---

|              |  |
|--------------|--|
| SD           | Standard error   |
| SFRP2        | secreted frizzled related protein 2                        |
| SPECT        | single-photon emission computed tomography                 |
| SPIO         | superparamagnetic iron oxide                               |
| t            | time   |
| T            | Temperature  |
| T2R          | transmit at twice resonance                                |
| TACS         | thrombin aptamer crosslinking strand                       |
| tMB          | targeted microbubble/microbubbles                          |
| tUCA         | targeted ultrasound contrast agent                         |
| Thy1         | thymocyte differentiation antigen 1 (CD90)                 |
| TNF $\alpha$ | tumor necrosis factor $\alpha$                             |
| TR           | transmit at resonance                                      |
| U            | Unit   |
| UCA          | Ultrasound contrast agent                                  |
| UMI          | Ultrasound molecular imaging                               |
| UMMD         | ultrasound and microbubble mediated drug delivery          |
| US           | Ultrasound   |
| UtMMD        | ultrasound and targeted microbubble mediated drug delivery |
| VEGF         | Vascular endothelial growth factor                         |
| VEGFR2       | Vascular endothelial growth factor receptor 2              |
| VCAM-1       | Vascular cell adhesion molecule 1                          |
| v/v          | Volume per volume  |
| w/w          | Weight per weight  |



## Curriculum Vitae



**Ilya Skachkov** was born on July 3, 1984, in Gukovo, Rostov region, Russia. He studied at Faculty of Biology at Lomonosov Moscow State University in Russia and obtained his degree from the Department of Cell Biology and Histology in 2009. From 2009 to 2010, he was working in Institute for Biomedical Problems studying molecular pathways involved in muscle degeneration in response to hypogravity. In 2010 he joined the Department of Biomedical Engineering of the Thorax Centre, Erasmus MC as a Ph.D. student where he works till present. His

main topics are ultrasound contrast agents for molecular imaging and drug delivery and revealing mechanisms of sonoporation.



## Acknowledgements

Writing this afterword, probably, is the most difficult part for me but also very pleasant. Starting my PhD was starting a long journey not only figuratively but also literally. It started in May 2010 when I took my train from Moscow to Amsterdam (what a strange decision to take 37 hours train instead of 3 hours flight). And it also took a bit longer then I expected. I was at the border one day ahead then my visa started and had to spend one day in Brest, which was quite nice stop though. My first day at BME department started with the tour given me by Ying. Now I want to repeat the same tour to remember every member of the BME family who became almost like a real family for me for this five years.

**Ton's office.** I am very grateful to Ton not only because of giving me this job, but also for giving me the final push to complete my PhD. I can not imagine anyone else governing this lab, not only because of you are a great researcher and manager but also because of the very warm atmosphere inside the group. The atmosphere of co-operation and friendship instead of competition and just neutral colleague relationships.

**Nico and Hans office.** Nico, thank you very much for being my promotor. Your influence to me is much deeper than you probably think. I appreciate you as a great scientist with a very broad interests and purview and also as a very generous person. I was always amazed of your ability to find the essential point in any text (even in pure biological) and to distill the exact words to describe it. Hans, you will always be for me an example of real scientist, who did not loose passion to the real experimental work even after becoming a professor. I never heard as many words of thanks from the students to their supervisors as I heard from your students addressed to you.

**Secretary office.** Mieke, you were the first person who I contacted with. I would not tell you how important you are for the lab (you have been told it so many times). I would like to tell you how important you were for me, especially in the beginning of my PhD. Thank you for all your help! Gracia, thank you for being so helpful, generous and nice person to talk, who can empathize and give a good advice. I will always remember your mother in law's chocolate cake.

**First trench.** Zeynettine, thank you for being my friend and fellow in my travels and nights out. I will always remember our talks about ladies and career opportunities. Verya, you are the most diverse person I know. I hope your dream to die in the mountain will not come true at least in coming fifty years. Guillaume, you are a great researcher but I will always remember you as someone who introduced me to a very special person in my life.


**Robert's trench.** Although, officially this trench belongs to electronic technicians and actually to everyone who has to or more likely likes to glue, solder or crafting, it will always be a Robert's trench for me. Thank you Robert for being helpful in all means! You are the person who you can talk for hours about almost any subject and will definitely discover something new for yourself. I like your jokes, even when some ladies did not like them, they were always funny and smart. And thank you for being my paranimph at that day! Jan, it is

## Acknowledgements

---

difficult to find someone being so enthusiastic to come to work even after retirement. I will always remember you as a guy who you can nicely chat and who is always willing to help.

**Tom and Ying's trench.** Tom and Ying, my friends, you will be always in my heart. The amount of time we spent together can not be counted. Not only in the lab, but also traveling and visiting each other. The amount of tea we drink together with Ying could easily fill a pond in Het Park, and the beer bottles we complete together with Tom should be enough to build a nice house. Thank you for being in my life and supporting me during all this year. And thank you Tom for inviting me to be your paranimph, now I am paying you back. Jason, I know you as a very organized and neat guy, this are some qualities I always want to have myself. You also became a very special person to my good friend. Good luck in everything and take care of her! Tom van Rooij and Kirby, thank you for that help you gave me for making this thesis ready. Tom, without your help it probably would not be possible to make it in time.

**Klazina's trench.** Klazina, you are my supervisor and my mentor. The amount of help you gave to me was enormous. You are a great researcher and organizer with the brilliant future. These qualities of you make any work with you very easy and pleasant. You are also the person who always encourage me and give me the example how to overcome all possible difficulties. I call this trench Klazina's, but it was also mine trench. I spent all the years of my PhD sitting there and being surrounded by many very nice people. All of them will stay deep in my memories and heart. Telli, you are great example of a strong and independent woman in science. I was always happy to share with not only the office but also meal, tee, cookies and my hospitality. Enrico, although you were not officially sitting in that spot, you were always welcome to stay there. It was a pleasure to have chat with you about everything, but especially about  , you was my only mac buddy in the lab. Jacopo, thank you for being my friend and participating in all kind of activities you been suggested to take part. I am glad not only being roommates with you but also sharing our defense. Congratulazioni Dr. Viti! Deep, you are the most recent of my friends but it does not make you less important. I will always remember our talks about science and history, about philosophy and politics, and all kind of things. Thank you for introducing Indian cuisine to me and me to Indian cuisine.

**Alex and Gerard's trench.** I would like to thank Alex for being my friend and roommate and teaching me how to be a German. I hope I picked up some good habits because of you. Gerard, you are very nice and friendly guy always willing to help, with the tons of stories about traveling and diving. Guys, I will remember your trench as the most joyful one. I think everyone on our floor could hear when you were laughing.

**Rik and Hans Verdoes's trench.** Rik, you are a great researcher and a very nice guy to talk with. I am really happy to know you. Hans, although, other people always say thanks to you with the computer help, I am very grateful to you for letting me play with the computers myself and providing all the assistance to make this process very pleasant.

**Mouse lab.** Kim and Leah, although this is not really your spot, this is the place we always meet. Kim, you are very nice and joyful person. I always enjoy chatting with you and a bit gossiping. Leah, you a very nice girl and a great cook. I believe, everyone in the department enjoy your food every time you bring something.

## Acknowledgements

---

**Biomechanics group.** Guys, you are great! I really enjoy every time we hang out. Kim and Lambert, you are a very nice example how two researchers could not only share the bench but also create a family. Ruoyu, thank you for organizing so many very nice days and nights out, it was always a lot of fun.

**Fritz's trench.** This place looks like a magic forest full of different machines with the Great Magician busy of inventing new magic tricks. Being serious, Fritz is a very nice guy to whom you can address any question about programing and also chat with about any news in electronics. This trench is also remarkable for me because of my only Russian colleague and friend Mike (Михаил). I can not count how many hours we spend together with Mike drinking coffee and chatting about the life. Thank you for your support and for helping me to get around in the Netherlands.

**Gijs's group.** Gijs, you are a really smart guy and a great researcher with the brilliant future in academia. I appreciate all your comments you made during my BME presentations. Muthu, you a great Indian guy who knows how to enjoy the life, it is pity we did not spend more time together. Thank you for teaching me how to cook Indian food together with Deep. Tianshi and Cherry you are another great example of the successful scientific couple. Good luck in your future life! Thank you hanging out together! Jovana, from my first impression (without even talking to you) I did not like you. I was so wrong!!! You are great person. Many thanks to you and Enrico for making my last year in the Netherlands so joyful. I would also like to thank Sophinese for changing my opinion about women in engineering. I know many brilliant examples of women in engineering, but I never expect that they can and would like to do soldering. Min, I will always remember our cooking and filming experience. I always think that Russian dumplings are the best, but you shifted my taste to Chinese ones. You are also the most charming Asian Milla Jovovich I ever directed.

Krista, thank you very much for being my friend and helping me with many things. I would also like to thank you for bringing me two new friends: Harriet and Pavlov. I will never forget our long walks. David, you are a really great researcher who follows his dream. And a very nice host. Thank you for your hospitality, while I was visiting Paris. It was a great time. I wish you good luck in your future path! I was really happy to meet you.

**The workshop.** Michiel and Geert without you help not only my PhD, but almost everyone's in the lab research would be lame. You are really great!

**Twente University.** I would also like to say many words of thanks to our Twente colleagues and friends. Michel Versluis, you are a great example of a very successful scientist who's social live is even more rich than his scientific career. Guillaume, I will always keep warm memories not only about our partying but also about our work together. I would like to thank my friend Alex (Olexander Shpak) for very nice and valuable talks about almost every topic. You are a great example of the person who fellows his goal disputing all the difficulties. You and your wife Kseniya made me to change my opinion on a lot of things.

That was my flashback journey to BME family, where I had honor to work for more than four years. Now it is over and I continue with my other friends and my real family.

## **Acknowledgements**

---

### **Moscow**

I would like to say a lot of words of thanks to my friends Lubov and Sergey, who gave me a lot of help and support at very difficult period of my life before I came to the Netherlands.

I would like to thank my good friend Artem (Артём) for visiting and supporting me during these years. These memories are unforgettable and could not be faded away.

And especially I would like to thank my girlfriend Natalia for supporting me during her visits and all the time we were not together. It was thousands of kilometers between us, but I always felt you were very near, helping and supporting me. Thank you for making this relationship to work out. And many thanks for all the valuable discussions and your help in preparations of this book.

And finally I would like to add some words in Russian to my friends and my beloved parents: Svetlana and Vladimir, without whom I would not become a person who I am. Thank you very much for all the love, care and support you gave and continuing to give me.

Дорогой Вовка, спасибо тебе за ту роль которую ты сыграл и продолжаешь играть в моей жизни!

Дорогие мои родители, спасибо вам огромное, за вашу поддержку, за то как вы старались, чтобы из меня вышел толк, за бессонные ночи когда я болел и за часовые разговоры по скайпу, когда я был далеко. Вы всегда поддерживали меня во всех моих начинаниях, к моей тяге к науке. Вы дали мне все, что только могли, чтобы сделать меня счастливым, и я безмерно счастлив, что у меня есть такие родители!

# Publications

## Papers in preparation

1. **I. Skachkov**, Y. Luan, S. van Tiel, A. F. W. van der Steen, M. Bernsen, N. de Jong, K. Kooiman, "Targeted microbubbles and ultrasound improves SPIO cell labeling at low acoustical pressure," – in preparation.
2. **I. Skachkov**, T. J. A. Kokhuis, Y. Luan, A. F. W. van der Steen, N. de Jong, K. Kooiman, "Cell membrane permeability dynamics after sonoporation by targeted and non-targeted microbubbles," – in preparation
3. **I. Skachkov**, V. Daeichin, A. F. W. van der Steen, J. Bosch, N. de Jong, K. Kooiman, "Molecular imaging of VEGF receptor expression in fast and slow growing tumours" – in preparation.

## Peer-reviewed papers

4. V. Daeichin, Z. Akkus, **I. Skachkov**, K. Kooiman, J. Sluimer, A. F. W. van der Steen, N. de Jong, J. Bosch, "Quantification of bound microbubbles in ultrasound molecular imaging," IEEE Transactions on UFFC, vol. 62(6), pp. 1190-200, Jun 2015.
5. T. van Rooij, V. Daeichin, **I. Skachkov**, N. de Jong, K. Kooiman, "Targeted ultrasound contrast agents for ultrasound molecular imaging and therapy," Int J Hyperthermia, Review, vol. 31(2), pp. 90-106, Mar 2015.
6. **I. Skachkov**, Y. Luan A. F. W van der Steen, N. de Jong, K. Kooiman, "Targeted microbubble mediated sonoporation of endothelial cells in vivo," IEEE Transactions on UFFC, vol. 61(10), pp. 1661-67, Oct 2014.
7. T.J.A. Kokhuis, **I. Skachkov**, B.A. Naaijken, L.J.M. Juffermans, O. Kamp, K. Kooiman, A.F.W. van der Steen, M. Versluis, N. de Jong, "Intravital microscopy of localized stem cell delivery using microbubbles and acoustic radiation force," Biotechnology and Bioengineering, - vol. 112(1), pp 220-227, Aug 2014.
8. K. Kooiman, T. J. A. Kokhuis, T. van Rooij, **I. Skachkov**, A. Nigg, J. G. Bosch, A. F. W. van der Steen, W. A. van Cappellen, and N. De Jong, "DSPC or DPPC as main shell component influences ligand distribution and binding area of lipid- coated targeted microbubbles," European Journal of Lipid Science and Technology, pp. 12117-1227, Jun. 2014.
9. Y. Luan, G. Lajoinie, E. Gelderblom, **I. Skachkov**, T. van der Steen, H.J. Vos, M. Versluis, and N. De Jong, "Lipid shedding from single oscillating microbubbles.," Ultrasound Med Biol, vol. 40, no. 8, pp. 1834-1846, Aug. 2014.
10. D. Maresca, **I. Skachkov**, G. Renaud, K. Jansen, G. van Soest, N. De Jong, and A. F. W. van der Steen, "Imaging microvasculature with contrast-enhanced ultraharmonic ultrasound.," Ultrasound Med Biol, vol. 40, no. 6, pp. 1318-1328, Jun. 2014.
11. T. Faez, **I. Skachkov**, M. Versluis, K. Kooiman, and N. de Jong, "In vivo characterization of ultrasound contrast agents: microbubble spectroscopy in a chicken embryo," Ultrasound Med Biol, vol. 38, pp. 1608-17, Sep 2012.



12. Y. Luan, T. Faez, E. Gelderblom, **I. Skachkov**, B. Geers, I. Lentacker, T van der Steen, M. Versluis, N de Jong, "Acoustical properties of individual liposome-loaded microbubbles," *Ultrasound Med Biol*, vol. 38, pp. 2174-85, Dec 2012.
13. M. S. Golovkina, **I. V. Skachkov**, M. V. Metelev, a. V. Kuzevanov, K. S. Vishniakova, I. I. Kireev, A.Ya. Dunina-Barkovskaya, "Serum-induced inhibition of the phagocytic activity of cultured macrophages IC-21," *Biochemistry (Moscow) Supplement Series A: Membrane and Cell Biology*, vol. 3, pp. 417-424, 2009.

### **Conference papers**

14. V. Daeichin, K. Kooiman, **I. Skachkov**, J.G. Bosch, A.F.W. van der Steen, N. de Jong, "Optimization of ultrasound contrast agent for high frequency ultrasound molecular imaging using subharmonic oscillation," 2014 IEEE International Ultrasonics Symposium (IUS), pp. 1766-1769, 2014.
15. T. Kokhuis, **I. Skachkov**, and B. Naaijken, "Microbubble spectroscopy of microbubble-loaded stem cells for targeted cell therapy," *The Journal of the Acoustical Society of America*, 135, 2310-2310 (2014).
16. T. Kokhuis, **I. Skachkov**, and B. Naaijken, "StemBells: Localized stem cell delivery using targeted microbubbles and acoustic radiation force," *The Journal of the Acoustical Society of America*, 135, 2310-2310 (2014)
17. T. J. A. Kokhuis, **I. Skachkov**, B. Naaijken, L. J. M. Juffermans, O. Kamp, A. F. W. Van Der Steen, M. Versluis, and N. De Jong, "Characterization of microbubble-loaded stem cells for targeted cell therapy," 2013 IEEE International Ultrasonics Symposium (IUS), pp. 1146–1149, 2013.
18. **I. Skachkov**, S. van Tiel, Y. Luan, T. van der Steen, K. Kooiman, M. Bernsen, N. de Jong, "Ultrasound contrast agents mediated cell labeling for MRI tracking," in *Ultrasonics Symposium (IUS)*, 2012 IEEE International, 2012, 2012, pp. 2278-2281.
19. Y. Luan, E. Gelderblom, G. Lajoinie, **I. Skachkov**, H. Dewitte, B. Geers, I. Lentacker, A. F. W. van der Steen, M. Versluis, N. de Jong, "Characterizing ultrasound-controlled drug release by high-speed fluorescence imaging," in *Ultrasonics Symposium (IUS)*, 2012 IEEE International, 2012, pp. 1-4.
20. V. Daeichin, A. Needles, **I. Skachkov**, K. Kooiman, J. G. Bosch, A. F. W. Van Der Steen, et al., "Optimized high frequency nonlinear contrast imaging using self-demodulation," in *Ultrasonics Symposium (IUS)*, 2012 IEEE International, 2012, pp. 1110-1113.
21. **I. Skachkov**, K. Kooiman, Ying Luan, A. F. W. van der Steen, N. de Jong, "Sonoporation of endothelial cells in vivo," in *Ultrasonics Symposium (IUS)*, 2011 IEEE International, 2011, pp. 1467-1469.
22. Y. Luan, T. Faez, **I. Skachkov**, E. Gelderblom, B. Geers, I. Lentacker, A. F. W. van der Steen, M. Versluis, N. de Jong, "Optical characterization of individual liposome-loaded microbubbles," in *Ultrasonics Symposium (IUS)*, 2011 IEEE International, 2011, pp. 1890-1893.

## PhD Portfolio

### Summary

#### Summary of PhD training and teaching activities

|  |  |                 |
|--|--|-----------------|
| Name PhD student: Ilya Skachkov<br>Erasmus MC Department: Biomedical Engineering, Thoraxcenter<br>Research School: COEUR | PhD period: 2010-2015<br>Promotor(s): Prof.dr.ir. N. de Jong<br>Prof.dr.ir. A.F.W. van der Steen<br>Dr. Klazina Kooiman<br>Supervisor: Dr. Klazina Kooiman |                 |
| 1. PhD training  |  |                 |
|  | Year   | Workload (ECTS) |
| General academic skills  |  |                 |
| - Presentation skills in science   | 2011   | 1.5             |
| - Ultrasound contrast agents. Theory and experiment. Orlando, USA  | 2011   | 0.4             |
| - Adobe Photoshop and Illustrator (Molmed)   | 2012   | 1.0             |
| Research skills  |  |                 |
| - Biomedical Research Techniques (Molmed)  | 2010   | 1.6             |
| - Article 9  | 2010   | 3               |
| In-depth courses   |  |                 |
| - Animal Imaging workshop (AMIE)   | 2010   | 1.8             |
| - Small Animal Imaging (Munster DTSL)  | 2010   | 1.5             |
| - In Vivo Imaging; from Cell to Organism (OIC)   | 2011   | 1.4             |
| - Winter School Therapeutic Ultrasound (ESPCI, Les Houches)  | 2011   | 1.5             |
| - Molecular biology in cardiovascular research (COEUR)   | 2011   | 1.5             |
| Presentations  |  |                 |
| - IEEE International Ultrasonics Symposium, Orlando, USA (poster)  | 2011   | 0.5             |
| - European Symposium on Controlled Drug Delivery, Egmond aan Zee, the Netherlands (poster)                               | 2012   | 0.5             |
| - IEEE International Ultrasonics Symposium, Dresden, Germany (poster)  | 2012   | 0.5             |
| - European Symposium Ultrasound Contrast Imaging, Rotterdam, the Netherlands (poster)                                    |  |                 |
| - Microbubble Symposium, Leeds, UK   | 2013   | 0.5             |
| - European Symposium Ultrasound Contrast Imaging, Rotterdam, The Netherlands (poster)                                    | 2013   | 0.5             |
|  | 2014   | 0.5             |
| International conferences  |  |                 |
| - IEEE International Ultrasonics Symposium, Orlando, USA   | 2011   | 0.9             |

## PhD Portfolio

|   |              |                        |
|---|--------------|------------------------|
| - European Symposium on Controlled Drug Delivery, Egmond aan Zee, the Netherlands     | 2012         | 0.6                    |
| - IEEE International Ultrasonics Symposium, Dresden, Germany (poster)                 | 2012         | 0.9                    |
| - European Symposium Ultrasound Contrast Imaging, Rotterdam, the Netherlands (poster) | 2013         | 0.6                    |
| - Microbubble Symposium, Leeds, UK  | 2013         | 0.6                    |
| - European Symposium Ultrasound Contrast Imaging, Rotterdam, The Netherlands (poster) | 2014         | 0.6                    |
| <b>Sonodrugs meetings, workshops and presentations</b>                                |              |                        |
| - Sonodrugs workshops   | 2010-2012    | 0.9                    |
| - Sonodrugs presentations (oral)  | 2010-2012    | 4.8                    |
| <b>Seminars and lectures</b>  |              |                        |
| - COEUR research seminars:<br>- Cardiovascular imaging                                | 2010         | 0.4                    |
|   |              |                        |
| <b>2. Teaching activities</b>   |              |                        |
|   | <b>Year</b>  | <b>Workload (ECTS)</b> |
| <b>Supervising practicals and excursions</b>  |              |                        |
| - AMIE workshop demonstrations  | 2013         | 0.3                    |
| - AMIE workshop demonstrations  | 2014         | 0.3                    |
| - Microinjection technique in chicken embryo for PhD students                         | 2010-2014    | 1.2                    |
|   | <b>Total</b> | <b>ECTS 30.3</b>       |